Faculty of Science and Engineering
Department of Petroleum Engineering

Experimental and Numerical Study of Ultrasonic Monitoring of Hydraulic Fracture Propagation

Amin Nabipour

This thesis is presented for the Degree of
Doctor of Philosophy
of
Curtin University

May 2013

Declaration

To the best of my knowledge and belief this thesis contains no material previously published by any other person except where due acknowledgment has been made. This thesis contains no material which has been accepted for the award of any other degree or diploma in any university.

Name:

Signature: *Date:*

Abstract

Hydraulic fracturing of rock is one of the most common stimulation techniques which has been practiced in the oil and gas industry for many years. Due to the complex nature of the phenomena associated with hydraulic fracturing in subsurface reservoirs, predicting the outcome of the operation is difficult. Hence, real-time monitoring techniques should ideally be used, to track the propagation of hydraulic fractures and to prevent the development of undesired consequences which become costly to manage. Conventional microseismic monitoring methods have limitations which inhibit gaining adequate information about the fracture geometry. The focus of this research, therefore, is on active seismic monitoring techniques which are shown to have several advantages over the more conventional methods.

In this study, particle flow code in two dimensions (PFC2D), a discrete element code, was used for numerical modelling of fracture propagation during stimulation operations. After systematic validation of the wave propagation capability of the code, for the first time it was shown that the easy to implement *smooth-joint* contact, which conventionally has been used for modelling rock joints for geomechanical applications, behaves in accordance with displacement discontinuity theory. Furthermore, taking advantage of the fluid-solid coupling capability of the code, the initiation and propagation of a straight hydraulic fracture was modelled and the re-distribution of stresses around the hydraulic fracture was analysed. For the first time, I have measured different ultrasonic events due to the development of such a modelled hydraulic fracture and compared the results with the displacement discontinuity theory, all aiming at determining fracture geometrical parameters in real-time. The numerical experiments provided valuable indications of the expected ultrasonic events to be observed in laboratory experiments and showed the high potential of discrete element methods for research in this area.

In order to confirm the numerical modelling results, it was necessary to design and build a physical fracture stimulation and ultrasonic monitoring system in the laboratory. I carried out considerable modifications on a unique true triaxial stress cell (TTSC), which had previously been used for geomechanical studies in our laboratory, in order to establish the necessary platforms for hydraulic fracturing monitoring experiments using a multi-channel ultrasonic data acquisition system.

Several complex challenges of the experiments were resolved including sample preparation, experiment procedure, and real-time data acquisition of microseismic recording during fracture stimulation.

Hydraulic fracture ultrasonic monitoring experiments were carried out for comparison with numerical modelling results, using the TTSC on cubic samples subjected to different stress regimes. Different ultrasonic events were recorded including transmissions, reflections, and diffractions. In several occasions, experimental results were compared to numerical results and good agreements were observed. Analysis of the ultrasonic measurements and their validation against the actual fracture path as well as the recorded real-time pressure and injection rate data demonstrated important advantages of active seismic monitoring of hydraulic fractures over the conventional techniques. These include the ability for early detection of fracture initiation, estimation of local fracture specific stiffness using spectral transmission coefficients hence estimation of local fracture width, and an accurate measurement of the fracture extent from its both wings hence determining the symmetric or asymmetric propagation regimes of the fracture over its propagation period.

Several novel observations made in this study showed the high potential of active seismic monitoring methods to be considered as the next generation of hydraulic fracturing monitoring techniques, providing the industry with a more comprehensive and more accurate monitoring of fracturing operations.

Acknowledgements

I would like to express my sincere appreciation to all those who provided me the possibility to complete this thesis.

My deepest gratitude goes to my research supervisors, Professor Brian Evans and Dr. Tobias Müller for persuading me to take on this research and being always available to offer me help and encouragement. Many tanks to my associate supervisor Dr. Peter Cundall for giving me valuable advice on numerical modeling part of this research.

I would also like to thank Associate Professor Bruce Hartley for his endless support and valuable help in development of the laboratory data acquisition system used in this study. Many tanks to Associate Professor Vamegh Rasouli for his help during the years I have been studying in the Department of Petroleum Engineering.

I would like to thank Curtin University and the Department of Petroleum Engineering for providing me with a scholarship and also to the Australia-China Natural Gas Technology Partnership Fund and MERIWA for the top-up scholarships paid towards my PhD study.

I would also like to thank the many friends and colleagues at the Department of Petroleum Engineering and CSIRO who contributed to this work by helping me in carrying out the experiments, taking the time to answer questions and giving advice and encouragement, in particular Dr. Mohammad Sarmadivaleh, Dr. Ali Saeedi, Dr. Ahmadreza Younessi Sinaki, Dr. Joel Sarout, Mr. Bruce Maney, Dr. Mohammad Sadegh Asadi, Mr. Bahman Joodi, and Mr. Sam Battah.

To:

My beloved wife, Miaad, for her unconditional support, love, and patience

and my family for their continued support and encouragement

Table of Contents

Page

List of Figures

List of Tables

List of Equations

Nomenclature

A	Area of smooth joint contact
AE	Acoustic emission
BPM	Bonded particle model
C	Centi
cP	Centipoise
D	Distance
d_h	Horizontal distance
d_v	Vertical distance
D	Darcy
DAS	Distributed acoustic sensing
DCHSA	Differential cased-hole sonic anisotropy
DDT	Displacement discontinuity theory
DEM	Discrete element method
DPS	Discrete particle scheme
DTS	Distributed temperature sensing
E	Young's modulus
$\boldsymbol{F}$	Force vector
F_n	Normal component of force vector
F^n	Normal contact force
F_s	Shear component of force vector
FDM	Finite difference method
FEM	Finite element method
FFT	Fast Fourier algorithm
G	Giga
HIT	Hydraulic impedance testing
Hz	Hertz
K	Kilo
k_n	Particle normal stiffness
K^n	Contact normal stiffness
$K_{n,spec}$	Normal specific stiffness of fracture

k_n^{sj}	Normal specific stiffness of smooth joint
k^s	Contact shear stiffness
k_s	Particle shear stiffness
$K_{s,spec}$	Shear specific stiffness of fracture
k_s^{sj}	Shear specific stiffness of smooth joint
K_{spec}^{dyn}	Dynamic specific stiffness of fracture
kg	Kilogram
KHz	Kilohertz
LVDT	Linear variable differential transformer
m	Metre
m	Mili
M	Mega
MPa	Megapascal
$\boldsymbol{n}_j$	Unit vector normal to smooth joint contact
PFC2D	Particle flow code in two dimensions
psi	Pound per square inch
P	Compressional (wave)
Pa	Pascal
PEEK	Polyether ether ketone
R	Particle radius
$\|R\|$	Reflection coefficient modulus
RSG	Rotated staggered grid
RA	Radioactive
s	Second
S	Shear (wave)
S	Sample
S_b	Total area of the model
S_g	Total area of particles
t	Time
T	Tera
$\bar{t}$	Thickness of disk

$\boldsymbol{t}_j$	Unit vector tangential to smooth joint contact
t_g	Group time delay
t_{ph}	Phase time delay
$\|T\|$	Transmission coefficient modulus
TPa	Terapascal
TTSC	True triaxial stress cell
TWRL	Tube wave reflection log
$u_{fractured}$	Displacement in the rock containing the fracture
u_{intact}	Displacement in the intact rock
$\boldsymbol{U}$	Translational displacement vector
U_n	Magnitude of normal translation displacement
U^n	Normal component of overlap
U_s	Magnitude of shear translation displacement
UDEC	Universal distinct element code
V	Wave velocity
V^s	Relative shear velocity of particles
VSP	Vertical seismic profiling
x	Distance
Z	Seismic impedance
ΔF^s	Shear contact force increment
Δt	Time step
Δu_n	Normal component of displacement discontinuity across the fracture
Δu_s	Shear component of displacement discontinuity across the fracture
ΔU^s	Shear component of contact displacement increment
θ	Phase angle
$\overline{\lambda}$	Radius multiplier
μ	Micro
μs	Microsecond
ν	Poisson's ratio
ρ	Density
σ_h	Minimum horizontal stress

σ_H	Maximum horizontal stress
τ_n	Normal stress on the fracture
τ_s	Shear stress on the fracture
φ_{2D}	Two-dimensional porosity
ω	Angular frequency

List of Publications

Nabipour, A., Evans, B., Mueller, T., Sarmadivaleh, M., "*Numerical and Experimental Study of Hydraulic Fracture Active Source Monitoring*", EAGE 2011, Vienna, Austria

Nabipour, A., Evans, B., Sarmadivaleh, M., "Active Monitoring of a Hydraulic Fracture Propagation: Experimental and Numerical Study", APPEA journal, 2011

Nabipour, A., Evans, B., Mueller, T., Sarmadivaleh, M., "*Evaluation of PFC 2D for Modeling Seismic Monitoring of Hydraulic Fracture*", 2nd International FLAC/DEM Symposium, February 2011, Melbourne, Australia

1 Introduction

1.1 Introduction to Hydraulic Fracturing

Historically, conventional hydrocarbon reservoirs, which have a sandstone layer containing hydrocarbons capped by an impervious shale layer, have been the most common reservoir types for producing hydrocarbons. However, the depletion of these fields and the lack of new discoveries of such conventional reservoirs over recent decades, plus the development of new technologies have resulted in the industry paying greater attention towards exploiting unconventional hydrocarbon reservoirs around the world. In Australia, for example, there are a number of tight gas reservoirs, that are reservoirs with extremely low porosity and permeability, which require some form of stimulation operations to be able to produce commercially. One of the most important technologies currently being practiced to aid commercial production of such hydrocarbon reservoirs is that of hydraulic fracturing. In the case of a tight gas reservoir, for example, the reservoir must be hydraulically fractured to provide conduits for hydrocarbons to flow at desirable rates into the producing wellbore.

A typical hydraulic fracturing operation consists of the injection of a special fluid, called the '*pad*', into the formation under high pressure conditions. The continuous injection of the fluid leads to creating planar discontinuities, called a hydraulic fracture in the rock. Figure 1-1 shows a schematic of a vertical hydraulic fracture induced in a reservoir layer. The fluid pressure prior to the rock cracking is initiated is called the *initiation pressure*. Due to the continuous flow of the fracturing fluid into the formation, the wellbore pressure increases to a maximum value called the *breakdown pressure*. Following this stage, the fluid pressure constantly decreases

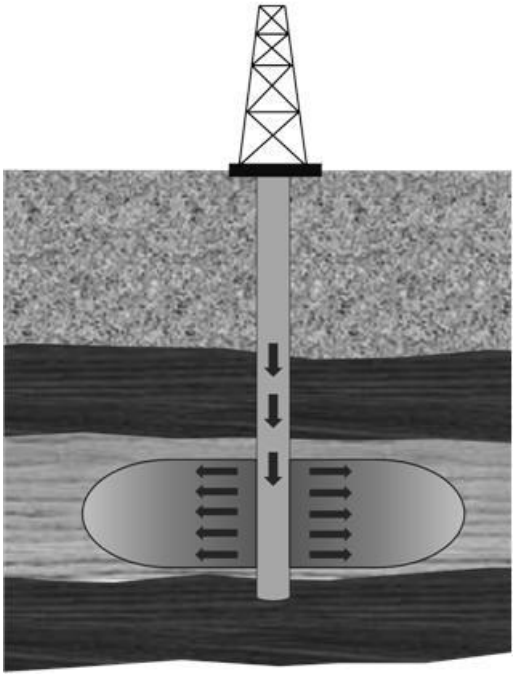

Figure 1-1 A schematic of hydraulic fracturing in reservoir section

which indicates the propagation of the induced hydraulic fracture into the rock. The resulting fluid-driven fracture provides a permeable path improving the flow of hydrocarbons into the wellbore. In the next step, a slurry containing a well-sorted mix of sand (or similar material), called a *proppant*, is injected into the fracture. The propping agent supports the fracture walls and prevents complete closure of the fracture, hence maintaining the permeability after removal of the fluid pressure. Depending on the purpose of the fracturing operation, it may be desirable to create single or multiple vertical or horizontal fractures.

The application of such hydraulic fracturing in the earth sciences is not new, nor is it solely limited to the stimulation of hydrocarbon reservoirs. Over recent decades, hydraulic fracturing has been used in different applications such as the stimulation of geothermal reservoirs (Sasaki, 1998; Legarth et al., 2005), water injection (Hunt et al., 1994), waste disposal (Keck and Withers, 1994; Hainey et al., 1999), fault reactivation (Board et al., 1991) and measurement of in-situ stresses of a formation (Zoback and Haimson, 1982; Raaen et al., 2001).

1.2 Hydraulic Fracture Monitoring

To ensure a successful outcome of a hydraulic fracturing operation, it is necessary to have a good understanding of the processes associated with the operation, and be able to determine the geometry of any fractures that have been created. It is normally desirable that the fracture remains contained in the reservoir interval and does not intersect the cap rock or nearby water-bearing formations since this may impose significant costs and unexpected delays in the operations. Furthermore, any misinterpretation in the hydraulic fracture propagation may cause the failure of proppant placement inside the fracture. To avoid such events, it would ideally be desirable to predict and, if possible, to determine precisely the geometry of the induced fracture in real-time.

To date, considerable laboratory, field, numerical and analytical work has been carried out to propose models capable of predicting the geometry of hydraulic fractures. Due to a large number of assumptions in such models, their results are associated with considerable uncertainties which necessitate their proper validation (Barree et al., 2002). In most of the studies, the induced fracture is assumed as a planar double-wing fracture (Sarmadivaleh, 2012). However, due to several factors influencing the induced fracture geometry (such as heterogeneity of formation properties, and the presence of natural discontinuities in the rock) this may not be the case in reality. Variation of such parameters significantly reduces the reliability of the models for predicting the growth of a hydraulic fracture. The process becomes even more complex when the hydraulic fracture propagates towards and arrives at a natural fracture. Developing methods to understand such mechanisms to predict their expected outcome is one of the most challenging problems currently under investigation (Cohen et al., 2012).

Diagnostics and mapping have shown that fractures in the real world are very complex and hence, many of the assumptions in the fracture models may be incorrect. Despite more than six decades of industry experience with hydraulic fracturing, it is still difficult to predict the behaviour of the fractures created during field operations. Although new models as well as modification of current criteria are currently under investigation, it is reasonable to claim that due to a variety of factors playing key roles in the hydraulic fracturing process, none of the methods can confidently foresee the outcome of the operation. There are reported cases showing

fracture behaviours largely different from what predicted by the fracture models. In reality, fractures can be induced in parallel planes, in different directions, in T-shaped form, with components in both horizontal and vertical directions, partially or entirely missing the perforated interval, or propagating into water-bearing formations. This is mainly due to the limited control on the fracturing process as well as a lack of understanding of a number of important factors such as the heterogeneity of formation physical and mechanical properties, the existence of natural fractures, and the complexity of the in-situ stress state. As a result, there are still some important questions about hydraulic fracturing such as the interaction between a hydraulic fracture and natural fractures (Renshaw and Pollard, 1995; Sarmadivaleh et al., 2011), proppant-related effects (Cleary et al., 1993), fracture tip region (Lenoach, 1995) and fluid lag at the fracture tip (Jeffrey, 1989; Adachi, 2001).

This discussion indicates that relying solely on any available fracture models, unfortunately cannot determine the actual path of the hydraulic fracture to be induced. It seems that a robust hydraulic fracture monitoring technique capable of determining the induced fracture geometry (and possibly physical properties) in real-time would be the ideal tool which not only would ensure the successful application of the fracturing operation, but also will help predict any unwanted event which might take place without an appropriate understanding of the geometry of the induced fracture. Such a monitoring technique could provide information on parameters such as the real-time fracture width and length, and the fracture growth rate. Furthermore, the product of such a monitoring technique could be used as a calibration against the proposed fracture models. Having real-time fracture geometry on-hand, can assist a more confident interpretation of the events occurring during hydraulic fracturing and gain a better understanding of the relevant phenomena. Accordingly, any available models can be verified or modified, based on the specific field conditions upon which they have been applied. This would be a major step towards predicting the final shape of a fracture during the fracturing operations.

Following the need to understand the geometry of an induced hydraulic fracture, a number of fracture monitoring techniques have been used so far. Furthermore, investigations are currently being carried out to establish efficient techniques for detecting, characterising, and monitoring hydraulic or natural fractures (or discontinuities). Such techniques focus on detecting and quantifying the specific hydraulic fracture and do not, for example, predict the result of another fracturing

operation going to be performed in the same wellbore. In order to achieve the most reliable results, it is preferred to use monitoring techniques combined with competent fracture simulators in order to monitor fracture data in real-time and simultaneously obtain valuable knowledge on the physics of the fracture growth in the reservoir (Barree et al., 2002).

The most common hydraulic fracturing monitoring technique practiced today is that using the microseismic method. In this method the small seismic activities resulting from the associated rock cracking are recorded by seismic receivers. Analysis of such events provides information on the extent of the fracture. These techniques have, however, a number of limitations such as a lack of data redundancy, low signal quality in some formations, inability to determine fracture width, and complex data processing and editing.

Another group of seismic methods which have the potential to be used as competent monitoring tools are those with active seismic sources. The focus of this research is on the application of these latter techniques in hydraulic fracture monitoring. In this research, active seismic monitoring of hydraulic fracture propagation is studied by performing numerical and experimental investigations.

1.3 Research Objectives

The overall aim of the research was to conduct numerical and experimental studies of ultrasonic waves affected by hydraulic fracture propagation. Within this broad theme, the specific objectives of this work can be summarised as below:

- To review the current methods used for monitoring hydraulic fracturing and to identify the weakness of these methods. Also, seismic methods used for characterisation of rock natural rock fractures are reviewed to identify their potential for application to hydraulic fracturing monitoring.
- To verify the capability of particle flow code in two dimensions (PFC2D), a discrete element code, for modelling ultrasonic wave propagation. For this purpose two different particle arrangements were used.

- To confirm the *smooth-joint* contact model, a contact model which has been conventionally used for modelling rock joints for geomechanical applications, and observe if it exhibits seismic behaviour in accordance with the displacement discontinuity theory. Afterwards, the aim is to simulate hydraulic fracturing monitoring using a smooth-joint fracture and record and analyse different fracture-induced seismic events.
- To numerically model the initiation and propagation of a straight hydraulic fracture by taking advantage of the fluid-solid coupling capability of the code and conduct hydraulic fracture real-time ultrasonic monitoring. Such a model will be shown to be a close representative for a laboratory hydraulic fracture. The results provide valuable information which greatly helps in the understanding and interpretation of experimental results.
- To develop a laboratory facility capable of performing multi-channel ultrasonic transmissions while a hydraulic fracture is being created in the sample. The modified laboratory set-up provides flexibility in the position of the source and receivers and allows capturing different ultrasonic events that occur due to the induced hydraulic fracture.
- To conduct preliminary ultrasonic transmission experiments on the fracturing fluid under different pressures and on dry and wet synthetic fractures under different normal stresses. The results of these experiments shed light on the effect of the pressure on transmission characteristics of the fracturing fluid used in this study as well as the effect of the fracturing fluid and normal stress on the transmission properties of a smooth fracture.
- To undertake vertical and horizontal hydraulic fracture monitoring experiments and record and analyse different fracture-induced ultrasonic events with the aim of determining fracture geometrical and physical properties. Such results provide valuable information on the nature of fracturing and possible application of active seismic methods for monitoring field hydraulic fracturing operations.

1.4 Research Methodology

As previously mentioned, this research focuses on active seismic monitoring of the hydraulic fracturing process. This subject is tackled by two different approaches: numerical modelling and laboratory experiments. Furthermore, the results obtained by both approaches are compared with the theoretical predictions.

Conventionally, wave propagation in rock has been modelled using methods based on continuum mechanics. In the numerical part of this study, however, a discrete element code is used. In this method, the medium is modelled by an assembly of round elements (particles) which can be bonded together. The discrete nature of the code provides the ability to model discontinuities in an efficient manner compared to the continuum mechanics codes. As the code has been mainly used for pseudo-static geomechanical modelling applications, its wave propagation capability is first validated by carrying out numerical experiments in arranged particle assemblies and comparing the results with verified codes. In the next step, a special type of contact, called a *smooth-joint* contact, which conventionally has been used for modelling rock discontinuities in geomechanical applications, is shown to exhibit seismic properties in accordance with the displacement discontinuity theory. This contact model provides a flexible tool for carrying out sensitivity analysis allowing different parameters of the fracture to be changed such as its normal and shear specific stiffness, friction angle, and cohesion. Afterwards, ultrasonic monitoring of a propagating fracture is simulated using this contact model. To do so, ultrasonic radiations are input in the model with a fracture of increasing length. The fracture-induced ultrasonic events are recorded by different receivers in the model. These events include reflections from the fracture surface, transmissions across the fracture, and diffractions from the fracture tip. The analyses of the results provide useful information on the expected experimental results and their interpretation. A further step in numerical modelling of hydraulic fracture monitoring is then taken by using the capability of the fluid-solid coupling of the code and inducing a numerical hydraulic fracture with a wedge-shape profile. Such a model provides valuable information on the propagation process of a hydraulic fracture and redistribution of stresses around the sample. The monitoring results are compared to those of the smooth-joint fracture monitoring results.

Building laboratory physical models has been proven to be a valuable approach for studying the details of complex processes such as hydraulic fracturing. Carrying out measurements on controlled laboratory experiments provides valuable information which may not be possible to obtain directly from the field measurements. The reality is that under laboratory conditions there is generally more control of the governing factors during the hydraulic fracturing process which reduces the uncertainties that are normally associated with the field hydraulic fracturing process. Furthermore, laboratory experiments allow the design of data acquisition configurations which in the case of field activities are too costly, difficult to achieve or not possible at all. In this study, a newly developed true triaxial stress cell was used for building physical models of hydraulic fracture propagation. For this purpose, I not only modified the multifunction stress cell, but I also developed a multichannel data acquisition system, and I installed and tested this system to deliver rapid ultrasonic data acquisition capability during the experiments. A number of ultrasonic experiments were carried out on dry and wet synthetic fractures to establish a comparison between the experimental results on smooth fractures with those predicted by the theory. As a result afterwards I performed horizontal and vertical hydraulic fracturing experiments on cubic samples. Different sets of ultrasonic data were recorded and analysed to extract information on real-time propagation of the hydraulic fractures including length, width and propagation rate. In several occasions the results were compared with numerical results and analytical predictions.

1.5 Research Significance

Active seismic monitoring of hydraulic fracture propagation is a relatively new research area which still has not been fully implemented in the industry. The current study aims at an investigation of seismic monitoring of hydraulic fracture propagation by numerical modelling as well as performing laboratory experiments, and comparing the results with the displacement discontinuity theory, a widely accepted theory for characterisation of rock fractures. It is hoped to be shown in this study that active seismic measurement methods have the potential to be used as a competent real-time hydraulic fracturing monitoring tool in field applications. A brief description of the significance of this research is given below:

- A discrete element code, PFC2D would be used in this study for modelling purposes. The wave propagation capability of the code would be verified systematically. This code has been rarely used for dynamic modelling of wave propagation and such a systematic verification would possibly be the first attempt of its type. This code has a number of advantages over the continuum mechanics codes. This verification would hopefully introduce PFC2D as a competent tool for studies on dynamic wave propagation in discrete particle assemblies.
- The smooth-joint contact model of PFC2D is hoped to be verified against the displacement discontinuity theory. To the best knowledge of the author, the seismic behaviour of this useful contact model had not been studied before. Furthermore, ultrasonic monitoring of propagating fractures modelled by this method was to be carried out to numerically show the expected fracture-induced seismic results
- The fluid-solid coupling capability of PFC2D was to be employed to model a straight hydraulic fracture in an arranged particle assembly. The study of the fluid pressure, fracture width profile and redistribution of stresses around the fracture could provide valuable information on the propagation process of the fracture and the fracture tip effects. Furthermore, ultrasonic monitoring was to be conducted on the numerical hydraulic fracture and different events including diffractions, reflections, and transmissions would be recorded and analysed. Such a numerical approach for seismic monitoring of hydraulic fracture propagation would be the first of its kind. This study could then establish the platform for further investigation of the subject using the discrete element models which allow studying the phenomenon at the micro-scale.
- A unique true triaxial stress cell (TTSC) would be used for the first time for hydraulic fracturing monitoring experiments. Due to several limitations in the initial design of TTSC, considerable modifications would be required to the equipment including the design of new spacers for transducer and development, testing and operating a multi-channel ultrasonic data acquisition system with source multiplexing capability. As a result of this study, the main platform for ultrasonic monitoring of different events, such as

hydraulic fracturing, was to be built in the geomechanics laboratory of the Department of Petroleum Engineering, Curtin University.

- Ultrasonic transmissions would be carried out on dry and wet synthetic fractures under different normal stresses and the specific stiffness of the fractures would be determined by measuring spectral transmission coefficients. The effect of normal stress and filling fluid on the specific stiffness of a fracture would be investigated. These results would then be used for interpretation of ultrasonic events observed in hydraulic fracturing monitoring experiments
- Horizontal and vertical hydraulic fracture monitoring experiments were to be conducted using the TTSC by employing a number of source and receiver transducers. Transmissions across the fracture, reflections from the fracture surface, and diffractions from the fracture tips were to be analysed. Transmission and reflections travel times were to be used to determine the location of source-receiver mid-points on the fracture.
- For the first time, the real-time specific stiffness of a hydraulic fracture would be determined by measuring spectral transmission coefficients and comparison of the results with the theoretical curves would be made. The changes in the specific stiffness of a fracture were to be studied to determine if they could assist in understanding the variations in the local width of the fracture. The degree of agreement with the theoretical predictions of the displacement discontinuity theory was of interest, which would indicate the necessity for including new effects, in the displacement discontinuity theory.
- Diffraction data from both wings of the vertical fracture would be studied to determine the initiation moment of the hydraulic fracture, which would be very difficult to determine solely based on fluid pressure data. Furthermore, the length profile of the hydraulic fracture as well as its propagation rate from its two wings were of extreme interest. This would hopefully show symmetric and asymmetric fracture propagation regimes in different stages of the experiment.

1.6 Thesis Structure

The previous sections in this chapter introduced the hydraulic fracturing and importance of hydraulic fracturing monitoring. Furthermore, the main objectives, methodology, and significance of this study were briefly explained.

Chapter 2 contains a broad review of the seismic response to rock fractures in general terms. Different theoretical, numerical, field and laboratory studies are reviewed in this section. The chapter then focuses on available hydraulic fracture monitoring techniques by dividing them into active and passive methods. The advantages and drawbacks of each group are explained accordingly.

Chapter 3 starts with an introduction to PFC2D and then the calculation procedure and main limitations of the code are discussed. Afterwards, point-source wave propagation is modelled and verified in a hexagonal particle arrangement. Similar modelling undertaken in a square assembly of particles is presented. In the next section, the focus is made on fracture simulation in PFC2D by employing a smooth-joint contact model. The procedure and results of the ultrasonic monitoring of smooth-joint fracture propagation are then discussed. Finally, it is shown how the fluid-solid coupling capability of the code is employed to model the propagation of a hydraulic fracture and monitoring results are discussed.

In Chapter 4 the different laboratory equipment used in this study is presented. This starts with an introduction on the core-holder equipment and is followed by a discussion of different parts of the TTSC. Next, major modifications carried out on TTSC, as a part of this study, are explained. These include the design of special spacers for the transducers and the development, testing and operation of a multi-channel data acquisition system. The chapter then presents the procedure for sample preparation and measurement of some of their properties. A number of practical aspects of ultrasonic data acquisition in the laboratory are explained later. This chapter finishes by explaining the procedure for conducting hydraulic fracturing monitoring experiments.

In Chapter 5 the experimental results are presented and discussed. These include the ultrasonic transmissions carried out on the fracturing fluid pressure as well as those conducted across dry and wet synthetic fractures under different normal stresses. The transmission results across the synthetic fractures are compared with the theory and representative fracture normal specific stiffnesses are calculated. The

results of horizontal and vertical hydraulic fracture monitoring experiments are included. Different transmissions, reflections, and diffraction data are presented and discussed in this section.

Chapter 6 draws the conclusions for this study. Afterwards, a number of recommendations are presented for further study in this area.

2 Theoretical Background

Fractures are some of the most important features observed frequently in different types of rock. They exist in various scales from micro cracks which are barely visible to faults having a size of a few kilometres in length. Fractures have significant effects on strength, mechanical and hydraulic properties of the rock. Without considering the existence of fractures in the rock, it is possible to make huge mistakes in estimating hydraulic, mechanical or strength properties of the rock. In some situations fractures can be considered very useful such as those which increase the permeability of a hydrocarbon bearing layer thus enhance the production rate considerably. However, in some other situations they can cause unwanted catastrophes such as reactivation of a fault which may cause destructive earthquakes or a leaking fault in a reservoir.

In the oil and gas industry particularly, natural fractures are of great importance. This is mainly due to the fact that the effective permeability of a rock may be under the influence of small or large fracture networks. Fractures can significantly enhance fluid flow in low permeability rocks, at least locally. For optimised production of hydrocarbons from low permeability reservoirs it is desired to connect the production wells to the natural fracture network of the rock. Hydraulic fracturing is by far the most common technique to increase permeability by ensuring a fracture intersects as many natural fractures as possible which leads to maximised production through enhanced permeability. Actually, in very low permeability gas reservoirs known as *tight gas reservoirs*, it is not possible to establish commercial production without carrying out some form of hydraulic fracturing.

It is desirable to use methods such as seismic characterisation to determine the location of the fractures in the rock. Furthermore, it would be very useful for improved hydrocarbon production to understand fracture properties such as roughness, aperture, stiffness, stress state and hydraulic conductivity. These properties have strong inter-relations with each other but there is still no robust

theoretical or numerical model which includes the individual effect of each of these factors (Toomey, 2001).

In this chapter firstly, a literature review on the seismic behaviour of rock fractures in general is presented along with the interaction of dynamic waves with such fractures. Secondly, focus is put specifically on hydraulic fractures, a particular type of fracture, and the different methods used for characterising them. These include methods which are based on passive seismic, active seismic or non-seismic techniques.

2.1 Response of Fractures to Seismic Waves

As mentioned above, fractures are important features of a rock which can significantly alter the different properties of a rock such as its mechanical and hydraulic properties. Characterising fractures is therefore of great importance. Seismic waves are commonly used for characterising fractures in the rock. For this reason it is essential to have an in-depth understanding of the interaction of seismic waves with fractures and the subsequent effects of a fracture on seismic wave propagation. Over the last few decades, a considerable amount of study has been carried out on the seismic characterisation of fractures and this is still a subject of ongoing research. The following sections contain a review of studies performed on seismic fracture characterisation, from field and laboratory studies, to theoretical and numerical studies.

2.1.1 Field and Laboratory Studies

Much has been studied about the effects of fractures on seismic waves in the field or at the laboratory scale. Thanks to the flexibility of laboratory physical models compared to field conditions, a variety of experiments have been carried out on natural as well as synthetic fractures. It has been shown that fractures in the rock exhibit seismic frequency-dependent properties which in turn cause a single fracture to behave differently when approached by seismic waves of different frequencies. Fractures are known to change the velocity and amplitude of seismic waves. Furthermore, there are a number of fracture-dependent waves shown to propagate along fracture interfaces. Morris et al (1964) reported that the amplitude of acoustic

borehole logs was decreased due to the presence of a single fracture in a borehole wall. A few years later, Yu and Telford (1973) reported that close to 96% of the wave energy was reflected back by a single fracture even after it was put under stress. Aki et al. (1982) carried out seismic experiments with the aim of estimating hydraulic fracture geometrical and physical properties. In that study, the presence of discrete planar cracks (fractures) was demonstrated by the strong attenuation of seismic waves which were transmitted across the fractures. It was reported that the attenuation effect of seismic waves is strongly frequency-dependent. Furthermore, they reported the conversion of the compressional mode to the shear mode and vice versa (P-to-S and S-to-P) across fractures. Laboratory results obtained by Kleinberg et al (1984) indicated that both the amplitude and phase of waves propagating across a fracture are affected by the fracture. Furthermore, reductions in acoustic velocity and amplitude (compared to their original values in the intact rock mass) obtained in cross-hole acoustic measurements by King et al. (1986) indicated an anisotropic and jointed rock mass. It has also been shown that the normal stress on a fracture's interface can affect its properties. Unloading a fracture was shown to cause a decrease in both velocity and amplitude of seismic waves transmitting across the fracture (Swolfs et al., 1981).

In some studies, a long wavelength approximation was used. In such a case, the fracture length and spacing is assumed to be very small compared to the dominant wavelength. As fractures are small, they are not considered as discrete fractures. This makes it possible to obtain fracture intensity and orientation from the splitting phenomenon that takes place when a polarised shear wave enters an anisotropic medium, called shear wave splitting (Crampin, 1988; Meadows and Winterstein, 1994).

Results of laboratory experiments on compressional and shear wave transmission across fractures showed that the stiffness of fractures increases by increasing the effective stress on the fracture (Pyrak-Nolte et al., 1990b). Pyrak-Nolte (1996) studied the inter-relationship among physical properties of the fractures by performing ultrasonic transmissions in laboratory experiments. The result indicated that the detectability of a fracture is dependent on its stiffness as well as is alteration of the seismic wave frequency. Furthermore, it was shown that the existence of interface waves along the fracture is dependent on fracture stiffness. With increasing fracture stiffness not only the velocity of the interface wave was

increased, but also the transmitted seismic frequency spectrum of the signal was altered (Pyrak-Nolte et al., 1996a).

Interface waves were also used to monitor rock failure. This was based on the fact that shear waves which are particularly sensitive to crack formation can couple into an interface wave which is propagating along the fracture. Because such an event is observed before any rock failure, the presence of an incipient interface wave was interpreted by a network of oriented but disconnected micro-fractures which evolve just before the rock failure (Pyrak-Nolte et al., 1996b). The laboratory study conducted by Nakagawa et al. (2000) indicated that compressional and shear waves normally incident on a sheared fracture are partially converted to waves having particle motions which are not present in the incident wavefield. The amplitude of the converted wave increased considerably with increasing shear stress applied to the fracture.

In an attempt to measure fracture compliance in the field, Lubbe and Worthington (2006) carried out seismic cross-hole surveys. Values obtained were reported to be an order of magnitude greater than the values obtained by other studies in laboratory experiments which were indicative of an increase in fracture compliance with the scale of the fracture medium. They stated that current understanding of wave propagation through fractured rock is limited by a lack of field-scale experimental data and they recommended field experiments to be conducted at a much broader range of scales. Lubbe et al. (2008) estimated normal and shear compliances of artificial fractures in laboratory experiments. Their results confirmed that the ratio of normal to shear fracture compliance is dependent on the fracture filling fluid. Acosta-Colon et al. (2009) experimentally investigated the effects of scale of measurement, i.e., field of view, on the interpretation of fracture properties from seismic wave propagation using an acoustic lens. They reported that the scale of the field of view affects the interpretation of fracture specific stiffness. It was concluded that non-uniform spatial distribution of fracture specific stiffness as well as overlapping geometric scales in a fracture cause a scale-dependent seismic response to the fracture. Full characterisation of a fracture therefore requires measurements to be conducted at different scales of field of view. Pyrak-Nolte et al. (2011) carried out laboratory experiments on synthetic orthogonal fractures in order to investigate the effect of fracture intersections on interface waves. It was shown that fracture interface waves are always present along fracture intersections. They

were also found to be also sensitive to stress concentrations along the intersections. They then introduced a potential method for locating and characterising fracture intersections by taking advantage of the distinct seismic response of intersection waves.

2.1.2 Theoretical Methods

The existence of fractures in a rock is known to affect the seismic waves by decreasing their velocities and amplitudes. The observed attenuation is related to a number of physical mechanisms such as frictional sliding of the fractures, viscosity and fluid flow in the fractures, and scattering (Pyrak-Nolte et al., 1990b). Over the last few decades, a number of different approaches have been used to theoretically study the effect of fractures on seismic waves. The most common methodology is to first develop expressions for the effective elastic moduli of the rock mass containing fractures and then relate these expressions of effective elastic properties to the velocity of seismic waves (O'Connell and Budiansky, 1974; Hudson, 1981; Crampin, 1984; Schoenberg and Sayers, 1995). This kind of approach is based on the assumption of interpreting long wavelength data, meaning fractures in the rock are assumed to be of small length and spacing compared to the seismic wavelength. They are each populated with different properties and their total effect is included in the effective elastic properties of the rock. The effective elastic properties of a rock mass containing fractures are theoretically based on factors such as fracture density, fracture shape and orientation, and pore fluid. By this means the overall effect of a rock fracture network on the elastic wave velocity and attenuation can be calculated.

It is obvious that the above mentioned type of approach does not explicitly take into account the effects of discrete fractures in the rock. Furthermore, the frequency dependent behaviour of fractures is not considered in such methods. As a consequence, their result is only valid when size and spacing of fractures are small compared to the wavelength. However, this is not always the case as fractures in the rock are present over a wide range of scales. There may be rock fractures having a size in the order of a wavelength. In such cases, the models based on a long wavelength approximation cannot be used for studying fractures as their assumption is violated.

For a complete understanding of seismic fracture response, one needs to take into account the discrete nature of rock fractures and include explicitly fracture parameters in the theoretical model. After characterisation of single fractures, one can then study the effect of multiple fractures on seismic waves (Toomey, 2001). The displacement discontinuity is a method for analytical representation of an imperfectly bonded interface between two elastic media. A fracture can be assumed to be such an interface across which the stress is continuous but displacement is discontinuous (Schoenberg, 1980). Compared to the first category of analytical methods mentioned above, the displacement discontinuity is an approach using which one can characterise fractures having size and spacing comparable to the wavelength. Therefore, compared to the first category of theoretical methods discussed above, this method suits better the application of hydraulic fracture seismic monitoring. The following section contains a more detailed discussion on this approach.

2.1.2.1 Displacement Discontinuity Theory

Displacement discontinuity theory (DDT) provides an analytical approach for modelling individual fractures in the rock. Also known as the linear slip model by Schoenberg (1980), DDT has been studied and successfully used for characterisation of laboratory fractures by many authors (e.g. Myer et al., 1985; Pyrak, 1988; Pyrak-Nolte et al., 1990b; Pyrak-Nolte and Nolte, 1992; Möllhoff et al., 2010). In DDT, a fracture is assumed to be smooth and infinitely long. In order to be assumed smooth, the mean fracture asperity separation needs to be much smaller than the wavelength. Furthermore, the wavelength must be smaller than the fracture spacing to be able to study a single fracture (Pyrak, 1988). In this model fractures can be either dry or fluid-filled. In fact, the representation of a fracture in this model is by a non-welded boundary condition along the fracture in which the stress across the fracture is continuous but the displacement across the fracture is discontinuous. That is why it is called the displacement discontinuity model. The ratio between the displacement and the stress across the fracture is dependent on a number of fracture physical properties. In DDT, this ratio is called the *specific stiffness*. The unit of specific stiffness is stress per unit of length (Pa/m). Specific stiffness is simply the inverse of specific compliance of the fracture. As should be expected, there are two different

specific stiffnesses defined for a fracture: fracture normal specific stiffness ($K_{n,spec}$) and fracture shear specific stiffness ($K_{s,spec}$). They are defined as follows:

$$K_{n,spec} = \frac{\tau_n}{\Delta u_n} \tag{2-1}$$

$$K_{s,spec} = \frac{\tau_s}{\Delta u_s} \tag{2-2}$$

$$\Delta u = u_{fractured} - u_{intact} \tag{2-3}$$

where τ is the stress applied to the fracture and Δu is the displacement discontinuity which is the difference between the resultant displacement in the rock with the fracture minus the displacement observed in the intact rock. $u_{fractured}$ is the displacement in the rock containing the fracture and u_{intact} is the displacement in the intact rock. Subscripts *n* and *s* refer to the shear or normal components of the variable respectively. Normal components are the components which are perpendicular to the direction of the fracture and shear components are those which are perpendicular to normal components (thus parallel to the fracture direction). Figure 2-1 shows a schematic of these parameters with respect to the orientation of the fracture.

It has been argued that fracture specific stiffness depends on various

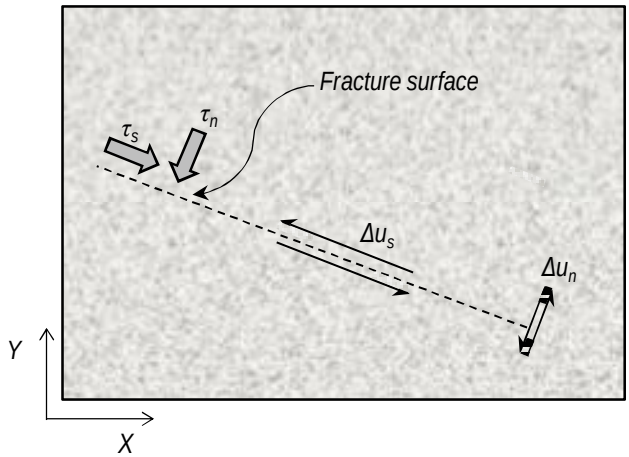

Figure 2-1 A schematic showing normal and shear components of stress and displacement used in displacement discontinuity theory

parameters such as elastic properties of the host rock, roughness of the fracture, area of contact between fracture faces, and aperture distribution (Brown and Scholz, 1986; Pyrak-Nolte and Nolte, 1992). Thus this parameter contains the combined effect of all these parameters on the seismic behaviour of the fracture.

The amplitude of a wave transmitted across a displacement discontinuity is shown to decrease by a certain amount depending on the fracture specific stiffness. Transmission and reflection coefficients for a plane wave incident upon a displacement discontinuity located in a homogeneous medium were derived by Schoenberg (1980). Furthermore, the solution for an incident plane wave upon a displacement discontinuity with different materials on each side of the discontinuity was developed by Pyrak (1988). Laboratory transmissions conducted by Pyrak-Nolte et al. (1987a) confirmed the appropriateness of DDT to model wave propagation across a fracture. The stiffness of the fracture was varied by applying different stresses to the fracture faces. It was reported with respect to DDT, that changes in group velocity and amplitude of laboratory transmissions are a function of frequency as well as the stiffness of the fracture. DDT showed that the time delay and reduction of signal amplitude occurred at the fracture and are not distributed throughout the whole rock medium as assumed by models based on effective moduli. Therefore, application of seismic tomographic techniques can provide information on location and stiffness of discrete fractures in the rock (Pyrak-Nolte et al., 1987a). Pyrak-Nolte et al. (1987b) reported that the increase in fracture stiffness due to increasing stress is due to the changes in fracture geometry (changes in size and distribution of asperities and voids). It was shown that such changes in stiffness of the fracture also considerably affected its hydraulic properties apart from its mechanical properties (Pyrak-Nolte et al., 1987b).

Frequency-dependent reflection coefficient modulus |R| and transmission coefficient modulus |T| for a plane compressional wave incident normally upon displacement discontinuity located in a homogeneous medium is as follows (Pyrak-Nolte et al., 1987a):

$$| R(\omega) | = \sqrt{\frac{\omega^2}{4\left(\frac{K_{spec}^{dyn}}{Z}\right)^2 + \omega^2}} \qquad (2\text{-}4)$$

$$|T(\omega)|=\sqrt{\frac{4\left(\frac{K_{spec}^{dyn}}{Z}\right)^2}{4\left(\frac{K_{spec}^{dyn}}{Z}\right)^2+\omega^2}} \qquad (2\text{-}5)$$

where ω is the angular frequency of the wave, Z is the seismic impedance of the medium containing the fracture ($Z = \rho V$ where ρ is density and V is the velocity of wave in the intact medium), and K_{spec}^{dyn} is the dynamic specific stiffness of the fracture. For incident P and S waves, the compressional and shear dynamic specific stiffness of the fracture are used, respectively. It is worthy to note that specific stiffnesses used in the previous equations are dynamic stiffnesses which are different from static stiffnesses of the fracture. Static stiffnesses can be obtained by pseudo-static loading of a fracture whereas dynamic stiffnesses are measured by analysing dynamic wave transmissions across the fracture. Generally, dynamic specific stiffness of a fracture is larger than its static specific stiffness. Nevertheless, in this study the term fracture specific stiffness refers to the dynamic specific stiffness of the fracture unless otherwise mentioned. Figure 2-2 shows how transmission and reflection coefficient moduli (|T| and |R|) vary as a function of fracture normal specific stiffness. These values are obtained from equations 2-4 and 2-5 for a wave of 1 MHz frequency normally incident on the fracture. The assumed parameters are a rock bulk density of 2000 kg/m^3 and compressional wave velocity of 4000 m/s. As can be seen, the stiffer the fracture, the higher portion of wave energy that is transmitted and the lower the portion of wave energy that is reflected from the fracture.

Besides calculating transmission and reflection coefficients of waves, DDT also predicts a group time delay in a wave interacting with a fracture. The equation is as follows (Pyrak-Nolte et al., 1987a):

$$t_g(\omega) = -\frac{d\theta(\omega)}{d\omega} = \frac{2\left(\frac{K_{spec}^{dyn}}{Z}\right)}{4\left(\frac{K_{spec}^{dyn}}{Z}\right)^2 + \omega^2} \tag{2-6}$$

The above equation is not unique with respect to the specific stiffness of the fracture (Möllhoff and Bean, 2009). Assuming arbitrary values of seismic impedance, the group time delay increases with increasing fracture specific stiffness up to a certain value and then decreases by increasing fracture specific stiffness beyond that certain value.

On the other hand, a phase delay which occurs due to a fracture is a unique function of fracture specific stiffness. Phase delay continually decreases by increasing specific stiffness of the fracture. Phase delay is determined as follows (Möllhoff and Bean, 2009):

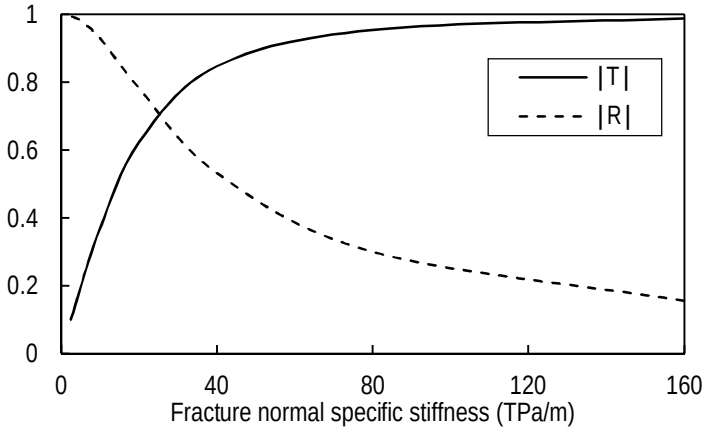

Figure 2-2 Transmission and reflection coefficients as a function of fracture normal specific stiffness

$$t_{ph} = -\frac{\theta(\omega)}{\omega} = -\frac{1}{\omega}\arctan\left(\frac{\omega}{2\left(\frac{K_{spec}^{dyn}}{Z}\right)}\right) \tag{2-7}$$

Figure 2-3 shows how P-wave phase time delay and group time delay vary with changes in fracture normal specific stiffness. Parameters used in this plot are the same as those used in Figure 2-2. The plot shows that phase time delay exhibits a unique decreasing trend when fracture specific stiffness increases. However, group time delay behaviour is not unique with respect to fracture specific stiffness. It is understood that group time delay is always smaller in magnitude than phase time delay.

Pyrak-Nolte et al. (1990b) derived complete solutions for seismic wave reflection, conversion, and transmission across a displacement as well as a velocity discontinuity. The ratio between seismic-induced stress and seismic-induced particle velocity was described by defining a specific viscosity for a fluid-filled displacement discontinuity. It was shown that a velocity discontinuity results in frequency-independent transmission and reflection coefficients and zero time delay as opposed to frequency-dependent coefficients and finite group time delay for a displacement discontinuity. Laboratory results of shear wave transmission across dry and saturated fractures were described best by a combined displacement and velocity discontinuity while for an incident compressional wave, use of the displacement discontinuity

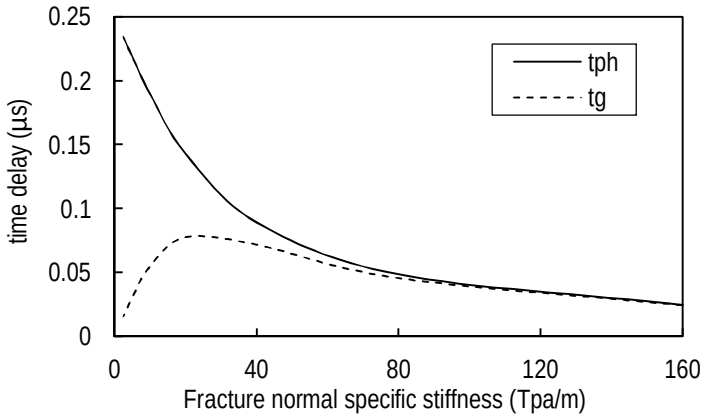

Figure 2-3 Phase time delay and group time delay versus fracture normal specific stiffness

model results in best fits.

Ignoring converted and reflected waves, Pyrak-Nolte et al. (1990a) derived expressions for transmitted wave amplitudes and group velocity for multiple parallel displacement discontinuities. The derived parameters were shown to be dependent on frequency, angle of incidence, and polarisation in the case of shear waves. Pyrak-Nolte and Nolte (1992) stated that different frequencies sample different subsets of the fracture geometry. Therefore, frequency-dependence of fracture stiffness may be a result of fracture geometrical properties. They reported that the highly inhomogeneous distribution of fracture stiffnesses results in a strong frequency dependence of fracture dynamic stiffness. Gu et al. (1996b) investigated the details of reflection, transmission, and conversion of plane wave incident upon a fracture at arbitrary angles. Their closed-form expressions revealed that a single fracture can produce a number of diagnostic waves. Boadu and Long (1996) introduced a new model, the modified displacement discontinuity model (MDD) in which fractures are treated as transmission lines for the passage of seismic waves. Gu et al. (1996a) theoretically and numerically investigated interface waves along a single fracture in an elastic solid. Their analysis yielded two dispersive equations for symmetric and asymmetric interface waves. Displacement discontinuity theory has been modified by Cai and Zhao (2000) in order to include the effect of multiple planar fractures which are periodically spaced in the medium. In their modified model there is no limitation on fracture spacing to wavelength ratio.

Again it is essential to note that the value of specific stiffness obtained from measurements of dynamic waves is generally different from those obtained from quasi-static experiments. Therefore it is required to distinguish between two terms: fracture dynamic specific stiffness and fracture quasi-static specific stiffness. As shown by Pyrak-Nolte and Nolte (1992) dynamic specific stiffness of a fracture is dependent on the frequency of the wave. From this point of view one can consider the quasi-static specific stiffness of the fracture as the limit of infinite frequency of dynamic specific stiffness of the fracture.

When using DDT it is important to bear in mind that this theory has its own limitations. For example, rough fractures are not basically considered in this theory. So it cannot be used for studying scattering from a fracture due to its rough faces. Furthermore, the effect of a fracture tip is not included in DDT because the fractures

are considered continuous. Furthermore, if the width of the fracture becomes large, the reliability of DDT results predicted, decreases (Groenenboom, 1998).

2.1.3 Numerical Methods

In parallel with the theoretical and experimental studies, a variety of numerical techniques have been developed for investigation of wave propagation in fractured media as well as the interaction of seismic waves with fractures. They can be categorised in two general groups: continuum numerical methods and non-continuum (discontinuum) numerical methods. The following sections provide a review of each of these two categories.

2.1.3.1 Continuum Methods

Generally, wave propagation in fracture media is numerically modelled using methods which are based on continuum mechanics such as the finite difference method (FDM) and the finite element method (FEM) (O'Brien et al., 2009). Mal (1970) numerically solved the boundary integral equations controlling fracture seismic behaviour for a range of wave frequencies incident upon a penny-shaped crack located in an infinite isotropic medium. Bouchon (1987) presented a boundary integral equation technique based on the potential theory approach to the Helmholtz equation and solved the integral equations using the discrete wavenumber method. Pointer et al. (1998) solved integral equations representing a fracture of arbitrary shape by implementing the boundary element method (BEM). Gu et al. (1997) conducted the two-dimensional boundary element simulations to investigate a Rayleigh-type fracture interface wave generated by a DDT-based fracture. They observed symmetric and asymmetric fracture interface waves in their numerical model.

Coates and Schoenberg (1995) numerically modelled fractures in finite difference grids. They accounted for the effect of a fracture on seismic waves assuming the traction vector and the displacement discontinuity vector to be linearly related to the fracture compliance matrix. As stated by Toomey (2001), such an implementation is effective when the fracture is in the direction of finite difference grids but it becomes difficult to use the same approach for a fracture with arbitrary non-planar fractures.

For modelling non-planar fractures an effective medium theory which is based on the linear slip model can be used (Coates and Schoenberg, 1995). In such a model, finite difference grids representing the fracture have elastic properties different from other grids. In this way it is possible to turn the behaviour of such a fracture as close as possible to a linear slip interface. As one has flexibility in choosing the grid cells representative of the fracture, this method can handle modelling fractures with arbitrary shape and direction. Generally grid cells representing the fracture are chosen to have lower values of seismic velocity and density compared to the grid cells of the intact medium. Fracture modelling using this approach is not associated with a discontinuity of stress or displacement so it can be said to be welded. Such a fracture is actually identical to the simulation of a "thin layer" in lithology terms which has elastic properties different from its surrounding medium (Toomey, 2001). Groenenboom (1998), and Groenenboom and Fokkema (1998) proposed a thin viscoelastic layer in a homogeneous elastic environment as a simplified fluid-filled fracture model. It was also discussed under which conditions the thin layer model reduces to a linear slip model. The thin layer model was implemented using finite difference code. The grid spacing was reduced for cells representing the fracture in order to capture small variations that occur across the fracture with a small width (Groenenboom, 1998; Groenenboom and Falk, 2000). The model was able to capture scattering of seismic waves across the fracture. Furthermore, different types of fracture interface waves were possible using this model. Although such events were captured in the thin layer model, that model did not consider the physics of scattering that occurs in real fractures. Orlowsky et al. (2003) used a rotated staggered grid (RSG) to accurately simulate wave propagation in fractured media. The finite difference scheme was used for comparison of predictions given by several effective medium theories. Vlastos et al. (2007) conducted a study of multiple scattering of seismic waves due to an evolving fractured network. Burns et al. (2007) estimated different fracture properties from scattering of seismic waves. Numerical and field results showed that the scattered energy varies with the seismic acquisition direction with respect to the orientation of parallel fracture sets. A scattering index method was used which could estimate the fracture orientation by comparing variations in wavelets recorded from azimuthal stacks.

Hall and Wang (2012) included fractures in their finite-difference forward modelling using the formulation of an equivalent medium. Different equations for the linear slip model, an open fluid-filled fracture, and more complicated fracture models of small cracks in a welded area were implemented in their model. Different waves were identified as P or S arrivals from the fracture tip, reflections, transmissions, and head waves and used for comparison of fractures.

2.1.3.2 Non-continuum Methods

There is another category of numerical methods which are based on non-continuum (discontinuum) mechanics. Chen and Zhao (1998) used the discontinuum-based numerical code, Universal Distinct Element Code (UDEC) for modelling blast wave propagation through fractured rocks. Fractures in the rock were modelled by considering a number of discrete blocks with planar interfaces between them. Each block was discretised into a finite difference mesh. Numerical results showed that the velocity of the blast wave was reduced by the presence of the joints. Furthermore, a velocity reduction was shown to be directly related to the compliance of the joints.

The discrete element method (Cundall, 1971) is a method that has been used for studying rock slopes, joints and fractures. Micromechanical behaviour of granular materials can be effectively modelled using the discrete element method (DEM) (Cundall and Strack, 1979). In DEM the granular material is numerically modelled by an assembly of discrete particles which can be bonded together. Particles can be sorted in arbitrary orders. They can also be randomly distributed in the model in order to account for the inhomogeneous texture of the rock. Discrete particles interact mechanically with their neighbouring particles depending on their contact law (Potyondy and Cundall, 2004).

The discrete element method has also been used for modelling wave propagation in granular assemblies. Experimental and numerical studies carried out on unbounded circular particles showed that the dynamic load transfer and wave propagation in such assemblies depend on the geometrical arrangement of particles in the assembly as well as the constitutive contact law between particles (Shukla, 1991; Zhu et al., 1991; Sadd et al., 1993; Sadd et al., 2000). Sadd et al. (2000) reported that wave speed in granular materials modelled by DEM is dependent upon the stiffness of the inter-particle contacts and distribution of branch vectors along the

propagation direction. Furthermore, the wave amplitude was shown to be dependent on the number of branch vectors in the direction of wave propagation.

Li and Holt (2002) used Particle Flow Code (PFC), a DEM-based code (Itasca Consulting Group, 2008), for modelling wave propagation in the reservoir rock. A strip of particles were chosen to be the movement source. The disturbance of the particle velocity propagated in the particle packing was recorded at several points as the receivers. The resulting wave velocities were used for calculating dynamic elastic moduli of the granular assembly which was compared to the recorded static moduli. O'Brien and Bean (2004) presented a three-dimensional elastic lattice method for simulation of seismic waves. They took into account any heterogeneity in the model by changing the elastic constants. Mouraille and Luding (2008) performed dynamic simulation of wave propagation in dense granular media with a narrow polydisperse size distribution and a linear contact force law. It was reported that in all disordered cases, a low frequency band transmitted the wave well, while higher frequency components were attenuated. Li and Fjær (2008) used a new constitutive contact model in the discrete element method to investigated the stress-dependence of static and dynamic moduli of sandstone. Thomas et al. (2009) conducted DEM numerical modelling of wave propagation to investigate the existence of wave dispersion effects in a set of resonant column tests on dry granular soils.

Because in DEM bonds between particles have finite strength, in the event of excessive loading bonds may break. One can assume that the discrete particles are representative of grains of the real granular material and bond breakages are modelling micro-cracking that occurs in the rock between its grains. Such capabilities of DEM have made it a suitable candidate for modelling cracking in the granular materials. Setting a low damping in the numerical model one can allow microseismic events to occur due to rock cracking (also called acoustic emissions) to propagate in the rock. Using this approach, DEM has been used for modelling seismicity due to rock cracking and failure (e.g. Hazzard et al., 1998; Hazzard et al., 2000; Hazzard and Young, 2004). Hazzard et al. (1998) carried out micromechanical modelling of acoustic emissions (AE) due to cracking of rocks. The mechanics of failure was modelled at the micro-scale while the models were run dynamically (with low numerical damping) to allow for dynamic fracture propagation and propagation of acoustic emissions. It was shown how to obtain information on parameters such as location, size and type of fractures by inversion of the synthetic AE model.

Hazzard et al. (2002) presented a distinct element numerical model to simulate fluid injection into a granite reservoir and recorded fluid-induced seismicity. Results showed that the deformation and resulting seismicity in the model occurs ahead of the fluid pressure front. Zhao and Young (2009) used PFC for numerical simulation of seismicity induced by hydraulic fracturing in naturally fractured reservoirs. Numerical microseismic records successfully showed the propagation of a hydraulic fracture as well as the interaction of a hydraulic fracture with the natural fractures in the rock.

The effect of fractures of granular media on seismic wave propagation has also attracted researchers to use DEM on this subject. Toomey and Bean (2000) presented a 'discrete particle scheme'(DPS), a particle-based model for simulation of wave propagation. Results obtained by DPS was compared with a high-order finite difference solution to the wave equation and found to be accurate. DPS was shown to be an alternative to traditional continuum-based wave simulators. It can provide new capabilities in numerical modelling of wave propagation by considering more realistic random particle sizes, properties, and distributions. It was shown that DPS can accurately capture the effects of a fracture in the rock. Furthermore, numerical modelling of wave propagation using fractures modelled in DPS showed that seismic data, in theory, can be used to distinguish fracture tensile and compressional properties (Toomey, 2001; Toomey et al., 2002a).

Nonlinear fractures are shown to leave a characteristic signature on the wavefield. Based on this fact, it was suggested that seismic data may be inverted to obtain cohesive as well as compressional properties of fractures (Toomey et al., 2002b). A discrete particle scheme was also successfully used for modelling field cross-well data (Lubbe and Worthington, 2006).

Potyondy and Hazzard (2008) numerically loaded a bonded particle of Crosland Sandstone in a polyaxial cell. During loading, dynamic and static moduli of the rock was measured. The dynamic moduli were measured using recorded P and S-wave velocities during loading cycles. The anisotropy which developed due to the applied stress as well as the induced damage (cracking) in the rock was then quantified. Möllhoff and Bean (2009) validated the two-dimensional discrete particle scheme for measurement of rock fracture compliance using transmission and reflection coefficients, group delay, and phase delay. Furthermore, the numerical scheme was used for studying the effect of multiple fractures on seismic waves.

Later DPS was employed for comparing rock fracture compliance measurement from different time delays of elastic waves across the fracture (Möllhoff et al., 2010). Resende et al. (2010) simulated the interaction of stress waves and rock fractures in a particle micromechanical model called bonded particle model (BPM). A new contact constitutive model was applied to the particles in the joint walls. Transmitted and reflected waves were extracted and used for calculation of joint dynamic stiffness.

In this study, PFC is used for micromechanical modelling of wave propagation in granular media. Furthermore, PFC capabilities in modelling fractures are examined against theoretical predictions of displacement discontinuity theory. Such capabilities are then employed for modelling real-time monitoring of a propagating fracture. These are explained in detail in Chapter 3.

2.2 Hydraulic Fracture Monitoring Techniques

Hydraulic fractures can be thought of as a special type of fracture. Based mostly on techniques used in fracture characterisation, a number of techniques for monitoring geometry and other properties of hydraulic fractures have been developed. This section contains a review of the attempts made on monitoring hydraulic fractures. Depending on the nature of the techniques, they are categorised in different groups.

2.2.1 Passive Seismic Methods

The most common hydraulic fracture monitoring technique currently in use is microseismic monitoring which is sometimes called *Passive Monitoring*. There is considerable published material on analytical, numerical, experimental and field studies carried out on microseismic monitoring techniques (e.g. Falls et al., 1992; Wills et al., 1992; Zhengwen et al., 2003; Le Calvez et al., 2007; Dobroskok and Linkov, 2008; Maxwell et al., 2009; De La Pena et al., 2010; Johnson et al., 2010). This method is based on recording and interpreting microseismic activities that occur due to the evolution of a hydraulic fracture (Toksoz et al., 1996; Peterman et al., 2005). This is mainly due to de-stabilisation and failure of planes of weakness in the formation zone near the hydraulic fracture. Using this method it is possible to determine extension of the hydraulic fracture. In some field activities the microseismic monitoring technique was used in conjunction with other hydraulic

fracture characterisation and monitoring techniques to provide better understanding of the fracture geometrical parameters (House and Shemata, 2008; Johnson et al., 2010).

A limitation of microseismic methods is the lack of data redundancy as the sources are not repeatable. For some materials the level of microseismic activities are very low which reduces data quality. Also, extracting reliable information from such data requires complex data processing and editing. Besides, microseismic methods are limited and do not readily allow a determination of width or permeability of the induced fracture (Henry, 2005). Advancements and new technologies have also altered the way microseismic monitoring is carried out. For example, a technique called Distributed Acoustic Sensing (DAS) was used recently which provides the ability to measure in-wellbore microseismic activities at the surface (Molenaar et al., 2011).

2.2.2 Active Methods

2.2.2.1 Non-seismic Methods

These methods can provide information on fracture height, width as well and proppant placement effectiveness. For example, electrical borehole scans (Luthi and Souhaite, 1990), have been used for detection of induced or natural fractures. Tiltmeters are sensitive electronic sensors which can detect and measure variations in earth tilt caused by deformations due to events such as hydraulic fracturing. Surface tiltmeters can measure dip and azimuth of an induced hydraulic fracture while those used downhole, are used to determine height and length of the fracture (Barree et al., 2002). This method is limited in terms of location of the tiltmeter which needs to be close enough to the wellbore. Lecampion et al. (2005) investigated the resolution of the dimensions and orientation of hydraulic fractures from tilt measurements. They conclude that at a distance longer than twice the characteristic length of the fracture, tiltmeter measurements are not able to determine dimensions of the fracture. There are also downhole tiltmeters which are placed inside the wellbore and can provide information on the width of the hydraulic fracture (Bennett et al., 2006).

Another technique used for monitoring hydrocarbon fluid flow through the fracture into the wellbore is called fibre optic distributed temperature sensing (DTS). DTS is shown to be capable of showing effectiveness of hydraulic fracture

treatments (Sierra et al., 2008). However, it cannot provide detailed information on the geometry of hydraulic fracture.

Spectral gamma ray data was also shown to be advantageous in estimation of vertical fracture heights following hydraulic fracture stimulation (Anderson et al., 1986). Other techniques used for evaluating the geometry of the hydraulic fracture include radioactive (RA) tracers (Holditch et al., 1993; Raymond, 1996; Reis et al., 1996; Scott et al., 2010) which can reasonably evaluate the success of hydraulic fracturing and proppant placement.

2.2.2.2 Active Seismic Methods

Another group of techniques that are shown to be useful for hydraulic fracture monitoring are *Active Seismic* methods in which the sources are controllable. Over the last few decades, both field and laboratory measurements proved the applicability of such methods for hydraulic fracture monitoring. Field measurements are carried out at different scales, from ultrasonic and sonic ranges to frequencies close to the seismic range. Included in this group are for example borehole televiewers, normal sonic logs, sonic anisotropy logs, Stoneley wave measurements, vertical seismic profiling (VSP), and cross-hole measurements. One of the first experimental attempts using the application of active source seismic measurements for monitoring propagation of a hydraulic fracture was made by Medlin and Masse (1984) which was followed by more laboratory studies on the subject.

Active source methods not only provide repeatability of the source and therefore data redundancy which is not present in the case of passive microseismic methods, but they also provide a degree of flexibility in choosing the location of the source. This assumes the adaptability of the data acquisition process enables acquiring different desirable seismic waves. Therefore, seismic waves including different types of body and interface waves are used for characterization of fractures including natural and hydraulic fractures. Active seismic methods have different depths of investigation. Each method can normally be considered to be a near-field method, a mid-field method, or a far-field method.

Near-field methods

Near-field methods can investigate the areas close to the wellbore and normally use higher frequencies in the sonic or ultrasonic ranges. Some of the

examples of application of seismic waves in the sonic and ultrasonic range are borehole televiewers which acquire acoustic images of the wellbore wall (Zemanek et al., 1970; Liu, 1985) and wellbore sonic logs (Newberry et al., 1985) which have been used for detection and characterisation of induced and natural fractures on the wellbore wall. Liu (1985) reported that height and dip angle of wellbore fractures can be determined when changes in amplitude and velocities obtained from sonic logs are used in conjunction with data from a dipmeter or a borehole televiewer.

Another seismic-based method for characterization of a hydraulic fracture is based on sonic anisotropy logs. Nikitin et al. (2006) measured differential cased-hole sonic anisotropy (DCHSA) by analysing cross-dipole shear sonic data recorded before and after hydraulic fracturing treatment. Their DCHSA measurements provided accurate results of propped hydraulic fracture height and orientation which were used for calibration of their pseudo-3D planar fracture model. Sonic anisotropy logs where also used with RA tracers in order to understand fracture height and revealing the complexities present in field fracturing treatments (Scott et al., 2010). It is worth mentioning that application of sonic anisotropy logs in such studies does not provide a real-time monitoring tool for hydraulic fracture geometry and it solely detects the changes made by the fracture, by comparing data acquired before and after fracturing operations. Near-field methods provide geometrical information only on the limited portion of the fractures which intersect the wellbore wall and for example cannot be used for monitoring the length of a hydraulic fracture away from the wellbore.

Mid-field methods

The study of Stoneley waves can be considered as a mid-field range method. The Stoneley wave is shown to be sensitive to open fractures on the wellbore wall. The attenuation of a Stoneley wave is reported to be due to fluid flow into the existing permeable fractures on the wellbore wall (Tang and Cheng, 1989). The same mechanism causes reflection of Stoneley waves which provides the ability to measure Stoneley wave transmission and reflection across a fracture for estimating the width of the fracture (Henry, 2005). Based on this fact a number of attempts were made to determine a borehole fracture's width by investigating the interaction of a Stoneley wave with an infinite planar fracture. Hornby et al. (1989) reported that their field data using reflected Stoneley waves showed good agreement with borehole

televiewer analysis. Tang and Cheng (1993) formulated a simple theory for calculation of Stoneley wave propagation across various inhomogeneous structures including fluid-filled fractures. Medlin and Schmitt (1994) used a tube wave reflection log (TWRL) to gain information on a hydraulic fracture's location, conductivity, and height. TWRL is based on reflection and attenuation of tube waves which is due to fluid flow through perforations into the hydraulic fractures. Paige et al. (1995) used the hydraulic impedance testing (HIT) technique for detection and measurement of formation fractures. In HIT, a pressure pulse is introduced into the well in an attempt to excite slow channel waves in the fracture and the resulting pressure response of the wellbore is interpreted with the aim of estimating fracture dimensions.

Kostek et al. (1998) developed a series of analytical models for interpreting Stoneley wave reflections from fractures intersecting a wellbore. They considered the effect of enlargements in borehole size (such as washouts) and fractures on the transmission and reflection coefficients of Stoneley waves. A few years later, Henry (2005) carried out a literature review on the application of Stoneley waves for borehole fracture characterisation. It was reported that until that time many authors had focused on the effect of permeability of an infinite fracture using Stoneley wave amplitudes (e.g. Hornby et al. (1989), Tang and Cheng (1993), and Kostek et al. (1998)), but not much effort was made on considering a finite-length fracture. Henry (2005) generalised the rigid formation model developed by Hornby et al (1989) and carried out a sensitivity analysis of transmission and reflection coefficients of the Stoneley wave to the frequency, elastic properties of the medium, and finite fracture and wellbore dimensions. The interaction of a Stoneley wave with the fracture tip was also considered in the model. To characterise fractures using Stoneley waves, an optimised frequency rage was suggested to be used in the field. Over such an optimised frequency range, not only the interaction of a Stoneley wave with fracture tip is visible, but also Stoneley wave reflections and transmissions are sensitive enough to be affected by the width of the fracture. It was also shown that in addition to the frequency and elastic properties of the surrounding medium, the finite length of the fracture affects transmission and reflection coefficients of the Stoneley wave. This is because of the resonant frequency of the fracture which is related to the fracture length. Furthermore, it was reported that in frequency ranges different from

the resonant frequency of the fracture, the transmission coefficient of the Stoneley wave is a function of fracture width.

A semi-analytical model was presented for studying the effect of fracture properties on the sonic imaging process by analysing amplitude and phase of the diffracted events (Henry, 2005). For that purpose, a direct scattering approach was used by implementing wavefield decomposition and the finite fracture was modelled by a distribution of surface sources of the deformation rate. The displacement and stress response of the fracture was estimated by the linear slip theory. It was reported that the computed scattered wavefield was sensitive to size, profile, and compliance of the fracture. Moreover, the amplitude of the diffraction events from the tip of the fracture were shown to be sensitive to how smooth the compliance of the fracture decreased to zero, suddenly or gradually tapering off.

Laboratory experiments on a finite fracture performed by Henry (2005) confirmed that in addition to the applicability of estimating fluid-filled fracture width using Stoneley wave transmission and reflection coefficients, arrival time and amplitude of the tip-reflected Stoneley waves can be detected and used for estimating length and width of the fracture respectively. It was observed that the amplitude of the tip-reflected Stoneley wave was affected by scattering effects of the fracture mouth at the wellbore wall. Therefore, in order to derive a quantitative relation between the width of the fracture and amplitude of the tip-reflected Stoneley wave, it is required to consider these scattering effects.

It was shown that for transverse fracture length to the Stoneley wavelength ratios of more than four or five, the fracture can be considered to be infinite. Under such conditions, models presented by authors such as Hornby et al. (1989), Tang and Cheng (1989), and Tang and Cheng (1993) which assume infinite fracture extent are valid for fracture characterisation. However, sensitivity analysis experiments on fracture length showed that for smaller ratios of fracture length to the Stoneley wavelength, the transmission coefficient of the Stoneley wave is sensitive to the fracture length (Henry, 2005). In this case, the previously mentioned models which assume infinite fractures are prone to errors in estimation of fracture width using the transmission coefficient of a Stoneley wave.

Ionov (2007) studied the generation of low-frequency borehole Stoneley waves (tube waves) generated by the incidence of a P-wave at an infinite-extent fluid-filled fracture. An analysis was performed on the amplitude and waveforms of

Stoneley waves generated by various incident P-wave pulses of seismic wavelength. It was reported that the amplitude and waveform of the Stoneley wave is largely dependent on two dimensionless parameters: ratio of borehole radius to dominant wavelength of the pulse, and ratio of fracture width to the borehole radius. The amplitude of Stoneley waves generated by P-wave pulses are shown to be in the order of P-wave amplitudes in the borehole fluid over a VSP surveys' typical frequency range. As in the most cases the generated Stoneley waveforms are considerably different from incident waveforms, identification of such waves becoming less complex. Therefore, such information from a Stoneley wave can be used in field VSP surveys for fracture characterisation.

In more recent studies, a new method for estimating the length of a hydraulic fracture is introduced. This is based on studying secondary tube waves excited at the tip of the fracture by an external seismic field (Derov et al., 2009; Maximov et al., 2010). Derov et al. (2009) reported that for a fracture with a length comparable or larger than the wavelength of the external seismic wave, a wavefield in the fracture can be excited both at the intersection point of the fracture and the wellbore wall, and the fracture tip. The latter is due to squeezing of the fracture tip which results in slow eigenmode propagation. This wave is different from the primary tube wave excited at the fracture-wellbore intersection. By recording both modes and comparing their travel times, an estimate of the fracture length can be found. Numerical modelling results showed that the amplitude of the secondary tube waves can reach the same order as that of the primary tube wave (Maximov et al., 2010). These findings make such measurements possible under field conditions for applications using active monitoring of fracture size.

Far-field methods

Far-field seismic-based methods are commonly used for hydraulic fracture diagnostics. Aki et al. (1982) carried out field active seismic experiments to determine geometrical and physical properties of a hydraulic fracture-induced fracture system. They used transmission, reflection, and attenuation data for their interpretations. A decade later, recorded shear-wave transmissions in conjunction with microseismic field experiments for monitoring hydraulic fracture in a diatomite showed shear-wave shadowing due to the interference of a hydraulic fracture (Vinegar et al., 1992; Wills et al., 1992). Actually, in these studies the observed

shear-wave shadowing results gave the most decisive data on where the hydraulic fracture was open. Crosswell surveys and vertical seismic profiling (VSP) are two active-source monitoring techniques which have proven to be successful for natural and hydraulic fracture detection and characterisation (Liu et al., 1991; Meadows and Winterstein, 1994; Majer et al., 1997). In more recent studies, hydraulic fracture quality was determined by integration of time-lapse VSP and microseismic data (Willis et al., 2008; Willis et al., 2009). Willis et al. (2008) and Willis et al. (2009) investigated the ability to detect and characterise hydraulic fractures from scattered seismic waves. A three-dimensional VSP was used as the reference for seismic reflectivity before hydraulic fracturing. During hydraulic fracturing operations microseismic data were recorded to estimate location of a hydraulic fracture. A second VSP measurement was conducted after hydraulic fracturing. The differences between the two VSP measurements were used to investigate changes in the reflected wavefield and addition of the scattered wavefield as a result of induced hydraulic fracture.

Parallel to field studies, a number of laboratory scale studies of active source monitoring of hydraulic fracturing have been carried out over the last three decades. Most probably the earliest attempt was made by Medlin and Masse (1984). In that study a number of laboratory ultrasonic transmission measurements were carried out across the predicted pass of a hydraulic fracture's growth. The amplitude decline of transmissions indicated interference of a dry tip of the hydraulic fracture which was followed by the fluid front and relative amplitude gain. Such measurements were used to determine the location of a fracture tip. Any subsequent decrease in amplitude was interpreted to be due to widening of the fracture.

A few years later a unique laboratory facility for physical modelling of laboratory hydraulic fracture monitoring was built and tested (Savic et al., 1990; Savic et al., 1991). The laboratory facility had the capability of placing a number of ultrasonic transducers around the physical model of a hydraulic fracture and it was possible to acquire ultrasonic data in time-lapse manner during the experiment time. Transmission and reflection pilot experiments on the physical models showed its capability for ultrasonic monitoring of a hydraulic fracture. These promising results encouraged more study using comprehensive measurements of hydraulic fracture monitoring and as a result a data recording system with 24 transducers was built which allowed rapid acquisition of reflection, pulse-echo and transmission data

during hydraulic fracturing experiments using synthetic samples. Data acquired by the modified data acquisition system showed that even for fractures of very small widths compared to the wavelength, it is possible to record meaningful ultrasonic signals which bear valuable information about the hydraulic fracture state. Apart from an observed amplitude reduction and arrival time delays in transmissions across the fracture, waves diffracted from the fracture tip provided a measure of fracture length over the experiment's time (Savic, 1995). It was reported that when the hydraulic fracture induced in a cement sample was closed, it still scattered a considerable amount of ultrasonic energy, while a sandstone sample did not show the same behaviour in a similar experiment. So it was concluded that the scattering properties of a hydraulic fracture are a function of material properties such as the grain size.

Furthermore, shear wave shadowing already observed in the field (Wills et al., 1992) was also again observed but this time under laboratory conditions. This opened new ways to study the mechanism of such events in more detail under controlled laboratory conditions (Savic, 1995). A few years later and following the mentioned laboratory studies, an attempt was made to estimate the width profile of a hydraulic fracture using laboratory experiments (Groenenboom, 1998). The main factors studied for characterising fracture width were amplitude reduction and time delay which occurred for waves transmitted across the hydraulic fracture. The triaxial stress machine used for the previous laboratory studies (Savic et al., 1993; Savic, 1995) was modified which led to an enhanced data quality. Furthermore, shear-wave transducers were used in the new series of experiments to study the potential of shear waves for hydraulic fracture monitoring- at least in the laboratory scale.

The first attempt to match numerical model with observed experimental results using linear slip model was reported by Savic (1995). A thin layer model for modelling a hydraulic fracture was presented and based on that a review was conducted on the assumptions that reduce the thin layer model to the linear slip model (Groenenboom and Fokkema, 1998). The linear slip model was shown to be improper if one wants to study channel waves in the fracture. Furthermore, it was reported that the linear slip model converges to the thin layer model only under low horizontal slowness conditions. Nevertheless, for relatively thin hydraulic fractures (up to 200μm during the laboratory conditions of these experiments) linear slip

theory agreed well with the thin layer model. For wider and more complex fractures (e.g. fractures with roughness or asperities), linear slip model theory simply provides an effective model for transmission and reflection measurements across the fracture while for example the thin layer model shows multiple arrivals as the fracture widens. This is due to the fact that in the thin layer model the detected events are due to the interaction of dynamic waves with a true open fracture having a certain width while in the linear slip model the interactions are as a result of fracture compliance which contains the combined effect of a number of fracture properties such as surface roughness, mechanical contact, and width of the fracture. Moreover, it was claimed that the amount of transmission dispersion taking place due to the presence of a fracture compared to the medium without a fracture can be predicted by convolving transmission through intact rock with the transmission coefficient of the fracture. This convolutional model was used for back-calculating width of the fracture after measurement of dispersions in transmissions (Groenenboom, 1998). Furthermore, several diffraction events were detected during laboratory hydraulic fracturing experiments as well as numerical models. They were reported to be excited mostly either at the fracture tip or at the intersection point of the wellbore and the fracture. Included in such events are waves which are re-diffracted at the fracture tips (Groenenboom and Falk, 2000; Groenenboom et al., 2001). Since then, the modified equipment has been used for determining geometry (mainly width of the fracture and location of the tip) in different laboratory hydraulic fracturing studies such as those performed on sandstone samples (Lhomme et al., 2002; Lhomme, 2005) or those with the aim of investigation of the interaction between a hydraulic fracture and natural fractures (Meng, 2010; Meng and de Pater, 2011).

2.3 Summary

This chapter firstly provided a review on the seismic behaviour of rock natural fractures. Investigations carried out on the subject included laboratory and field studies on the characterisation of fractures, theoretical models of rock fractures, and numerical techniques for modelling the interaction of seismic waves with fractures. Different types of waves, including body and surface waves were shown to interact with fractures. Distinctive properties of such interactions have been identified and have been used for characterisation of fractures at different scales.

Furthermore, a review of the different techniques used for monitoring hydraulic fractures was presented. These were categorised in different groups: passive seismic methods, which record microseismic events generated due to fracturing, active seismic methods and active non-seismic methods. Afterwards, the main limitations of microseismic and non-seismic methods were discussed. A broad review of different active seismic methods showed the competency of this group of techniques for more effective and detailed monitoring of the hydraulic fracturing process compared to the other methods. The focus of this study, as mentioned previously, is on the application of the active seismic techniques for monitoring hydraulic fracture propagation.

3 Numerical Modelling

3.1 Introduction

Wave propagation in fractured media has been a topic of research interest over the last few decades. Besides theoretical, experimental and field studies, some useful insights have been obtained from numerical modelling of this phenomenon recently. The literature review presented in the previous chapter indicated that most of the numerical studies for modelling the effect of fractures on seismic waves are based on continuum mechanics methods. Nonetheless, it was reported that numerical methods which are based on discontinuum mechanics have been shown to be successful in accurately modelling wave propagation in homogeneous media (Toomey and Bean, 2000). Methods which are based on modelling media using discrete particles can not only be used for modelling wave propagation in homogeneous media, but also can be used for modelling the propagation in inhomogeneous media. This includes inhomogeneity of a granular medium due to its different particle sizes, properties and distribution. Micro-cracking of granular materials due to the applied mechanical forces or excessive fluid pressure was also successfully modelled using this numerical technique (e.g. Hazzard et al., 1998; Hazzard et al., 2002; Hazzard and Young, 2004) . Furthermore, this technique has been shown to be capable of modelling fractures in the rock which behave in accordance with the theoretical models for fracture seismic behaviour (e.g. Toomey et al., 2002a; Möllhoff and Bean, 2009; Resende et al., 2010).

In this study, Particle Flow Code in two dimensions (PFC2D) was used for the purpose of numerical modelling. PFC2D is a discrete element code in which the rock is represented by a dense packing of non-uniform-sized circular particles (Potyondy and Cundall, 2004). This code has already been used for modelling

different phenomena such as seismic wave propagation, hydraulic fracture initiation and propagation, and interaction of hydraulic fracture with natural fractures (e.g. Hazzard et al., 1998; Sarmadivaleh et al., 2011). There is also a three dimensional version of PFC available which is suitable for modelling phenomena in three dimensions (PFC3D). The fractures modelled in this study are, however, simple straight fractures and the phenomena of interest can be efficiently modelled using a 2D numerical modelling approach. Furthermore, as will be seen in the next chapters, arrangement of ultrasonic transducers and the fractures geometries in the experiments are chosen to be simple to allow comparison with results of a 2D numerical analysis. Furthermore, due to large size of the models, 3D simulations for the purpose of this study would be highly computationally expensive. Considering the above factors it was decided to use PFC2D in this work.

3.2 Particle-Flow Model of PFC2D

In a general particle-flow model, the mechanical behaviour of a system composed of a collection of arbitrary shaped particles is simulated. Here, the term 'particle' indicates a body that occupies a finite amount of space. In such a model, distinct particles can be displaced independently of one another and interact only at contacts or interfaces between the particles. Particles are assumed to be infinitely rigid, meaning they do not deform. The interactions between the particles are characterised using a soft contact approach. In such an approach, contacts between the particles can be assumed as the equivalent of springs with defined stiffnesses. The mechanical behaviour of such a system is determined in terms of movement of individual particles and the inter-particles forces acting at the contact points (Itasca Consulting Group, 2008). The relationship between the force applied on each particle and movement of the particle is defined by Newton's law of motion.

It is also possible to add more complexity to the particle-flow model. Particles can be bonded together at their contact points. In this case, in addition to the particle-particle contacts, tension and shear forces occurring at particle-particle bonds will also contribute in the force-displacement equations. Contact bonds have a finite strength and in the event of excessive inter-particle forces leading to forces larger than the bond strength, the bond is broken. Independent shear and normal strength values can be defined for bonds. This allows, for example, investigating the

development of normal tensile forces between particles. The capability of taking into account breakage of the bonds allows one to model events such as damage, micro-cracking and fracturing in the rock. Furthermore, another type of bond, called a "parallel bond", can be assigned to particle pairs. Unlike a contact bond, this type of bond resists rotation as well. Particle-flow modelling included in PFC is based on these important assumptions (Itasca Consulting Group, 2008): particles are treated as rigid bodies, the contact between particles occur over a vanishingly small area, the behaviour of contacts is based on a soft-contact approach allowing particles to overlap at contact points, the magnitude of overlap is related to the contact force based on the constitutive force-displacement law, bonds can exist at particle contacts, and all particles are assumed to be circular.

3.2.1 Calculation Workflow of PFC2D

In this section calculating cycles in PFC2D is described briefly. For more information the reader is referred to PFC2D manual (Itasca Consulting Group, 2008). In each calculation cycle of PFC2D, a time-stepping algorithm is executed. At each time-step the list of contacts is updated from the known positions of particles (also called balls) and walls. The constitutive force-displacement law is then applied to each contact. This results in updating the contact forces based on constitutive contact law as well as the relative positions of entities present in the model (particles or walls). Subsequently, the law of motion is solved for each particle which causes the acceleration, velocity, and then position of the particles to be updated based on the resultant force (total of body and contact forces) and moments applied to each particle. However, force-displacement equations are not solved for walls. Wall positions are updated based on the specified wall velocities.

For each particle-particle contact, the normal vector of the contact is defined as the line connecting centres of the particles. The contact point is located on the normal line. For the special case of a pair of particles with identical radii, the contact point is located in the mid-point of the contact normal line. The force vector at each contact in PFC2D is decomposed into a normal component acting in the direction of the contact normal vector, and a shear component acting in the contact plane, perpendicular to the normal contact line. The magnitude of the contact force is related to the overlap between the particles. The normal overlap between two

particles is obtained by subtracting the distance between particle centres (in two dimensions) from the sum of the particle radii. The normal contact force is then obtained by multiplying the normal overlap, U^n, by the contact normal stiffness, K^n, (with the unit of force/displacement) as follows:

$$F^n = K^n U^n \tag{3-1}$$

For a contact between particles *A* and *B*, normal contact stiffness is obtained by the following equation:

$$K^n = \frac{k_n^{(A)} k_n^{(B)}}{k_n^{(A)} + k_n^{(B)}} \tag{3-2}$$

where $k_n^{(A)}$ and $k_n^{(B)}$ are normal stiffnesses of particles *A* and *B*, respectively.

The contact normal stiffness relates the total displacement and force in the normal direction. Shear stiffness is, however, a tangent modulus which relates the incremental shear displacement and force. By initialising to zero when a contact is formed, any relative shear-displacement increment results in an increment of shear force which is added to the current value of total shear force at the contact. The equations are as follows:

$$\Delta U^s = V^s \Delta t \tag{3-3}$$

$$\Delta F^s = -k^s \Delta U^s \tag{3-4}$$

where ΔU^s is the shear component of the contact displacement increment over a time-step of Δt and ΔU^s is the shear force increment whose direction is always opposite to that of the shear contact displacement. Contact shear stiffness is given by:

$$k^s = \frac{k_s^{(A)} k_s^{(B)}}{k_s^{(A)} + k_s^{(B)}} \tag{3-5}$$

where $k_s^{(A)}$ and $k_s^{(B)}$ are shear stiffnesses of particles *A* and *B*, respectively. Based on equations (3-2) and (3-5), if two contacting particles have the same normal or shear stiffness, normal or shear stiffness of their contact will be simply half of the particles normal or shear stiffness, respectively.

The resultant force and momentum obtained from the contribution of contact normal and shear forces are used for updating particle positions. Having the resultant force applied to the particle and mass of the particle, the particle acceleration is calculated. The equations of motion are integrated using a centred finite-difference scheme involving a time-step Δt. Assume at the time *t* the position of a particle is known. Accelerations obtained in time *t* are written, based on velocities in times $t \pm \Delta t/2$. As velocities in time $t - \Delta t/2$ are known, velocities in time $t + \Delta t/2$ can be obtained. Accordingly, the position of the particle at the start of the next time step (time $t + \Delta t$) is calculated, based on its calculated velocity in time $t + \Delta t/2$ and its previous position at time *t*. The updated position of the particle is now ready to be used in the next cycle in the force-displacement equations as described above. More detailed information on calculation cycles of PFC can be found in PFC2D manual (Itasca Consulting Group, 2008).

3.2.2 Limitations of Modelling with PFC2D

3.2.2.1 Two-Dimensional Nature of PFC2D

It is important to keep in mind that models generated in PFC2D are actually two-dimensional assemblies of circular particles. In PFC2D, all vector values such as force, displacement, velocity and acceleration exist only in two dimensions. Therefore, in PFC2D there are only two linear velocities and one angular velocity. Similarly, there are only two force components and one moment component. This is opposite to the three-dimensional case, in which there are three force components and three moment components. Actually, the out of plane force component and two in-plane moment components are not considered at all in equations of motion in PFC2D (Itasca Consulting Group, 2008). Particles in PFC2D are actually disks with the thickness of unity. So their third dimension, depth, is assumed to be one. PFC2D also provides the option to consider particles in a two-dimensional model as spheres whose centres are always in the plane of $z = 0$, where *z* is the depth dimension not

visible in two-dimensional analysis. In all numerical analyses presented here, particles are assumed to be unit-thickness disks.

It is important to consider these limitations while conducting numerical modelling. Accordingly, care should be taken in interpretation of numerical results. Furthermore, one needs to take into account this assumption when comparing laboratory results (which are obtained in three-dimensional media) with those of a numerical method.

3.2.2.2 Rigidity of Particles

As mentioned before, discrete particles in PFC are assumed to be infinitely rigid. When deformation of a physical system is assumed to be movements of individual rigid bodies along their interfaces, rigidity of particles is a proper assumption. In such a case, the deformation of the whole system of particle assembly is described by this assumption. This is because such deformation is mainly a result of sliding and rotations of rigid particles as well as opening and interlocking at the interfaces, and not from the deformation of individual particles.

3.3 Wave Propagation in PFC

PFC has been used by many authors mainly for micro and macro-scale geomechanical modelling of granular materials such as rock and soil. Some applications include simulation of laboratory biaxial experiments of a rock specimens (Potyondy and Cundall, 2004), loading-type failure around underground excavations (Fakhimi et al., 2002), perforation in a sandstone reservoir (Nabipour et al., 2010), and interaction of a hydraulic fracture with natural fractures in the reservoir (Sarmadivaleh et al., 2011).

As the dynamic behaviour of materials is not the point of interest in regular geomechanical modelling, a damping mechanism is incorporated in PFC to assist in dissipating the kinetic energy of the system and reaching the equilibrium state in a shorter time. The damping force is added to the equations of motion of individual particles and is controlled by a damping constant (Itasca Consulting Group, 2008). Nevertheless, to conduct wave propagation modelling, it is necessary to set the damping constant to a low value to be able to study dynamic behaviour of the particle assembly.

Based on the introduction of a particle-flow model in the previous section, it is understood that in PFC wave propagation is not modelled by solving wave equations; instead, the equations of motion and force-displacement equations are solved at each time-step for individual particles present in the model. Applications of PFC for dynamic wave propagation includes measuring velocities of P and S waves excited due to cracking and failure of the rock (Hazzard et al., 1998; Hazzard and Young, 2004), measurement of dynamic moduli of rock specimens and their stress-dependence (Li and Holt, 2002; Alassi, 2008; Li and Fjær, 2008), and modelling of a stress wave in rock and rock fractures (Resende et al., 2010).

In this study, PFC2D capability for modelling wave propagation is examined against a verified numerical code. To facilitate the interpretation of results, focus is made on sorted assemblies of particles. Two different particle packing systems are examined here: cubic packing and hexagonal packing. This constitutes the first step in modelling and provides confidence in using PFC2D for wave propagation. In later stages of the modelling, more complexities are included.

3.3.1 Hexagonal Assembly of Particles

Due to its distinct properties, a hexagonal arrangement of particles has been commonly used for analysis of wave propagation discrete particle assemblies (e.g. Sadd et al., 1993; Toomey and Bean, 2000; Case and Horie, 2007; Möllhoff and Bean, 2009). So far PFC2D has been mostly used for wave propagation modelling in randomly packed assemblies of particles. It was however, necessary to validate the capability of the code for wave propagation in sorted assemblies of particles before conducting more complicated modelling.

Toomey and Bean (2000) validated their particle-based model, called a discrete particle scheme (DPS), for wave propagation in a hexagonal assembly of particles. In this study, a model of a hexagonal assembly of particles similar to that of Toomey and Bean (2000) is generated. Wave propagation in such a model is examined and the results are compared to those of DPS.

3.3.1.1 Model Generation

A two-dimensional square-shape model comprised of a hexagonal assembly of particles was generated. In such a model each internal particle is in contact with six

other particles. The sample model size was 3000 m × 3000 m. Particle density, diameter, normal stiffness, and shear stiffness were taken to be 2210 kg/m^3, 10 m, 120 $\times 10^9$ N/m, and zero, respectively. The model contained 103,627 particles. The selected particle density resulted in the desirable macro-density (bulk density) of 2000 km/m^3. This was due to the fact that the area of the model is larger than the total area of particles, or to say, there is always some two-dimensional porosity in such a particle assembly. Here two-dimensional porosity is defined as follows:

$$\varphi_{2D} = \left(1 - \frac{S_g}{S_b}\right) \times 100 \tag{3-6}$$

where S_g and S_b are total area of particles and total area of the model, respectively. The two dimensional porosity of a hexagonal assembly of particles was determined to be 9.5%. Particles were bonded to their neighbouring particles by contact bonds of high strength in order to prevent any possible bond failure which currently would not be desirable. As particles have only a normal stiffness, only normal stiffness was assigned to the contacts and contact shear stiffness was set zero. Although there is no shear stiffness defined for the contacts in this hexagonal pack, due to the special arrangement of contact lines, shear forces (hence shear wave) can develop in such a model. Figure 3-1 shows a schematic of hexagonal assembly of particles in PFC2D. The source particle at the centre of the model is shown in green while all other particles are shown in yellow. Black lines show contact lines which connect the centres of each contacting particle pair. X and Y axes are also shown in the figure. As can be seen, each particle has six contacts with its neighbouring particles. Due to symmetry of the contact line arrangement, the angle between each two successive contacts of each particle is 60°. A hexagonal arrangement of particles results in a network of contact lines consisting of three main sets with contact lines in a set being parallel to other contact lines of that set. In Figure 3-1 one set of contact lines are in the direction of X axis, while two others make 60° angles with this group. Such a configuration results in forming successive equilateral triangles as shown in the figure.

The damping coefficient was set to zero to prevent dissipation of energy. This is due to the fact that waves are not dissipated in a homogeneous elastic medium. Furthermore, such discrete particle schemes are prone to numerical

dispersion which depends on the ratio of the wavelength to the radius of the largest particle in the model. To reduce the dispersion effects down to a desirable level, it is required to maintain a high ratio of wavelength to the particle radius (Toomey and Bean, 2000). This point was also considered when choosing modelling parameters. A Ricker wavelet with a centre frequency of 32 Hz was input into the Y velocity component of the source particle located at the centre of the model. In this case, the wavelength to particle diameter ratio was calculated to be 19 and 11 for P and S-wave, respectively. The amplitude of the source input wave was chosen high enough to be above the noise level and low enough to avoid generation of excessive contact force and possible bond failures. It is also important to choose a short enough time-step to ensure stability of the model in the calculation cycle while considering the computation effort required. After examining a number of values, a time-step of 1×10^{-4} seconds (100 μs) was chosen.

The input source velocity resulted in a displacement in the source particle which in turn caused overlapping of the source particle with its adjacent particles. As previously explained, such overlaps generate inter-particle forces at the particle-particle contact points with magnitudes related to the stiffness of the contacts as well as the length of the overlap. The force generated by this displacement was transferred to nearby particles via contacts between them. In this way, the dynamic wave was propagated in the medium. In the next section a visual analysis of induced

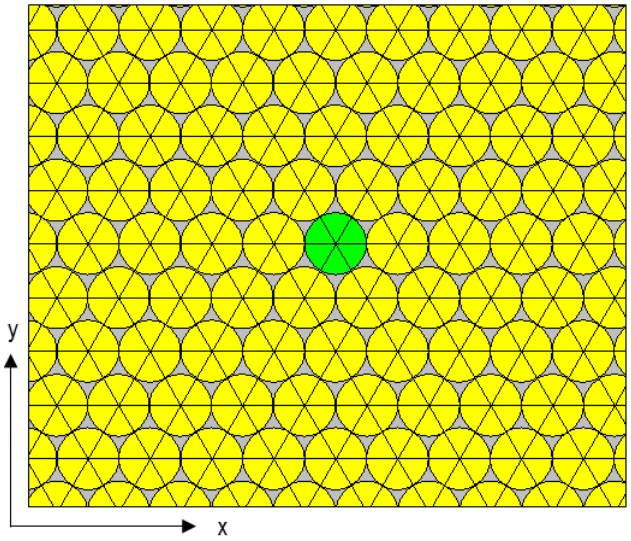

Figure 3-1 Schematic of Hexagonal Assembly of Particles and their contact lines in PFC2D

wavefronts is presented. For this purpose, different graphical capabilities are employed to study the details of generated dynamic waves.

3.3.1.2 Analysis of Wavefronts

Figure 3-2 shows snapshots of particle velocity vectors after allowing the wave to propagate radially from the source particle in the hexagonal assembly. The velocity vector of each particle is drawn from the centre of the particle. Length and direction of each velocity vector specify magnitude and direction of the particle velocity, respectively.

The top left picture is a snapshot from the whole model, showing two distinct wavefronts emitted from the point source. These are P and S-waves exited by the source particle. P-wavefront arrives earlier in time than the S-wave front which has a lower velocity. This snapshot was taken at a moment by which the P-wave front had just reached the boundaries of the model. Both wavefronts have a circular-shape wave front with centres coinciding with the source particle. This indicates that the medium has isotropic P and S-wave velocities which do not change with the direction of propagation. Furthermore, the thicknesses of the wavefront circles are

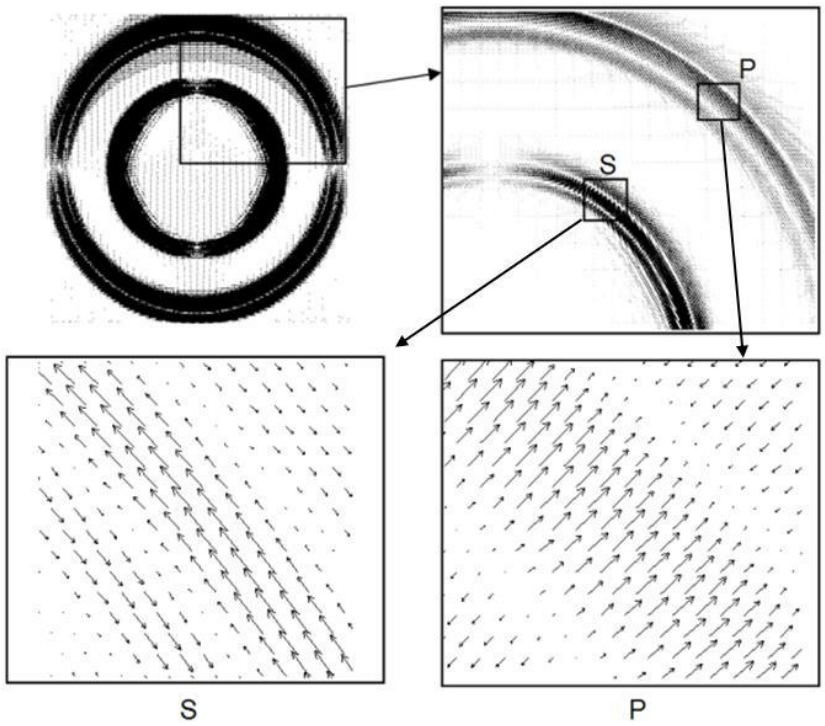

Figure 3-2 Snapshots of particle velocity vectors in hexagonal assembly of particles showing the P and S wave fronts as well as close-ups of vectors.

rough indicators of the length of the wave envelope.

The top right picture is a snapshot focusing more closely at only the top right quarter of the previous snapshot. A P-wavefront is clearly distinguishable from the S-wavefront. Looking more closely at the two bottom pictures in this figure which are close-ups of P and S-wavefront it is possible to see the details of particle velocity vectors. In the P-wavefront, all velocity vectors are in the radial direction (either inward or outward) which is the direction of wave propagation. On the other hand, the S-wavefront causes the particles to move in the tangential direction. At each point, this is perpendicular to the radial direction with respect to the source.

Furthermore, velocity vector plots indicate that any point with an X-position identical to the source X-position experiences movements solely in the Y direction. As for such a configuration the wave propagation path is parallel to the X-axis which is perpendicular to Y-axis, these points only record S-wave. Likewise, any point with a Y-position identical to the source Y-position only experiences movements in Y-direction hence, records merely P-wave.

Looking at the induced contact forces as the wave passes through the medium can also provide useful information about the nature of wave propagation in such assemblies. Figure 3-3 shows close-ups of contact forces generated due to the passage of P and S-wave through the hexagonal assembly of particles. These snapshots were taken at the same time and from the same location as for the two close-ups previously shown at the bottom of Figure 3-2. In this figure contact lines

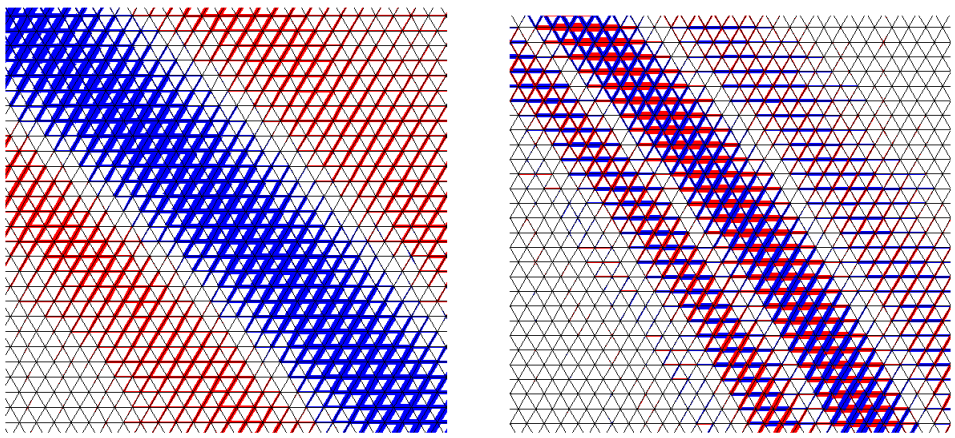

Figure 3-3 Close-ups of contact forces induced by P and S-wavefronts in hexagonal assembly of particles

are shown in black.

It is first necessary to explain the illustration manner of contact forces in PFC2D. Contact forces are also shown by lines of specific colour, thickness, and direction. In Figure 3-3 for example, the blue colour indicates the compressive state of the contact force, while the red colour shows the tensile state of the force. Thickness of the contact force lines is directly related to their relative force magnitude compared to other contact forces shown in each snapshot. Direction of the contact force lines defines the direction of the contact force. A purely normal contact force is shown by a contact force line which lies perfectly on the contact line, and a purely shear contact force is illustrated by a contact force line which is perfectly perpendicular to the contact line. Any contact force with both shear and normal components (with respect to the contact line) is shown by a force line which intersects the contact line at its mid-point (contact point). The angle between the contact line and contact force line indicates the ratio of normal to shear contact force. With such a representation, a contact force having identical normal and shear components intersects the contact line at the angle of 45°.

As the contact shear stiffness is taken to be zero in hexagonal assembly of particles, no shear contact forces should develop and as a result, all contact force lines must lie on contact lines. This is confirmed to be true by looking at snapshots of contact forces for either P or S-wavefronts. In the snapshot showing contact forces induced by P-wavefront (the left picture in Figure 3-3), the central part of the wavefront is distinguished by thick blue lines, indicating the main peak (either positive or negative) of the envelope. This main peak is surrounded by two smaller peaks with different sign (and colour). The figure shows that the state of the contact force in all contacts where the main peak is taking place is compressive.

In the snapshot of S-wavefront also a main peak surrounded by smaller events are distinguishable. Interestingly, unlike P-wavefront, the state of contact forces in the main peak of S-wavefront is not purely compressive or tensile. It is rather a combination of the two. Actually, at each of the events, the state of contact forces of one contact line set is different from that of other two sets. As mentioned before, although contact shear stiffness in the hexagonal assembly is taken to be zero, due to the nature of the hexagonal assembly, shear waves will develop in the model. It can be said that although no micro-shear force is possible to develop at individual contacts, the geometrical structure of the hexagonal assembly is capable of giving

rise to macro-shear forces (therefore shear waves) in the model. This observation highlights the important effect of each particles geometrical arrangement (besides other factors) in wave propagation properties of particle assemblies which was investigated in some previous studies (e.g. Shukla, 1991; Sadd et al., 2000).

3.3.1.3 Validation of Model by Recorded Waveforms

In this section, a PFC2D model is validated by comparing the results of wave propagation in a hexagonal assembly of particles to those published by Toomey and Bean (2000) which were already verified. In order to obtain more information on the propagated waves in the model, it is required to record the waveforms at points of interest. To acquire such data, X and Y velocity components of the particles of interest are recorded over the numerical time-stepping procedure. Figure 3-4 shows recorded X (top plot) and Y (bottom plot) velocity components of a particle located at the top left section and on the diagonal of the square-shape model. The distance of the receiver particle from the source is 1060 m. The source and the receiver are chosen to be far enough to allow propagation distance of at least a few wavelengths and to prevent contamination of data with near-field effects. Waveforms are normalised with respect to their maximum value at each graph. Both graphs show an early event which corresponds to the P-wave arrival, followed by an S-wave arrival. Waveforms in Figure 3-4 are very similar to those published previously for verification of a discrete particle scheme code (Toomey and Bean, 2000) with some minor differences due to slightly different source wavelets used in each study (Nabipour et al., 2011).

In order to further ascertain the validity of this PFC2D model for wave propagation, wave velocities were measured at different points in the model. P and S-wave velocities were then measured by measuring peak-to-peak travel times at different receiver particles. To make the model parameter closer to those of DPS (Toomey and Bean, 2000), the contact normal stiffness was varied in order to reach a P-wave velocity close to 6000 m/s. At the end of this step, P and S-wave velocities were measured to be 6173 m/s and S-wave 3569 m/s, respectively. This results in a P-wave to S-wave velocity ratio very close to 1.73 (with less than 1% error), the ratio which was reported by Hoover et al (1974) and numerically obtained by Toomey and Bean (2000). This confirms that providing appropriate modelling parameters are

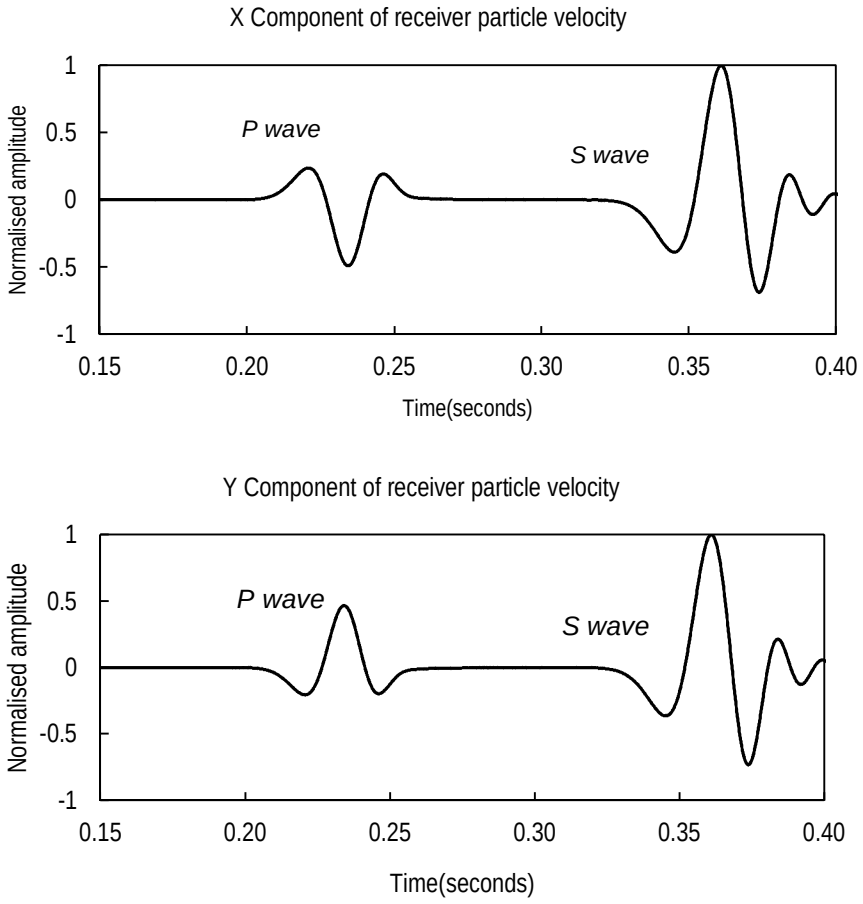

Figure 3-4 Normalised X and Y recorded velocity components of a particle located at the top left and on the diagonal of the model with a distance of 1060 m from the source particle

chosen, PFC2D is capable to accurately model wave propagation at least in such arranged granular assemblies.

Furthermore, keeping the source-receiver distance constant, P and S-wave velocities were measured by choosing receivers with different azimuthal directions. Measured peak-to-peak velocities showed almost no change with the direction confirming isotropic properties of hexagonal assembly. As observed previously in Figure 3-2 , in some azimuthal directions only P or S-wave motion is received. This was confirmed by looking at X or Y velocity components of the particles with the same X or Y-position as the source.

3.3.2 Square Assembly of Particles

Although wave propagation in a hexagonal particle assembly is the case of interest in many situations, wave propagation in a square assembly of particles also has its own advantages. For example, modelling a straight hydraulic fracture in the square

assembly is less complex than in the hexagonal assembly. The process of modelling a hydraulic fracture in PFC2D in arranged particle assemblies is explained in a later section in this chapter.

3.3.2.1 Model Generation

The square assembly of particles is generated by a process similar to that of the hexagonal particle assembly. An attempt was made to choose properties of a square assembly as close as possible to those of a hexagonal assembly. The sample model size is 3000 m × 3000 m, similar to a hexagonal assembly. Figure 3-5 shows a schematic of the square assembly of particles. As can be seen contact lines form a square-shaped network. Bulk density and particle diameter of a square assembly are also chosen to be the same as the hexagonal assembly. As by assigning a zero shear stiffness for particles in a square assembly no shear wave will be generated, both normal and shear stiffnesses of the particles were taken to be identical to the particle normal stiffness in a hexagonal pack. In total there are 90,000 particles in the model which is less than the number of particles in a hexagonal assembly. The square assembly has a two-dimensional porosity of 21.45% which is higher than the hexagonal assembly. Note that regardless of porosity difference, as the particle density is chosen to be 2546 kg/m^3 for the square assembly, both models have the same bulk density of 2000 kg/m^3. The source particle is again located at the centre of the model. The same source function as a hexagonal assembly was input into Y-component of the source particle velocity and the similar time-step length was used.

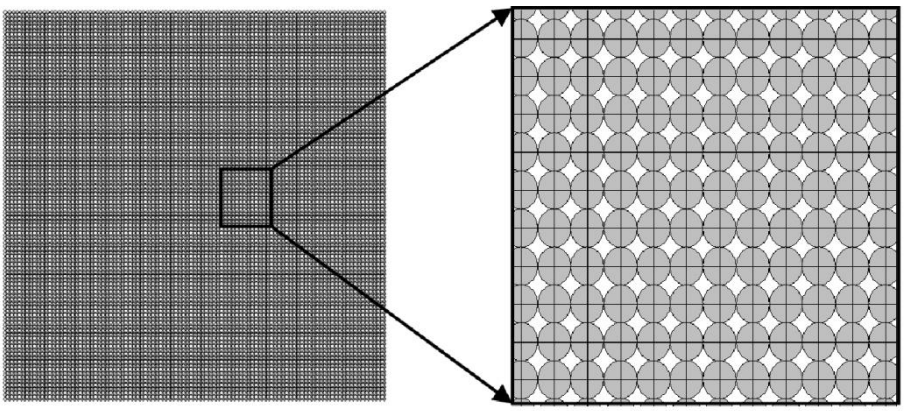

Figure 3-5 A schematic of square assembly of particles with their contact lines

3.3.2.2 Analysis of Wavefronts

Although most parameters selected for both assemblies are similar, the difference in micro-structure of contact networks was expected to affect their wave propagation behaviour. Figure 3-6 shows snapshots of particle velocity vectors from different parts of the model and with different magnifications. In this figure two distinct wavefronts corresponding to P and S-wavefront are apparent. This snapshot was taken at a moment by which the P-wave front had just reached the boundaries of the model. Both wavefronts have circular shapes which is evidence of isotropic properties of the assembly. Actually, this was expected as normal and shear stiffness of contacts are chosen to be equal. Looking more closely at the velocity vectors (two bottom section of the figure), it is understood that velocity vectors show the same behaviour as they did in a hexagonal assembly. That is the velocity vectors in a P-wavefront are in the radial direction while those in S-wavefront have tangential directions with respect to the source particle.

To further investigate a wave propagation process in this assembly, contact

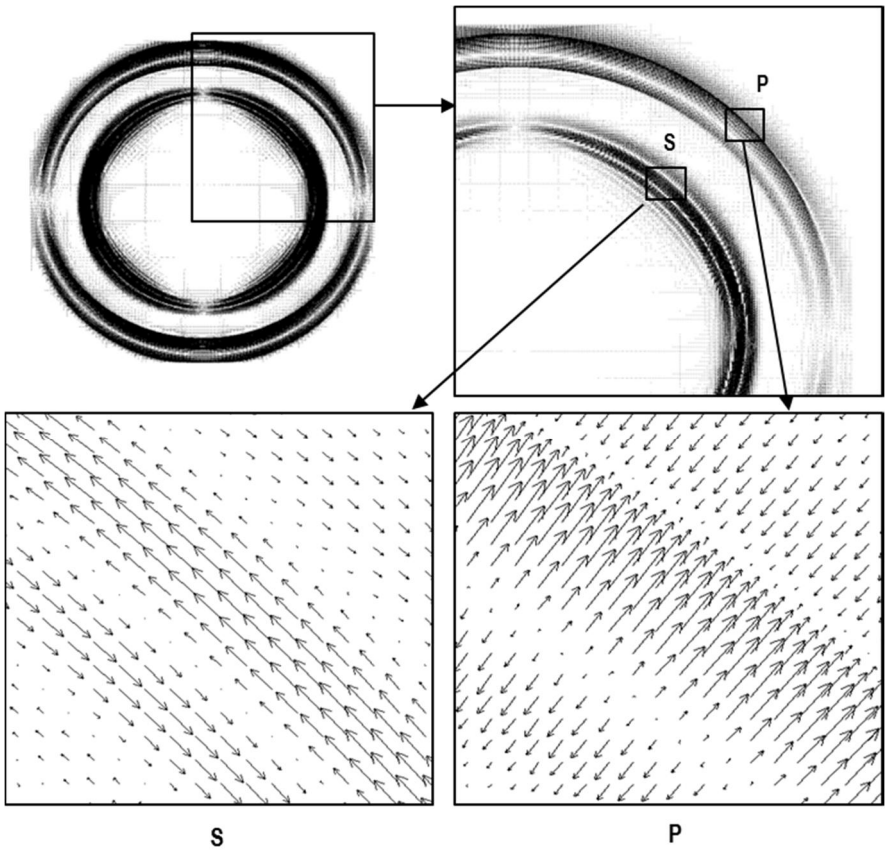

Figure 3-6 Snapshots of particle velocity vectors in square assembly of particles showing P and S wave fronts as well as close-ups of vectors.

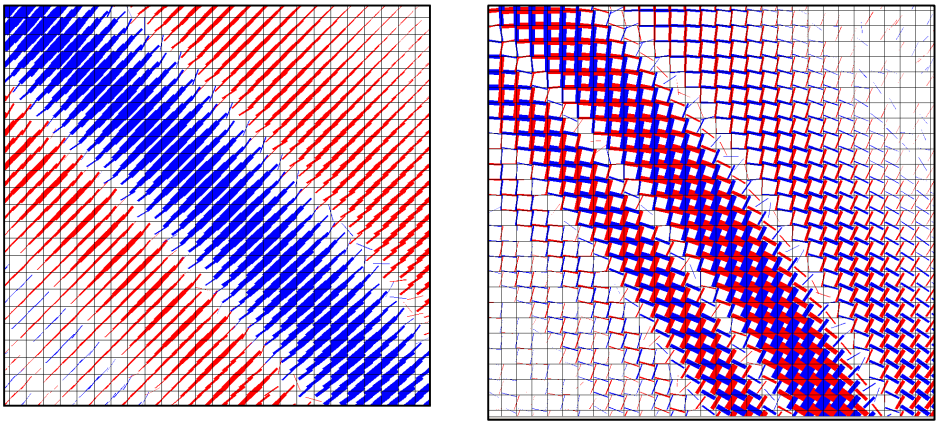

Figure 3-7 Close-ups of contact forces induced by P and S-wavefronts in cubic assembly of particles

force plots are shown in Figure 3-7. P-wavefront (left picture) shows a main peak in which contact forces are in a compressional state (blue lines). The peak is surrounded by two smaller events in which contact forces are tensile (red lines). All contact force lines are in the radial direction and have an angle of almost 45° with the X-axis (and with the contact lines). As per a discussion made earlier, the 45° angle is also a sign of equal shear and normal forces in the contacts. Note that because of existence of contact shear stiffness, contact force lines are not necessarily in the direction of contact lines similar to what was observed in the hexagonal assembly. The S-wavefront, on the other hand, shows a more complicated behaviour. A main peak with thick blue and red lines is distinguishable from the two weaker events around it. However, the state of the force in none of these events is purely compressive or tensile; it is rather a mix of the two. Furthermore, in the area shown by the snapshot the angle between the contact force lines and contact lines is clearly less than 45°.

3.3.2.3 Comparison of Wave Propagation Behaviour of Square and Hexagonal Assembly

In this section, waveforms recorded in each assembly of particles are plotted for comparison purposes. Figure 3-8 shows X-component of velocities recorded for the receiver previously mentioned in the hexagonal assembly as well as a receiver particle located on the sample position but in the square assembly. The figure shows that a P-wave in a square assembly arrives with a delay compared to the P-wave in the hexagonal assembly. However, an S-wave in the square assembly arrives earlier than that of the hexagonal assembly. Therefore, the ratio of P-to-S-wave velocity in

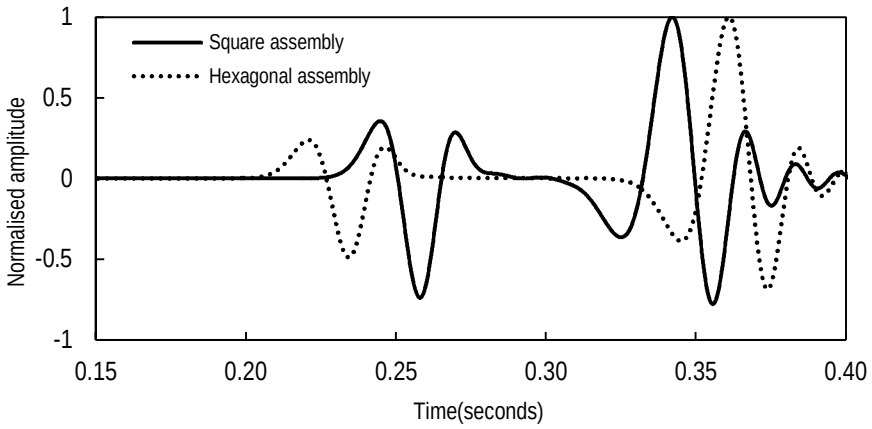

Figure 3-8 X-velocity recorded for receiver particles with similar positions in square and hexagonal assemblies

the square assembly is smaller than that of the hexagonal assembly. This ratio was found to be altered by changing the ratio of normal to shear stiffness of the contact.

The plot shows that the amplitude of a P-wave in the square assembly is greater than that of the hexagonal pack. Such differences are mostly the effect of difference in the micro-structure of particle assemblies which accordingly change their dynamic wave propagation behaviour. Due to the fundamental differences in geometrical arrangement of particles and contacts, it was required to assign a contact shear stiffness equal to the normal shear stiffness in a square assembly while in a hexagonal assembly no contact shear stiffness was assumed. These differences make the hexagonally packed model stiffer against normal forces generated by a P-wave than the square assembly. The opposite scenario takes place for S-waves. Although this behaviour may be undesired if one wants to model wave propagation in an elastic medium, the main purpose of this comparison was to confirm that the square assembly of particles also exhibits sensible wave propagation behaviour. The factors determining wave propagation behaviour of assemblies with different micro-structures are not investigated further in this study.

3.4 Fracture Simulation in PFC2D

Laboratory and field experiments carried out on natural and synthetic fractures in rocks have shown that the fracture effects on amplitude and travel times of transmitted and reflected waves are dependent on the frequency of the incident wave (Pyrak-Nolte et al., 1990b). Theoretical approaches that assume effective elastic

moduli of fractured rock do not consider the effect of discrete fractures and are not frequency dependent. The analytical displacement discontinuity theory (DDT) (Schoenberg, 1980; Pyrak-Nolte et al., 1990b) was shown to accurately predict the seismic response of individual fractures.

A particle-based scheme, called the discrete particle scheme (DPS), was used for modelling wave propagation across fractures in accordance with the theory (Toomey, 2001; Toomey et al., 2002a). A fracture was considered to be a mechanical discontinuity with compliance significantly higher than the surrounding material. This was achieved by choosing fracture compressional and tensile bond stiffnesses to be fractions of the intact rock bond. The same fracture model was later used for testing various methods of quantifying the compliance of single and multiple rock fractures from synthetic ultrasonic data (Möllhoff and Bean, 2009; Möllhoff et al., 2010).

In this study however, a contact model in PFC2D called the Smooth-Joint Model, is used. It is shown that its seismic behaviour is according to the theory. Easy implementation of this contact makes it a good candidate for further modelling studies of fracture behaviour in discrete particle models.

3.4.1 Smooth-Joint Model Basics

Defining interfaces in PFC2D models can be carried out by models consisting of two or more assemblies of bonded circular particles. This approach, however, can be troublesome as there will be inherent roughness of interface surfaces in the models. Furthermore, although small particles can be used to represent a band of material with different properties from the intact rock particles, for a large number of particles this method is inefficient. PFC2D has a distinct contact model, a smooth-joint contact model, which simulates the behaviour of an interface regardless of the local particle contact orientations along the interface. It is possible to model the behaviour of a frictional or bonded joint by assigning this model to all contacts that lie on opposite sides of the joint. When two particles are joined by a smooth-joint contact, instead of being forced to move around one another, they can overlap and slide past each other (Itasca Consulting Group, 2008).

A smooth-joint contact effectively eliminates the bumpiness in interfaces and allows specifications of macroscopic joint properties. This model has been

previously used for geomechanical applications and studying rock behaviour at different scales (e.g. Pierce et al., 2009; Arslan et al., 2010; Bai and Wu, 2011; Mas Ivars et al., 2011). By assigning a number of smooth-joint contact models to a region of the model, a joint set can be defined in PFC2D. Two sets of properties are assigned to the joint set: geometrical properties such as dip angle and length of the joint and physical and mechanical properties such as normal and shear specific stiffness of smooth-joints, friction coefficient, dilation angle, and bond strengths. When a smooth-joint contact is assigned between two particles, the existing contact model is deleted and their future behaviour will be based on the smooth-joint contact.

Smooth-joint contact can be assumed as a set of elastic springs uniformly distributed over a rectangular cross-section which are centred at the contact point and are oriented parallel to the joint plane. The area of a smooth-joint formed between particles *A* and *B* is given by

$$A = 2\bar{t}\left(\bar{\lambda}\min(R^{(A)}, R^{(B)})\right) \tag{3-7}$$

where $\bar{\lambda}$ is the radius multiplier with the default value of one when there is no parallel bond present in the model, $\bar{t}$ is the thickness of disks which always is equal to unity in PFC2D, and $R^{(A)}$ and $R^{(B)}$ are radii of particles *A* and *B*, respectively.

Figure 3-9 shows a schematic of the smooth-joint contact model in PFC2D and its associated notations $\boldsymbol{U}$, the translational displacement vector of surface 2 relative to surface 1, and $\boldsymbol{F}$ the force vector acting on surface 2 are given by

$$\boldsymbol{U} = U_n \boldsymbol{n}_j + U_s \boldsymbol{t}_j \tag{3-8}$$

$$\mathbf{F} = F_n \mathbf{n}_\mathbf{j} + F_s \mathbf{t}_\mathbf{j} \tag{3-9}$$

where $\boldsymbol{n}_j$ and $\boldsymbol{t}_j$ are unit vectors normal and tangential to the smooth-joint contact, respectively (see Figure 3-9), and *U* and *F* are shear or normal components of displacement and force depending on their subscripts.

Depending on the requirements, the smooth-joint contact can exhibit either Coulomb sliding with dilation or bonded behaviour. At each time-step the elastic

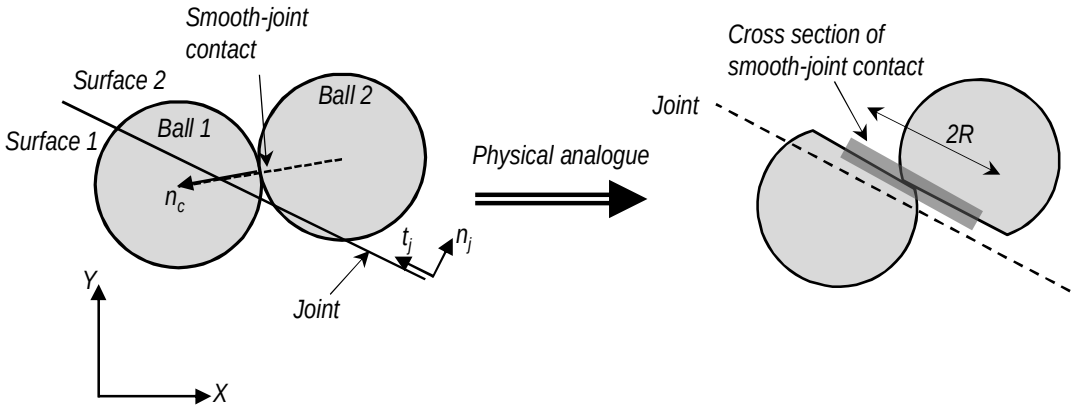

Figure 3-9 A schematic of a smooth-joint contact between to particles (reproduced from Itasca Consulting Group (2008))

portion of the displacement increment between two particle surfaces is determined based on the state of the bond of the smooth-joint and is multiplied by the smooth-joint normal and shear stiffnesses to produce joint force increments. Having values of normal and shear forces in time t-Δt (previous step), their values in the current time, t, are obtained from following equations:

$$\mathrm{F}_{\mathrm{n(t)}} \coloneqq F_{n(t-\Delta t)} + k_n^{sj} A \Delta U_{n(t)} \tag{3-10}$$

$$\mathrm{F}'_{\mathrm{s(t)}} \coloneqq \mathrm{F}_{\mathrm{s(t-\Delta t)}} + k_s^{sj} A \Delta \mathrm{U}_{s(t)} \tag{3-11}$$

where A is the area of the smooth-joint, and k_n^{sj} and k_s^{sj} are specific normal and shear stiffnesses of the joint (with the unit of Pa/m), respectively. After calculation of the abovementioned normal and shear forces, the state of the smooth-joint is checked. Joint behaviour depends on the values of these forces in time t, calculated by equations (3-10) and (3-11). If the joint is bonded, it can break in tension, break in shear, or remain intact. If the joint is unbonded, the joint can remain stationary or slide depending on its friction coefficient and the force values. More details on smooth-joint behaviour can be found in PFC2D Manual (Itasca Consulting Group, 2008).

3.4.2 Seismic Behaviour of Smooth-Joint Contact

As mentioned above, the smooth-joint contact model has been already used for numerical modelling of rock joints and fractures for geomechanical applications. However, to the best knowledge of the author, this useful contact model has not been used for modelling seismic behaviour of fractures so far. In this section, seismic behaviour of a smooth-joint contact model is investigated in order to find out if it has the potential for further applications in numerical modelling of wave propagation in fractured media.

3.4.2.1 Model generation

In order to study the seismic behaviour of a smooth-joint, a simple numerical model containing smooth-joint contacts is generated. The model contains a square assembly of particles which form a rectangular model as shown in Figure 3-10. For presentation purposes, the dimensions of the schematic in this figure do not represent the true scaled dimensions of the actual model. The strip of particles located at the bottom of the model is chosen as the source particles. A Ricker wavelet function was applied to the Y-component of the velocity of these particles. As a result, a

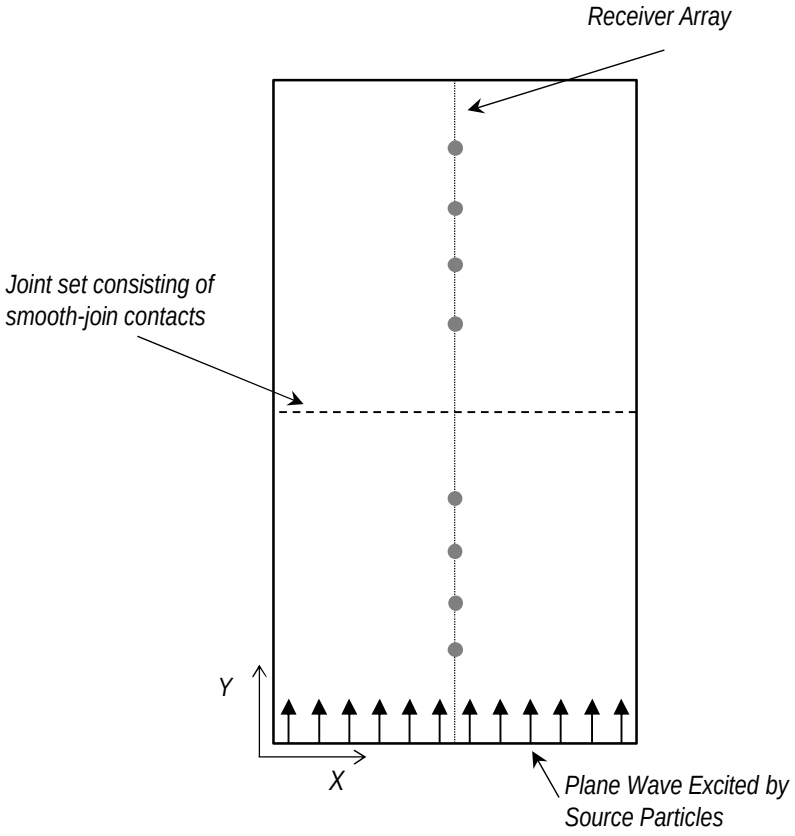

Figure 3-10 A schematic of numerical model generated for evaluation of seismic behaviour of a smooth-joint

compressional plane wave was excited and propagated from the bottom of the model towards its top section. Table 1 shows parameter values used while generating the model. The above parameters result in a peak-to-peak P-wave velocity of approximately 4450 m/s and an S-wave velocity close to 2570 m/s. As will be seen later, the main model parameters (i.e. bulk density, wave velocities, and frequency of source wavelet) were chosen to be close to those of experiments in this study in order to make the comparisons easier.

Waveforms were recorded in a number of receiver particles located on the vertical axis of symmetry of the model. After conducting transmissions in the intact model (with only contact bonds present), a horizontal joint set was assigned into the centre of the model. This resulted in deletion of existing contact bonds between particles that lie on opposite sides of the joint set and addition of smooth-joint contacts between them. According to Equation (3-7), the area of each smooth-joint in the model (A) is equal in magnitude to the particle diameter (but with the unit of m^2). Smooth-joints were taken to be bonded with high-strength bonds that are not likely to break due to small displacements caused by seismic wave amplitudes. For simplicity, normal and shear specific stiffnesses of the smooth-joints were assumed to be identical. Specific stiffnesses of the smooth-joints were varied and transmissions and reflections across the joint set were recorded.

3.4.2.2 Transmission and Reflection Analysis

Studying transmissions and reflections from a fracture can provide useful

Table 1 Properties of square assembly of particles used for examining seismic behaviour of smooth-joint

Parameter	Value
Sample Length (cm)	22
Sample Width (cm)	3
Bulk Density (kg/m^3)	2100
Particle Density (kg/m^3)	2317
Particle Diameter (mm)	0.1
Particle Normal Stiffness (N/m)	6.4×10^{10}
Source Frequency (MHz)	0.5
Stiffness Ratio	1
Time step (Sampling Interval) (μsec)	0.005

information on fracture properties. According to the displacement discontinuity theory, transmission and reflection coefficients are dependent on fracture stiffness and wave frequency. Therefore, knowing the frequency of the wave, one can estimate the dynamic fracture specific stiffness by measuring wave transmission and reflection coefficients. Theoretically, it is assumed that the fracture specific stiffness is constant along the length of the fracture. However, fracture specific stiffness can vary considerably from point to point. It is actually a factor representing the total effect of different physical and mechanical properties of the fracture such as aperture of voids, spatial distribution of voids, and infilling fluid properties. For hydraulic fracture monitoring application, it is emphasized that fracture specific stiffness is inversely proportional to the width of the fracture (Groenenboom, 1998). So transmission and reflection coefficients are parameters which can lead us to a measurement of fracture width.

In order to examine seismic behaviour of the smooth-joint contact model, various values of fracture normal specific stiffness were chosen for the smooth-joints. Corresponding transmission and reflections were then analysed and checked if they agree with the available experimental and theoretical data. Figure 3-11 shows the Y-component of two receiver particles located 10 cm away from the fracture and on its opposite sides. The top plot shows the transmitted waveforms recorded by a receiver on top of Figure 3-10 and the bottom plot shows the reflected waveforms recorded by s receiver at the bottom of Figure 3-10. Furthermore, for comparison purposes, both plots include the waveform recoded by the transmission receiver (top receiver) but in the intact sample (without any smooth-joints). All values are normalised with respect to the peak amplitude of the source wavelet.

Looking at the top plot it is understood that the fracture causes time-delays in the first peak arrivals of the waves transmitted across the fracture compared to the wave transmitted through the intact medium. Decreasing fracture stiffness causes waves to arrive later and have longer time-delays. It is also observed that the amplitude of transmissions is reduced by decreasing fracture stiffness indicating less transmitted energy across the fracture as the fracture stiffness is reduced. The fracture seems to alter the shape of the waveform particularly at lower stiffness values. Such waveform deformation is the effect of frequency-dependent fracture properties (Pyrak-Nolte and Nolte, 1992) which causes the fracture to affect different frequency components of the waveform in different ways.

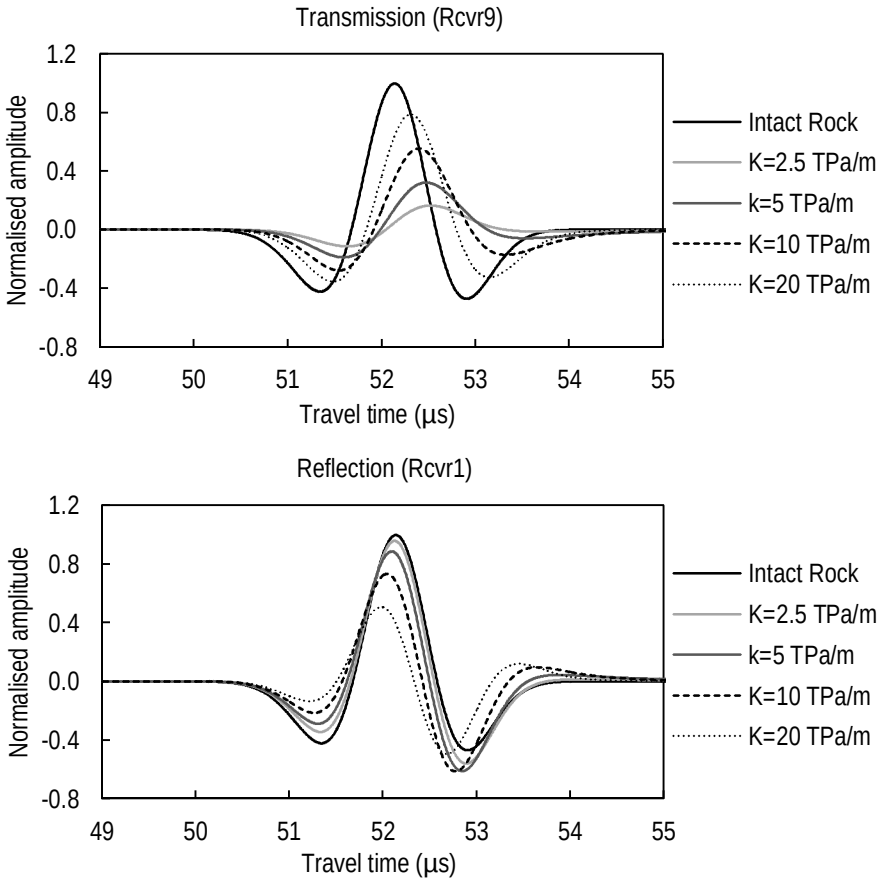

Figure 3-11 Recorded waveforms at two different receivers showing transmission (top) and reflection (bottom) of waves

On the other hand, reflection waveforms show that there is an increase in the amplitude of reflections as the fracture stiffness decreases. Travel distance from the source to the transmission receiver is equal to the travel distance from source to the fracture and then back to the reflection receiver. Therefore, the transmission receiver recording in the intact rock is plotted together with different records of the reflection receiver. As expected, by increasing the fracture compliance (or decreasing fracture stiffness), less energy is transmitted across the fracture and more energy is reflected from the fracture causing smaller transmission amplitudes and larger reflection amplitudes. The reflection record for the fracture with 2.5 TPa/m specific stiffness is more similar in shape to the intact sample record. This was expected as in the limit of zero specific stiffness, the fracture behaves as a free boundary and should perfectly reflect the whole energy in the wavelet.

It is also shown that reflections with larger amplitudes arrive with a delay compared to those with smaller amplitudes. For instance, peak of the reflected wave for the case of 2.5 TPa/m fracture arrives around 0.2 μs later than that of 20 TPa/m

fracture. The delay is comparable to that observed between the transmitted waves for these two cases. Therefore, the numerical results qualitatively show that similar to transmissions, reflections also experience a time-delay which is directly related to the fracture stiffness. Nonetheless, the time delay and amplitude behaviour of reflections and transmissions are different in the sense that the higher the reflection amplitude the longer the arrival time while the higher the transmission amplitude the shorter the arrival time. This is consistent with the displacement discontinuity theory which predicts that for a normal compressional wave, by increasing the fracture specific stiffness phase time delay decreases for both transmission and reflection events (Toomey, 2001). This dependency is expressed by Equation (2-7) and Figure 2-3. However, transmission and reflection amplitudes show different behaviours with a change in fracture specific stiffness (see equations (2-4) and (2-5)).

Plotting the spectra of transmissions and reflections across fractures with different stiffnesses can shed light on the phenomenon. For this purpose, the frequency spectrums of the recorded waves were obtained using a Fast Fourier Transform (FFT) algorithm and are shown in Figure 3-12. The top plot shows the spectra of waves transmitted across the fractures with different stiffnesses while the

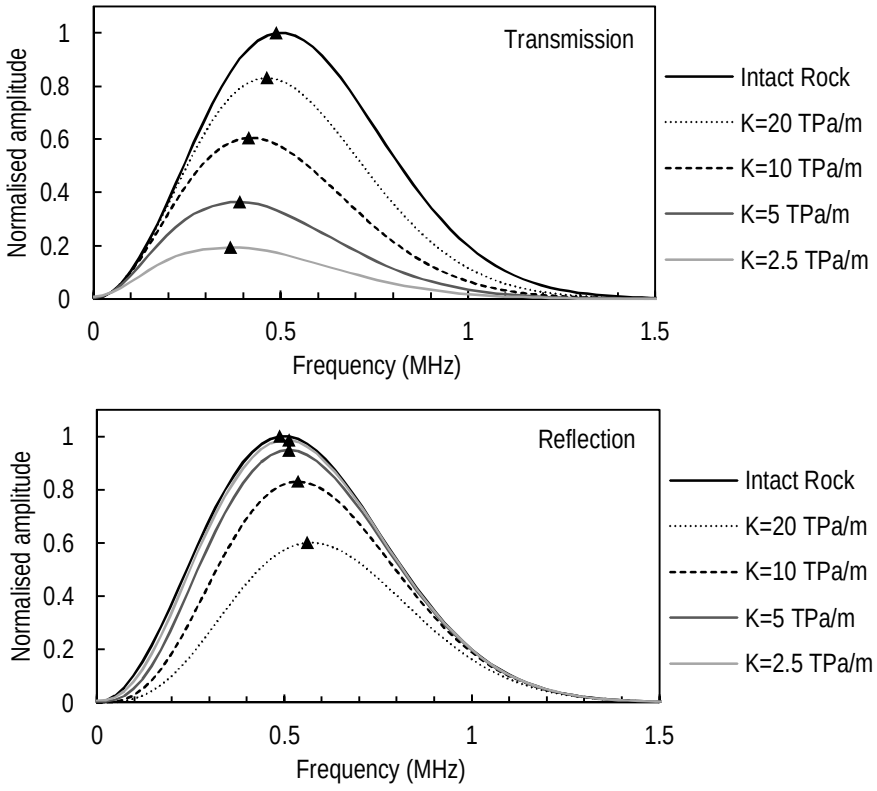

Figure 3-12 Frequency spectrum of recorded waveforms at two different receivers showing transmission (top) and reflection (bottom) of waves

bottom plot shows the frequency component of reflections from fractures with different specific stiffnesses. Similar to what followed in Figure 3-11, the spectra of the wave transmitted in the intact rock is also shown in both graphs. All values are normalised with respect to the maximum spectral amplitude of the source wavelet. The markers indicate the peak amplitude and its corresponding frequency for each curve, with the intact rock having the highest peak equal to one.

The top plot shows that the peak spectral amplitudes of transmitted waves decline by decreasing specific stiffness of the fracture. This is in accordance with the previous observation in time-domain data. Furthermore the graph shows a shift in spectral frequencies of transmitted waves towards lower frequency values. In the intact rock the peak frequency is 0.5 MHz and its normalised peak amplitude is one. The same parameters are 0.46 MHz and 0.83 for the fracture with a specific stiffness of 20 TPa/m and 0.37 MHz and 0.19 for the fracture with 2.5 TPa/m specific stiffness, respectively. When the fracture is stiff enough, it can transmit almost all energy of a wave in all frequency ranges. As the fracture stiffness reduces, less and less energy and only the lower frequency components can pass across the fracture. Similar experimental results of transmission across fractures with varying specific stiffnesses were reported by Pyrak-Nolte et al. (1990b). This behaviour of fractures makes them act as low-pass filters.

The bottom plot shows by increasing fracture specific stiffness spectral peak amplitude of reflected waves decrease, indicating a reduction in the reflected energy from the surface of fracture. This again agrees with the time-domain data presented earlier in Figure 3-11. However, it appears from the graph that the lower peak amplitudes have higher corresponding frequencies. Interestingly, the peak frequencies increase beyond the peak frequency of the wave transmitted through the intact rock. This shift towards higher frequencies is opposite to the trend observed in the transmissions. For a fracture with a specific stiffness of 2.5 TPa/m the peak frequency and normalised peak amplitude are 0.51 MHz and 0.99, respectively. The same values for a fracture with 20 TPa/m specific stiffness are 0.56 MHz and 0.60. Although stiffer fractures reflect less energy, the wave reflected by stiffer fractures has higher peak frequencies. This again recalls the low-pass behaviour of fractures which makes them reflect the high frequency components of the incident wave energy.

3.4.2.3 Transmission and Reflection Coefficients

In this section seismic behaviour of a smooth-joint contact is studied quantitatively. The goal is to verify if the specific stiffness values assigned to the smooth-joints correspond to the specific stiffness of fractures which behave according to the displacement discontinuity theory. For this purpose, an attempt was made to measure transmission and reflection coefficients of the simulated smooth-joint fracture.

Calculating peak amplitude ratios is the most straightforward approach to obtain transmission and reflections coefficients from recorded waveforms. As these coefficients are frequency dependent, theoretically, the frequency of all peak amplitudes needs to be the same. This is only true when a monochromatic source is used. Nonetheless, the source wavelet used for numerical modelling in this study is non-monochromatic. Therefore, one cannot expect all peak amplitudes to contain necessarily the same frequency. To overcome this difficulty, transmission and reflection coefficients were calculated in the frequency domain. This method delivers the required coefficients at discrete frequencies. This approach is similar to the method used by Möllhoff and Bean (2009). To do so, the waveform recorded in the intact sample was used as the reference for calculating transmission and reflection coefficients for each fracture. Frequency spectra of the intact as well as fractured rock were obtained using an FFT algorithm. The transmission coefficient for each fracture was then obtained by dividing the spectra of a transmitted wave by the spectra of an intact sample at each discrete frequency. This results in the transmission coefficients of the fracture at individual frequencies.

Figure 3-13 shows transmission coefficient versus frequency for fractures

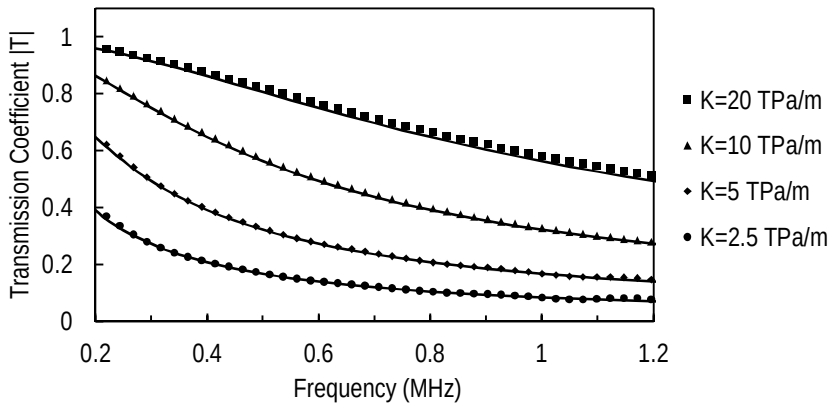

Figure 3-13 Numerical and analytical transmission coefficients versus frequency for different fracture stiffnesses obtained from numerical model and DDT, respectively

with different specific stiffnesses. Markers on the graph indicate numerical results of transmission coefficient and corresponding lines show the values obtained analytically from DDT, using equations 2-4 and 2-5. Comparison of the graphs shows that a smooth-joint contact generates results that closely match those of the theoretical approach at different frequencies and stiffnesses. The graph shows that a larger stiffness of the fracture results in a larger transmission coefficient at each specific frequency. In the limit of infinite fracture specific stiffness, the transmission coefficient is expected to reach unity for all frequency components. Recall Equation 2-1 where the specific stiffness of the fracture is defined. For the transmission coefficient to reach unity, the fracture effect in the intact rock should disappear so the fractured rock behaves the same as the intact rock. This requires the displacement discontinuity (which is the difference between the resultant displacement in the rock with the fracture minus the displacement observed in the intact rock) to be essentially zero. Based on Equation (2-1) this condition takes place when specific stiffness of the fracture reaches to infinity. Similar conclusions can be made from equations (2-4) and (2-5).

On the other hand, for a constant fracture specific stiffness, the transmission coefficient decreases with increasing frequency. The displacement discontinuity seems to behave stiffer for lower frequency components of the incident wave, and thus it has higher transmission coefficients in those frequencies. The fracture seems to behave more compliantly with high frequency components. As a result, it reflects most of the energy and has a low transmission coefficient in higher frequency ranges.

Similarly, reflection coefficients for each fracture were obtained by dividing the spectra of the reflected wave by the spectra of the intact sample at each discrete frequency. Figure 3-14 shows the reflection coefficient versus frequency for different fracture specific stiffnesses. The graph shows the higher the specific stiffness of the fracture, the lower the reflection coefficient. For a constant fracture specific stiffness, reflection coefficient is larger at the higher frequency ranges.

Note that as there are no viscous effects considered in the displacement discontinuity model, no energy is lost while transmitting through or reflecting from the fracture. The condition for this is as follows:

$$|T|^2 + |R|^2 = 1 \qquad (3\text{-}12)$$

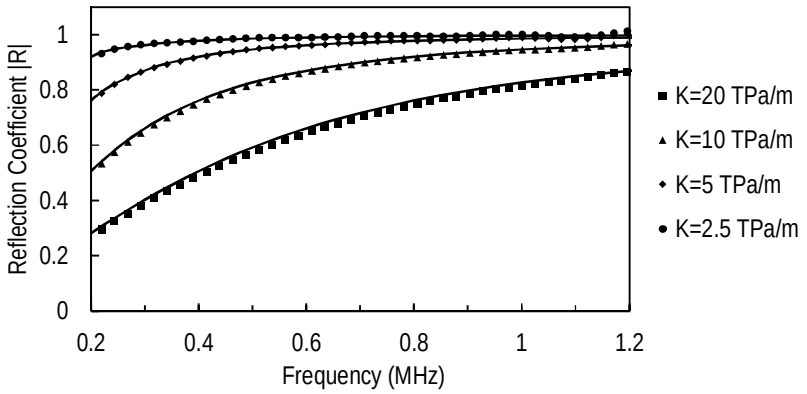

Figure 3-14 Numerical and analytical reflection coefficients versus frequency for different fracture stiffnesses obtained from numerical model and DDT, respectively

This condition was tested for numerical results of the fractures simulated by smooth-joint contacts. For the range of frequencies and specific stiffnesses of interest in this study, it was confirmed that the above condition is satisfied with low error values of less than 0.2%.

3.4.2.4 Time Delays

Displacement discontinuity theory predicts that a fracture causes the transmitted waves to be delayed. This delay is observed in both phase velocity as a phase time delay (t_{ph}) and in the group velocity of the wave as the group time delay (t_g). In this section, an attempt is made to measure the fracture-caused time delays and use them as indicators of the fracture specific stiffness, which in turn will lead to an estimate of hydraulic fracture width.

Figure 3-15 shows phase and group time delays versus fracture specific stiffness predicted by displacement discontinuity theory for the current model. Phase and group time delays are obtained from the right side of equations (2-7) and (2-6), respectively. Input parameters are those from the simulated model. Central angular frequency of the source wave is input into the above equations for ω. The two vertical dashed lines in the graph show the limits of the fracture specific stiffness discussed in previous sections, from 2.5 TPa/m to 20 TPa/m. The figure shows the phase delay decreasing with increasing fracture stiffness. This trend is monotonic for the whole range of fracture specific stiffness. So measuring phase time delay can be

thought as a direct indicator of fracture specific stiffness. However, the relation between group time delay and fracture specific stiffness is non-unique (Möllhoff and Bean, 2009). For low fracture stiffness ranges, the group time delay increases by increasing fracture stiffness, while after reaching a peak it decreases with further increases in fracture specific stiffness. The largest separation of phase and group delays takes place in the lowest frequencies. These values, however, merge as fracture specific stiffness increases to large values.

Möllhoff et al. (2010) showed that ultrasonic phase delays measured in laboratory experiments are better suited to evaluate the fracture specific stiffness than group delays. Furthermore, as shown in Figure 3-15, group time delay is constantly smaller in magnitude than phase time delay. Due to the limited sampling frequency of experimental data acquisition equipment, it is difficult to measure such small group time delays in our hydraulic fracture monitoring experiments. More detail on the specification of experimental set up is presented in the next chapter. In this study focus is made, therefore, solely on phase delay measurements.

It is important to note that the above time delays correspond only to the 500 KHz frequency component of the source wave. As the source wave is not monochromatic and includes a range of frequencies, each frequency component experiences a time delay different from others. Therefore, similar to the approach taken in calculating transmission and reflection coefficients, phase time delays are calculated in the frequency domain for each frequency component. To do so, phase angle of the wave transmitted in the intact rock was obtained for each frequency component by the FFT algorithm already used for computing transmission and

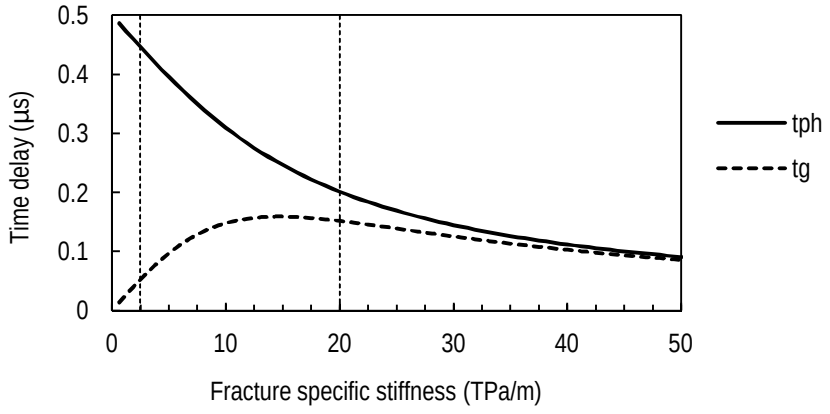

Figure 3-15 Phase and group delay versus fracture specific stiffness

reflection coefficients. Similarly, the phase angle of transmitted waves was obtained for each transmission experiment. In each case, the frequency component's phase shift ($\theta(\omega)$) was obtained by subtracting the phase angle of the transmitted wave from the phase angle of the intact rock wave. The middle part of Equation (2-7) was then used to obtain the phase delay versus frequency from the numerical data.

Figure 3-16 shows phase time delay versus frequency for different fracture specific stiffnesses. Markers in the figure show phase delays obtained from numerical data while solid lines show analytical results obtained from the right side of Equation (2-7). The vertical dashed line shows the wave central frequency line. Intercept points of this line with each specific stiffness curve match the phase delays shown in Figure 3-15 for that specific stiffness. This graph shows that the numerical results of transmission across a smooth-joint contact closely match those predicted by theory. By increasing fracture specific stiffness phase time delay decreases. This is in agreement with the discussion earlier for Figure 3-15. Furthermore, it is shown that the phase time delay is largest in low frequencies and decreases as the frequency increases. The most compliant fracture with a specific stiffness of 2.5 TPa/m causes the 200 KHz frequency component to be delayed more than 0.93 μs while it creates an approximate time delay of only 0.21 μs in 1.2 MHz frequency component of the wave. This is a phase time delay difference of about 0.72 μs. In addition to frequency-dependent amplitude transmission across the fracture, this frequency-dependent difference in phase time delay also causes deformation of transmitted waves observed in previous sections. A delay difference of 0.72 μs can significantly

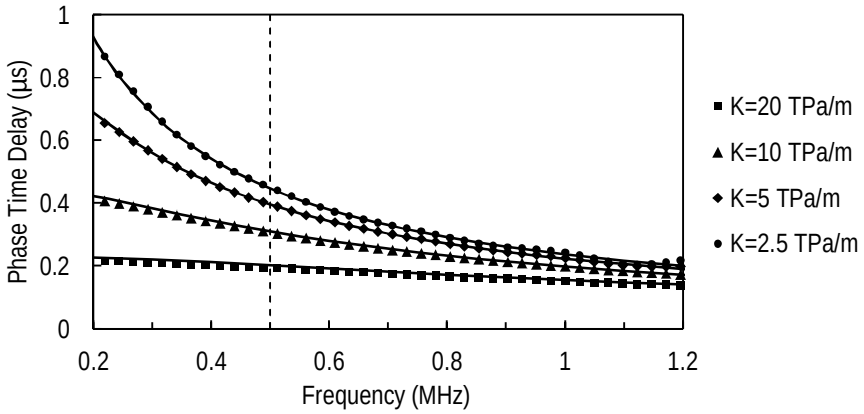

Figure 3-16 Numerical and analytical phase time delay versus frequency for different fracture stiffnesses obtained from numerical model and DDT, respectively

affect the shape of a waveform whose length is about 4 μs (see Figure 3-11). The top plot in Figure 3-11 shows that as the fracture specific stiffness increases the transmitted wave is deformed more. This is particularly evident in the weakening of the second trough of the transmitted waves in the plot. The second trough is almost deleted for the wave transmitted across the fracture of 2.5 TPa/m stiffness.

Figure 3-16 also shows that the phase delay caused by the stiffest fracture (20 TPa/m stiffness) does not vary as much from low frequencies to high frequencies. In this case, phase time delays for 200 KHz and 1.2 MHz frequencies are around 0.22 μs and 0.14 μs, respectively. This leads to a phase delay difference of only 0.08 μs. It is not expected that this relatively small delay difference creates a considerable deformation of the waveform as here some low frequency components arrive only 0.08 μs after the high frequency components. Looking at the top plot of Figure 3-11, it is seen that the wave transmitted across the stiffest fracture does not experience any deformation as expected. It seems that all its components are delayed equally with respect to the reference wave.

Analyses of transmission and reflection coefficients and the phase time delay due to a smooth-joint contact verify that this contact model behaves according to the displacement discontinuity theory. Therefore, it can be used as an efficient tool for simulation of linear slip discontinuities including fractures in the rock. Implementation of the smooth-joint contacts in particle assemblies is straightforward and it is possible to define fractures with arbitrary geometries in the model. In addition to its common use for geomechanical modelling of rock fractures, this contact model has the potential to be used more for dynamic wave propagation studies.

3.4.2.5 Diffractions

So far, diffractions from a fracture were not considered in the modelling as the smooth-joint contacts were assumed to be infinite. Apart from transmission and reflection measurements which can be used as diagnostic tools for detection of hydraulic fracture width, it has been shown that measurement of diffractions from the tip of the hydraulic fracture can provide valuable information on tip location and thus radius of the fracture (Groenenboom and Falk, 2000). This section discusses the diffraction behaviour of a finite fracture which is propagating in time to model a propagating laboratory hydraulic fracture. The results provide valuable information

on the expected diffraction events which may be captured during a hydraulic fracture monitoring experiment.

In general, diffractions from a fracture depend on its specific stiffness, its geometry, and filling fluid properties. Nevertheless, for modelling purposes in this study, a finite fracture with constant specific stiffness of 5 TPa/m is generated using a smooth-joint contact model which previously was shown to behave in agreement with DDT. The specific stiffness is assumed to be constant along such a fracture.

An 8 cm × 8 cm model of hexagonally packed particles was generated for this purpose. Apart from the dimensions, other model parameters are the same as the previous model used for examining transmissions and reflections of smooth-joint contact. This model contains about 738,000 bonded particles. As it will be seen later, the cubic cement samples used in the experimental part of this study are 15 cm or 20 cm cubes. However, as generating numerical models with these sizes would become highly computationally expensive, it was decided to perform the modelling on 8 cm samples. To compare the results of such a model to those of laboratory experiments, parameters such as travel time can be up-scaled via multiplication by relevant factors.

A Ricker wavelet function with a central frequency of 500 KHz was applied to the Y-component of velocity of source particles at the bottom of the sample. A damping boundary condition similar to that used by Toomey (2001) was implemented in the model in order to diminish reflections from boundaries of the model. It was found that although the applied boundary condition was efficient in damping the wave which propagate parallel or perpendicular to the boundary, there were still some reflections from waves with oblique angles. Nevertheless, this boundary condition damped the main portion of unwanted reflections and helped in better identification of different events due to the interaction of the incident wave with the fracture.

Figure 3-17 shows a schematic of the generated model with a finite horizontal fracture in the middle of the model. This figure shows the fracture when its length is 4 cm, which means the fracture extends from one end (right of the sample) to the centre of the sample. A number of events that occur after the wave is sufficiently propagated in the model are identified in the figure. The wavefront identified by number 1 is a reflection from the surface of the fracture. Event number 2 represents that part of the wave energy which has transmitted across the fracture.

Amplitudes of both of these events are smaller than the amplitude of the source wave. These events are similar to those discussed in the previous model with an infinite fracture. As the fracture extends only up to the centre of the sample, the wave in the left side of the sample propagates in the intact medium. This wavefront is identified by number 3. Note that Event 2 is delayed and has smaller amplitude with respect to Event 3 due to the effect of the fracture.

The diffraction behaviour of a fracture can be determined by Huygen's principle. To do so, it is necessary to consider each point on the fracture as an individual source point which emits waves identical to the source wavelet. Such a wave then propagates from the point sources in all directions with the speed equal to the speed of the original incident wave. This will result in geometrical spreading as the wave propagates in the medium. This is however not the case for plane waves which do not experience amplitude reduction simply by propagation. An incident P-wave will generate both P and converted P-to-S diffractions (Toomey, 2001). Number 4 shows the P-wave diffraction and Event number 5, shown by grey arrows, indicates P-to-S converted diffraction. As can be seen, these two waves originate from the end point (tip) of the fracture and propagate circularly in this isotropic two-dimensional model.

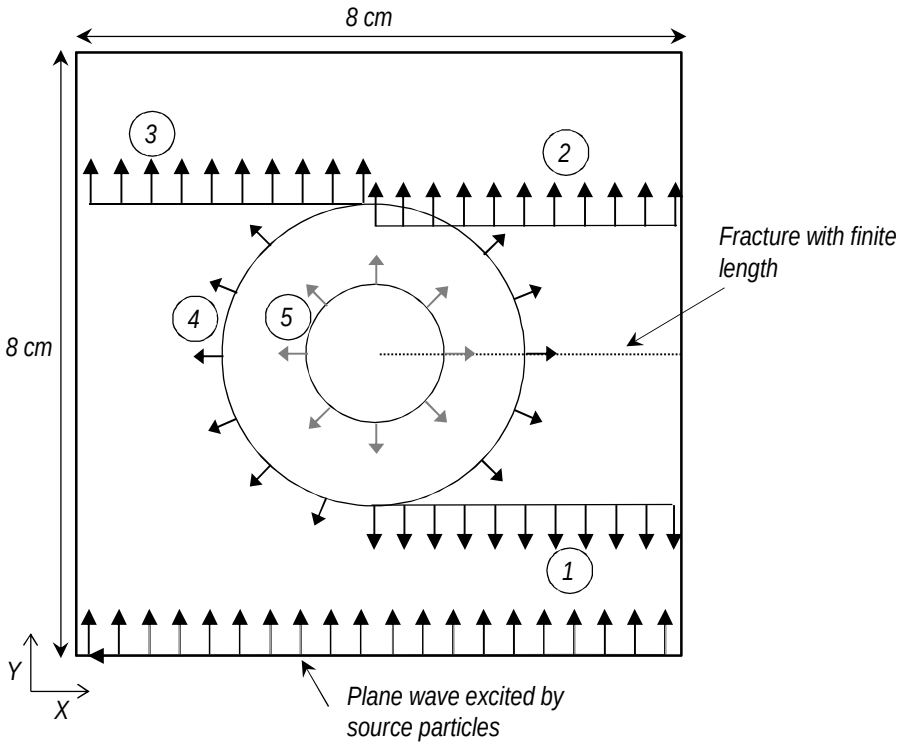

Figure 3-17 A schematic of the model showing different events due to a finite fracture

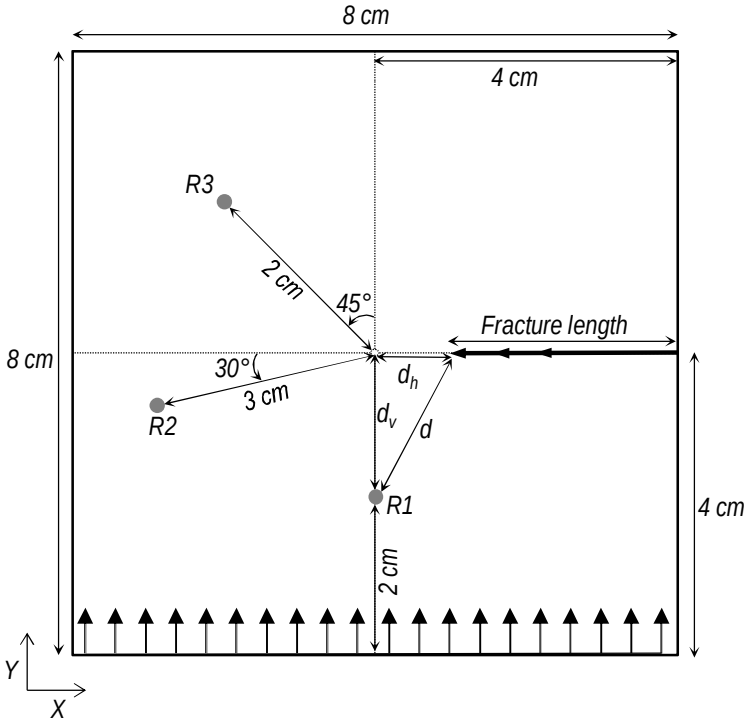

Figure 3-18 A schematic showing location of receivers in the mode with respect to the propagating fracture

Analysis of the results from the intact model with those from the models with fractures of different length reveals different waves which emerge due to the presence and propagation of the fracture in the model. Furthermore, the effects of location of receivers as well as fracture specific stiffness on recorded events are analysed. These inspections can assist in interpretation of results of experiments whose conditions are imitated by the numerical model. Figure 3-18 is a schematic of the model showing a propagating fracture as well as the location of different receivers in the model. The following sections contain discussion of the results recorded by different receivers in altered circumstances of fracture length and specific stiffness.

Propagation of a fracture with a constant specific stiffness

In order to investigate the effect of a moving fracture in the model a horizontal fracture was modelled starting from the right boundary of the sample (see Figure 3-18). Fracture length was increased in 0.5 cm steps and ultrasonic wave propagation was conducted for each fracture length. Concurrently, X and Y velocity components of the receiver particles shown in the figure were recorded while wave propagation was being conducted. Afterwards, the data recorded by each receiver in

the intact model (without any fracture) was subtracted from the data recorded by that receiver in the fractured models. This is to illuminate only events that have emerged as a result of the fracture in the model and remove events such as direct arrivals and possible boundary reflections.

The top plot in Figure 3-19 shows the recorded trace of horizontal (X) component of receiver R1's velocity in the models with fractures of different length. The vertical axis shows the travel time of the recorded waves in microseconds. Only that portion of traces which are of interest are shown here. As can be seen in the plot, as soon as the fracture is created in the model (starting from the far left trace), two

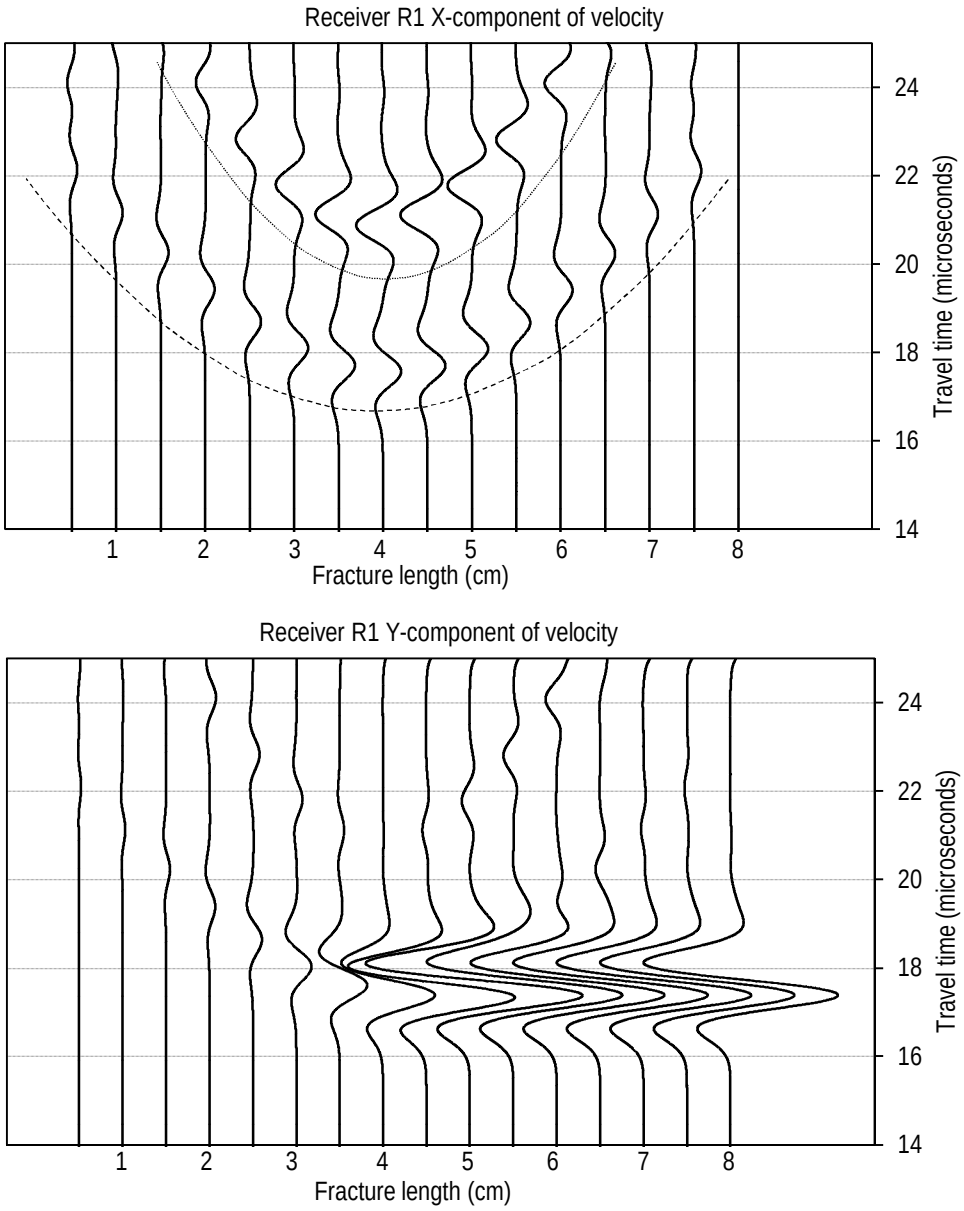

Figure 3-19 Recorded traces of X and Y component of receiver R1 at different fracture lengths

different events are recorded by the receiver. Travel times of both events change with increasing fracture length. Initially these events arrive earlier as the fracture length increases up to 4 cm. However, for fractures with a length of more than 4 cm their travel time increases. Considering the tip of the fracture (here right end of the fracture) as the source of diffractions, it becomes clear that the distance between the tip and receiver R1 is initially decreasing until it reaches a minimum of 2 cm at the fracture length of 4 cm. Having in hand horizontal (d_h) and vertical distance (d_v) between source and fracture tip, the distance, d, can simply be obtained as follows:

$$d = \sqrt{d_h^2 + d_v^2} \tag{3-13}$$

This defines a hyperbolic shape for the arrival times of these events. The event arriving earlier is the diffracted P-wave from the fracture tip. The approximate arrival time of P-wave diffractions is identified by the dashed line in the top plot of Figure 3-19. The second event is attributed to P-to-S converted diffractions from fracture tip. The approximate arrival time of this event is shown by the dotted line in the plot. One can examine the travel time of these events to confirm their source. For instance, in the case of fracture with a length of 5 cm, the distance between tip diffractor and source is around 2.2 cm. Therefore the total travel distance for compressional wave diffraction is 6.2 cm (the distance between source of plane wave and fracture is 4 cm). Now considering the fact that for this Ricker source wave the peak amplitude occurs at 4 microseconds and recalling the peak-to-peak compressional wave velocity of around 4450 m/s, it can be predicted that the peak of the diffracted P-wave should arrive at around (0.062/4450) + (4×10^{-6}) =17.4 microseconds which is close to the peak time shown in the plot. For P-to-S diffractions however, P-wave velocity should be considered for the calculation of travel time of the wave from source to fracture while S-wave velocity should be used for obtaining the travel time from the fracture tip to the receiver. This similar process results in an expected peak arrival time of around 21 microseconds which is again in accordance with that of the relevant trace of a 5 cm fracture. Following a backwards procedure it is possible to back-calculate fracture length from travel time of P-wave or P-to-S converted diffractions. This approach has been used previously by other researchers (e.g. Savic, 1995; Groenenboom, 1998; Lhomme, 2005) and was also

followed for calculation of the fracture tip location in the experimental part of this study.

The plot also shows that the shorter travel times of diffractions, the larger the amplitude. Recalling the fact that a wave radiated from a diffractor point spreads in all directions, a geometrical spreading effect comes into play which causes amplitude reduction as the wave travels. The closer the fracture tip is to the receiver, the less the distance travelled by diffraction events, and hence less reduction of amplitude before it is recorded by the receiver.

The bottom plot in Figure 3-19 shows the Y-component of the receiver particle velocity versus fracture length. Again P and P-to-S diffraction events are visible in this plot. However, it is observed that from a fracture length of more than 4 cm, there is an event with a constant arrival time. This is actually the portion of wave energy which is reflected from fracture surface as soon as the fracture reaches the vertical line passing from the receiver. The plot also indicates that the diffraction's amplitude is considerably smaller than the amplitude of reflections and that is why in this plot the diffractions are not pronounced as well as the plot of X-component of velocity. It is expected that similar waveforms are recorded by a transducer which is placed on the same face of the sample as the source transducer. This will be discussed in more detail in Chapter 5 where similar experimental configurations are presented. Note that the waves emitted by ultrasonic transducers cannot strictly be assumed as perfect plane waves. However, in numerical modelling of this study only plane waves are used as the source waves in order to make the interpretations easier. As will be seen later, despite this simplifying assumption, the numerical results are helpful in interpretation of diffractions observed in experiments.

In order to exclusively capture the diffractions in the laboratory hydraulic fracture monitoring experiments, it is required to place a receiver transducer on the surface of the sample perpendicular to the fracture path and a source transducer on the sample surface parallel to the fracture path. More details on such a configuration can be found in Chapter 5 where experimental results are discussed. To numerically model this situation, waveforms in models with different fracture length were recorded in receiver R2 (see Figure 3-18). As this receiver is not located on the symmetry line of the square-shape model, it is not expected that recorded diffractions result in a symmetric shape similar to those observed for receiver R1.

Figure 3-20 shows traces of X and Y components of receiver R2 velocity recorded at each fracture length. As can be seen in the top plot, both diffraction events are visible: P-wave diffractions whose approximate arrivals are marked by the dashed line, and P-to-S diffractions which arrive later and are shown by the dotted line.

Due to an almost linear relationship between fracture length and the distance between the fracture tip and receiver R2, the arrival time shows an almost linear trend. Interference of P-wave diffractions, P-to-S diffractions, and the boundary reflection of the P-wave diffraction causes deformation of the wave form at a fracture

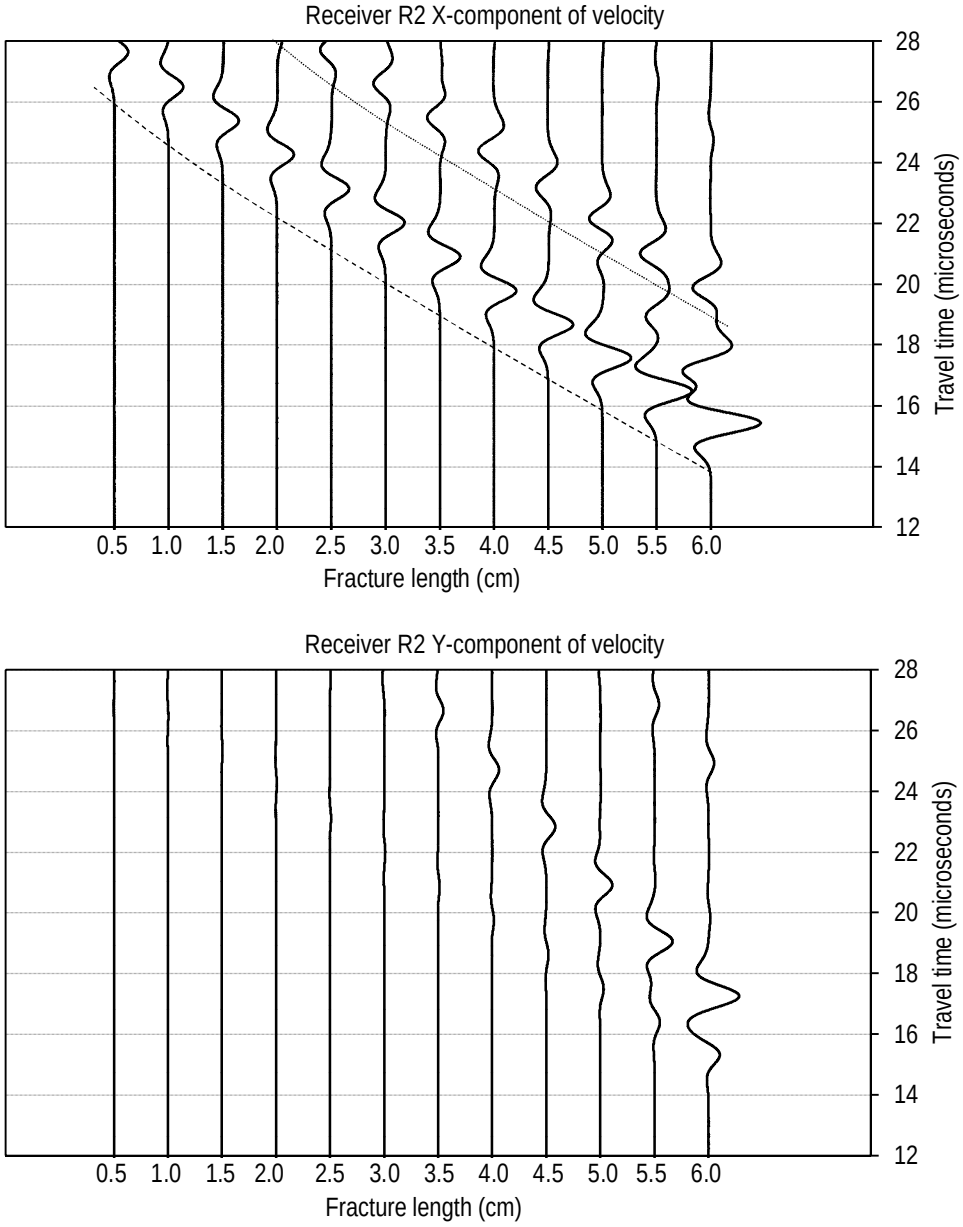

Figure 3-20 Recorded traces of X and Y component of receiver R2 at different fracture lengths

length of more than 5 cm compared to other fracture lengths. Furthermore, the weak events which are observed with a fracture length of more than 5.5 cm, a few microseconds after P-to-S diffractions are boundary reflections of these diffractions. The bottom plot shows the Y-component of the abovementioned events for the same fracture lengths. The plot shows that Y-component peak amplitudes of the P-wave recorded at R2 are considerably smaller than the Y-component peak amplitudes of P-to-S converted diffractions while in the top plot the X-component peak amplitudes of the P-wave diffraction is larger than those of P-to-S diffractions. Similar to what followed for receiver R1, as a useful tool, it is possible to back-calculate the length of the fracture from travel times of P-wave or P-to-S converted diffractions.

Receiver R3 in Figure 3-18 is located in a position where transmissions across the fracture are expected to be recorded as soon as the fracture intersects the vertical line that passes from the receiver. Furthermore, even before the fracture reaches the source-receiver line, it is expected to record diffractions from the fracture tip at this receiver, similar to that observed in R1 and R2.

Figure 3-21 shows X and Y components of receiver R3 velocity recorded at different fracture lengths. The top plot (X component of velocity) clearly shows the arrival of two distinct diffractions, P-wave diffractions which arrive earlier, and P-to-S converted diffractions which arrive later. The approximate wavefront of the former is shown by the dashed line and that of the latter is shown by the dotted line. The closer the fracture tip to the receiver, the higher the amplitude of both diffraction events. The bottom plot shows the Y component of receiver R3 velocity. It is observed that at small fracture lengths where the fracture has not yet interfered in the source-receiver line, the direct arrivals are recorded with a constant peak arrival time of approximately 16.7 μs. Due to relatively high amplitude of direct arrivals compared to that of diffractions, diffraction events are not visible at early stages but they start to appear as the fracture tip becomes closer to the receiver which results in less geometrical spreading before being recorded by the receiver.

For fracture lengths larger than 5.5 cm, it is shown that not only the amplitude of the direct arrivals is decreased, but they are also delayed. This indicates the interference of the fracture with the source-receiver line. Reduction of amplitude and time delay occurring for the transmissions is related to the fracture specific stiffness as was discussed in detail in section 3.4.2.2. This receiver thus successfully

captures properties of two events: transmissions across the fracture and diffractions from the tip of the fracture.

When the fracture tip reaches the area close to the source-receiver line, transmission and diffractions may interfere as their arrival times become closer. This is when P-wave diffractions arrive just after the direct transmission arrivals. Figure 3-22 shows an example where this interference occurs at receiver R3. The dashed line shows the direct arrival recorded in the intact model and the solid line is the record in the model with a 4.5 cm fracture. At this length the fracture has not reached the source-receiver line yet (according to Figure 3-18 this occurs at a length

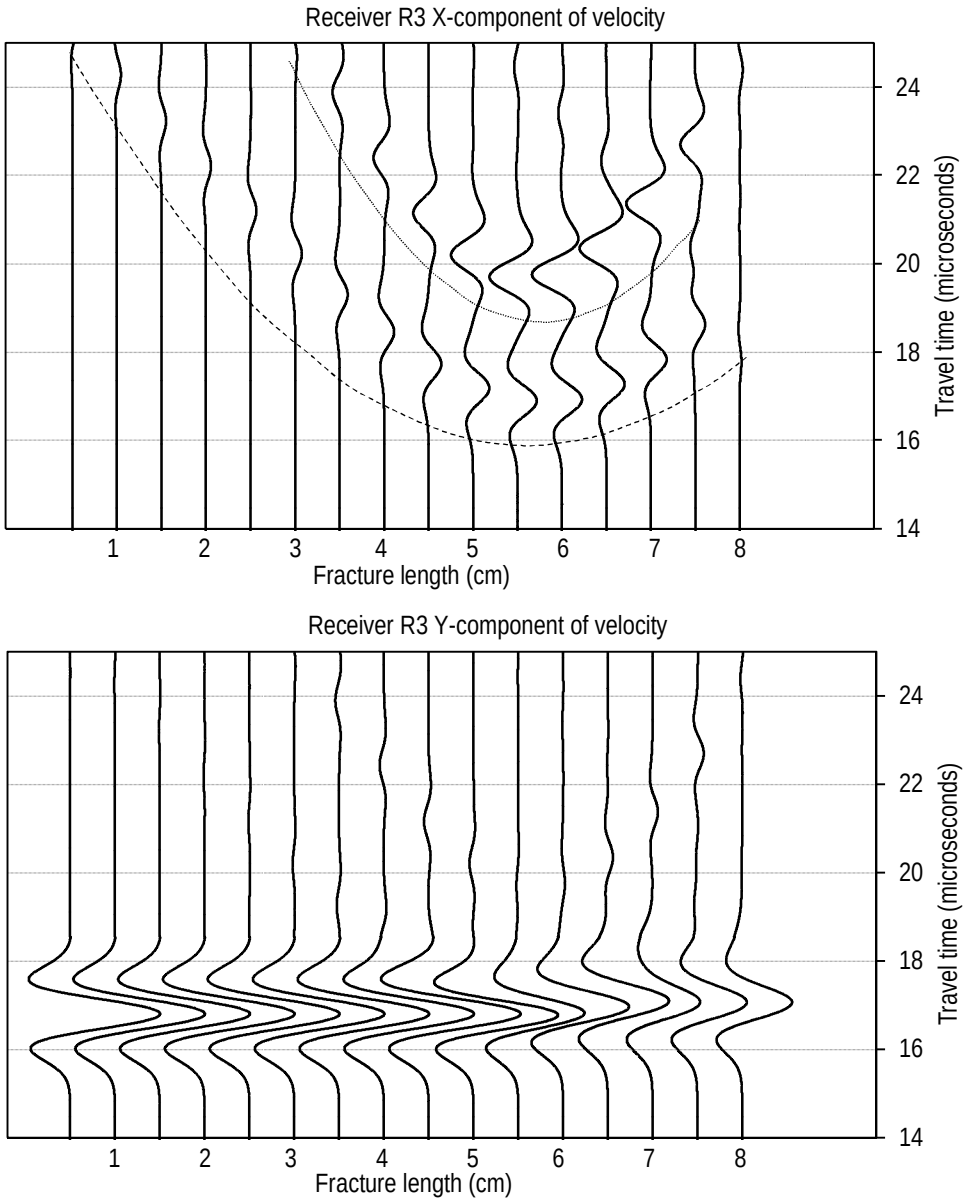

Figure 3-21 Recorded traces of X and Y component of receiver R3 at different fracture lengths

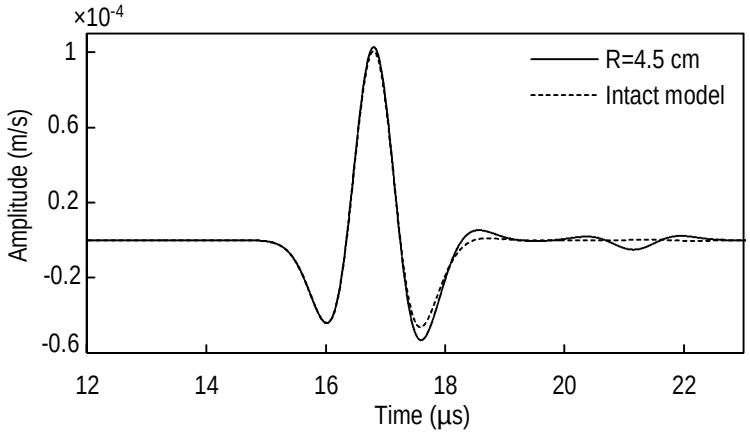

Figure 3-22 Y component of receiver R3 velocity in the intact model and a model containing 4.5 cm long fracture

of 5.4 cm). The figure shows that at a fracture length of 4.5 cm, constructive interference of P-wave diffractions with the direct arrival results in an apparent increase in the amplitude of the late part of the direct arrival. This is particularly identifiable in the second trough of the recorded arrival where the amplitude was increased by almost 20 %. Note that due to the relatively small amplitude of the diffractions compared to the amplitude of direct arrivals, it is difficult to identify this effect in the bottom plot of Figure 3-21. Depending on the amplitude of the diffractions (which in turn is a function of fracture specific stiffness as will be seen in the next section), this effect can be more or less significant. This should be taken into account when interpreting laboratory results which are generally more complex than this simple model.

The second event observed in the model with a 4.5 cm long fracture is a P-to-S converted diffraction. As the fracture reaches closer to the source-receiver line, the direct arrivals also become affected by the fracture and their amplitude decreases as shown in the bottom plot of Figure 3-21.

Effect of Fracture Specific Stiffness on Diffractions

Similar to reflections and transmissions across a fracture, diffractions from the fracture tip are also dependent on the specific stiffness of the fracture. In order to study the effect of the fracture stiffness on diffraction patterns, a simple numerical experiment was conducted on the previous model by generating a fracture with a constant length of 4 cm and varying the specific stiffnesses of the fracture.

Figure 3-23 shows plots of X (top) and Y (bottom) velocity components of receiver R2 recorded in the models having fractures with different specific stiffnesses. In these plots P-wave diffractions and P-to-S converted diffractions are also identified.

It is seen that the more compliant fracture results in diffractions with higher amplitude. This is the same for P-wave diffractions as well as P-to-S converted diffractions. Sensitivity of diffractions amplitude to specific stiffness of fracture has been already recognised in the literature (e.g. Toomey, 2001; Henry, 2005). Toomey (2001) noted that diffractions are even more sensitive to the specific stiffness of a fracture than the frequency of the incident wave.

The change of diffraction's amplitude resembles the trend observed previously for reflections from fractures with varying stiffnesses (see the bottom plot of Figure 3-11). This can be understood by recalling the fact that reflection from a surface is basically a constructive interference of the diffractions from individual points on its surface. This leads to a similar behaviour for these two events. Changing the fracture specific stiffness from 20 TPa/m to 2.5 TPa/m causes an

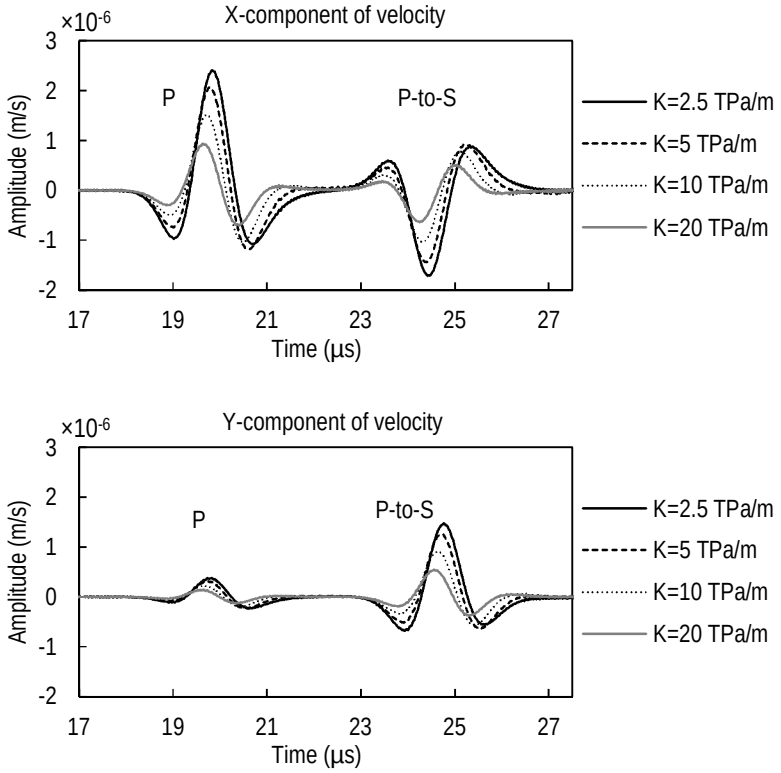

Figure 3-23 X and Y velocity component of receiver R2 in different fracture specific stiffnesses

approximate 89% increase in the peak amplitude of reflections (see the bottom plot of Figure 3-11). The same change of fracture specific stiffness results in increases of around 160% and 170% in the peak amplitude of P-wave diffractions and P-to-S converted diffractions, respectively. This observation indicates that although the behaviour of amplitude variations in reflections and diffractions are similar, the diffractions are considerably more sensitive to changes in specific stiffness of the fracture compared to reflections. In addition, the results suggest that the effect of the fracture specific stiffness on the amplitude of P-to-S converted diffractions is slightly more than its effect on P-wave diffractions.

According to the displacement discontinuity theory, reflections are delayed by fractures based on a relationship with the frequency and specific stiffness of the fracture. Previous numerical results of normal reflections from a facture based on the smooth-joint contact also showed that more compliant fractures cause longer delays in reflections (see section 3.4.2.2). Having this in mind, it is also observed that diffractions are delayed which is based on the specific stiffness of a fracture: a more compliant fracture results in longer time delays in diffractions compared to a stiffer fracture.

3.5 Modelling Hydraulic Fracture Monitoring

In the previous section fracture simulation in PFC was conducted using a smooth-joint contact model. It was shown that this contact model which previously had been used solely for geomechanical modelling of rock joints, exhibits seismic behaviours in accordance with the displacement discontinuity theory. The relatively easy implementation of smooth-joint makes this contact model a useful tool for modelling seismic behaviour of fractures. Transmissions, reflections, and diffractions from a fracture were modelled using this contact and results were showed to be valid.

In the work of Groenenboom (1998) however, a hydraulic fracture was modelled using a thin fluid layer model. It was pointed out that linear slip assumptions have some limitations compared to the thin fluid layer model. For example, in the case of an ideal fluid-filled fracture, the linear slip model does not appropriately include the explicit boundary condition of complete shadowing of shear stresses across the fracture. Nevertheless, for perpendicular transmissions the linear slip model (fracture based on DDT) and thin fluid-filled layer are

indistinguishable. Furthermore, it was shown that for thin enough hydraulic fractures, the displacement discontinuity and thin layer model agree well.

This section discusses an attempt that was made to model the seismic response of hydraulic fracture propagation in PFC using a new approach: the incorporation of fluid-solid coupling in discrete particle models. PFC2D has been previously used for modelling different aspects of hydraulic fracturing such as the interaction of a hydraulic fracture with natural fractures (e.g. Sarmadivaleh et al., 2011; Sarmadivaleh, 2012; and Han et al., 2012), and seismicity induced by hydraulic fractures (e.g. Zhao and Young, 2009; Yoon et al., 2012). To model hydraulic fracturing due to fluid injection into the rock, the fluid-solid coupling capability of PFC is employed. This allows modelling fluid-solid interactions at the micro-scale.

In the following sections, firstly, the procedure for modelling hydraulic fracturing in PFC2D is briefly discussed. Afterwards, the focus is made on hydraulic fracturing monitoring in PFC using active seismic sources. The results obtained from such a model are then compared to those of a smooth-joint contact model.

3.5.1 Hydraulic Fracturing in PFC2D

The aim of this section is to present a brief overview of the process through which hydraulic fracturing by fluid injection into a cubic rock sample can be modelled in PFC2D

For generating a hydraulic fracture in the bonded-particle model, a fluid-solid coupling of PFC2D is used. The algorithm is written in such a way that two different sets of equations are solved by the code. The first one, a mechanical set, includes calculation of forces and momentum applied on the particles. The second set is the hydraulic set of equations which includes different parameters such as fluid pressures, pore throat size, pore volume and mechanical force.

Before solving the equations, required entities (e.g. pore spaces, conduits, etc.) are defined in the code. The location of pore spaces (which are called fluid domains in PFC) are determined using the geometry of the group of particles which have bonded contacts with each other and form an inner empty space (Itasca Consulting Group, 2008). This empty inner space is regarded as the pore space.

Special conduits (which are also called pipes in PFC) are then generated in order to connect adjacent pore spaces. Fluid flow through the conduits is calculated assuming a parallel-plate channel configuration. The flow rate of each conduit is dependent on the pressure difference between its two pore spaces, the length of the conduit, the given conductivity factor, and aperture of the conduit. The aperture of the conduit is in turn dependent on a given initial aperture value as well as the mechanical force applied to the conduit. Under compressional forces the conduit apertures are reduced and under tensile forces they are increased. The calculated flow rate through a conduit results in the corresponding changes in the pressure of its pore spaces. In summary, in such a scheme fluid and solid coupling is achieved in three different ways: variation in aperture due to changes in contact force, exertion of forces due to pore fluid pressures on surrounding particles, and changes in pore space pressures due to mechanical changes in domain volumes. For more details and relevant formulations of fluid-solid coupling the reader is referred to the PFC2D Manual (Itasca Consulting Group, 2008).

3.5.2 Model Generation

An 8 cm × 8 cm square-pack assembly of bonded particles was generated in a way similar to the previous models. Normally, hydraulic fracturing modelling in PFC is conducted in random assemblies of particles in order to take into account the effect of the inherent inhomogeneity of the rock on the fracture propagation path. Nonetheless, the purpose of this study is to create a straight hydraulic fracture in a homogeneous model. This is to reduce complexities associated with interpretation of seismic waves in the model. That is why a square pack assembly of particles is used in this section. Because running the model in the fluid-solid coupling mode would take a much longer time for the same model without fluid coupling, a larger particle size (0.2 mm radius) was selected for the model. The model had a bulk density of 2100 kg/m^3 and the elastic modulus of the particles was selected in such a way to result in a compressional wave velocity similar to that of previous models (around 4450 m/s).

As will be seen in the next chapters, in hydraulic fracturing experiments, the cubic samples are placed under mechanical stress before commencement of hydraulic fracturing. To resemble these conditions, similar stresses were applied to

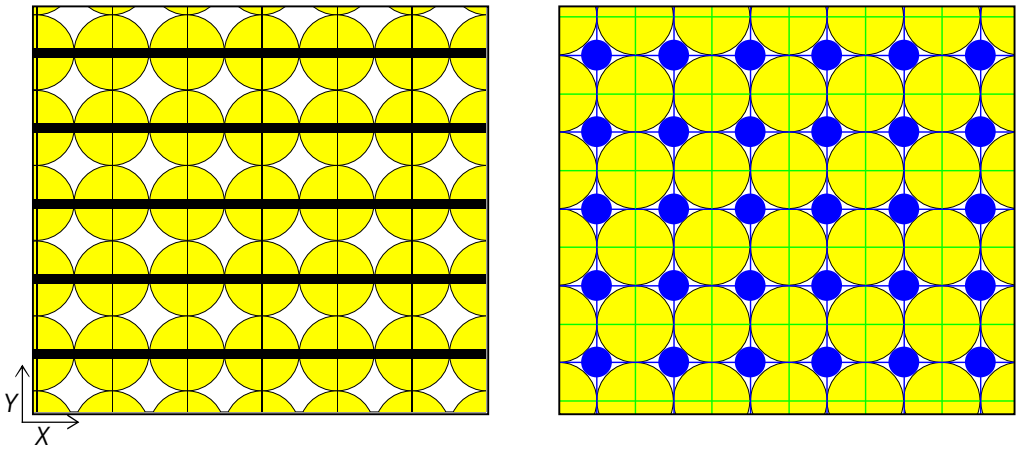

Figure 3-24 Snapshots of the square pack particle assembly showing contact forces between particles (left) and pore spaces, conduits, and domain boundaries (right)

the particle assembly model. This was achieved by taking advantage of step-wise servo-control movements of particles located on the boundary of the sample (Itasca Consulting Group, 2008). In the case of a two-dimensional sample and looking at the sample from the top, two independent horizontal stresses can be applied to the sample: minimum horizontal stress (σ_h) and maximum horizontal stress (σ_H). A maximum horizontal stress of 8 MPa (1160 psi) and a minimum horizontal of 0.8 MPa (116 psi) was applied to the model. At this stage the model can be perceived to resemble conditions of a laboratory sample which is under mechanical stress. The left picture in Figure 3-24 shows a snapshot of the contact forces in the square pack particle assembly. Particles are shown in yellow. The tick black lines in the X direction represent the maximum horizontal stress and thin black lines in the Y direction indicate the minimum horizontal stress. As expected all forces are in the normal direction.

The next step was to incorporate fluid-solid coupling in the model. In a square assembly of particles, pore spaces are located simply at the centre of squares formed by connecting centres of each group of four particles. Conduits and pore spaces, therefore, construct a square-shape network. The right picture in Figure 3-24 shows a snapshot of the generated pore spaces and conduits in the model. Blue circles show the location of pore spaces and blue lines represent the conduits which connect nearby pore spaces. Green lines in this picture illustrate the boundaries of the domains which coincide with the contact lines between particles.

Fluid injection into the model was taken to occur at its centre. A constant-pressure scheme was used for this purpose. Pressure of the central domain (pore

space) of the model was set to a constant value of 20 MPa (2900 psi) and the model was cycled for adequate time steps in order to let the pressure propagate in the nearby domains. Fluid pressure in this domain not only pushes the nearby particles apart, but also causes the fluid to flow towards nearby domains through the conduits. Due to the fact that an inhomogeneous stress is applied to the model, the fluid flow preferentially occurs parallel to the maximum horizontal stress. This is because the large compressive normal force in the direction of maximum horizontal stress attempts to push and close the conduits perpendicular to it. On the other hand, the minimum horizontal stress causes a small resistance to the opening of the conduits perpendicular to it. Therefore, the fluid preferentially flows in the conduits which are perpendicular to the minimum horizontal stress and parallel to the maximum horizontal stress. Opening of any conduit results in an increase in the pressure of the following domain. Moreover, if the fluid pressure is large enough, it can overcome the contact bond strength and can cause the contact bond to break. This will in turn result in the separation of corresponding particles.

By cycling the numerical model, the above processes repeat which results in evolution of a hydraulic fracture. The left picture in Figure 3-25 is a snapshot of the model which shows the induced hydraulic fracture. The location and size of magenta circles in this picture indicate the location and pressure of pore spaces, respectively. As the hydraulic fracture propagates symmetrically from the centre of the model,

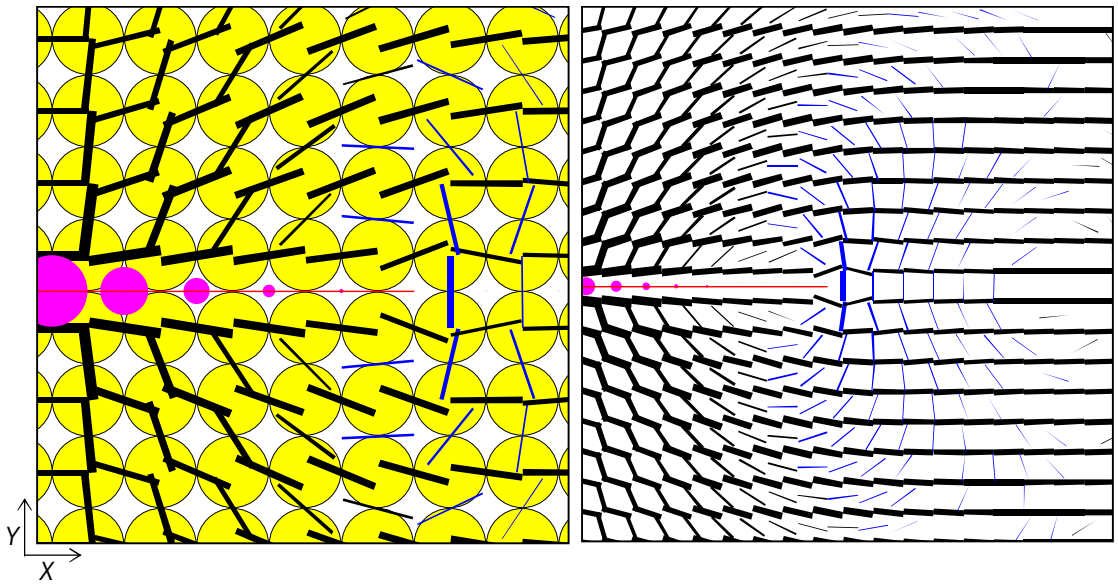

Figure 3-25 Snapshots of the model showing fluid pressure in fracture, broken bonds, and the state and direction of contact forces in the model

only the right wing of the fracture is shown. The largest magenta circle to the left of the picture specifies the pressure at the injection point. Fluid pressure is shown to decrease from the injection point to the fracture tip.

Black lines and blue lines show compressional and tensile contact bond forces, respectively. Furthermore, the thickness and direction of the force lines represent the magnitude and direction of the forces, respectively. A high fluid pressure in the fracture applies a tensile stress on the corresponding particles trying to pull them apart. If the fluid pressure is high enough, the contact bond may break. Red lines in this picture show contact bonds broken due to excessive tensile forces. The fracture path can be realised by following these broken bonds which continue in the X direction to the right. As can be seen, there is no contact force line between the particles lying on two sides of the fracture. This indicates they are no longer in solid-solid contact and it is only the fluid inside the fracture which can transfer the force between fracture particles. This situation resembles an open hydraulic fracture in the rock whose walls are not in mechanical contact.

Furthermore, comparison of this picture with the left picture in Figure 3-24 can help in understanding how the state of stress in the sample has changed due to fracture propagation. Before the start of injection and introducing a fracture to the model, all force lines lie on their corresponding contact lines indicating purely normal components of the forces. However, bond force lines are tilted due to the generation of the fracture which indicates development of shear forces in the model. The more tilted a force line is with respect to its contact line, the larger its shear component is. It is also shown that along the hydraulic fracture a large normal force is generated in the Y direction. The thickness of the lines show the magnitude of this force is comparable to that of the maximum horizontal stress. Fluid pressure inside the fracture pushes the particles on two sides of the fracture mostly in the Y direction (upward for particles on the top wall of the fracture and downward for particles on the bottom wall of the fracture). These particles in turn transfer the load to the nearby particles which results in a new stress distribution in the model.

The near-tip region of hydraulic fractures is a complex region which has attracted considerable research work (e.g. Thiercelin, 1993; Desroches et al., 1994 and Lenoach, 1995). Assuming the fluid reaches the tip of the fracture, a particular singularity in the pressure and the stress field around the fracture tip is developed (Desroches et al., 1994). The hydraulic fracture model in this arranged particle

assembly can deliver interesting information on the fracture tip region. The last particle pair whose bond is broken is the last point of the fracture which is open. The picture shows there is a large tensile normal force between the next particle pair (the tick vertical blue line). This point represents the tip of the fracture which shows particular tensile stress concentrations. The tensile stress is generated by the fluid pressure inside the fracture. If the model is cycled enough, this tensile force overcomes the bond strength and causes the bond to break. As soon as the bond is broken, particles become separated even more and lose their solid-solid contact. As long as the pressure support is high enough, this process continues and the fracture propagates forward. The right picture in Figure 3-25 shows a snapshot of the contact bond force distribution in a larger scale. As shown in the picture, the stress distribution is altered in an area well ahead of the fracture tip. These changes are particularly evident in generation of tensile forces in the Y direction (direction of the minimum horizontal stress). These forces are normal ahead of the fracture tip but have shear components in the vicinity of the tip. Although in the current model no bond breakage is seen in this area, in reality this process could lead to damage and generation of micro-fractures in the rock. Seismic monitoring was shown to be able to capture the early generation of such micro-cracks in the rock (Pyrak-Nolte et al., 1996b).

It is worth noting that the tip process is a complex phenomenon and an ongoing research topic whose investigation is out of the scope of this study. The goal of this section is to model seismic monitoring of a simple straight hydraulic fracture, which is believed to be a more realistic representation of a hydraulic fracture compared to the displacement discontinuity model. Therefore, the hydraulic fracture model at this point was deemed to be appropriate for the purpose of modelling hydraulic fracture monitoring.

3.5.3 Time-Lapse Ultrasonic Monitoring of a Straight Hydraulic Fracture

The hydraulic fracture model generated in the previous section was used for modelling seismic monitoring of fracture propagation. For this purpose, the distance between the particle pairs that lie on the hydraulic fracture was measured at different times of the modelling period. Figure 3-26 shows the separation between the particles located on two sides of the fracture, from the injection point up to a distance

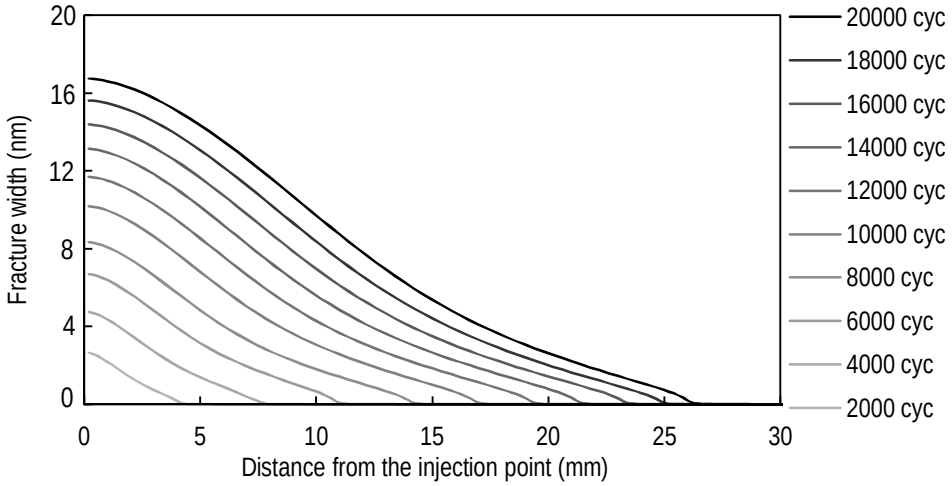

Figure 3-26 Hydraulic fracture width versus length at different moments of simulation

of 3 cm from the injection point. Such a plot of separation between consequent particle pairs along the fracture forms the width profile of the fracture. The tip of the fracture in this plot can simply be found by the latest point which has non-zero width. At each time step (cycle), the fracture width is maximum at zero radius which is actually the injection point. The fracture width then reduces by a tapered trend from this point to the tip of the fracture.

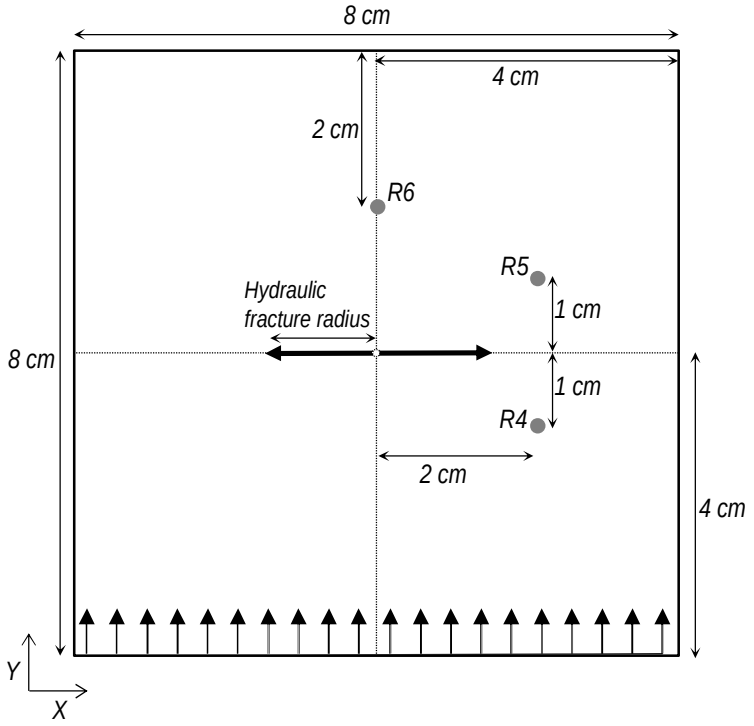

Figure 3-27 Schematic of the hydraulic fracture model showing the location of receivers

At the same times when a fracture width measurement was undertaken, ultrasonic transmissions were conducted by introducing a compressional plane wave to the lower boundary of the model. The same source wavelet used in the previous smooth-joint model was used here. However, a slightly lower frequency (400 KHz) was used here in order to reduce numerical dispersion due to the larger particle size in the hydraulic fracture model. Figure 3-27 shows a schematic of the model with the hydraulic fracture propagating from the centre towards left and right directions. The figure also shows locations of receivers where ultrasonic data were recorded.

3.5.3.1 Reflections and Diffractions

Figure 3-28 shows recorded traces of the Y component of Receiver R4 at different moments of the modelling time. The figure shows two distinct recorded events. The travel time of the first event decreases with the modelling time. On the other hand, its amplitude increases with the modelling time. The normal distance between the vertical line (parallel to the Y direction) passing through the receiver R4 and the centre of the model is 2 cm (see Figure 3-27). According to Figure 3-26, the fracture intersects this line sometime between 12000 and 14000 numerical time steps. The approximate first peak arrival time of this event is marked by a dashed line in Figure 3-28 . It seems that the arrival time of this event decreases until 12000 time steps after which it remains constant. On the other hand, the amplitude of this

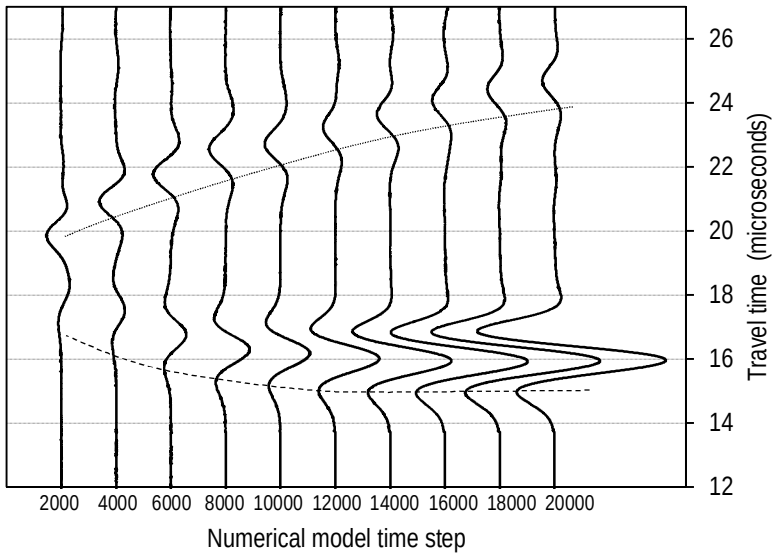

Figure 3-28 Recorded traces of Y component of Receiver R4 particle velocity at different numerical model time steps

event increases with decreasing travel time. Comparing this trend to the trend previously shown in the bottom plot of Figure 3-19 makes clear that this is due to the diffractions from the moving fracture tip. As soon as the fracture intersects the R4 line, the receiver starts recording reflections from the fracture surface. It seems that the travel time of these reflections remain constant as the distance between the reflector point on the fracture and the receiver is constant. It also appears that the amplitude of reflections remains unchanged.

In order to investigate these events more closely, reflections recorded at receiver R4 after three different values of numerical time steps, and after the fracture intersected the R4 vertical line, are plotted in Figure 3-29. The plot clearly illustrates that unlike reflections recorded in Figure 3-19, the reflection amplitudes increase with the modelling time. Furthermore, it seems that there is a slight time delay in the peak arrival time of the reflections.

Recalling the fracture profile in Figure 3-26, it is known that the local fracture width at a point 2 cm from the centre of the model (which is the reflector point for receiver R4) increases as the injection continues. As a result, although the location of the reflector point is constant, reflection behaviour varies. Any increase in the width of the fracture corresponds to a decrease in the fracture specific stiffness. The trend observed in this plot is in agreement with the predictions of the displacement discontinuity theory: reflections become stronger and they are delayed longer as the specific stiffness of the fracture reduces. This plot is very similar to the bottom plot in Figure 3-11 where the effect of variations in the specific stiffness of

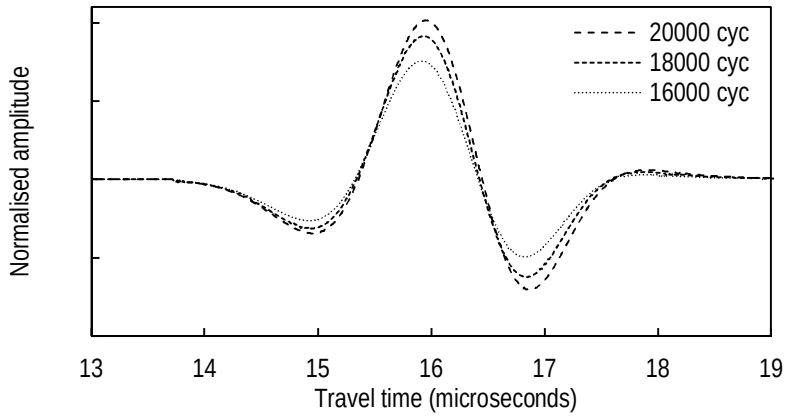

Figure 3-29 Reflections recorded at Receiver R4 after three different moments of numerical time step

the smooth-joint fracture on reflections is shown. Therefore it provides a tool for back-calculating the local specific stiffness, and hence the fracture width from fracture reflection data. Recording data in real-time also allows constructing a real-time width profile of the fracture.

The amplitude of reflections recorded in Figure 3-19 however, remains constant as a constant specific stiffness was assumed for the smooth-joint contact. In real hydraulic fracturing operations, the local fracture width is dependent on fracture roughness and fluid pressure. These also are, in turn, dependent on factors such as injection rate, local opening of new volumes to the fracture closed system, and leak-off rate. These numerical results suggest that the current numerical hydraulic fracture model is a better candidate for modelling more realistic seismic monitoring of hydraulic fracture propagation compared to the displacement discontinuity model or thin fluid layer. This is because fluid-solid interactions and their corresponding effects on fracture seismic properties are modelled in a more realistic way in a DEM-based hydraulic fracture model- one example of its better suitability is taking into account the tapering profile of the fracture.

The second event in Figure 3-28 shows a different behaviour: its travel time increases and its amplitude decreases as the fracture propagates. Therefore, it has to be related to a feature of the model whose distance from the Receiver R4 increases over the modelling time. Looking at Figure 3-27, it is realised that the only feature of the model with this property is the far tip of the fracture (the left tip in Figure 3-27). Unlike the near tip of the fracture which becomes closer to receiver R4, the far tip travels further away from the receiver.

Such travel time of the diffractions recorded from both fracture tips can be used to construct the propagation profile of the fracture similar to what was discussed in the previous section for the smooth-joint fracture. In this case however, it is possible to back-calculate the location of both tips of the fracture from their corresponding diffractions to determine how far the fracture tips have propagated and to find out if the fracture has propagated symmetrically in the medium.

3.5.3.2 Transmissions and Diffractions

It is expected that the waveforms recorded by Receiver R5 also show the effect of fracture on ultrasonic transmissions as well as diffractions from both fracture tips. Figure 3-30 shows recorded traces of the Y component of Receiver R5 velocity at

different numerical time steps. The trend shown in this figure for the diffractions from the far tip of the fracture is similar to that of Figure 3-28 indicating increasing arrival time and decreasing amplitude over the numerical modelling period.

The first recorded event, however, is different in this case. The far left trace shows the waveform recorded in the intact sample, before commencement of fluid injection. Travel time of the main peak of the direct arrival to receiver R5 is very close to 16 μs. As the fracture is initiated in the model (time steps 2000 and later) the diffractions from both fracture tips arrive at the receiver. However, due to the fact that the diffractions from the near tip arrive just after the direct arrivals (due to their relatively similar travel distance as appears from Figure 3-27) and recalling the fact that the diffraction amplitude is smaller than the amplitude of direct arrivals, it may not be easy to distinguish the two in this figure.

The plot shows that the amplitude and travel time of the direct transmissions peak remain almost constant until 12000 time steps. Afterwards, the amplitude is considerably reduced and the main peak is clearly delayed as the fracture propagates. Before direct intervention of the hydraulic fracture, small variations in the first event are solely due to the diffractions from the near tip of the fracture. As soon as the fracture intersects the R5 line (between 12000 and 14000 time steps), direct transmissions are affected by the fracture. The hydraulic fracture causes transmissions to be delayed and their amplitude to be reduced depending on the local specific stiffness of the fracture at the transmission point. According to Figure 3-26

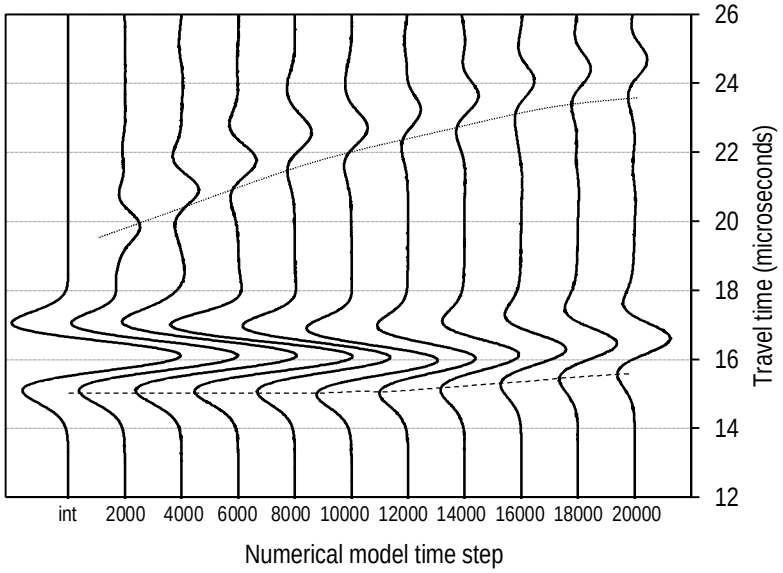

Figure 3-30 Recorded traces of Y component of Receiver R5 velocity at different numerical model time steps

the local fracture width at the transmission point (2 cm away from the centre of the model) increases with the modelling time. This in turn causes the local specific stiffness to be reduced. As shown in Figure 3-30, this gradual decrease in stiffness has caused longer time delays and more pronounced decreases in the amplitude of the first arrivals.

Figure 3-31 shows direct transmissions recorded at different times by Receiver R5. The effect of the hydraulic fracture in the transmissions is clear in this figure. It shows that after generation of the hydraulic fracture in the model, the transmissions were delayed and their amplitude decreased. The amplitude reduces and time delay increases as the fracture propagates and its local width at its centre increases (see Figure 3-26). The trends shown in this plot are very similar to those of the top plot of Figure 3-11.

The abovementioned results indicate that the simulated hydraulic fracture model in PFC shows seismic behaviour which is at least qualitatively in accordance with the theory. Due to the fact that this hydraulic fracture model is more complex than a displacement discontinuity fracture, such as a smooth-joint fracture, its seismic behaviour is not expected to exactly match the displacement discontinuity predictions.

It is also important to note that due to the two-dimensional nature of PFC2D code, seismic amplitude reduction due to geometrical spreading has a relation with square of distance. In laboratory experiments, however, the amplitude decays with a cube of distance. This limitation must be considered when comparing 2D numerical model amplitude reduction with that of experiments.

It is worth mentioning that this model is still in its early stages. For a valid

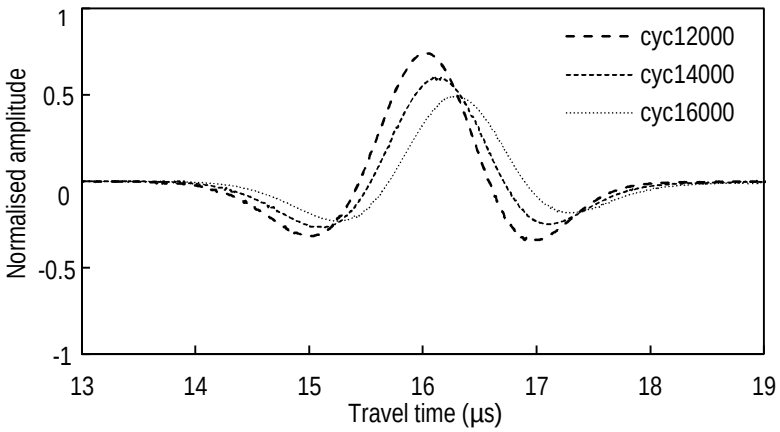

Figure 3-31 Transmissions recorded at Receiver R5 after three different moments of numerical time step

quantitative analysis, one requires to conduct proper calibration of the model parameters such as viscosity of the fracturing fluid, permeability of the sample, and mechanical strength properties of the sample. Such a model will then be able to deliver results which can be quantitatively compared to analytical, numerical, or experimental data. Apart from taking into account the width profile of the fracture and stress distribution around the fracture tip, such a model has the potential to be utilised as a platform for investigation of squirt flow through porous media as a result of dynamic wave propagation.

3.6 Summary

After introducing the discrete element code, PFC2D in this chapter, a brief discussion was presented on the calculation cycle of the code as well as the main limitations associated with it. Wave propagation from a point source in a hexagonal assembly of particles was then modelled and the results were verified. Afterwards, a similar numerical experiment was conducted but in a square assembly of particles. The results were compared by investigating the details of wave-induced contact forces at the micro-scale which showed the importance of the micro-structure of the network on its seismic properties.

Afterwards, the smooth-joint contact model, a contact model which has been commonly used in geomechanical studies for modelling rock joints and fractures, was used for fracture simulation. Seismic characteristics of this contact model were compared to the displacement discontinuity theory predictions and excellent agreement was observed. This was achieved by measuring transmissions and reflections on a smooth-joint contact model with different specific stiffnesses, and plotting the numerical spectral transmission and reflection coefficients together with the theoretical values. The smooth-joint contact model was then used for modelling different seismic events by introducing a propagating fracture to the intact medium. Transmissions, reflections, and diffractions recorded in selected receivers were then presented. The amplitude and travel time of the events were used to determine fracture growth.

In the next step, a simple straight hydraulic fracture was numerically modelled by taking advantage of a fluid-solid coupling algorithm in the discrete element code. This resulted in a wedge-shape fracture profile, gradual fluid pressure

reduction from the injection point to the fracture tips, and redistribution of stresses around the fracture, similar to what takes place in the propagation of a real hydraulic fracture. Ultrasonic monitoring of the hydraulic fracture was modelled by conducting transmissions as the fracture propagated. Interesting transmissions, reflections, and diffractions were recorded and the results were compared to those obtained from the smooth-joint fracture. Ultrasonic events recorded for the numerical hydraulic fracture are expected to be a more accurate representation of the actual event compared to those obtained from the smooth-joint fracture model. This is due to the fact that in the hydraulic fracture model, factors such as fluid-solid interactions and fracture surface contact are explicitly modelled while the smooth-joint model, which is based on the displacement discontinuity theory, considers the combined effect of different parameters in the specific stiffness of the fracture.

The numerical experiments presented in this chapter not only provided valuable information and indications on the likely events expected in similar hydraulic fracture monitoring experiments, but also showed the high potential of discrete element methods for further studies in this area aiming at investigating the related phenomena in more detail.

4 Experimental Set-up

In this chapter the development of laboratory equipment used for carrying out the experimental modelling part of this study is discussed. The experimental results are, however, presented in Chapter 5. The true triaxial stress cell (TTSC) and a core-holder are the two main pieces of equipment used for experiments in this study. There are two major components of equipment: the mechanical module which includes all different parts and tools used for applying mechanical stress and fluid pressure on samples, and the data acquisition module which has the role of acquiring and recording different data such as fluid pressure, stress on the sample, and ultrasonic waves. Most of the equipment was not available or operational when this study commenced. Therefore, the design, development, modification, and calibration of the major parts of the experimental equipment were carried out as a part of this study. At the end of the study, apart from acquiring valuable experimental results, the platforms for further experimental studies on this research subject and other related areas where established at the Department of Petroleum Engineering of Curtin University. In the following sections specifications of the different experimental equipment, their development, modifications, and calibrations are discussed. Focus is put initially on the mechanical parts of equipment while the data acquisition modules are explained afterwards.

4.1 Core-Holder Hardware

The core-holder is one of the laboratory pieces of hardware used for experiments in this study. This equipment was used for two purposes in this study: measurement of P and S-wave velocities in core-sized samples under different stress conditions, and measuring ultrasonic velocities in the fluid used for fracturing under

different pressures. In the following sections its main mechanical parts as well as the data acquisition system are explained.

4.1.1 Mechanical Parts

As the name suggests, the core-holder is used for carrying out experiments on core-sized samples. Different designs of core-holders are used in laboratory experiments depending on the purpose of the tests. The core-holder used in this study had some special capabilities suited for performing ultrasonic experiments under different conditions of stress and pore pressure changes.

Figure 4-1 shows a schematic of the core-holder, illustrating its most important parts. It consists of a steel cylindrical body which can resist pressures of up to 51.7 MPa (7500 psi). It has enough space for core-sized samples of a length up to 10 cm. After placing the core sample inside the equipment, the two end caps are screwed and fixed at each end of the core-holder. Special O-rings provide strong pressure seals as soon as the end caps are fixed in location. Each end cap is equipped with a polyether ether ketone (PEEK) cap. Inside each PEEK cap a dual element (shear/longitudinal) ultrasonic transducer is placed firmly with a spring behind it. The springs maintain a constant force on ultrasonic transducers and a stable contact between the transducer and the PEEK cap. PEEK material is resistant to high pressures. It also has an acoustic impedance similar to that of the cement samples used in this study. Therefore, possible reverberations due to the difference in acoustic impedance of the caps and sample are minimised and ultrasonic energy efficiently is

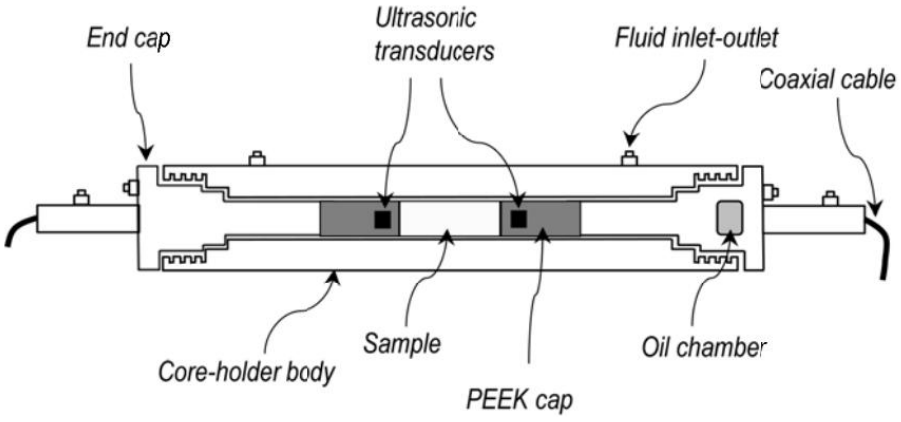

Figure 4-1 Schematic of the Core-holder showing its main parts

transferred from crystals to the rock. Each ultrasonic transducer is capable of receiving or generating either a P or S-wave.

The core-holder is equipped with a number of fluid inlet/outlet ports which provide the ability for applying stresses and pore pressure to the sample. One of the end caps is equipped with an oil chamber. Pressurisation of this oil chamber causes the movable inner rod of the cap to push the sample and induce an axial stress on the sample. Normally, a pressure resistant sleeve is placed inside the core-holder. In such a case, the cylindrical sample and end PEEK caps are placed inside the sleeve. By pressurisation of inlet ports located on the core-holder body, oil pressure is exerted to the outer side of the sleeve and then to the core sample. In this way an isotropic confining stress is applied to the core sample. Furthermore, there are inner pipes with their own pressure inlet ports placed inside each end cap. They are connected to small holes on the PEEK caps enabling fluid to flow inside the core-holder. Therefore, the fluid injected into the inlet will flow towards the inner chamber where the core sample is located. If large enough confining and axial stresses are applied to the sample, the flow will have to pass through the sample until it flows from the other end of the sample to the fluid outlet of the end cap. This is how core-flooding experiments can be performed using the equipment. Obviously by closing one of these outlets and injecting from the other one it is possible to apply the required pore pressure on the sample or change the fluid pressure.

4.1.2 Data Acquisition

As mentioned before, each core-holder end cap is equipped with a dual element piezoelectric ultrasonic transducer. The elements have a diameter of 1.27 cm (0.5 in) and their central frequency is 1 MHz. Each element is connected to special coaxial cables suitable for carrying electrical pulses to or from the transducer crystals. The cables pass through inner hollow sections of end caps to be connected to data acquisition equipment (see Figure 4-1). Depending on the configuration of the data acquisition system, each element can act as a source or receiver.

The main components of the data acquisition system for the core-holder are an arbitrary waveform generator, a flexible-resolution digitiser, a wide-band power amplifier, and a variable-gain high-speed current amplifier. A workstation is dedicated to the experimental data acquisition system. Using a PXI-type platform the

workstation is connected to the data acquisition modules which are installed on a special chassis.

The data acquisition routines are programmed in LabVIEW, a graphical programming language (National Instruments, 2003). A waveform of interest and its parameters are defined in the form of a time function in the program. In the next step data acquisition parameters such as sampling frequency, number of stacked traces, wait between data acquisitions, and total data acquisition period are defined. By running the program an electrical signal mimicking the pre-defined waveform is generated by the arbitrary waveform generator. The electrical signal passes to the transducers with a set gain applied to the signal. Concurrent with this process, the output electrical signal of the receiver transducer is carried by its corresponding coaxial cable to the variable gain current amplifier. The amplified signal is then input to the flexible resolution digitiser which digitises the received analogue signal. The digitised signals are plotted by the computer program in real time. The data can then be recorded on the workstation hard drive for further processing.

4.2 True Triaxial Stress Cell

The True Triaxial Stress Cell (TTSC) is the main laboratory facility used for carrying out experimental work in the current study. The TTSC hard ware, its specifications and capabilities will be explained in the following sections. Furthermore, the modifications carried out by the author on the TTSC's mechanical parts as well as the data acquisition system are described.

4.2.1 TTSC Hardware

Firstly, the initial hardware of the TTSC is discussed by focusing on its two main modules: mechanical parts and data acquisition system. In the next section modifications performed on each of these aspects of the TTSC are explained.

4.2.1.1 Mechanical Parts

As suggested by the name, the TTSC is a piece of equipment used for applying true triaxial stresses on any sample under test. Figure 4-2 shows two different views of the TTSC. The left picture shows the TTSC's main frame, cell, moveable top arm,

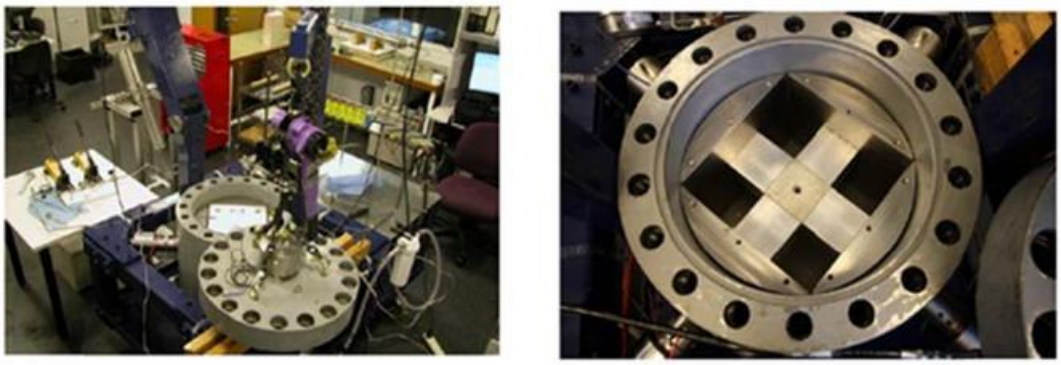

Figure 4-2 TTSC's main frame, cell and accessories (left) and a close-up of cell interior (right) (after Sarmadivaleh, 2012)

and hydraulic pumps. The right picture is a close-up of the cell showing four side ram plates and a cubic sample placed inside the cell.

Figure 4-3 shows schematics of the TTSC's top view (left) and side view (right). The main components of the equipment are identified in the figure. As shown in the figure, the TTSC consists of a cylindrical cell placed inside a main frame. The cubic sample is placed inside the cell. Figure 4-3 shows the maximum sample size that can be placed inside the cell which is 30cm. It is possible to perform experiments on smaller samples by placing special spacer blocks of required sizes between the sample and the steel plates. For example, the right picture in Figure 4-2 shows a 10cm cubic sample which is placed inside the cell using 10 cm spacer blocks.

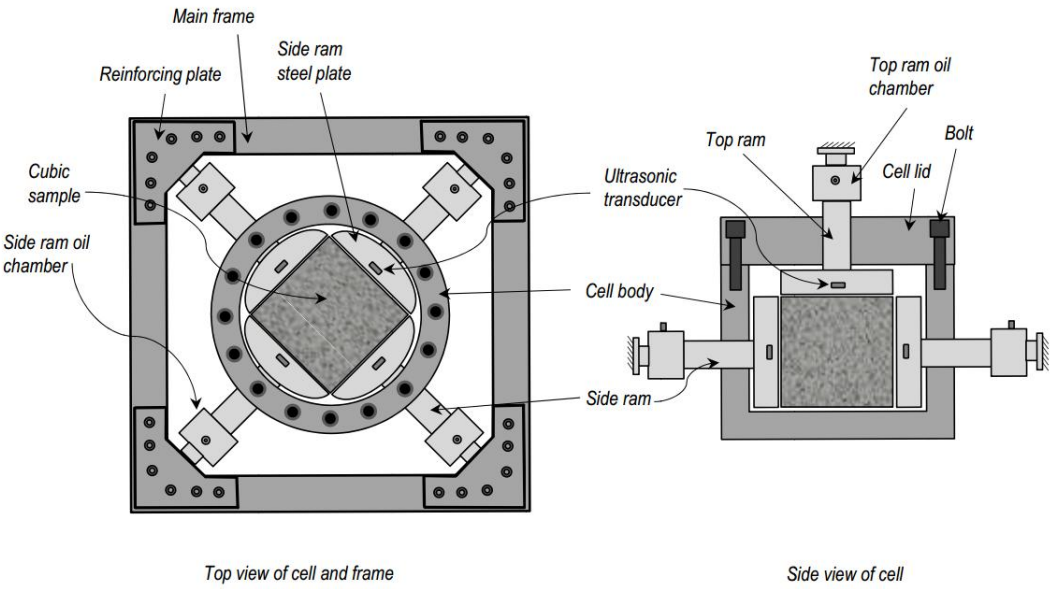

Figure 4-3 Schematics of TTSC top view (left) and side view (right)

The TTSC's cell has four holes through which four side rams pass. Each pair of opposite rams can apply the required mechanical stress in the corresponding horizontal axis. The rams are equipped with oil chambers which can be pressurised by injecting hydraulic oil through their inlet/outlet ports. The injection of hydraulic oil can be carried out using hand pumps or automatic pumps which can function in a constant-rate or constant-pressure mode. There is a piston in each oil chamber and each piston is connected to its corresponding ram. So, pressurisation of the oil chambers will cause movement of their corresponding ram. Side rams are fixed to the TTSC's main frame. Each corner of the frame is reinforced at the points of contact with the rams to make it more rigid. Therefore, once pressurised, the oil pressure will be transformed to the rams and then to the steel plates which in turn are in contact with the sample. In this way, the mechanical stress is applied to the sample. The magnitude of such a stress on the sample is dependent not only on oil pressure, but also on the ratio of the oil chamber piston area and the area of contact between the sample and the steel plates. The plate surfaces are machined flat to ease even distribution of the load to the sample. The cell holes, which provide space for movement of rams, are sealed using special O-rings. Each side ram can be pressurised independently of the others. This provides flexibility in applying the required stress regime on the sample.

The TTSC frame is also equipped with a rotatable arm which can be fixed in place. The rotatable arm is shown in the left picture of Figure 4-2 in a standing vertical position. The right picture in Figure 4-3 shows the TTSC's cell lid which is fixed in place by fastening a number of bolts. There is also another ram which passes through a hole in middle of the lid. This is the top ram which can apply vertical stress on the sample. The top ram also has an oil chamber which works similar to those of the horizontal rams. However, it is different in that before pressurising its oil chamber, the top rotatable arm must be placed in the horizontal position and pinned to the standing body of the frame to provide rigidity against the moving ram. In this way, the top ram moves downward and the steel plate applies the required stress on the sample. The top arm has enough freedom in rotation to allow sufficient space for the heavy cell lid to be placed in location. As is apparent from the design, functioning of the top ram is also independent from horizontal rams. With such a configuration it is possible to apply anisotropic stresses on the samples of different size.

There is a 2.5 cm diameter hole in the centre of the bottom section of the cell. This hole is used for accessing the sample while the lid is positioned in place. This will be discussed more when the procedure for hydraulic fracturing experiments is explained. When the lid is positioned and fastened in place, the space between cell and lid is sealed using large O-rings mounted on the cell lid.

Taking advantage of capabilities discussed above, a number of different experiments can be carried out using the TTSC. The experiments include but are not limited to shear testing, triaxial testing, sand production, and hydraulic fracturing.

4.2.1.2 Data Acquisition

The schematics in Figure 4-3 show that there are ultrasonic transducers placed inside each steel plate. Similar to the set-up used for the core-holder, there are springs behind each TTSC's transducer in order to maintain a stable contact to the steel plates. These transducers where considered in the TTSC's initial design to facilitate ultrasonic monitoring experiments with the equipment. Transducer coaxial cables pass through the hollow inner space designed in each ram. The cables are extended from special ports on the exterior of the rams and can be connected to the data acquisition system.

The TTSC ultrasonic data acquisition system was initially used to function the same as the core-holder. Depending on the configuration of the experiment, one of the transducers could be used as the source and another one as the receiver. Parameters such as source wavelet parameters, sampling frequency, and waiting time between data acquisitions could be chosen for each experiment.

Fracturing fluid pressure and mechanical stresses applied to the sample are other parameters which are normally recorded throughout laboratory hydraulic fracturing experiments. A number of pressure transducers are used for this purpose. The fracturing fluid injection pressure is measured just before the fluid enters the injection tube connected to the sample. To measure mechanical stresses applied to the sample, the hydraulic oil pressure of the ram chambers are measured by other pressure transducers. The measured pressure is then multiplied by the appropriate area factor to compute the mechanical stress on the sample. A pressure transducer generates an electrical current as soon as the fluid pressure changes. The electrical current (or voltage, depending on the pressure transducer type) is then digitally

sampled by an eight-channel data acquisition card. Visualisation of pressure and stress data enables monitoring these parameters in real-time.

4.2.1.3 Major Limitations of the Original Design of TTSC for Fracture Monitoring

The original ultrasonic data acquisition configuration of the TTSC explained above had some major limitations for hydraulic fracturing monitoring experiments of this study.

Although the transducers were forced by supporting springs to maintain a stable contact with the steel plate, the signal quality was not as good as was expected in the initial design of the equipment. Several preliminary experiments showed that only after applying large stresses on the sample would it be possible to record signal transmissions above the noise level. Polishing surfaces of the cement samples and applying grease on sample surfaces did not improve the signal quality much. The fact is that due to the considerable difference in acoustic impedance of steel plates with those of the transducers and cement samples, ultrasonic energy could not efficiently be transferred from the transducers to the samples. The ram plates are made from steel to be strong enough for applying an even stress on surfaces of the sample. However, the fact that placing a steel material between the transducers and the sample deteriorates the transmitted signal was overlooked in the design of the TTSC.

On the other hand, there is only one transducer placed in each steel plate. By recording data from a single transducer on each face of the sample, it was only possible to obtain limited information on a propagating hydraulic fracture during the experiment. Therefore, no certain decision could be made on the extension or geometry of the hydraulic fracture which is an important objective of this study. Regretfully, it was not possible to place more transducers inside the ram as flexibility for such a modification was not considered in TTSC initial design. Furthermore, there was no freedom in changing source and receiver transducers in such a design. It is not possible to change the location of transducers as they are all fixed in location. This fact severely restricted data acquisition geometry to the original location of the transducers. Besides, only one pair of source-receiver transducers could be used at a time. The only way to use another pair for transmission is to manually connect the cables to the new pair. With the limited time involved in experiments this would be a tedious and inefficient approach.

As will be seen in the next sections, laboratory hydraulic fracturing monitoring experiments require a time-consuming process consisting of different steps such as sample mortar preparation, sample moulding, drilling and injection tube installation, placing the sample and spacers in the TTSC's cell, setting up the equipment, and carrying out the experiment. Therefore, a major part of the author's effort was devoted to improvements to the TTSC's ultrasonic data acquisition capability and required modifications.

4.3 Modifications Performed on TTSC

This section covers modifications and improvements made by the author to the TTSC and its ultrasonic data acquisition system. In order to monitor a process such as hydraulic fracture propagation in laboratory experiments, it is generally desirable to acquire as much data as possible from different locations around the sample. However, there are always practical constraints which limit the flexibility of data acquisition and the amount of data that can be acquired. Therefore, an attempt was made by the author to make best use of the available resources and to optimally carry out necessary modifications in order to make the hydraulic fracture monitoring experiments viable. To do so, several parameters where considered including the number and type of ultrasonic transducers, the geometry of data acquisition, a strong contact between the transducers and the sample, the required amplification for recording high quality data, flexibility of the data acquisition configuration, and a suitable sampling frequency.

Carrying out modifications and improvements on the TTSC's ultrasonic data acquisition for hydraulic fracture monitoring took more than a year. The process included several steps such as conducting preliminary hydraulic fracturing experiments, design and ordering special transducer spacers to be manufactured, choosing suitable ultrasonic transducers and ordering them, installation and operation of multifunction cards, development of a data acquisition program and implementing algorithms for high-speed multichannel data acquisition, ordering, and installation and operating a multiplexer by modification of the data acquisition routines.

4.3.1 Preliminary Hydraulic Fracture Monitoring Experiment

As mentioned before, the quality of data recorded by transducers placed in the TTSC rams was not satisfactory. One of most effective ways to improve data quality is to the place transducers in direct contact with the sample. It is also required to ensure the contact remains stable during hydraulic fracturing experiments.

Before deciding the final improvement approaches for the TTSC, the idea of direct contact of transducer and sample was tested by conducting a preliminary hydraulic fracturing experiment. For this purpose, a 20cm sample was prepared for a hydraulic fracturing experiment. The procedure for sample preparation and hydraulic fracture monitoring, however, will be discussed in separate sections in this chapter.

As discussed previously, only two transducers could be used for acquiring data with the original data acquisition system. A pair of half-inch P-wave transducers with a central frequency of 1 MHz was used for this experiment. After the sample was placed in the TTSC's cell, the transducers were placed in contact with two opposite surfaces of the sample. The location of transducers was mirrored and they formed a source-receiver line which was expected to be intersected by the hydraulic fracture. Horizontal stress was then applied to the remaining two vertical surfaces of the sample to ensure the hydraulic fracture would propagate parallel to the direction of applied horizontal stress. The hydraulic fracturing fluid was then continuously injected into the sample which resulted in inducing a vertical hydraulic fracture. Concurrently, ultrasonic data transmissions were conducted between the transducers. As expected, shortly after initiation of the fracture, ultrasonic transmissions were clearly attenuated and delayed. This was due the interference of the fracture as it intersects the source-receiver line. More details on this experiment and its results are discussed by Nabipour et al. (2011a, 2011b).

The promising results of the preliminary hydraulic fracturing experiments with only two transducers justified upgrading the data acquisition capability by placing future transducers in direct contact with the sample.

4.3.2 Designing Special Spacers for Transducers

One of the main steps in enhancing data acquisition capability of the TTSC was to provide direct contact of a number of transducers to the sample while the experiment is being conducted. As there is no space left between a 30 cm sample and the TTSC

steel plates, these modifications were required to be carried out considering a smaller sample size. The idea was to design special spacers on which a number of ultrasonic transducers can be mounted. Learning from preliminary hydraulic fracture monitoring explained in the previous section, it was understood that a spring needed to be installed behind each transducer. Furthermore, the spacers needed to be thick enough to ensure they will not deform under high stress conditions.

Considering the amount of space required for transducers and springs, it was decided to design the spacers to suit 20 cm samples. This is the maximum possible sample size which could be considered for hydraulic fracture monitoring with several transducers. Spacers were made from aluminium due to its suitable mechanical properties as well as considerably less cost of machining compared to steel spacers. To prevent contacting adjacent spacers while they are in contact with a 20 cm sample, a small clearance is required. For this purpose, the spacer's size was chosen to be 19.5 cm × 19.5 cm. To fill the gap between a 20 cm sample and the rams, spacers have a depth of 5 cm.

Based on the successful application of half-inch transducers in the preliminary experiments, it was decided to design the spacers for the same transducer size. However, there were initially only six ultrasonic transducers available in the laboratory. Therefore, parallel to the design of spacers, a total of 20 transducers were ordered most of which were P-wave transducers. All P and S-wave transducers used for hydraulic fracturing experiments are half-inch diameter, and have a central frequency of 1 MHz.

Each spacer is intended to have a number of blind holes to be machined for positioning transducers and springs. Vertical movement of transducers was required by their supporting springs while they were in place. Therefore, blind holes were chosen to have a diameter and depth of 2 cm and 2.8 cm, respectively.

One of the factors which limit the number of holes in each spacer is the amount of stress expected to be applied to the spacer. There is a practical limitation on the number of 2 cm holes possible to be drilled in a spacer. Furthermore, if too many holes are drilled on a spacer, not only the aluminium spacer may fail by excessive stress due to substantially decreased contact area, but also the stress applied to the sample will be strongly uneven. This would lead to stress concentrations on the contact points of sample and spacers, which in turn, would affect the stress distribution in the sample. This would result in unexpected fracture

paths which was undesirable. An optimum spacer design in terms of number and location of transducer holes was finalised. This spacer design has 27 transducer holes. Before ordering the spacers to be machined, a computer model was built. Using a finite element package, simple static stress analysis modelling was performed on the sample by simulating a constant normal stress of 40 MPa on the smooth surface of the spacer which would be in contact with the steel plates of TTSC. This value was chosen to ensure the simulated stress is higher than the maximum stress expected to be applied to the spacer from TTSC steel plates during the experiments. The analysis showed that generated stress concentrations in the aluminium spacer would not damage the spacer. Therefore, the selected design was considered suitable for the purpose of experiments in this study. Another spacer design with less number of holes, 12 in each spacer, was also prepared and tested for stress concentration. A total of six aluminium spacers were then ordered to be manufactured based on the selected designs.

Four out of six spacers have similar designs with 12 holes each. The spacer to be placed at the bottom of the sample has also a central through hole. As will be seen later, the tubing used for fluid injection into the sample passes through this hole. The left picture in Figure 4-4 shows a photo taken from such a spacer with 12 holes. The picture shows the blind holes as well as two transducers in place. There are also special grooves designed and machined to be connected to each blind hole. These are for placement of the Microdot connection assembly to the transducers and their coaxial cables. The pattern of holes is symmetric around the axes of the spacers. The holes are far enough from one another to prevent strong stress concentrations and reduce the chance of spacer deformation. Furthermore, they are distributed evenly on the spacer to provide necessary flexibility in their data acquisition location. When a spacer is pressed by a ram to the sample surface, only the transducers, which are forced by their supporting springs, will be in contact with the sample. All sensitive cables and connections are placed inside the grooves and will not experience any force. In this manner, the required mechanical stress is applied by the spacer while the transducers are constantly pushed onto the sample by their spring force.

Out of six spacers, two were designed to have 27 holes each. The right picture in Figure 4-4 is a photograph taken from one of such spacers. An attempt was made to drill as many blind holes as possible in them. These spacers were designed to be used for applying a minimum horizontal stress which, at least in our hydraulic

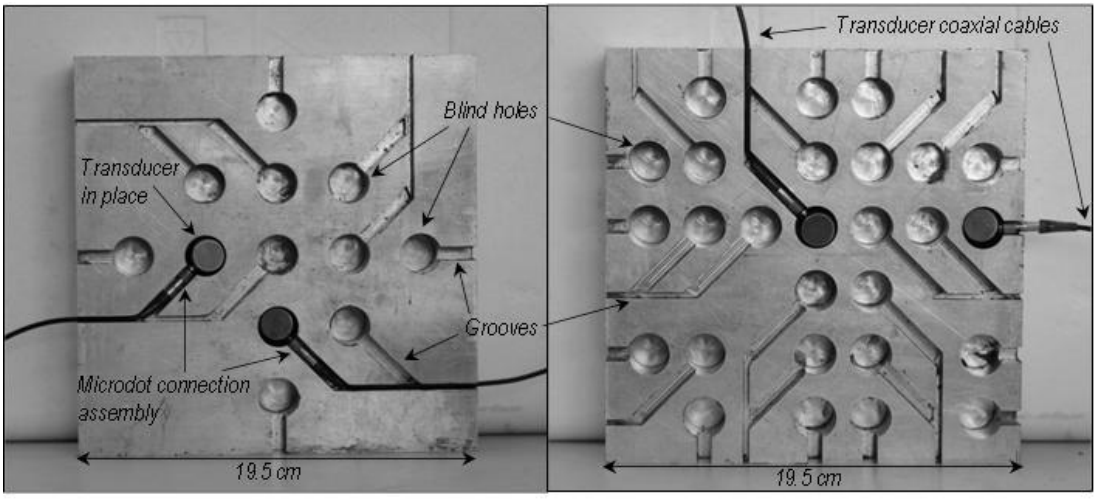

Figure 4-4 Two of the designed spacers with 12 (left) and 27 (right) holes, used for directly contacting transducers with the sample while applying mechanical stress on the sample.

fracture monitoring experiments, is an order of magnitude smaller than the maximum horizontal stress and vertical stress. Therefore, the resultant stress irregularities were not expected to noticeably affect the outcome of fracturing experiments.

4.3.3 Development of Multi-Channel High-Speed Data Acquisition System

One of the main goals of modification to the ultrasonic data acquisition system was to increase the number of ultrasonic transducers to act as sources or receivers. These modifications were carried out with the support of one of professors from the Department of Exploration Geophysics who is also the writer of the original data acquisition code for the core-holder.

The aim was to upgrade the available data acquisition system to a system with multi-channel recording capability. For this purpose, four multifunction cards were borrowed from the Rock Physics Laboratory of Department of Exploration Geophysics, Curtin University. Each card is equipped with four high-speed analogue inputs with 10 MS/s per channel and on-board anti-aliasing filters. The resolution of cards is 12 bits. Furthermore, each card has two analogue outputs which could be used independently of its input channels. There were also one breakout box and four amplifiers available for each of the cards. All the amplifiers were mounted in a portable frame.

Sampling frequency of the data acquisition cards is high enough (10 MHz) for detecting frequencies as high as central frequency of the transducers (1 MHz).

Moreover, as will be seen later, most of the high frequency components are attenuated in the experimental samples and analysis of experimental results will be carried out on frequencies lower than 1 MHz. The resolution of 12 bits was also found to be high enough for detecting ultrasonic events that take place in hydraulic fracturing experiments. As specifications of the abovementioned cards seemed to meet the critical data acquisition requirements for hydraulic fracture monitoring experiments and considering the high cost of purchasing more or newer data acquisition cards, a decision was made to use the available equipment for data acquisition with the TTSC's fracturing experiments of this study. Such a configuration would provide a total of 16 high-speed recording channels which was considered a good starting point for comprehensive fracture monitoring experiments. Although it would be desirable to have as many acquisition channels around the sample as possible, a total of 16 data acquisition channels seemed to be sufficient for the purpose of experiments in this study which include monitoring fractures which are typically straight.

To make use of this hardware equipment for hydraulic fracturing experiments, it was required to code the necessary data acquisition algorithms in LabVIEW graphical programming software. Some parts of the data acquisition program were similar to those used for the core-holder ultrasonic data acquisition. However, it was essential to make considerable modifications or additions to some parts particularly for synchronisation of different input and output channels.

The source waveform of interest was defined in the program by choosing the type of waveform parameters such as frequency, phase, and amplitude. In the next step data acquisition parameter values are set. These include the sampling frequency of input channels, the number of stacked traces (if required), the length of each continuous trace of data, the delay between each continuous data acquisition which is actually the waiting time between each continuous trace, and the total data acquisition time. The number of recorded traces at the end of experiment can be simply be determined by dividing the total data acquisition time by the product of length of each trace and the delay between each subsequent trace.

The output channel of one of the multifunction cards is used for generating the analogue source signal. To do so, the defined source waveform is input as a task to the mentioned output channel. Output electrical signal is then amplified through an amplifier and transferred to the source transducer by means of coaxial cables.

Afterwards, an ultrasonic signal is emitted by the transducer. Properties of the actual ultrasonic signal not only depend on the defined electrical pulse, but also are a strong function of the specifications and behaviour of its crystal.

One of the most important modifications performed on the data acquisition program was associated with the proper timing of the data acquisition channels. They were programmed in such a way to allow them to be triggered to acquire data at the same time as the output channel triggering time. In this way all the output and input channels are synchronised. Furthermore, the data recorded by different channels represented the same physical event over the experiment's recording time. When running the data acquisition system all input analogue signals are amplified by their corresponding amplifiers and then they enter the multifunction cards, where they are digitised. To have more control on an experiment, it is possible to monitor the recorded waveforms from all different 16 channels in real time. During developing different parts of the program, they were tested and modified several times to confirm their functionality.

4.3.4 Adding Source Multiplexing Capability

Based on what is explained above, the system previously had the capability of carrying out ultrasonic experiments between one source and 16 receivers at the same time. Although there are enough receivers in such a system, the experiments were still limited to only one source transducer. To overcome this limitation, it was initially tried to selectively use some transducers as receiver as well as source in the same experiment. However, it was noticed that such a configuration would lead to strong cross-talk between the devices which deteriorated the signal. Thus, another approach was chosen.

A multiplexer card was added to the system which allows multiplexing between one common line and a number of output lines. The data acquisition code was accordingly modified to include the functionality of this newly added multiplexer to the system. The multiplexer was programmed to multiplex between one input line and a maximum of eight different output lines. No changes were required to be made to the source waveform. Depending on the configuration of interest in the experiment, an arbitrary number of output lines could be defined for the multiplexer. The amplified source signal initially enters the multiplexer as its

input. Each multiplexer line is connected by a coaxial cable to one ultrasonic transducer. In each data acquisition cycle, the source signal only passes through one of the multiplexer's output lines while the others remain inactive. Subsequently, only one transducer acted as the source in each cycle while all receivers were constantly active. The multiplexer continuously switches between the source transducers.

The maximum multiplexing speed obtained with such a configuration is about four cycles per second, when multiplexing is performed on four output lines. This was fast enough for the purpose of the experiments in this study. With such an improvement it was possible to carry out ultrasonic transmissions between a maximum of eight sources and 16 receivers. Figure 4-5 shows a schematic of the configuration of the resulting data acquisition system illustrating the data acquisition chassis and cards connected to the computer, the wide-band power amplifier, the multiplexer and 16 amplifiers for amplifying the signals from the receiver transducers.

4.4 Sample Preparation for Hydraulic Fracture Monitoring Experiments

This section covers the procedure for preparation of cubic cement samples for hydraulic fracturing experiments. Furthermore, some of the properties of samples which were measured in the laboratory are reported here.

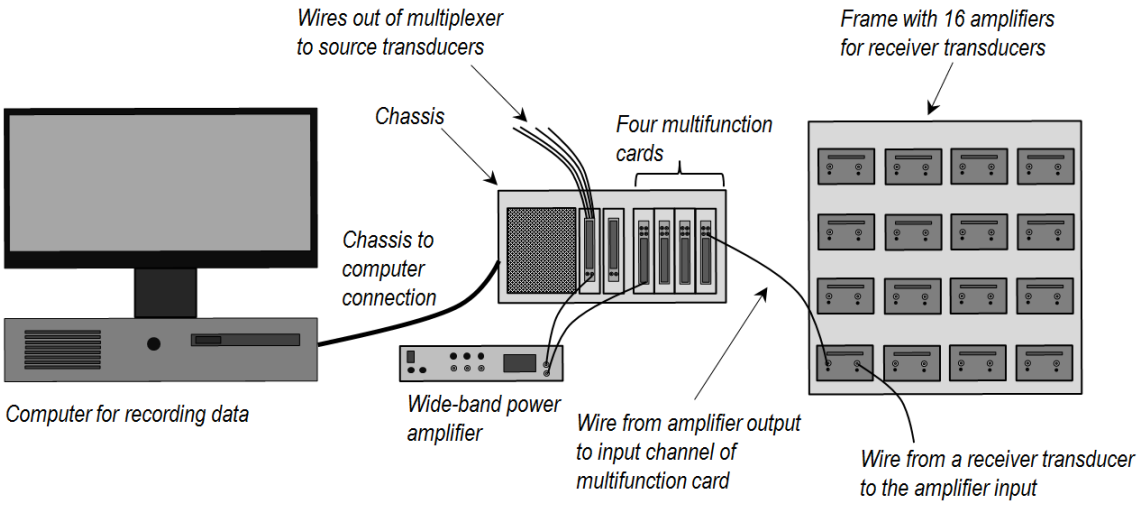

Figure 4-5 A schematic of developed ultrasonic data acquisition system

4.4.1 Preparation of Samples

As previously discussed, although with the TTSC it is possible to perform experiments on cubic samples with a maximum size of 30 cm, the maximum size suitable for carrying out hydraulic fracture monitoring experiments was determined to be 20 cm. Nonetheless, as will be mentioned in the next chapter, some experiments were carried out on 15 cm samples. This was to ensure the fracture would be forced to propagate horizontally by applying a large horizontal stress on the sample. Furthermore, another group of experiments were undertaken on 10 cm samples to examine the interaction of ultrasonic waves with wet and dry synthetic fractures.

All of the samples used in this study were made from cement mortars of similar compositions. For preparing the mortars, cement, water and sand were mixed with a cement-to-sand mass ratio of one and water-to-sand mass ratio of 0.4. This was to ensure properties of different samples would be as similar as possible. Grain size distribution of the sand showed that the effective grain size, $D_{10,}$ (the sieve mesh size through which 10 % of sand can pass) is around 0.25mm (Sarmadivaleh, 2012). The mortar was mixed for a long enough time in a mixer to ensure the mixture is consistent and homogeneous. The mortar was then poured into the moulds of different sizes of interest. These include cubic moulds as well as cylindrical moulds. The moulds were immediately placed on a vibrator to ensure as many air bubbles trapped in the mix would be removed as possible. They were then rested for a few hours to let the mortar set and solidify. However, it is important not to let the samples dry because there is a chance of cracking while the cement is dried. Therefore, all of the samples were submerged into the water in a large water tub.

One day prior to conducting the experiment, the sample was taken out of the water bath and all of its surfaces were smoothened using a sand paper. This was to ensure the best possible contact between transducer and smooth sample surfaces was achieved. In the next step, a vertical hole with a diameter of 7 mm was drilled in the centre of one of the sample faces. To minimise damage to the sample, a slow drilling rate was used.

Afterwards, in order to facilitate initiation of a vertical fracture in the sample, two vertical notches were made on two opposite sides of the simulated wellbore wall and around the centre of the sample. For experiments where the purpose of fracturing

was a horizontal fracture, a round circumferential groove was made perpendicular to the wellbore axis. Creating proper notches is very important in laboratory hydraulic fracturing since fracturing a model without a notch may initiate a fracture travelling from an unwanted point(s) which in turn could result in undesirably complicated fracture geometries.

The drilled hole was then cleaned by blowing high pressure air through it. A quarter inch rod with a length of about 1 cm less than the half-length of the sample (e.g. a 9 cm rod for a 20 cm cubic sample) was inserted in one end of the hole. Before inserting the rod its outer surface was well coated with a high strength glue in order to provide a resilient seal between the rod and the hole wall. Similarly, a quarter inch tube was coated with glue and inserted at the other end of the hole in such a way that an open hole section with a length of about 1-2 cm was left in the wellbore. The sample was then rested enough in order to make sure the glue has adequately set to provide a good seal between the drilled hole wall and outer surface of the injection tube. At this stage the sample was ready for the fracturing experiment. The experiment has to be carried out as soon as the glue is set to avoid cracking of the sample which may occur if the sample became extremely dry.

4.4.2 Hydro-mechanical Properties of the Samples

As previously stated, all samples in this study were made from mortars with the same composition. During the sample preparation process, in addition to cubic samples, a number of cylindrical core size samples were cast to be used for measurement of hydro-mechanical properties. Due to the similarity of the mortars used the average properties of the cubic samples were taken to be the same as the properties measured on core samples.

The average Young's modulus (E) and Poisson's ratio (v) measured by uniaxial compressive tests were 27.7 GPa and 0.2, respectively. The average density of the samples was determined to be around 2100 kg/m^3. Furthermore, porosity and permeability of the samples were measured using the transient Boyle's law porosity test and transient gas permeability test (Champoux et al., 1991). These tests showed an average porosity of 14.7 % and a permeability of 0.018 mD. For more details on measurement of hydro-mechanical properties of the samples the reader is referred to the work of Sarmadivaleh (2012).

4.5 Some Practical Aspects of Data Acquisition

The data acquisition system explained in the previous section was considered to have the necessary capabilities for carrying out hydraulic fracture monitoring experiments. However, there are a number of aspects which need to be taken into account before carrying out such experiments. The following sections cover discussions on subjects such as radiation pattern of transducers, time-delay of the system, repeatability of experiments, and configuration of ultrasonic data acquisition in the fracturing experiments.

4.5.1 Frequency of Ultrasonic Waves

As previously explained, ultrasonic transducers in this study are used as source or receiver. The source waveform was defined in the software by its analytical formulation. It was then converted to an electrical signal by the output channel of a multifunction card. Source transducers generate ultrasonic signals as soon as they are excited by such an electric signal. Properties of the ultrasonic wave transmitted into the sample, however, may not necessarily be the same as the electrical signal that excites the transducer's piezoelectric element. The difference between the two can be affected by factors such as properties of the piezoelectric element, coupling between the crystal and its shield layer, coupling between the transducer and the sample, and differences in acoustic impedance of the media.

Furthermore, depending on the properties of the sample, ultrasonic waves travelling through the medium experience other changes (e.g. due to geometrical spreading and energy losses) before they are picked up by the receiver transducer. Re-conversion of ultrasonic signal to an electrical signal in the receiver transducer can modify the shape of the signal more. This analogue signal is then digitised by the digitisers with limited sampling capability and recorded in the computer.

This discussion briefly and simply notes several steps that a pre-defined source waveform requires before it reaches the receiver transducer and is digitised again. Therefore, when analysing results of ultrasonic experiments it is important to consider these processes and their corresponding effects on the data.

The frequency of an ultrasonic wave is one of the most important parameters needed to be selected before conducting the experiments. All transducers used in this study had a central frequency of 1MHz. The source wave used in the ultrasonic

experiments is a Ricker wavelet with a central frequency of 1 MHz unless otherwise mentioned. It was however noticed that the central frequency of the recorded direct compressional transmissions was about 500 KHz which indicated a loss of the high-frequencies. Investigation of the details of such events is not the focus of this study. Nonetheless, the frequency of the recorded waves and its relative variations, rather than its absolute value, will be used as a part of the monitoring of hydraulic fracture progress in this study. More details are included in the next chapter where experimental results are presented.

4.5.2 Radiation Pattern of Ultrasonic Transducers

One of the practical aspects when performing ultrasonic transmissions is consideration of the transducers' radiation pattern. Depending on the relative size of the transducer and transmission distance, one can assume the transducer as either a point sources or a line source. Whichever the case is, it is important to note that the radiation pattern of ultrasonic transducers is neither perfectly spherical nor planar. Actually, the ultrasonic energy emitted from a piezoelectric crystal is preferentially focused on the element's axis of symmetry parallel to the propagation direction of the ultrasonic wave.

To be able to explain ultrasonic waves recorded in a complex configuration of transducers, it is useful to have knowledge of the radiation pattern of the transducers. A simple experiment was carried out to measure angular dependency of ultrasonic transducers performance. For this purpose a special half-cylinder made from plexiglass material was used. The circumference of the half cylinder was divided into a number of flat surfaces each making a different angle with its bottom flat base. Figure 4-6 shows a schematic of the half cylinder and the transducers. The angle between the subsequent circumferential surfaces of the half cylinder and the bottom flat surface changed by10 degrees. A P-wave transducer was placed below the half cylinder at its centre. Another P-wave transducer was placed on different points on the circumference of the half-cylinder.

P-to-P (P-P) wave transmission was carried out at each angle by keeping the bottom transducer constant and moving the transducer around the circumference of the half-cylinder to the next point. As the distance between the centre of the transducers at each angle is constant (because of the constant radius of the half

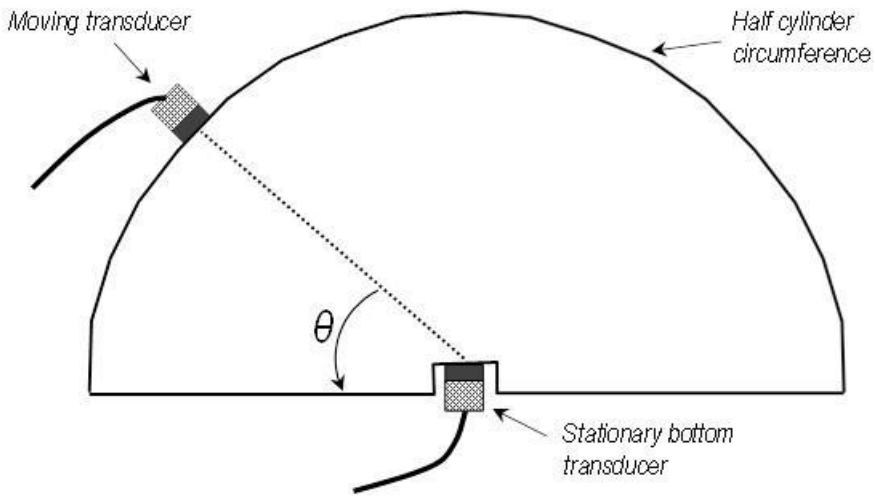

Figure 4-6 A schematic of plexiglass half cylinder and corresponding data acquisition configuration

cylinder), the only factor that varies by moving the top transducer is the angle between the transducers. The peak amplitude recorded at each angle was then determined. A similar experiment was carried out with a pair of S-wave transducers.

Figure 4-7 shows the plots of normalised peak amplitude of P and S-waves versus the angle at which the measurement was conducted. The figure shows that the maximum amplitude is recorded at an angle of 90 degrees, which corresponds to the normal transmission between the transducers. Both P and S-wave amplitudes drop suddenly by diversions up to about 20 degrees from the normal transmission line. A 20 degree diversion results in a reduction of about 60 % in P-wave amplitude while it causes S-wave amplitude to reduce by 80 %. This shows energy emitted from S-

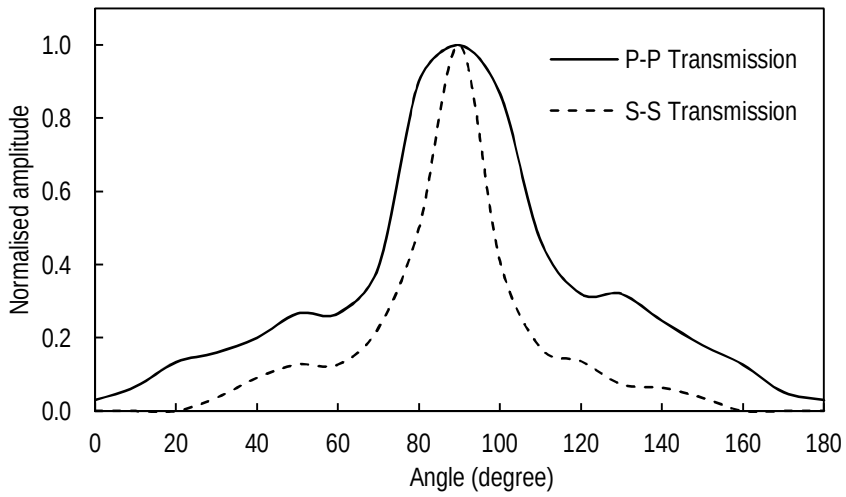

Figure 4-7 Normalised amplitude of P and S-waves versus angle

wave transducers is more even concentrated in the area close to symmetry axis of transducer compared to that of P-wave transducers. This makes S-wave angle measurements more difficult.

The radiation pattern of transducers needs to be considered when a decision is to be made on the configuration of data acquisition. If the receiver location has a large offset from the normal line of the source transducer, only a slight amount of wave energy will reach the receiver. This may not result in an acceptable signal to noise ratio due to the noise level present in the measurements. This can be particularly severe for S-wave transmission due to the intrinsic sensitivity of S-wave transducers.

4.5.3 Time-Delay and Velocity Determination

In order to appropriately understand an ultrasonic wave in a sample, it is important to consider that the recorded travel time may not necessarily represent the true travel time of an ultrasonic wave in the medium. The recorded travel time can also be affected by factors such as the thickness of the wear plate covering the piezoelectric element and stabilisation time of data acquisition equipment.

To measure the total time delay of the system, a number of direct P-P and S-S transmissions where performed on a calibration block made from plexiglass. The transmissions were carried out on different dimensions of the block with different lengths. Arrival times of transmissions were measured for each transmission. Then plots of travel length versus travel time were constructed. The intercept of the line with the time axis (zero-distance axis) was the value of the system time delay. The determined system delays were shorter than 2 microseconds. The delays are used to measure the correct velocity of waves.

P and S-wave velocities of representative cement core samples were measured using the core-holder. Furthermore, after taking into account appropriate corrections for time delay, both velocities were measured in cubic cement samples placed in the TTSC cell. Measurements resulted in an average velocity of 4450 m/s for P-wave and 2500 m/s for S-wave. As was previously mentioned, the average density of the cement samples was about 2100 kg/m^3. Values of P and S-wave velocities and density of the samples results in an average dynamic elastic moduli of about 33 GPa and a dynamic Poisson's ratio of about 0.27 for cement samples.

Neglecting the system delays would result in errors of about 4-5%. Nonetheless, as will be seen in the next chapter, focus was mainly put on the variations of velocities (time delays) in the experiments rather than determination of the exact wave velocities in the medium.

4.5.4 Data Acquisition Configuration

Taking advantage of the multichannel data acquisition system and the transducer spacers, there was considerable flexibility in choosing the configuration of the ultrasonic data acquisition for monitoring the hydraulic fracture. To select the optimum configuration, it is required to determine the main features of the fracture with which ultrasonic waves are expected to interact. These interactions in turn cause variations in properties of the recorded waves which can be captured and recorded by the system.

Normally, before starting hydraulic fracturing, ultrasonic data acquisition is started in order to record any physical change in the sample. When fracturing fluid injection starts and before a fracture is initiated, the only physical property of the medium which is varied is the fluid pressure inside the simulated wellbore drilled into the sample. The increase in fluid pressure in turn changes the distribution of stress in the sample around the drilled hole. However, experiments showed no detectable event was recorded by ultrasonic transducers. This was perhaps due to the high elastic moduli of the cement samples

When the fluid pressure is large enough and a fracture is initiated, a damaged area is formed in the vicinity of the tip of the fracture. Furthermore, it has been shown that fracturing fluid is moving behind the dry tip of the fracture (Savic, 1995; Groenenboom, 1998). Therefore, the fracture tip can be expected to cause strong wave diffractions. Recording tip-induced diffraction events can be useful in that they provide useful information on the location of the tip, thereby offering a tool for estimating fracture length in real-time. Since during fracture propagation the tip of the fracture is moving, arrival times of the diffractions recorded in a stationary receiver are expected to change. In the hydraulic fracturing experiments, source transducers were placed on the surfaces of the sample parallel to the expected propagation direction of fracture. When waves emitted from such sources reach the fracture tip, their energy is diffracted by the tip acting as a point source. Therefore, in

principal, it is possible to record diffractions by installing receiver transducers in all sample faces. However, experiments carried out showed that the best place for capturing diffractions was on the face of the sample perpendicular to the fracture propagation direction. This is mainly due to the radiation pattern of the transducers. Therefore, in the experiments where capturing diffractions was of interest, it was desirable to place a number of receivers on surfaces of the sample perpendicular to the fracture propagation direction to increase the chance of recording such events.

Interference of the fracture with the ultrasonic data can be also recorded by carrying out time-lapse transmissions between a pair of transducers placed on two surfaces on either side of the sample which are parallel to the direction of fracture propagation. This would result in a right angle between the source-receiver line and the fracture expected propagation direction. Before the fracture reaches the source-receiver transmission line, no change is expected to occur in such transmitted data. However, as soon as the fracture reaches close to the source-receiver line, transmissions are expected to be affected by the fracture. The interfering fracture not only disturbs the transmissions, but it also reflects a part of the incident wave energy. Therefore, for capturing such interferences of the fracture, the data acquisition configuration is selected in such a way to place one or more source transducers on surface(s) of the sample parallel to the fracture propagation path, with corresponding receivers on the opposite surface(s) to record normal transmissions between pairs of source and receivers, and a number of transducers close to the source transducer(s), as well as on the same surface of the sample as source transducers in order to record possible reflections from the fracture surface.

Depending on the goals of specific experiments, the configuration of the transducers is selected in order to meet a number of the abovementioned conditions. When discussing experimental results in the next chapter, this will also be explained in more detail for each experiment. Figure 4-8 shows typical transducer configurations for experiments with a horizontal fracture (left) and a vertical fracture (right). In this figure the source transducers are shown in dark grey while receiver transducers are shown in light grey.

In the horizontal fracture experiment, it is assumed that the propagating fracture has a horizontal circular shape. A number of source transducers are placed on the top face of the sample with a number of receivers close to them in order to record reflections from the hydraulic fracture surface as soon as the fracture reaches

the mid-point of a source-receiver pair. There are also receivers placed in locations below the source transducers and in contact with the bottom surface of the sample. These can capture any changes in transmission signals when the fracture intersects the source-receiver line and possibly diffractions from the fracture tip even if the fracture has not yet reached the source-receiver line.

The schematic on the right shows how transducers can be arranged around the sample to capture different ultrasonic events due to a vertical fracture. For simplicity, the vertical fracture is assumed to propagate with a rectangular profile in the direction parallel to the minimum horizontal stress. As can be seen, for capturing reflections from a fracture surface, the receiver transducers are placed close to the source transducers and on the same side of the sample. The transmission receivers are placed opposite to the source transducers and on the other side of the fracture. Furthermore, for recording diffractions from the fracture tip, a number of transducers are placed on the side of the sample perpendicular to the fracture propagation direction. It is worth mentioning that in the case of transmissions by shear wave transducers, their polarity directions should be aligned in order to enhance the signal quality.

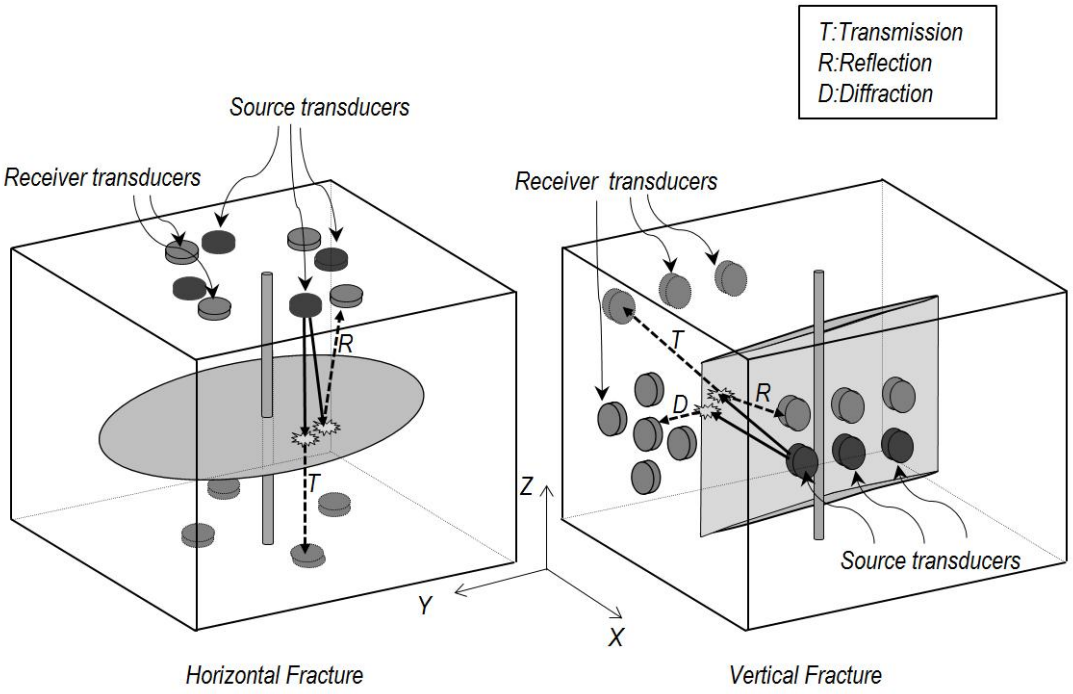

Figure 4-8 Schematics of typical configurations for experiments with horizontal and vertical fracture

4.5.5 Repeatability of Experiments

It was noticed during loading the sample or injection of fracturing fluid into the sample, a small movement of the sample with respect to the ram plates may significantly affect the quality of recorded ultrasonic waves. This is mainly due to the fact that even a slight readjustment of the location of transducers, while they are in contact with the sample, may enhance or deteriorate the contact between the transducers and the sample. The worst case scenario is that a small movement degrades the contact between a source transducer and the sample which virtually results in loss of all data recorded by the receiver transducers from that source. Unfortunately, with the current set up of the equipment it was not possible to improve this matter and resolving this issue proved to take more time which would not allow the study to be completed in the expected time frame. Nevertheless, during the experiments attempts were made to vary the mechanical load on the sample as well as fluid pressure as slowly as possible to prevent such events.

In addition, due to the high sensitivity of data quality to transducer-sample contacts, it was understood that the repeatability of ultrasonic data in different experiments would be limited. For example, using a particular pair of transducers with the same supporting springs placed on two arbitrary sides of a sample, the amplitude of recorded transmissions were not exactly the same for different repeated experiments with the same conditions. Although in all experiments the force by which the transducer is pushed to the sample is the same, because surfaces of the sample and transducer wear plate are not perfectly smooth, in different attempts at the experiment, their contact quality, thereby the ultrasonic transmission quality, often varied.

It was realised that even a very small sand particle in between the two surfaces could deteriorate the contact quality. Therefore, all the experiments were conducted bearing in mind the fact that the absolute values of individual experiments results may not be directly comparable to those of other experiments due to the limited repeatability of data. After a number of experiments, it was shown that variation of recorded amplitude can be as high as 10 % of the initial recorded amplitude. Nonetheless, in the current study, in most of the cases it was not required to compare the absolute values obtained from two different experiments. The focus was rather put on variations of the absolute values in each individual experiment and

the comparisons between the different experimental data were based on general trends of the data rather than their absolute values.

4.6 Hydraulic Fracture Monitoring Experiments Procedure

Hydraulic fracturing monitoring experiments were carried out using the TTSC and its improved multichannel data acquisition system. To do so, the sample of interest which was already prepared for the test was required to be placed inside the TTSC's cell and the special transducer blocks were to be placed between the sample and steel rams. Before doing so, it was required to place the transducers and their supporting springs in place. The transducers in the bottom spacers (if there were any) were put in their locations first. The sample was then placed on top of the bottom block. As mentioned previously, the bottom transducer block had a hole in its centre through which passes the injection tube already set on the bottom face of the sample. There was also a hole at the centre of the TTSC cell. By this configuration, the injection tube came out from the bottom of the cell and provided access for making further connections to the tube. Side blocks and their transducers were then placed in their position one by one. If any vertical stress was to be applied to the sample, the top spacer was placed on the sample and mechanical force applied to the spacer (and the sample) using a hydraulic jack. Otherwise, transducers were placed directly on top of the sample with some weights of about 500 grams on top of them to maintain a steady sample-transducer contact during the experiment. It is important to note that sufficient amount of Vaseline was applied between each transducer and the sample in order to enhance the signal quality.

Figure 4-9(a) shows a 15 cm sample placed inside the TTSC's cell with a number of aluminium spacers around it. The picture also shows a number of transducers placed on top of the sample. Here, some transducers had been already placed in the bottom spacer which is not visible in the picture. Figure 4-9(b) shows another picture of this sample displaying steel weights placed on top of transducers to push them with a contact force to the sample and prevent any possible movement of the transducers. In this specific experiment, an isotropic horizontal stress was applied to the sample. However, as a horizontal fracture was desired, no vertical stress was applied to the sample which eliminated the requirement for a spacer for top transducers.

As another example, Figure 4-9(c) shows a picture taken from a 20 cm sample. In this figure the left and right spacers around the sample contain transducers. This experiment focused on creating a vertical fracture. Therefore, it was required to apply anisotropic horizontal stress as well as a vertical stress. The directions of maximum and minimum horizontal stresses (σ_H and $\sigma_{h'}$ respectively) are also shown in the picture. Figure 4-9(d) shows another picture of the same experiment when the set-up of the experiment was complete. The hydraulic jack on top of the sample is used for exerting the vertical stress. A number of spacers of similar size are placed between the hydraulic jack and the sample.

After placement of the sample in the TTSC's cell, the required mechanical stresses were applied to the sample in sequential steps. This was done by injection of hydraulic oil into the oil chamber of the TTSC rams using special computer-controlled pumps. After reaching the required level of oil pressure (and corresponding stress on the sample), the pumps were set to work on a constant-pressure mode in order to maintain a constant stress on the sample over the experiment period.

To conduct injection of fracturing fluid into the sample, the injection tube, which was already inserted and glued to the sample, was connected to the outlet of a

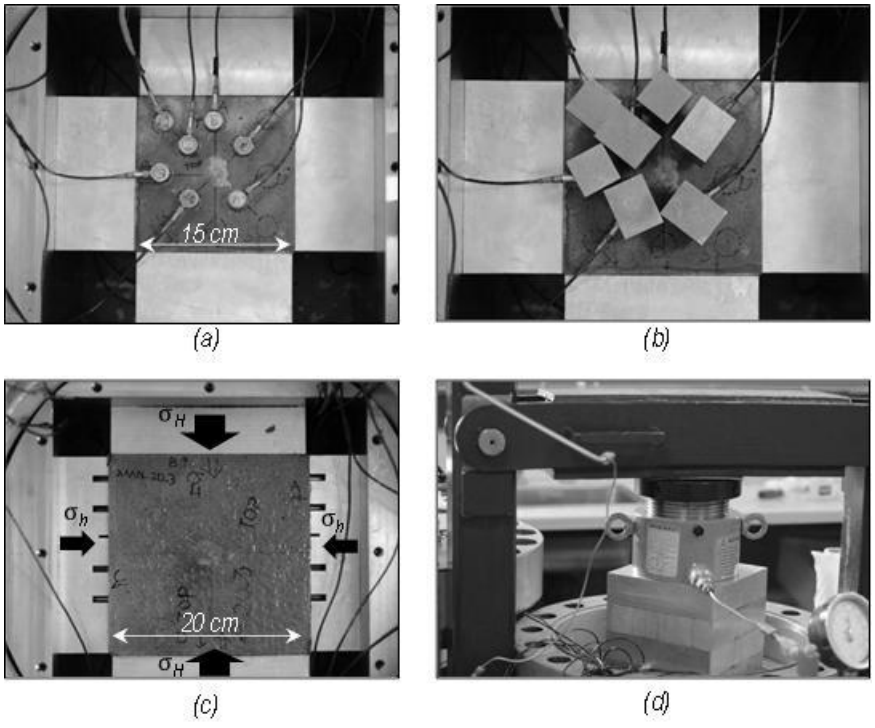

Figure 4-9 Top views of a 15 cm sample placed in TTSC with a number of ultrasonic transducers around the sample

displacement chamber. The displacement chamber had an inner piston which separated fracturing fluid from the hydraulic oil. By means of a syringe pump, the oil was injected with the required rate into the inlet of the displacement chamber. This caused displacement and thereby injection of fracturing fluid into the sample. The fracturing fluid used is silicone oil with a high viscosity of 100,000 cP. The reason for using such a high viscosity fluid is to obtain stable fracture propagation in the laboratory. For laboratory hydraulic fracturing studies this is an essential factor required for up-scaling the obtained results to the field scale (Lhomme, 2005; Sarmadivaleh, 2012).

Depending on the purpose of the experiment different regimes of stress loading and fluid injection rate/pressure scenarios may be selected. Nevertheless, during a normal laboratory hydraulic fracture the fluid is injected by a constant rate into the sample which is under desired mechanical stress. The fluid pressure increases until it reaches a peak which is called the breakdown pressure. At this point, the fracture has been opened and the pressure starts to fall. Before the start of injection, the fluid pressure and mechanical stresses on the sample are continuously recorded using a dedicated data acquisition system for these parameters.

On the other hand, before applying mechanical stress and starting injection of fluid into the sample, ultrasonic data acquisition is carried out to register any possible variations in the data due to loadings. The most important portion of the ultrasonic data is from the initiation moment of the hydraulic fracture. As stated earlier, there are different events which can be captured while the hydraulic fracture is initiating and propagating in the sample over the experiment time. These include transmissions across the fracture, reflections from the fracture wall, and diffractions from the tip of the fracture. While discussing the experimental results in the next chapter, the configuration of transducers in each experiment will also be explained.

4.7 Summary

This chapter aimed at explaining different aspects of the experimental equipment used in this research. This started with explaining the mechanical and data acquisition parts of the core-holder equipment which was used for conducting ultrasonic transmissions on cement samples as well as fracturing fluid under different pressures.

A discussion on the various components of the unique true triaxial stress cell (TTSC), the main experimental facility used in the current work, was then presented. As this equipment was not operational when this study commenced, considerable effort was spent by the author on operating the equipment, identifying its weaknesses and strength for conducting hydraulic fracturing monitoring experiments, and modifications and upgrading mechanical and data acquisition parts accordingly. These were explained in separate sections in this chapter. Afterwards, the procedure was provided for the preparation of experimental samples. Some important practical aspects were presented of experimental data acquisition which need to be taken into account for the optimised design of the tests and correct interpretation of the results.

This chapter concluded by explaining the procedure for typical horizontal and vertical hydraulic fracturing experiments. This included placing the transducers and the sample in place, installation of mechanical stress on the sample, commencement of fluid injection, fracture propagation and concurrent ultrasonic measurements. Various experimental results of this study and their discussions are presented in the next chapter.

5 Experimental Results

Chapter 4 discussed the laboratory set-up used in this study by explaining the capabilities of the TTSC and major modifications carried out on it to make it suitable for hydraulic fracturing experiments. This chapter covers the results of such experiments. For interpretation of the results, it is prudent to bear in mind the different aspects of data acquisition discussed in the last chapter. These include frequency (and wavelength) of ultrasonic waves, radiation pattern of transducers, system time delays, and limited repeatability associated with the equipment set-up. Before discussing the results of horizontal and vertical hydraulic fracture monitoring experiments, the procedure and results of the experiments performed on fracturing fluid as well as smooth synthetic fractures are presented. The results of these experiments will shed light on the events observed later in the more complex case of hydraulic fractures involving fluid-filled fractures under pressure. The results of horizontal and vertical hydraulic fracturing monitoring experiments are then presented. Different ultrasonic events generated due to the hydraulic fractures are investigated including transmissions and reflections from the fracture surface and diffractions from the fracture tip. Analysis of these events provides valuable information for the identification of the fracture geometry and properties in real-time.

5.1 Ultrasonic Transmissions in Fracturing Fluid

To be able to monitor a hydraulic fracture in the laboratory, length of the experiment should be long enough to allow acquisition of ultrasonic data during propagation of the fracture. Therefore, in such laboratory-scale hydraulic fracturing experiments a highly viscous fluid is used as the fracturing fluid. By this means, it is possible to extend the propagation period of the hydraulic fracture while maintaining a stable fracture propagation regime. This is also required to apply laboratory-scale fracturing

results for field conditions. Normally, to perform the scaling process, a set of dimensionless groups of physical parameters that represent a particular fracturing regime are defined in such a way that they result in the same values using laboratory and field conditions. These dimensionless variables are determined from fluid flow and rock behaviour. The fracturing fluid used here was based on the work of Sarmadivaleh (2012). His work contains details of the scaling process used for fracturing experiments in this study. However, it should be kept in mind that any laboratory results, even those with non-field like propagation regimes, represents a particular type of fracturing (Sarmadivaleh, 2012).

To interpret the interaction of ultrasonic waves with the hydraulic fracture, it is required to have some information about ultrasonic the properties of the fracturing fluid (silicone oil with a viscosity of 100,000 cP) particularly at high pressures that occur in the hydraulic fracture. Therefore, ultrasonic transmissions were carried out on the fracturing fluid before conducting hydraulic fracturing. These experiments were carried out using the core-holder. However, instead of a core-size sample, the fracturing fluid was used. For this purpose, after fastening end caps, all fluid communication outlets of the equipment were closed except one inlet port which was used for injection of the fracturing fluid into the core-holder. In this way, by injecting the fluid into the main chamber of the equipment, the fracturing fluid occupies the space between the two PEEK caps (see Figure 4-1). The fluid pressure was then increased incrementally from 0.7 MPa (100 psi) to up to 20.7 MPa (3000 psi) while all other parameters were kept constant. At each pressure, compressional ultrasonic transmissions were carried out between the transducers placed in the PEEK caps using a source wave frequency of 1MHz. The distance between the PEEK caps is 11 cm. The time delay for the core-holder ultrasonic data acquisition system had been already measured using a calibration block and all travel times were corrected with respect to this delay.

Figure 5-1 shows selected transmission arrivals recorded at different pressures. It is observed that by increasing the fluid pressure its travel time decreases considerably. At a low pressure of 0.7 MPa, the first break arrival time is 105.3 µs while the same parameter at 20.7 MPa is 95.3 µs. These result in a compressional wave velocity of 1045 m/s and 1154 m/s at 0.7 MPa and 20.7 MPa, respectively. This corresponds to an increase of about 10.4 % in velocity. It is worth mentioning that the fracturing fluid was not air flushed prior to the experiment because in actual

hydraulic fracture monitoring experiments also air is present in the fluid. The increase in the ultrasonic velocity at higher pressures is significantly dependent on the presence of air in the media. The air could easily dissolve in the fluid at higher pressures.

The figure also shows that the amplitude of the first arrivals increased during increasing pressure. It was observed that by increasing the fracturing fluid pressure from 0.7 MPa to 20.7 MPa, the largest positive peak of first arrivals increased by 4.7%. Similar measurements were also carried out with shear elements of the transducers to see if S-wave can propagate in the fluid. However, no detectable shear wave was observed in the experiments as expected.

It is worth noting that during the hydraulic fracturing experiments, the fluid pressure is measured close to the wellbore at the lower end of the injection tube. However, the fluid pressure decreases considerably along the fracture. It is highest at the opening of the fracture on the wellbore wall and is lowest at the fracture tip. This pressure drop is mainly due to fluid viscous forces and friction effects. Measurements carried out on fracturing fluid showed that with the extreme changes in fluid pressure, the change in the amplitude and velocity of the compressional ultrasonic wave is about 4.7 % and 10.4 %, respectively. Considering the fact that width of the created hydraulic fracture is very small (in the order of tens of microns), these changes are not likely to affect ultrasonic measurements considerably. For example, assuming a fluid thickness of 100 microns, the time it takes the ultrasonic wave to travel across the fluid-filled fracture is less than 0.1 μs at 0.7 MPa of fluid

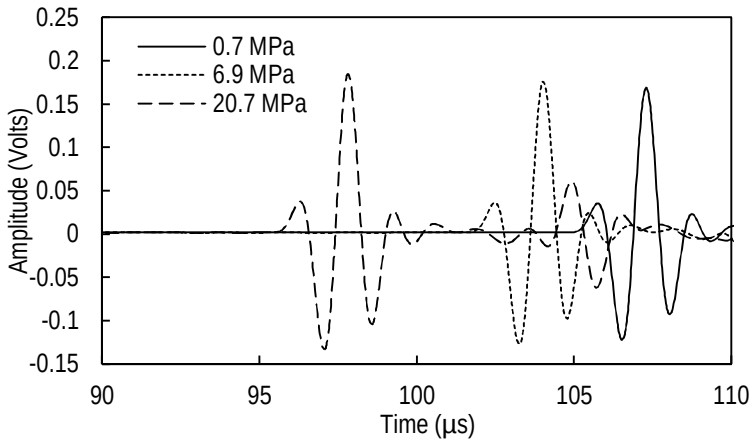

Figure 5-1 Selected traces of compressional transmissions in fracturing fluid under varying pressure

pressure. Furthermore, the change in the travel time caused by a pressure increase to 20.7 MPa is less than 0.01 μs which is an order of magnitude less than the temporal resolution of the ultrasonic data acquisition system used in this study (10MS/s). Therefore, it is expected that the variations of the fracturing fluid pressure in different points of the fracture have a negligible effect on the ultrasonic measurements.

5.2 Synthetic Fracture Experiments

As mentioned previously, a hydraulic fracture causes time delays and changes in the amplitude of the transmitted and reflected waves. In numerical or theoretical approaches for studying these phenomena, it is normally assumed that fractures, whether hydraulic or natural, are straight and their surface is smooth. In reality, however, fractures do not normally occur in perfectly straight lines and their surface has roughnesses of different scales. Although in this study an attempt was made to create straight hydraulic fractures with the least roughness (by applying highly anisotropic stresses on the sample), they do not normally meet these conditions. Therefore, before moving to hydraulic fracturing monitoring experiments and in order to provide confidence in the measurement of fractures transmission properties, a number of ultrasonic transmission experiments were carried out on simple synthetic fractures. These fractures are actually formed by smooth surfaces of two different samples which are put in contact under normal stress. The results of transmission experiments on the synthetic fracture are compared to theoretical values predicted by the displacement discontinuity theory (DDT) to inspect their degree of agreement. These will be helpful in the interpretation of the transmissions and reflections from hydraulic fractures which have more inherent complexities than synthetic fractures.

5.2.1 Test Procedure

In these series of experiments, 10 cm cubic cement samples were used. The composition of these samples is the same as the other cement samples used in this study. Synthetic fractures are actually not cut; they are rather formed by placing two 10 cm samples in contact and then applying normal load to their contact face. Two surfaces which are to be placed in contact were already polished properly using sand

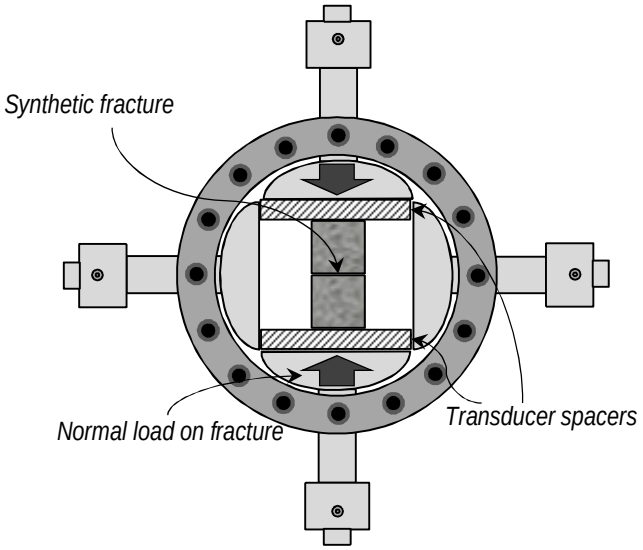

Figure 5-2 Schematic of synthetic fracture experiment set-up

paper to reduce the roughness of the surfaces and provide a good contact. The two 10 cm samples were then placed in the TTSC's cell. The gap between the samples and the steel rams was filled by two transducer spacers containing transducers and supporting springs. Transducers were placed in such a way to allow ultrasonic transmission across the fracture. By injection of hydraulic oil into the TTSC rams' oil chamber, the samples (and the fracture between them) were placed under constant normal stress. Figure 5-2 shows a schematic of the laboratory set-up for ultrasonic measurements of a synthetic fracture. As can be seen in the figure, only two TTSC rams are pressurised here.

A number of P-wave ultrasonic measurements were carried out at each constant stress level after which the stress was increased to a higher level. Different records acquired under constant stress were averaged to increase the signal-to-noise ratio. The increase in the normal stress was expected to enhance the contact between the synthetic fracture walls thereby increasing the fracture normal specific stiffness. Therefore, the recorded transmissions can be attributed to the stress-dependent specific stiffness of the fracture. It is important to note that the specific stiffness which is the focus of this study is actually the dynamic specific stiffness of the fracture as is determined by dynamic waves. This value is generally different from the static specific stiffness of the fracture which is determined by pseudo-static loading of the fracture.

In the above mentioned experiment, no fluid is applied to the fracture walls and the samples are dry. In order to make a simple physical model of a wet fracture, before contacting the samples, an appropriate amount of hydraulic fracturing fluid was applied on the contact surfaces. The experiments on a wet synthetic fracture were then carried out using a procedure similar to the dry fracture.

To have measurements of transmissions in an intact sample, a 10 cm × 10 cm × 20 cm sample was used. Similar to the above experiments, the sample was placed in the TTSC's cell and it was put under different stress values. A number of ultrasonic measurements were also conducted at each stress level.

5.2.2 Results

Figure 5-3 shows the recorded normal transmissions across the dry and wet synthetic fractures and under different normal stresses. Selected normal stresses were 0.7 MPa (100 psi), 1.4 MPa (200 psi), 3.4 MPa (500 psi), 6.9 MPa (1000 psi), and 13.8 MPa (2000 psi). Only the early sections of waveforms corresponding to the first arrivals

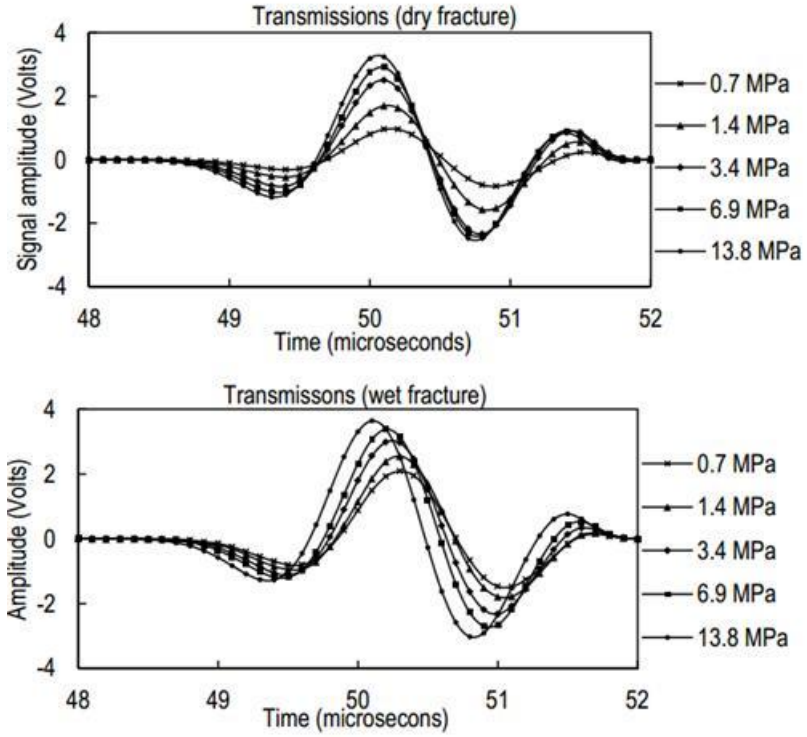

Figure 5-3 Recorded transmissions across dry (top) and wet (bottom) synthetic fracture under different normal stresses

are shown in the figure.

Looking at the top plot, it is seen that as the normal stress on the fracture increases, transmission amplitudes also increase. A higher normal stress forms a firmer contact between the fracture walls which in turn enhances the transmission of energy across the fracture. In other words, the specific stiffness of the fracture is increased by a larger normal stresses. Therefore, the effects observed due to the increasing normal stress can be attributed to the corresponding increases in the fracture specific stiffness. This is in agreement with the predictions of the displacement discontinuity theory which states that the transmission amplitude increases as the fracture specific stiffness increases. Furthermore, the plot shows that the peak arrival time of transmissions is reduced as the stress on the fracture increases. This is also what is predicted by the theory. Comparison of this plot with the top plot in Figure 3-11 which shows numerical transmissions across the smooth-joint fractures with different specific stiffness, indicates the good agreement between the laboratory results of synthetic fractures and the numerical results of smooth-joint fractures transmissions.

The bottom graph in Figure 5-3 shows the wet fracture transmissions plotted in amplitude and time scales similar to that of the dry fracture. Similar trends are observed in the case of a wet fracture: an increase in the amplitude and a decrease in the travel time at higher normal stresses.

On the other hand, a comparison of the dry and wet fracture transmissions reveals that the transmission amplitude is enhanced in the wet fracture compared to the dry fracture. The amplitude increase is particularly considerable in low stresses than high stresses. For example, at 0.7 MPa stress, the ratio of the peak transmission amplitude in the wet fracture to that of the dry fracture is almost 2.2 while the same ratio is only 1.1 at 13.8 MPa. In fact, although the fracture surfaces had been already polished using sand papers they still have some degree of roughness. Therefore, only a small portion of fracture surfaces are in mechanical contact at low stresses. In the wet fracture, however, the highly viscous fracturing fluid enhances the contact between fracture walls by carrying a considerable portion of compressional wave energy from one side of the fracture to the other side, resulting in an increased transmission amplitude. However, at large stresses, most of the energy is transmitted through solid materials of the fracture walls which have more contact area as well as firmer contacts compared to a fracture at low stress states.

According to the displacement discontinuity theory, for the given parameters of the experiment, the approximate variations in phase time delays would be less than 0.3 μs. The limited sampling interval of the ultrasonic data acquisition system (0.1 μs) prevented measurement of changes in group and phase time delays. Therefore, focus was put mainly on quantification of the fracture using amplitudes of waves rather than the time delays.

In order to investigate the properties of transmissions in more detail, the signals were also studied in the frequency domain. To do so, a half cosine window was applied to the recorded signals to separate the section of interest. Afterwards, the frequency spectra of the filtered signals were determined using a Fast Fourier Transform.

Figure 5-4 shows the plots of the obtained frequency spectra for the wet and

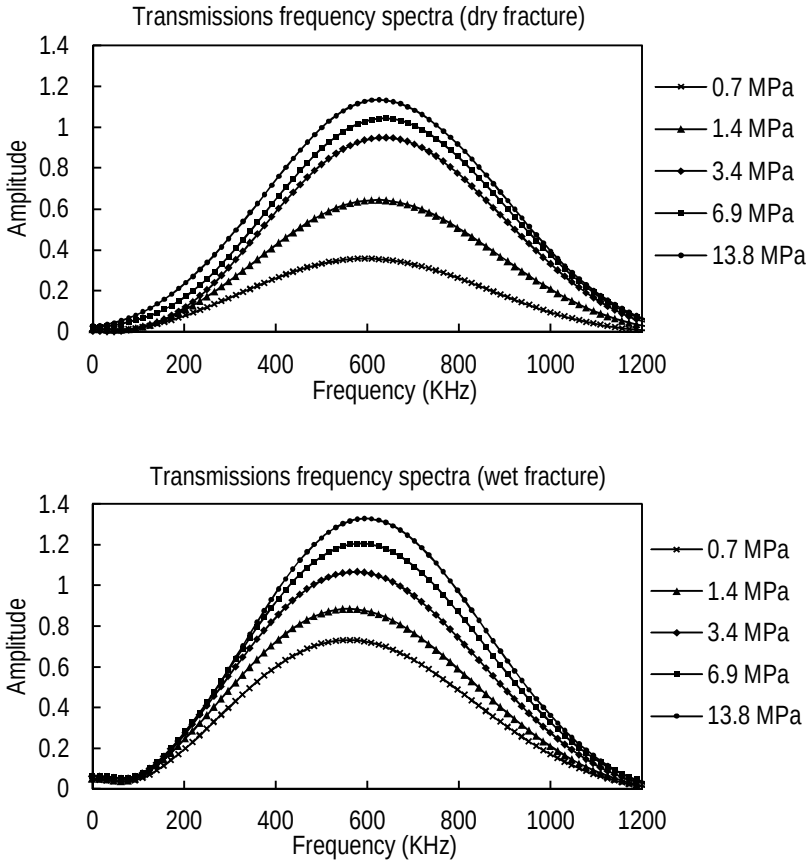

Figure 5-4 Transmissions amplitude spectra of wet and dry fractures at different stresses

dry fractures. Both plots show the increase in spectral amplitudes with the increasing stress. The increased normal stress on the fracture reduces the void areas in the fracture and enhances mechanical contact between the solid particles in the fracture.

As expected, this incremental increase, particularly at low stresses, is more pronounced in the dry fracture than the wet fractures. Nevertheless, comparing the dry and wet fractures spectral amplitudes with similar applied normal stresses, it is understood that the wet fracture transmissions have consistently larger amplitudes. Furthermore, the peak spectral amplitudes occur at frequencies around 600 KHz and generally exhibit increasing trends at higher stress levels. These plots closely resemble the numerical transmission results presented in the top plot of Figure 3-12, where the increase in the peak spectral amplitudes due to an increase in the fracture specific stiffness was observed. These results are also in agreement with the experimental results of Pyrak-Nolte et. al (1990b) in which increases in peak spectral amplitudes and peak frequencies due to increasing normal stress of the fracture were reported.

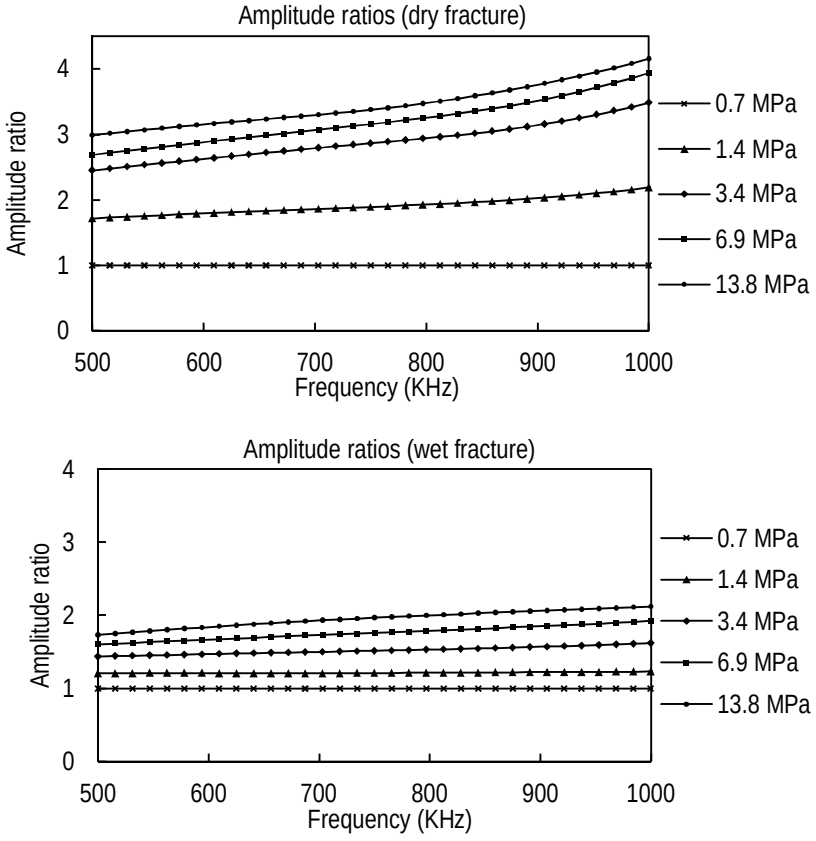

Figure 5-5 Ratio of spectral amplitudes in different stresses to their corresponding values at 100 psi normal stress

To take a further step, focus was cast on the rate of change in the spectral amplitudes as the stress on the fracture is varied. For this purpose, the spectral amplitudes at each stress level were divided by their corresponding values at 0.7 MPa which is the lowest stress level. The calculated amplitude ratios for the dry and wet fractures are plotted in Figure 5-5. Due to the low reliability of the frequency components less than about 500 KHz and more than 1 MHz, only the frequencies between these two boundaries are analysed and plotted. The top plot shows that in the case of the dry fracture any increase in the normal stress corresponds to a rise in the spectral amplitude. Such amplitude gains are particularly noticeable in the early steps of stress increase. This can be attributed to a high void area and low contact area of fracture surfaces at low stress. As the stress on the fracture is increased, considerably firmer contacts between solid particles on two sides of the fracture are formed and simultaneously, the void area of a fracture is reduced as the solid particles of fracture surfaces are pushed together. This results in a considerable improvement in transmissions across the fracture. However, as the stresses reach some high levels, solid particles are placed tightly and no more noticeable compaction is likely to occur. In this situation, increasing the normal load on the fracture surface may not result in a considerable improvement in transmission across the compacted fracture. That is why the amplitude ratio curves of fractures experiencing larger stresses of 6.9 MPa and 13.8 MPa are much closer to each other than those under 0.7 MPa and 1.4 MPa stress.

The plot also shows that the rate of increase in the spectral amplitude is larger in higher frequencies. In other words, at a constant stress, the gain in spectral amplitudes of high frequencies is higher than those of low frequencies. As a result, the spectral amplitude curves show a positive slope which increases in high frequency areas. For example, for the dry fracture under 3.4 MPa normal stress, the spectral amplitude corresponding to 1 MHz frequency is about 3.5 times as much as its corresponding amplitude at 0.7 MPa psi while the spectral amplitude of 500 KHz under 3.4 MPa stress is only 2.4 times its corresponding amplitude at 0.7 MPa. This trend can be attributed to the nature of the contact between fracture walls. Fractures are known to act as low-pass filters with more compliant fractures passing lower frequencies. At low stresses, there is a loose contact between fracture surfaces which does not allow efficient transmission particularly for high frequency components. But as the stress is increased, more high frequency components of the waves can pass

through the facture compared to the low frequency components (which already could transmit through the fracture even at low stresses).

The bottom plot shows the amplitude ratios in the wet fracture experiment. Similar to the previous plot, this plot shows that spectral amplitudes increase with any increase in the normal stress applied to the wet fracture. However, the rate of transmission improvement due to larger stresses is not as high as those observed in the dry fracture. As previously mentioned, the presence of a viscous fracturing fluid in the fracture considerably enhances transmission across the wet fracture at a low stress of 0.7 MPa compared to the dry fracture. Therefore, in the case of the wet fracture, the stress increments do not improve transmissions as significantly as they do in the dry fracture. For instance, in the dry fracture experiment, the spectral amplitude of 800 KHz frequency at 13.8 MPa is almost 3.5 times as much as its amplitude at 0.7 MPa while for the case of the wet fracture, the spectral amplitude of the same frequency at 13.8 MPa is only 2 times its amplitude at 0.7 MPa. A similar observation was reported by Pyrak-Nolte et. al (1990b): the effect of water saturation in increasing wet fracture specific stiffness compared to a dry fracture is reduced at high stresses. This was attributed to the fact that at high stress the fracture has much less void spaces compared to a fracture at low stress. Furthermore, the specific stiffness of a fracture under high normal stress is greater than that of a fracture under low stress. Consequently, addition of fluid in between the voids produces a negligible effect on transmission.

The amplitude ratio plot of each stress level on a wet fracture has a lower slope compared to those for a dry fracture. For the case of 1.4 MPa curve, the plot is almost horizontal. This reveals an important fact: at a constant stress the rate of increase in spectral amplitude of different frequency components does not vary as much as the dry fracture. In other words, the particularly considerable increase in the amplitude ratios which was noticed at high frequencies in the dry fracture experiment is less pronounced in the case of the wet fracture. The nearly constant slope of the lines corresponding to different stresses indicates an almost stress-independent effect. Actually, at a low stress of 0.7 MPa, the viscous fluid present in the wet fracture enhances the transmissions in all frequency components. Although the subsequent increases in normal stress on the fracture enhances wave transmission, the effect of the fluid in improving transmission is constant and stable at all stresses.

To quantify these measurements and then relate them to the specific stiffness of the fracture, an attempt was made to obtain the transmission coefficients. Although normally peak amplitude ratios are used for obtaining the transmission coefficient, because the laboratory ultrasonic wave is not monochromatic, it is not valid to use these ratios. Therefore an approach similar to the method used in Chapter 3 was used to calculate a transmission coefficient for each frequency component of the signal. For this purpose, the direct ultrasonic transmission experiments were carried out at different stress levels on an intact sample with a length of 20 cm. The frequency spectra of these transmissions were then obtained and used as the reference measurements in the intact sample. Finally, at each stress level, the transmission coefficients were obtained by dividing the spectra of transmissions across the fracture (dry and wet) by the spectra of intact sample transmissions.

Figure 5-6 shows plots of experimentally obtained transmission coefficients

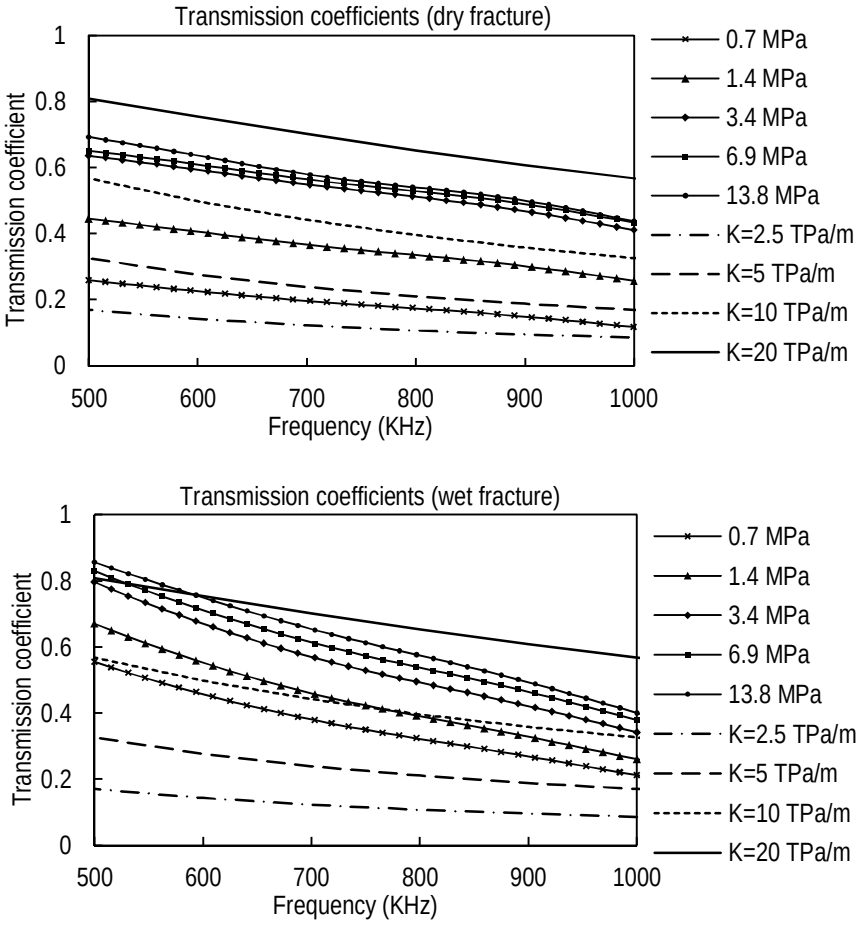

Figure 5-6 Experimentally obtained transmission coefficients at each stress level for dry and wet fractures and theoretical transmission coefficients for fractures with different specific stiffnesses

for dry and wet fractures at different stress levels. Shown in the plots are also the spectral transmission coefficients predicted by the displacement discontinuity theory at different fracture specific stiffnesses (see Equation (2-5)). The experimental transmission coefficients are shown by the lines containing markers while the theoretical values are shown by the lines without markers.

The top plot shows the transmission coefficients obtained for the dry fracture at different stress levels. Here, the trends observed in the experimental transmission coefficients are shown to be in good agreement with those predicted by the theory. In other words, at a constant stress level, experimental transmission coefficient of the fracture reduces as the frequency is increased. This is in agreement with what is predicted by displacement discontinuity theory for a fracture with constant specific stiffness. Furthermore, there is a raise in the transmission coefficients at all frequency components as the normal load on the fracture is increased. As discussed before, this increase is more noticeable at early increasing stress increments.

Having observed the agreement with this figure, it is now desirable to attribute the transmission properties of the fracture at each stress level to a specific stiffness predicted by the theory. In this way, the transmission coefficient curve at each stress state is matched to the closest theoretical curve. The specific stiffness of the fracture is then the stiffness used for obtaining the theoretical curve closest to the experimental curve. This process results in a best-fit normal specific stiffness of 4.0 TPa/m and 14.4 TPa/m for dry fractures experiencing 0.7 MPa and 13.8 MPa normal stress, respectively.

The bottom plot in Figure 5-6 shows the transmission coefficients calculated for the wet fracture experiment. The trends observed for the wet fracture are generally similar to those of the dry fracture: at a constant stress the transmission coefficients of high frequency components are less than those of the low frequency components, and any increase in the normal stress on the fracture leads to improved transmission coefficients at all frequency components. A comparison of the dry fracture and wet fracture plot reveals that the presence of the fluid inside the fracture has enhanced the transmission coefficients. These variations are mainly at low frequencies but are lesser in the high frequency components, as stated earlier. This has resulted in a deviation of the experimental transmission coefficients from the trends predicted by the theory. The presence of the fluid inside the fracture adds to the complexity of the situation by introducing viscous-related effects. Therefore, the

results are in less accordance with the displacement discontinuity model in which viscous effects are not accounted for. A larger mismatch between the displacement discontinuity theory and the transmissions across saturated fractures compared to transmissions across dry fractures was also reported by Pyrak-Nolte et. al (1990b). It was stated by them that P and S-waves even under dry conditions had a viscous coupling component across the fracture.

The above discussion suggests that in order to obtain more accurate matches with the experimental data, modifications are required to be made on the displacement discontinuity theory to include factors such as viscous effects. Such an attempt, however, was not the focus of this study. Bearing the in mind, DDT limitations and assuming the transmission properties of the fracture are attributed to its dynamic specific stiffness based on DDT, some representative specific stiffnesses for wet fractures are calculated. Such specific stiffnesses are assumed to contain the total effects of different factors such as the fracture geometry, surface roughness, asperities, and stress on the fracture. Therefore, following the same procedure used for the dry fractures, representative dynamic specific stiffnesses were computed for the wet fracture at different stresses.

Figure 5-7 shows experimentally obtained transmission coefficients for the dry and wet fracture, both at a stress of 0.7 MPa. In addition, for each set of experimental coefficients the best-fit curve of theoretical transmission coefficients based on DDT is plotted. The best-fit curves have the least square errors. Each theoretical curve corresponds to a representative fracture normal specific stiffness.

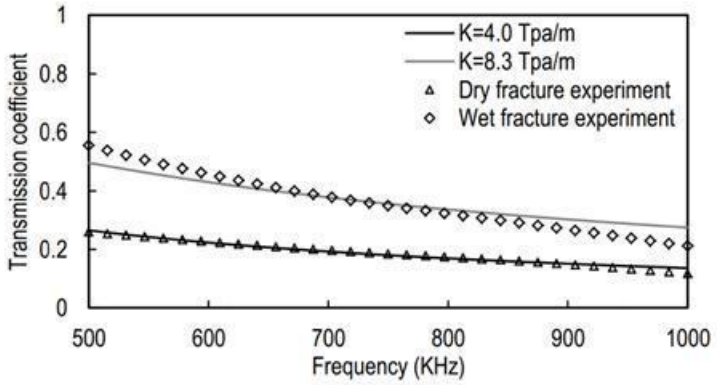

Figure 5-7 Experimental transmission coefficients obtained at 0.7 MPa stress in dry as well as wet fracture experiments and best-fit theoretical curves for corresponding representative fracture stiffnesses

The figure shows first of all, the considerable increase in the fracture specific stiffness in the wet fracture compared to the dry fracture at the same conditions.

The match between the displacement discontinuity theory and the dry fracture experiment is good while for the wet fracture experiment the agreement is not as good. At 0.7 MPa and 13.8 MPa normal stresses the best-fit specific stiffness for the wet fracture was calculated to be 8.3 TPa/m and 14.4 TPa/m, respectively. The fluid has, thus, resulted in a growth of almost 108% in the representative fracture specific stiffness at 0.7 MPa stress while at 13.8 MPa this increase is only around 4%. This again signposts the considerable effect of the filling fluid on enhancement of transmission in high compliance fractures (corresponding to small stress levels) which decreases as the fracture specific stiffness increases.

5.3 Hydraulic Fracture Monitoring Experiments

In this section the results obtained from hydraulic fracturing monitoring experiments are discussed. These include transmissions, reflections, and diffractions which were obtained in experiments including horizontal and vertical hydraulic fractures. Only specific conditions of experiments which may be different between individual experiments are explained and for the details of equipment specifications and general laboratory hardware the reader is referred to Chapter 4.

Normally, an excessive amount of data is acquired during hydraulic fracturing experiments. Using the full capability of the data acquisition system, 4 ×16 = 64 sets of ultrasonic data between individual source-receiver transducers can be recorded over the experiment time. If such an experiment takes one and a half hours, each of 64 sets of data will contain more than 5,000 traces of data. Each trace in this study contains at least 2,000 samples acquired with a sampling frequency of 10 MHz. Nevertheless, when placing the sample and the transducer spacers in the TTSC cell, small movements may inevitably deteriorate data acquired by some transducers. In such a case, the data recorded from the corresponding channel(s) will be of no use. Therefore, in the following sections only selected data sets are presented for each experiment.

5.3.1 Horizontal Hydraulic Fracture

A horizontal hydraulic fracture was created in A15, a 15 cm cubic sample. After placing the sample in the TTSC's cell, an isotropic horizontal stress of 14.5 MPa (2100 psi) was applied to the sample. During the experiment the stresses were kept constant using a computer-controlled pump by setting it in a constant-pressure mode. While increasing stress on the sample, ultrasonic data were acquired to record any possible changes in data. Four source transducers were used in this experiment. Application of the multiplexer allowed one complete set of ultrasonic data emitted from each source transducer to be acquired almost every second. Figure 5-8 shows the schematic of the horizontal fracture and the configuration of source and receiver transducers. All transducers used in this experiment were P-wave transducers. Before start of fluid injection, constant stresses were maintained on the sample and ultrasonic data were acquired for a period of time to confirm no detectable change in ultrasonic data was identified and ultrasonic measurements were repeatable.

In the next step, fluid injection into the sample commenced. After starting injection and before initiation of a hydraulic fracture, because mechanical stress was kept constant, the only major physical change in the experimental model was the fluid pressure inside the wellbore (hole at the centre of the sample) which increased with time. At the early times of injection, a high flow rate was chosen in order to increase fluid pressure rapidly and record corresponding changes in the ultrasonic

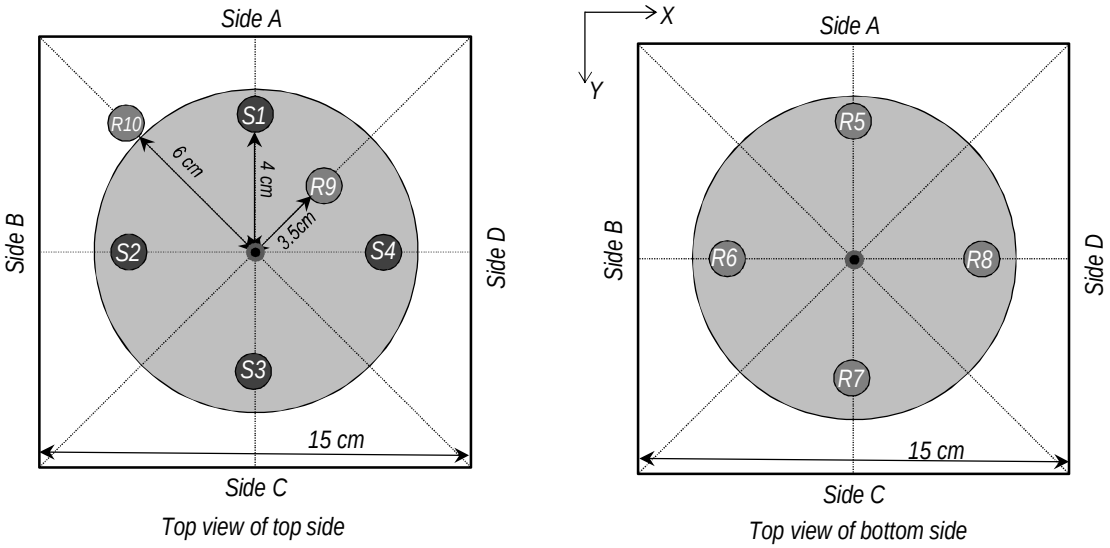

Figure 5-8 Schematics showing location of source and receiver transducers in experiment A15

data.

Figure 5-9 shows the plot of fluid pressure versus experiment time recorded by a pressure transducer installed in the flow line at a connection just before injection tube of the sample. Shown in the figure is also the injection rates used in different periods of the experiment after initial rapid pressurisation. Neglecting the relatively small pressure loss that occurs between the pressure transducer and the wellbore, it can be assumed that the recorded pressure corresponds to the pressure inside the wellbore. The plot shows that the breakdown pressure (maximum pressure after which the pressure starts to drop) of 21.2 MPa occurs at a time of about 4900 seconds. Fracture initiation starts sometime before this moment, when the plot of pressure derivative deviates from a horizontal linear trend. This was determined to occur around 4300 seconds of experiment time.

During the injection period, no change in recorded ultrasonic data was observed. This included ultrasonic transmissions between transducers whose transmission line would intersect the hole inside the sample (e.g. transmission from source S1 to receiver R7). Similar observations were made in other hydraulic fracturing experiments. Therefore, provided there was not alteration in location of transducers (due to, for example, possible movements of rams and transducer spacers), the effect of stress installation on the sample as well as increasing the fluid pressure in the hole before initiation of a fracture seemed to be minor as they did not disturb the ultrasonic data. This is important in the interpretation of the results as any subsequent changes in the data should then be attributed to the initiation of a hydraulic fracture and subsequent damages occurred in the cement sample. In the following sections, different ultrasonic results obtained during the A15 horizontal

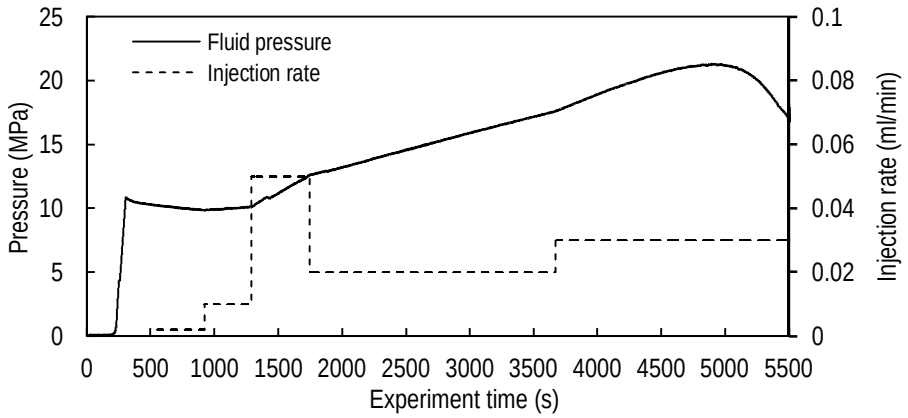

Figure 5-9 Injection pressure and rate versus time for experiment A15

hydraulic fracturing experiment are discussed.

5.3.1.1 Transmissions and Diffractions

The configuration depicted in Figure 5-8 allows experiments of transmissions to be conducted between different source-receiver pairs. Figure 5-10 shows traces recorded in receiver R7 from source S3 radiations over the experiment time. The top plot shows the original data while in the bottom plot background data has been deducted from all traces. Here, the background data is referred to a trace which is recorded in the intact sample before the initiation of a hydraulic fracture. The background data contains all events, including direct transmissions and boundary reflections, which take place in the intact sample. For visualisation purposes, different amplitude scales have been chosen for the two plots.

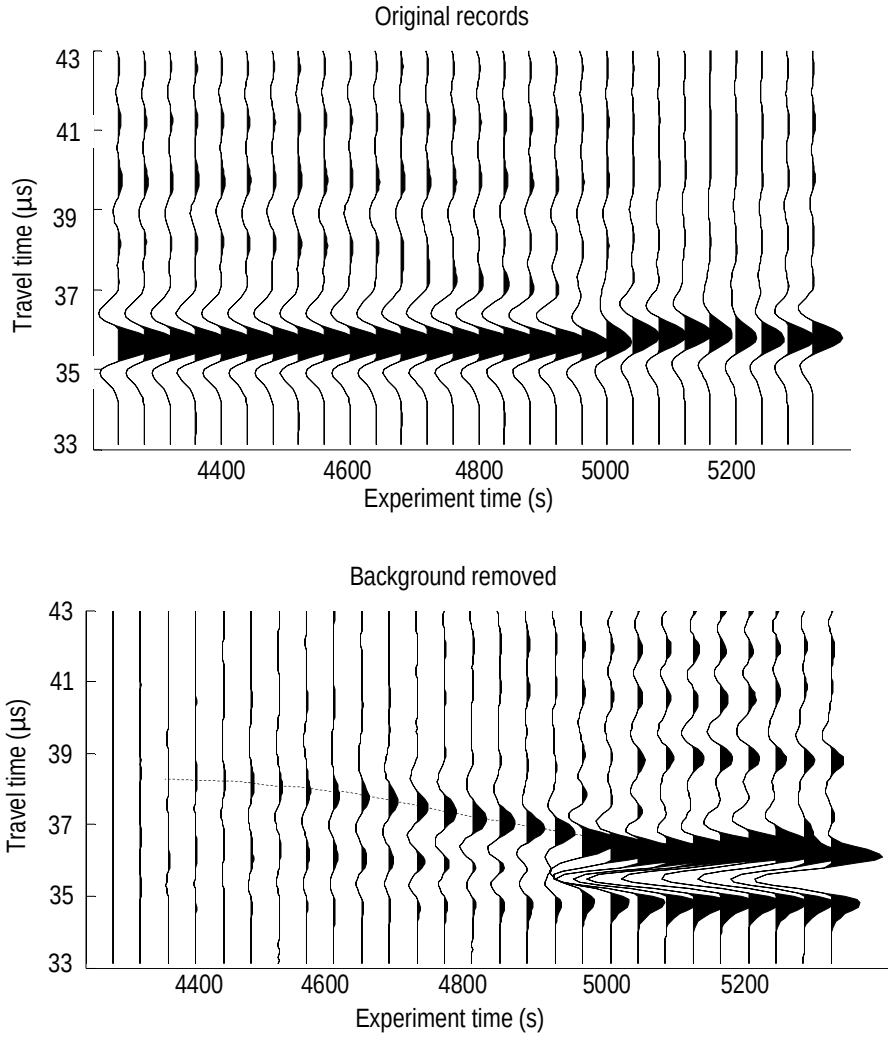

Figure 5-10 Original and background-removed transmission records between S3 and R7

In the top plot the events with smaller amplitudes which are recorded after the direct arrivals are due to reflections from the sample boundary as well as the simulated wellbore wall. These stationary events are not of interest in this study. The plot shows that before the experiment time of 4960 seconds, no considerable change has occurred in the direct arrivals. After about 4960 seconds of experiment time, a decrease is observed in the amplitude of the first arrivals. Furthermore, after this moment the peak arrival time of this event starts to be slightly delayed. Measured values of the delay were smaller than 0.2 μs. These two effects are attributed to the direct interference of the fracture when it intersects the source-receiver line. Therefore, based on data from this transducer pair, the horizontal fracture has reached to a radius of about 5 cm (distance of S3-R7 line from the wellbore) at a time of 4960 seconds, at least at its boundary close to side C of the sample (see Figure 5-8).

The trends observed in this plot are similar to those previously obtained using the numerical model where the effect of the interference of a fracture on transmissions was shown (see the bottom plot of Figure 3-21).

Although isotropic stresses are applied to the sample, the fracture may not propagate symmetrically in the sample. This can be due to factors such as an improper notch, the injection rate used, inhomogeneities in the wellbore wall and the sample, and uneven stress distribution in the sample. Therefore, the transmission data of each transducer is related to the intersection point of the corresponding source-receiver line and the fracture surface (see Figure 4-8). Nevertheless, looking at the transmissions from other transducer pairs, it was realised that the fracture had propagated almost symmetrically to all directions with the same propagation speed.

In the bottom plot of Figure 5-10, the amplitude scale was increased to reveal possible diffractions which are expected to emit from the fracture tip. As can be seen in the plot, from the experiment time as early as about 4360 seconds, there are waves which arrive after the first arrivals. The arrival time of the main peak of these events is shown by the dashed line in the plot. Their arrival time decreases and their amplitude increases as the injection continues. However, this trend stops sometime after 4960 seconds where the fracture has intersected the source-receiver line. The amplitudes of these events are considerably smaller than those of direct transmissions as they are not easily detectable in the top plot.

The continuous change in the arrival time of these events indicates they are related to a moving feature in the physical model, which in this case, is the moving tip of the fracture. As mentioned before, although the breakdown pressure occurs at 4900 seconds, pressure data showed fracture initiation occurs at earlier times at around 4350 seconds. This is in agreement with the ultrasonic diffractions from the fracture tip which are a sign of fracture initiation. Once the first micro-cracks are created as the sample matrix is damaged, their wave transmission properties is also varied compared to the intact rock. This gives rise to diffractions from the tip area. The fracture tip and processes around it is itself a complex phenomenon and a subject of on-going research. The nature of diffractions is also tied to the processes that take place at the tip.

In the horizontal hydraulic fracturing experiment, it was found that the quality of diffraction data recorded with transmissions and reflections are not particularly good due to the fact that the diffractions do not arrive at the receivers at a normal angle which is due to the radiation pattern of the transducers, and results in low quality signals. After conducting the test the sample was broken to investigate its propagation path. It was observed that while the fracture deviated at some points more than 2 cm from its conceptual horizontal plane, it was initiated from the circular notch made on the simulated wellbore wall at the centre of the sample. Therefore, recalling P-wave velocity of about 4450 m/s for the sample, the expected P-wave diffraction arrival time recorded in receiver R7 at early stages of fracture initiation at the wellbore, can be estimated as follows (see Figure 5-8):

$$t = \frac{x}{V} = \frac{2 \times \sqrt{(4^2 + 7.5^2)}}{4450} = 38\mu s \qquad (5\text{-}1)$$

The estimated arrival time of 38 μs is in reasonable agreement with the arrival time shown in the bottom plot of Figure 5-10. It is prudent to bear in mind that the diffraction pattern from the tip of the hydraulic fracture is more complex that just simple diffractions from a diffractor point. Apart from the diffracting zone at the tip of the fracture, it is known that the fluid front normally lags behind the dry fracture tip. This results in diffraction patterns from both wet and dry tips of the fracture (Groenenboom, 1998).

To further investigate the effect of the fracture on transmissions, selected records of S3-R7 transducer pair acquired at different times of the experiment are shown in Figure 5-11. The trace at 4600 seconds was recorded in the intact rock where no fracture was present. Also, at a time of 4800 seconds the fracture has not yet reached S3-R7 line so transmissions should not be affected. However, the figure shows although the travel time of transmissions has not changed, there are some changes in amplitudes of the trace recorded at 4800 seconds. In particular, there is an increase in the amplitude of the second transmission trough. This is attributed to the constructive interference of the diffractions from the fracture tip with the transmissions across the fracture. This recalls the interference of diffractions with transmissions which was previously shown by the numerical model in Figure 3-22. This phenomenon occurs when the fracture reaches the area close to the source-receiver line. The effect is more pronounced in the later parts of the first arrivals, where diffractions interfere the most with the transmissions. The second positive peak of this trace at around 39 μs is also due to the diffractions.

After of 5000 seconds of experiment time, the fracture has reached the source-receiver line (see Figure 5-10). It is obvious that the amplitude of the transmission first arrival is significantly reduced. Furthermore, there is a clear delay in the first peak arrival time of the transmissions. These are the two main seismic signatures of the fractures which were also observed in synthetic fracture experiments. The seismic behaviour of transmissions seen in this plot is comparable to the behaviour of numerical transmissions plotted in the top graph of Figure 3-11.

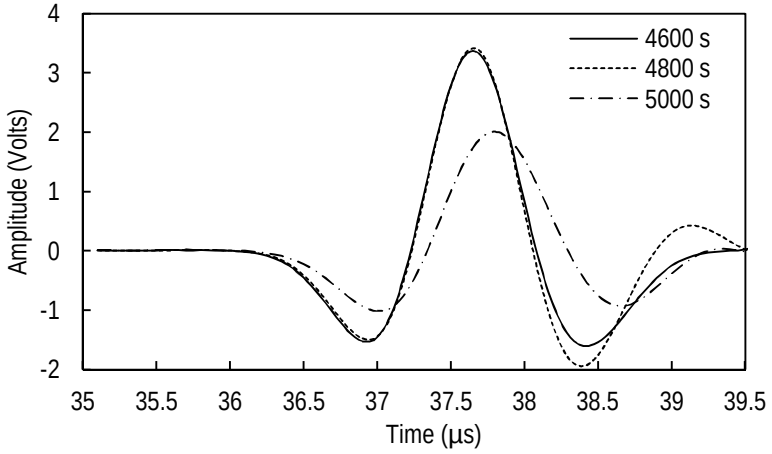

Figure 5-11 Selected traces from transmissions between S3 and R7

5.3.1.2 Reflections and Diffractions

Receiver transducers placed on top of the sample A15 can be used for measuring reflections from the fracture when the fracture crosses source-receiver line (see the left schematic in Figure 5-8). As an example, Figure 5-12 shows the data recorded by receiver R10 when the ultrasonic wave was emitted by source S2. The top plot shows data up to about 5500 seconds of the experiment while the bottom plot shows the data up to about 5200 seconds of experiment time and with a different amplitude scale. The background data has been removed from data in both plots in order to exclude the unwanted boundary-reflections.

The top plot shows after removing background data no detectable event is observed until around 5100 seconds time. From then on, an event with a very small but increasing amplitude is recorded by R10. Furthermore, the arrival time of this event is rapidly decreasing. Therefore, this event must be related to a moving feature in the physical model, the fracture tip. These are actually diffractions from the fracture tip generated after the incident P-wave reaches the tip and is diffracted in all directions. Therefore, they are detectable by receiver R10 located close to the source R2.

However, after 5400 seconds in time, the arrival time and amplitude of the recorded events become constant. The constant arrival time of the events after 5400 seconds indicates a stationary source for these events. The individual points on the fracture surface act as stationary reflectors although the tip of the fracture is moving. The amplitude of the reflections is considerably larger than the amplitude of diffractions from the tip of the fracture. This was also expected, based on numerical results presented earlier. As stated earlier, it is important to note that amplitude decay due to geometrical spreading from a point source occurs with cube of distance while in 2D numerical model it is related to the square of the distance. Therefore, the diffraction amplitude recorded in these experiments decay more than those predicted by PFC2D. Nonetheless, in this study the absolute values of numerical seismic amplitudes are not compared to those obtained experimentally, the focus is rather made on comparing their trends.

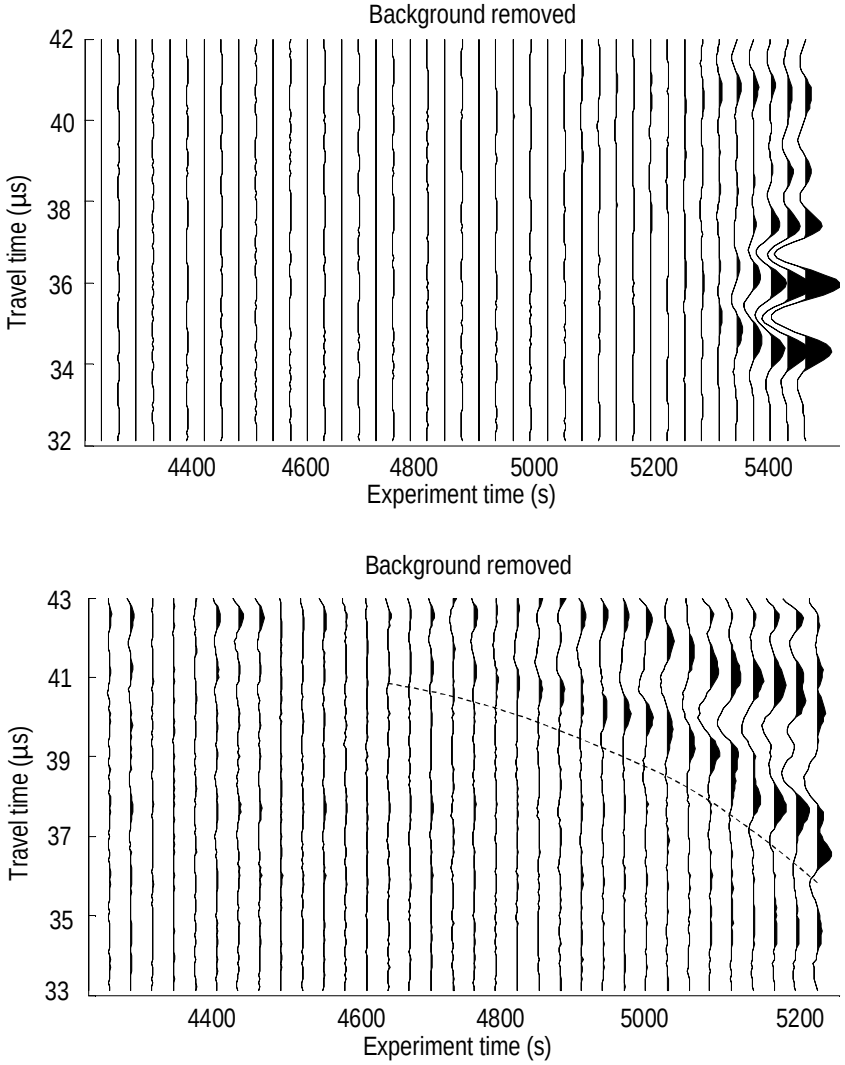

Figure 5-12 Background-removed data recorded by receiver R10 from ultrasonic emissions by source S2 in different time ranges

Looking from the top (see Figure 5-8), the reflector point is located on the lines that connect S2 and R10 (the mid-point between source and receiver). The arrival time of reflections is close to 33 µs which after multiplication by the P-wave velocity results in a travel distance of 14.8 cm. Now, assuming a horizontal fracture and considering the horizontal distance between the source and receiver (4 cm), a simple estimation of the vertical distance of the fracture from the top side of the sample can be obtained:

$$2\times\sqrt{\left(\frac{4}{2}\right)^2+h^2}=14.8cm\Rightarrow h\cong 7.1cm$$

This was confirmed to be the case after breaking the sample. Using other transducer pairs similar estimations of fracture location based on the travel time of reflections resulted in estimation of fracture location within a few millimetres in accuracy.

The bottom plot in Figure 5-12 shows the same set of data but in different time ranges. In this plot the amplitude scale of waves is increased to reveal the low amplitude diffractions. The plot shows diffractions that occur as early as 4600 seconds of experiment time. Because of their significantly low amplitude, these are not visible in the top plot. The arrival time of these events can be used to calculate the radius of the fracture over the experiment time, similar to what was carried out for S3-R7 results.

To have a closer look at the diffraction events, Figure 5-13 shows selected reflection traces recorded by the same transducer (R10) from the same source (S2). According to Figure 5-12, before 5400 seconds of experiment time, the fracture has not yet reached S2-R10. Therefore, the event shown in the trace obtained at 5370 seconds indicates diffractions from the fracture tip. By 5430 seconds the fracture has reached the source-receiver midpoint therefore the corresponding trace for this time shows reflections from the fracture surface. As expected, the amplitude of the 5430-seconds record is considerably larger than the amplitude of diffractions in the 5370-seconds record. Furthermore, the reflection arrival time is earlier than the diffraction which is due to the location of the moving tip of the fracture.

Interestingly, at 5500 seconds, the reflection amplitude is increased while it

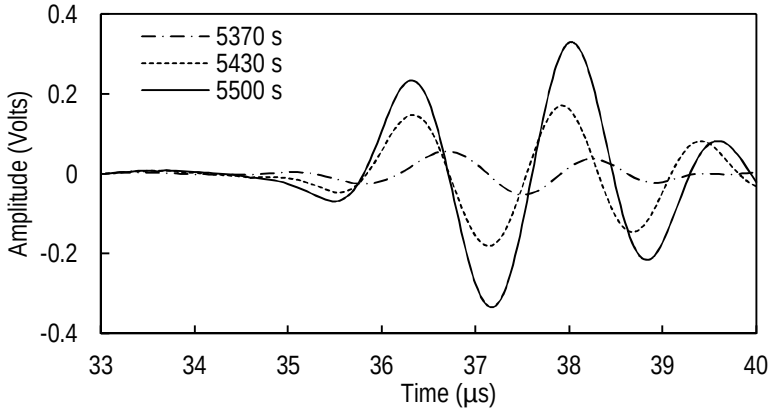

Figure 5-13 Selected fracture reflection traces recorded by receiver R7 from source S3 ultrasonic emissions

arrives later compared to the reflection recorded at 5430 seconds. The longer peak arrival times for 5500 seconds trace are particularly apparent in late peaks of the wave. The increase in the amplitude of the reflections from the fracture indicates a decrease in the fracture specific stiffness. For displacement discontinuities, it was numerically shown that this increase in reflection amplitudes due to lower fracture specific stiffnesses is also accompanied by an increase in the peak arrival time (see the bottom plot in Figure 3-11). Therefore, these experimental results suggest that the specific stiffness of the hydraulic fracture was decreased from 5430 seconds to 5500 seconds. As discussed before, this parameter is in turn dependent on several factors. In this experiment, the main feature of the hydraulic fracture which changes the specific stiffness of the fracture is its width. Normally, the fracture propagates with a wedge-shape profile. Therefore, at early moments that the fracture reaches the source-receiver midpoint, the local fracture width is small. This leads to a larger fracture specific stiffness at that point. As the fracture propagates more, the width at the midpoint increases which results in a locally larger fracture compliance. At this time, the fluid pressure is also larger at the midpoint which should enhance transmission across the fracture. As mentioned before, the effect of fluid pressure on the fracture specific stiffness is insignificant compared to the effect of the fracture width.

Such analyses on reflection data from hydraulic fractures have the potential to be used for constructing a real-time width profile of the fracture, at least locally. This could also greatly help in monitoring the propagation of field hydraulic fractures. Furthermore, placement of proppant inside the fracture is another factor which can affect seismic reflection and transmission results.

5.3.2 Vertical Hydraulic Fracture

This section covers the results of a selected vertical hydraulic fracturing experiment, A20. The sample size used for the vertical hydraulic fractures was 20 cm. To create a vertical hydraulic fracture, it is necessary to apply anisotropic horizontal stresses on the sample. The larger the anisotropy is, the higher is the chance of generating a vertical fracture. In this experiment, a normal stress regime was applied to the sample. Vertical, maximum horizontal, and minimum horizontal stresses applied to the sample were 9.65 MPa (1400 psi), 8.27 MPa (1200 psi), and 0.69 MPa (100 psi),

respectively. The two transducer blocks with the largest number of holes were used for applying minimum horizontal stress on the sample. In such a configuration, the fracture initiates and propagates preferentially parallel to the minimum horizontal stress.

The left picture in Figure 5-14 shows sample A20 placed in the TTSC's cell and confined by the transducer blocks. Transducer cables are also visible in the picture. The right picture shows the sample which was broken after the experiment. This picture shows the profile of the vertical fracture and invasion of the fracturing fluid inside the sample.

Similar to the horizontal fracturing experiment carried out on the 15 cm sample, different ultrasonic events, namely reflections, transmissions and diffractions were recorded in this experiment by placing source and receivers in suitable locations around the sample. Figure 5-15 shows schematics of the sample, the vertical hydraulic fracture, and position of the transducers around the sample. The injection tube is also shown in this figure. Multiplexing was conducted between three source transducers S1, S2 and S3 and for each cycle of source transducer radiation, ultrasonic waves were recorded by all receiver transducers. Ultrasonic data acquisition commenced before starting the fluid injection to register any possible effects of injection on the data. Due to the excessive amount of acquired data, only those of interest are discussed here.

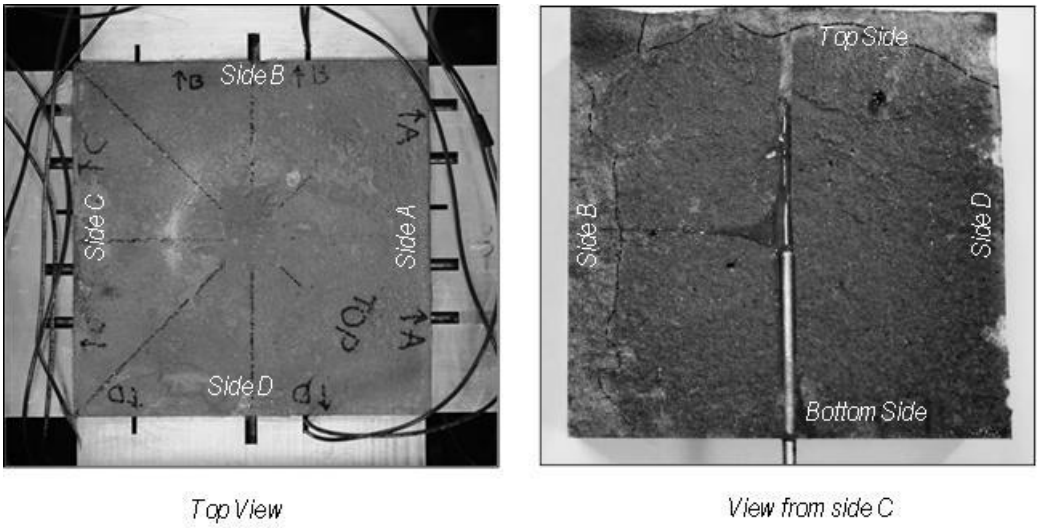

Figure 5-14 Sample A20 in TTSC's main cell confined by transducer blocks (left) and the same sample broken along the fracture plane showing the wellbore and fracturing fluid invasion into the sample (right)

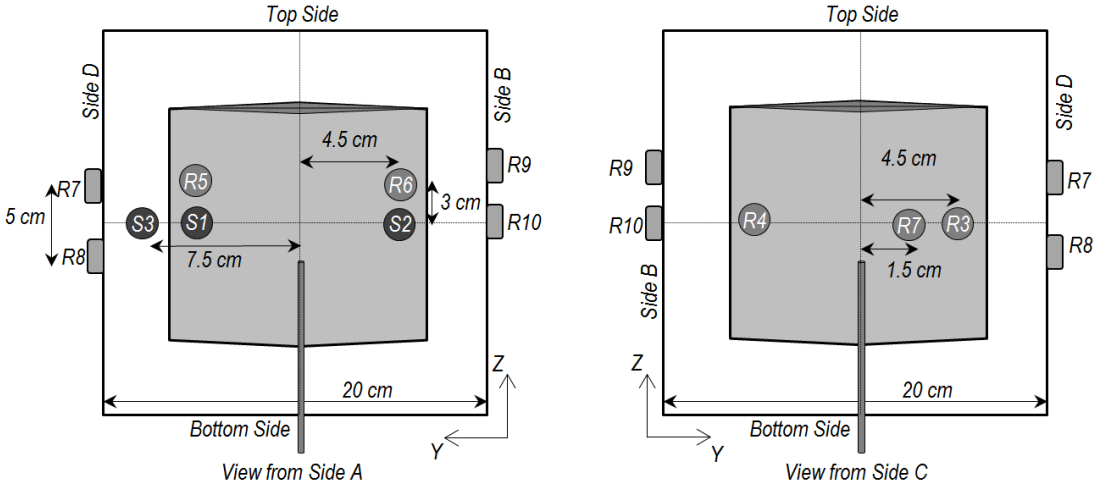

Figure 5-15 Schematics of sample A20 showing position of transducers with respect to the vertical fracture

At the early moments of the experiment a high injection rate was selected for quick initial pressurisation of the fluid. Afterwards, the injection rate was decreased to allow for a steady propagation of the fracture.

Figure 5-16 shows the plot of fluid pressure and injection rate versus experiment time. The fluid pressure is recorded at the lower end of the injection tube. Due to the pressure loss along the tube, the pressure at the fracture opening in the wellbore is slightly smaller than the recorded pressure. The trends however, are similar. Furthermore, the fluid pressure inside the fracture reduces from the wellbore pressure at the fracture opening to zero at the fracture tip. As a result of the inherent

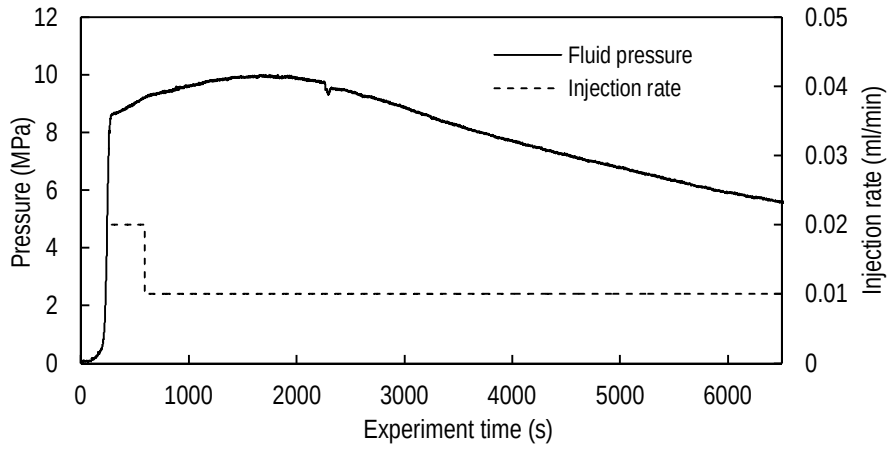

Figure 5-16 Injection pressure and rate versus experiment time for experiment A20

inhomogeneities in the sample, the fracture may not propagate symmetrically and the local fluid pressure may be quite different from what is expected. It is, therefore, thoughtful to take into account the effect of these factors while interpreting the ultrasonic data. The fluid pressure reaches its peak of 10 MPa at approximately 1700 seconds of the experiment time after which it gradually decreases which indicates a steady propagation of the fracture in the sample. There is also an abrupt pressure drop of approximately 0.4 MPa recorded in the pressure data at around 2250 seconds. This pressure drop could be attributed to a sudden volume increase in the fracture closed system which in turn could have occurred due to a quick propagation of the fracture from a weakness point in its path.

The peak pressure recorded in this experiment is less than half of the peak pressure shown in Figure 5-9 for experiment A15. This was expected because generally, initiation of a vertical fracture in a vertical wellbore requires less pressure. In the case of the horizontal fracture, the fracture has to initiate through a small-area circular notch while for a vertical fracture, the contact area on which the fracture can initiate is much larger which eases the initiation process.

5.3.2.1 Concurrent Measurement of Reflections and Diffractions

The configuration shown in Figure 5-15 provides the ability to record reflections from a fracture surface through two transducer pairs: S1-R5 and S2-R6. Figure 5-17 shows the ultrasonic data recorded by receiver R5 from source S1 emissions. The

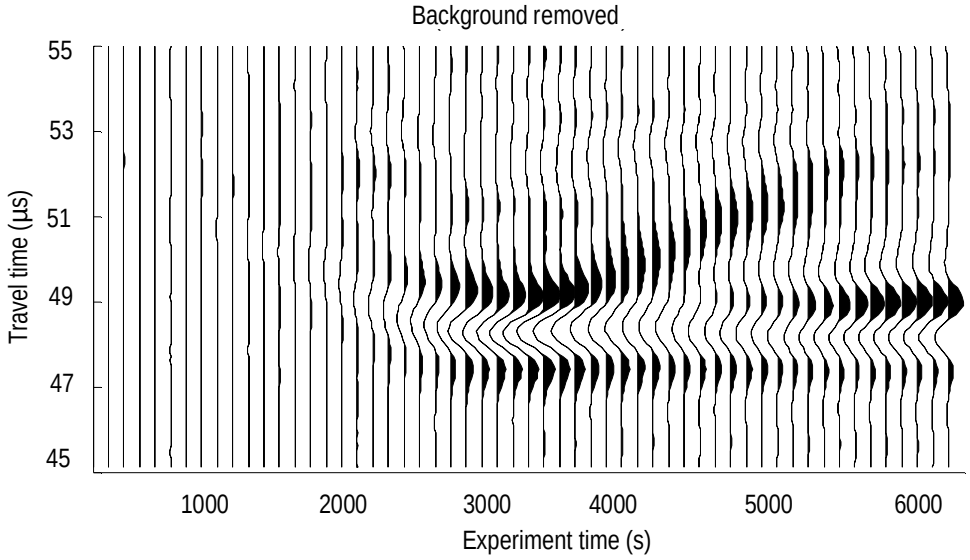

Figure 5-17 Background-removed data recorded by receiver R5 from ultrasonic emissions by source S1 over the experiment time

background data (corresponding to a trace recorded in the intact rock and before initiation of fluid injection) was removed from all traces. Therefore, any remaining ultrasonic event indicates a change in the medium due to initiation and propagation of the hydraulic fracture. As shown by the figure, no detectable event is recorded by the receiver until after 1000 seconds of experiment time. Afterwards, the receiver starts to record an initially weak event whose arrival time gradually reduces from about 51 μs to 47 μs. Furthermore, its amplitude increases during the experiment time. This trend continues until a time of 3300 seconds, after which an event with a constant arrival time is recorded. This set of experimental data is very similar to the numerical plots shown in Figure 3-19. A comparison between these two sets of data signifies the usefulness of such numerical investigations particularly in understanding the anticipated fracture-induced ultrasonic events and determining the optimum arrangement of ultrasonic transducers for capturing these events.

The first event with a varying arrival time is attributed to the diffractions from the fracture tip. Although receiver R5 is positioned in a place which is ideal for recording reflections from the fracture surface, the fracture tip diffractions are also detected by the receiver, but with smaller amplitudes. Their amplitude is small, particularly at the early moments that they are first captured by the receiver. This can be attributed to two different factors: geometrical spreading and radiation pattern of the transducers. When the fracture length is small, the two-way travel distance of the diffractions, from the source transducer to the fracture tip and then back to the receiver transducer, is large. As the fracture tip moves forward, this distance shortens. This in turn leads to a lower geometrical spreading effect. Furthermore, the radiation pattern of the transducers, as discussed in previous chapter, is not spherical. Based on the trend observed in Figure 4-7, the transducers do not perform efficiently when the angle between the incident wave propagation direction and the transducer surface is not close to the normal angle. This is the case for early diffractions from the fracture tip which arrive at relatively small angles to the receiver, and therefore are not detected efficiently.

After almost 3300 seconds, the arrival time of the first event recorded by the receiver remains constant. This constant-travel time event is attributed to the reflections from the fracture surface after the fracture intersects the midpoint between the source and the receiver. Hence, it can be inferred from the data that the fracture reaches S1-R5 midpoint at a time of approximately 3300 seconds. As soon as the

fracture intersects the midpoint, reflections from the fracture surface are the first events recorded by the receiver. Because the location of the reflector point on the fracture remains stationary, reflection travel times also appear to remain constant.

As the tip of the fracture passes the S1-R5 midpoint, the arrival time of the diffractions also increases which results in the separation of diffractions from reflections. This is clearly apparent on the plot from 4000 seconds onwards. Nevertheless, at the moments close to 3300 seconds, when the fracture tip is close to the midpoint, interference of the reflections and tip-diffractions occurs. This is one of the reasons the amplitude of the diffractions appears to be larger between 3000 and 4000 seconds compared to later times over which diffractions and reflections are separated enough. Furthermore, normally the tip of the fracture is dry due to the fluid lag inside the hydraulic fracture. When the dry tip is located on the source-receiver midpoint, it can result in stronger reflections compared to the other points along the fracture which are fluid-filled.

Figure 5-17 shows that the diffraction arrival times change gradually over the entire experiment time, as the two-way travel distance of diffractions reaches a minimum and then increases again. Based on this trend it can be stated that the fracture propagation is quite stable, at least from its boundary which moves towards Side D of the sample (see Figure 5-15).

Furthermore, the travel times recorded by receiver R5 can be used for obtaining the location of the fracture over the experiment time. The left picture in Figure 5-18 shows how the travel times of S1-R5 records can be used for inferring the fracture location. The right picture in this figure shows a three-dimensional view of the fracture and selected transducers in this experiment. The S1-R5 midpoint is located on a point where the two way travel distance of reflections or diffractions is a minimum. This condition is met when d_1 and d_2 are equal. The following equation can then be used for determining "*d*" the normal distance of the midpoint from the sample boundary:

$$d = \sqrt{d_1^2 + (\frac{h}{2})^2} = \sqrt{(\frac{Vt}{2})^2 + (\frac{h}{2})^2} \qquad (5\text{-}2)$$

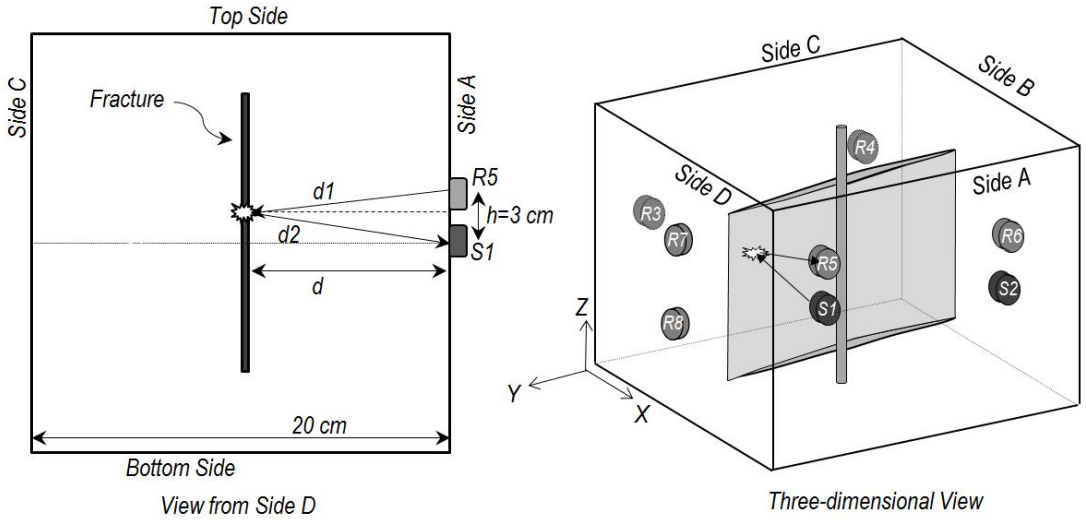

Figure 5-18 Schematics illustrating transducer configuration for measurement of fracture location (left) and three-dimensional configuration of selected transducers in experiment A20

Using the P-wave velocity of 4450 m/s, the recorded reflections travel time of close to 47 μs, after correction for the measured system delay of 1.6 μs, can be used in Equation (5-2) to obtain the normal distance between the fracture and the transducers as follows:

$$d = \sqrt{\left(\frac{4450\times(47-1.6)\times10^{-6}}{2}\right)^2 + \left(\frac{3\times10^{-6}}{2}\right)^2} \cong 0.102m$$

which indicates the fracture has propagated almost to the symmetry line of the sample (close to 10 cm from sample boundary) at least at the midpoint location which is 4.5 cm far from the wellbore. The accuracy of the above number is dependent on the accuracy of measurement of the arrival time of the waves, measured wave velocity in the sample, and system time delay.

The above conclusion is made on the location of the midpoint which is stationary during the experiment. With a similar method, and assuming the vertical fracture propagated on the symmetry line of the sample (this was confirmed to be true after breaking the sample, see the right picture in Figure 5-14), the diffraction travel times can be used for calculation of location of the fracture front over the experiment time. For instance, at 1800 seconds of the experiment time, a travel time of 48.1 μs was measured for the first arrival, corresponding to the P-wave diffraction. Applying this figure in Equation (5-2), results in a distance of 10.5 cm between the transducers and the fracture tip. Finally, considering that the transducers are 4.5 cm

away from the sample centre (see Figure 5-15), the radius of the fracture can be simply obtained as follows:

$$Rad_{frac} = \sqrt{10.5^2 - 10^2} \cong 3cm$$

Therefore at 1800 seconds of the experiment time, the fracture had a radius of approximately 3 cm, at its wing moving towards side D of the sample.

In Figure 5-17 no diffraction events are detectable before 1000 seconds of experiment time. To investigate the onset of the diffractions, the same set of data up to 1800 seconds are plotted and shown in Figure 5-19. The top plot shows selected trace plots and the bottom plot shows a two dimensional view from the surface plot of the data. In this plot the black colour intensity shows the relative amplitude of the troughs, the white colour intensity indicates the relative amplitude of the peaks, and the grey colour indicates amplitudes close to zero.

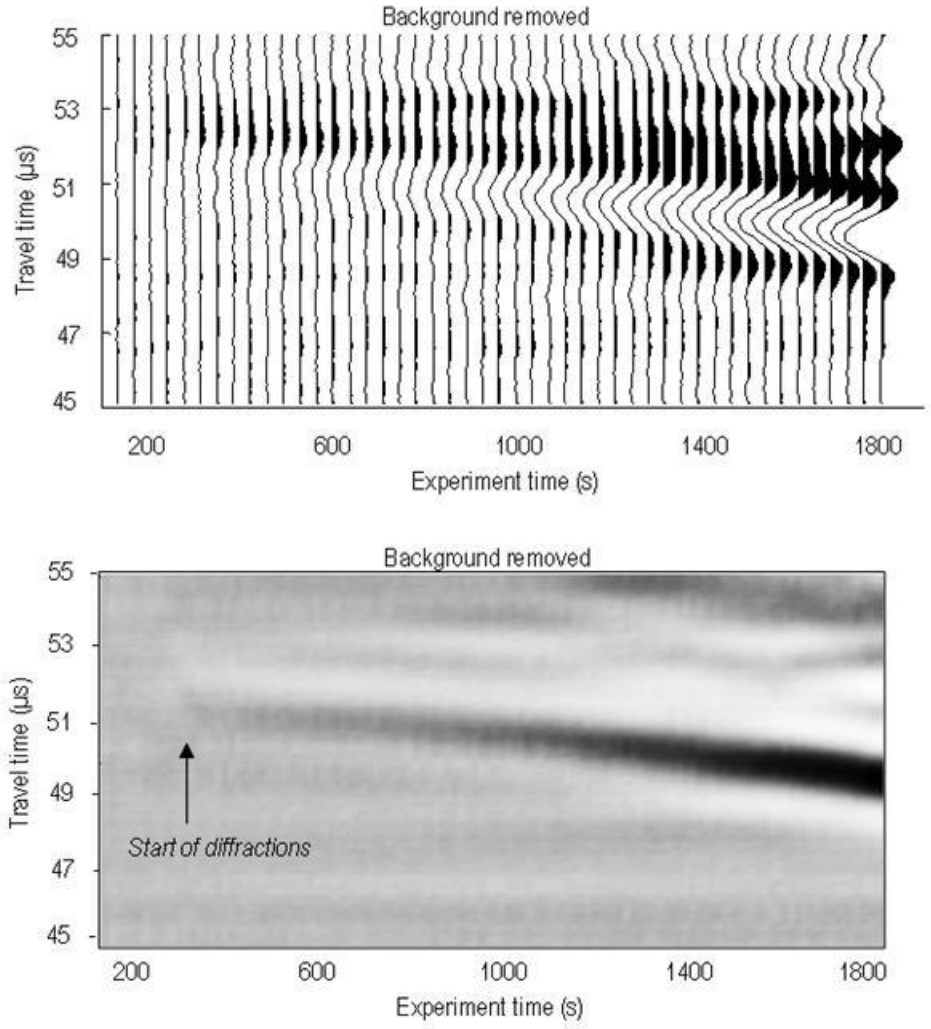

Figure 5-19 Trace plot (top) and surface plot (bottom) of background-removed data recorded by receiver R5 from ultrasonic emissions by source S1 up to the experiment time of 1800 seconds

These two plots show that the diffractions had actually started much earlier than 1000 seconds, at sometime around 300 seconds of the experiment time. Perhaps the onset of diffractions is better seen in the surface plot where the start of diffractions is identified on the plot. The earliest diffractions arrive at approximately 50.5 μs. Using the above-mentioned procedure, this travel time results in a distance of 4.5 cm between the transducers and the wellbore. This is equal to the actual distance shown in Figure 5-15. This confirms that the earliest diffractions detected in Figure 5-19 specify initiation of the fracture from the simulated wellbore wall corresponding to a very small fracture radius. As soon as the first crack is generated in the rock, it starts to diffract the incident ultrasonic waves. Looking at the fluid pressure plot (Figure 5-16) it is deduced that the fracture initiation commenced at the early stages of the pressurisation, just after the injection rate was reduced to 0.02 ml/min. An attempt was made to determine the fracture initiation from the deviation of the fluid pressure derivative from the initial linear trend. It was, however, noticed that using merely the pressure and injection rate plot it is difficult to make a decision on the initiation moment of the hydraulic fracture. This denotes another usefulness of such ultrasonic measurements, which by cross-checking with other available data, they can potentially deliver qualitative and quantitative information on the real time fracture geometrical and physical properties.

As stated earlier, in this experiment, some of the transducers were positioned in locations where taking into account the radiation pattern of the transducers, were ideal for measurement of the fracture tip diffractions. Further analysis of the fracture tip location over the experiment time, therefore, was carried out on such data which generally contained higher quality diffractions than the data recorded by receivers such as R5. This will be discussed in a later section.

Determination of the location of the source-receiver midpoint is not the only use of the recorded reflections. As previously mentioned, displacement discontinuity theory states that reflections from the fracture surface are dependent on the specific stiffness of the fracture as well as the frequency of the incident wave. A more compliant fracture reflects more wave energy and causes longer reflection time delays. Figure 5-20 shows waveforms and frequency spectra of selected reflections recorded by receiver R5. The top plot shows fracture reflection arrivals in the time domain. As seen in Figure 5-17, these waveforms which are related to experiment

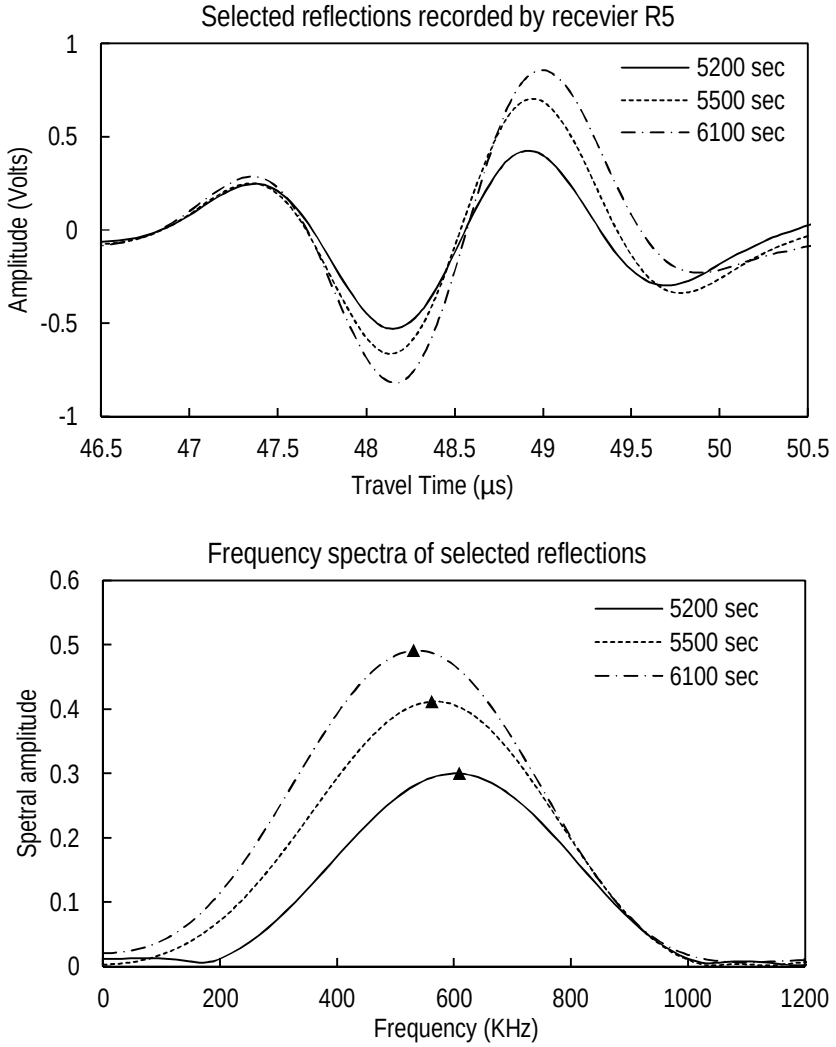

Figure 5-20 Waveforms (top) and frequency spectra (bottom) of selected reflections waveforms recorded by receiver R5

times after 5200 seconds, are not contaminated by diffractions which arrive well after the first arrivals.

As the experiment time passes, the reflection amplitudes increase steadily indicating higher portions of energy are reflected back by the fracture. Furthermore, the plot shows that peak arrival times become longer as the amplitudes increase. Increase in reflection amplitude and time delays are indicators of the well-known property of the fracture, that of specific stiffness. As the fluid injection continues and the fracture tip moves forward, the local width at the S1-R5 midpoint increases, similar to what was shown numerically for the straight hydraulic fracture (see Figure 3-26). Thus, any increase in the local fracture width at the reflector point (midpoint) results in a decrease in the local specific stiffness of the fracture.

Consequently, the reflections from the same point of the fracture change in amplitude and arrival time. These two effects were also already observed in the numerical results of reflections from a smooth-joint fracture as the fracture specific stiffness changes (bottom plot in Figure 3-11), and the numerical reflections from a straight hydraulic fracture as its width changes (Figure 3-29). These experimental measurements confirm that the laboratory hydraulic fracture also exhibits behaviours which are qualitatively in accordance with numerical and theoretical predictions. These results are in agreement with the experimental results of Pyrak-Nolte et at. (1990b) obtained on dry and wet fractures under different normal stresses.

The frequency spectra of the reflections shown in the bottom plot of Figure 5-20 were obtained using a Fast Fourier Transform algorithm. As expected, as the local fracture width increases and the local fracture specific stiffness increases, the spectral amplitudes increase. The markers indicate the peak amplitude and its corresponding frequency for each curve. Interestingly, it is observed that although by decreasing the fracture specific stiffness the reflection amplitudes increase, the corresponding peak amplitude frequency decreases. At 5200 seconds the peak amplitude is 0.3 Volts with a corresponding frequency of 610 KHz, while at 6100 seconds, the peak amplitude and its corresponding frequency are 0.5 Volts and 530 KHz, respectively. A very similar trend also was previously shown by numerical modelling of reflections from a smooth-joint fracture with varying specific stiffness (the bottom plot in Figure 3-12). For interpretation of this event, it is worth recalling the low-pass filter attribute of fractures. When the fracture width is still small, low frequency components of the incident wave pass through the fracture. At this stage only high frequency components are reflected. However, as the injection continues and the fracture widens, as a result of the decrease in the fracture specific stiffness, some lower frequency components also start to be reflected by the fracture. This consequently results in a decrease in the frequency of a reflection's peak spectral amplitudes.

Based on the configuration depicted in Figure 5-15, data recorded from S2-R6 transducer pair can lead to reflection and diffractions similar to those discussed for S1-R5 pair. Although symmetrical propagation is the common assumption in hydraulic fracture models, in reality it may not propagate symmetrically (Sarmadivaleh et al., 2011). In a hydraulic fracturing experiment, surface imperfections at the wellbore wall, improper notch, asymmetrical stress distributions

on the sample and inherent heterogeneity of the sample texture could cause a fracture to initiate or propagate asymmetrically. This means the fracture may propagate more from one of its wings while propagation of its other wing may be stopped or slowed down by the factors mentioned above. As it is not possible to simply infer such behaviours from pressure-rate data, acquiring ultrasonic data from two different wings of the fracture and comparing them could prove very useful.

Figure 5-21 shows a two-dimensional surface plot of the background-removed reflections recorded by receiver R6 from source S2. The plot shows the emergence of fracture tip diffractions at early times of the experiment (about 500 seconds). As the injection continues, the fracture tip moves towards side B of the sample and causes the two-way travel distance of diffractions to reduce. This results in a trend similar to that observed for S1-R5 pair. Interestingly, the plot shows an abrupt drift in the data at almost 2250 seconds of the experiment time. This drift must be a result of a sudden change in the physical model. At this moment, the arrival time of the diffractions is measured close to 49 µs indicating that the abrupt event took place when the fracture length was approximately 3.7 cm. As discussed earlier, S1-R5 pair did not record such a sudden change in the data. Hence, the change in S2-R6 data must indicate a sudden change in the fracture propagation on its wing heading toward side B of the sample. This abrupt change was also shown in the pressure data at the same experiment time (see Figure 5-16). However, prior to investigation of the ultrasonic data, it was not possible to infer from the pressure drop

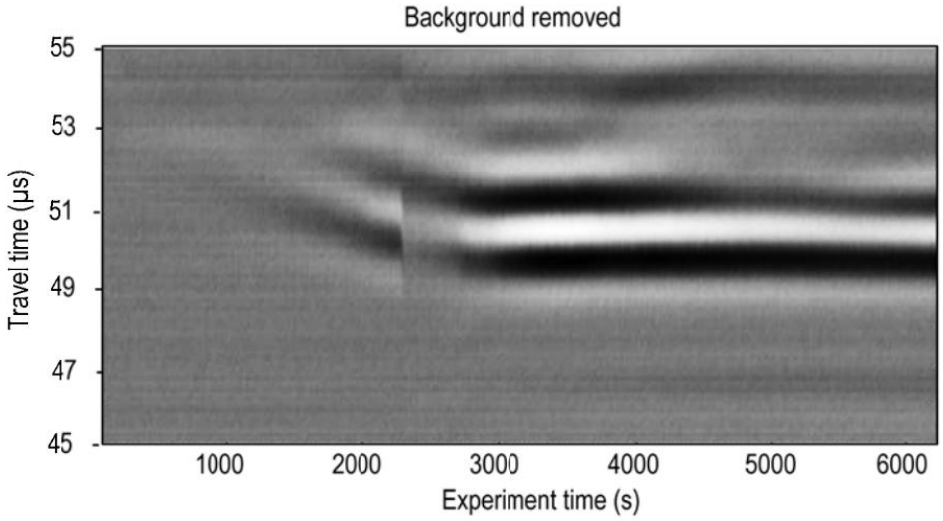

Figure 5-21 Two-dimensional surface plot from the background-removed data recorded by receiver R6 from ultrasonic emissions by source S2 over the experiment time

the location of this event. It was only after comparison of the ultrasonic data that such a decision could be made on the location of the event on the fracture and the state of the fracture.

Another difference between this plot and that of Figure 5-17 is that although S1-R5 diffractions are recorded until about 6000 seconds, sometime after the fracture tip passes S2-R6 midpoint, the diffraction arrivals are not recorded anymore. The last diffractions are also considerably interfered by the reflection data. This shows that the fracture tip close to sample side B has perhaps stopped propagating sometime after it passed S2-R6 midpoint. Breaking the sample after the experiment confirmed this judgement and proved that the fracture did not propagate symmetrically. Although the fracture reached the sample boundary on side D, its propagation was halted at a radius of about 7 cm on its wing towards side B of the sample. This case is a good example of the high potential of such active seismic measurements for detecting the propagation profile of hydraulic fractures.

5.3.2.2 Concurrent Measurement of Transmissions and Diffractions

Figure 5-15 shows that the data from a number of transducer pairs such as S1-R3 and S2-R4 provide information on transmission properties of the hydraulic fracture. Furthermore, it is expected that similar to the reflection receivers, some diffraction data are recorded.

Figure 5-22 shows surface plots of the data obtained from S1-R3 pair. The top plot shows the original recorded data. It is shown that the strong direct arrivals are constantly recorded by the receiver with no considerable change. However, at a time of about 2500 seconds it seems that the direct arrivals are affected, particularly in their second trough (shown in black) showing the possible interference of the diffractions with the direct transmissions. Thereafter, from around 3000 seconds the direct transmissions are clearly delayed and their amplitude is decreased which is distinguishable by the dimness of black and white colours in the plot. The pronounced delay and amplitude reduction can be the effect of fracture tip processes. In particular, a dry fracture tip can have a lower specific stiffness compared to other points along the fracture, thereby causing longer time delays and more distinct amplitude reductions. The effect of the local specific stiffness at the dry fracture tip was also previously noticed in reflections data of S1-R5 pair where reflections were particularly strong from the area close to the fracture tip. After about 4300 seconds,

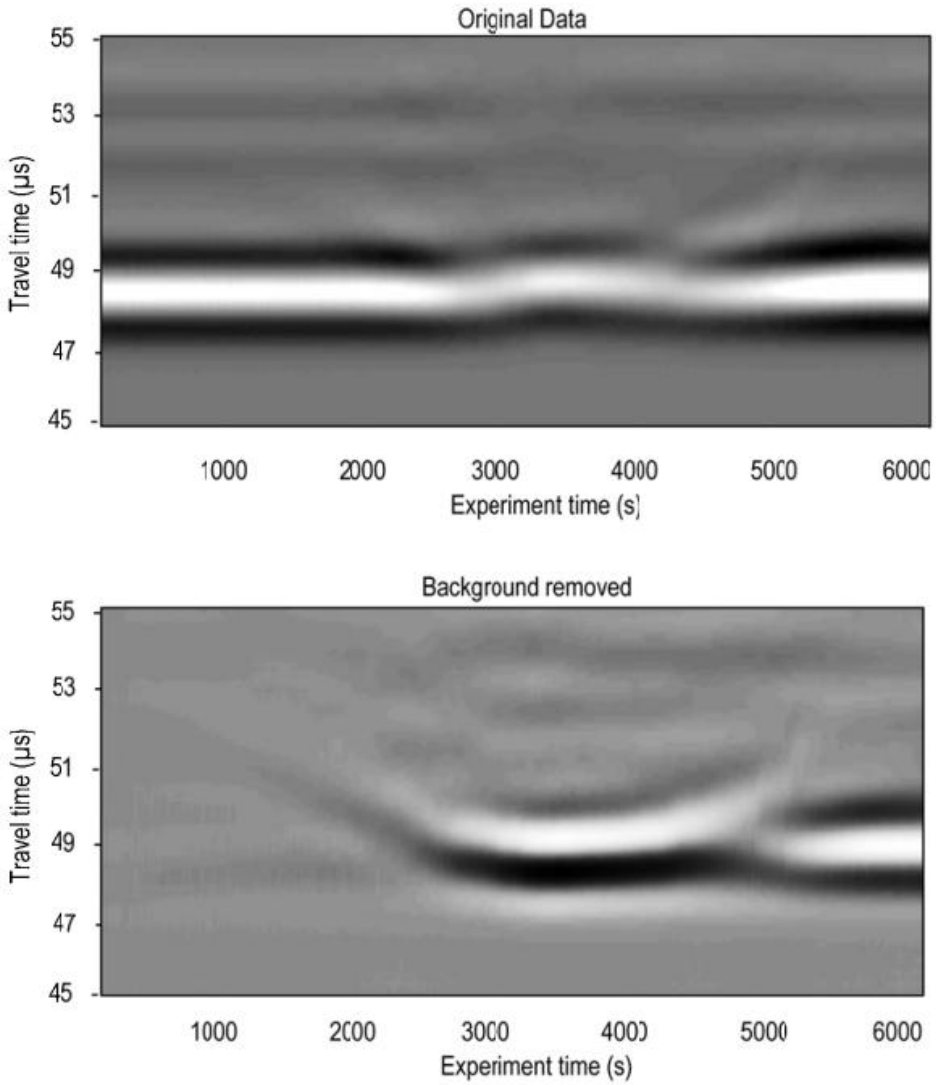

Figure 5-22 Two-dimensional surface plots of original (top) and background-removed (bottom) data recorded by receiver R3 from ultrasonic emissions by source S1 over the experiment time

the delay in the direct arrivals seems to disappear and their amplitude increases again.

The bottom plot in Figure 5-22 shows the background-removed data. Hence, any event seen in this plot is a change from the original transmission records in the intact sample. In this plot, development of the diffractions from early times of the experiment, as early as 300 seconds, is clearly detectable. The early diffraction arrivals, however, are not visible in the top plot of the original data. The diffraction arrival time decreases as the fracture tip moves forward. As soon as the fracture tip reaches close to S1-R3 line, the direct transmissions are also affected and that is why from about 3000 seconds, the background-removed plot shows some constant travel time events, which are attributed to delayed transmissions across the fracture. The

increasing travel time events observed after 4000 seconds are actually diffractions from the moving tip.

Selected original transmission records shown in Figure 5-23 provide an opportunity for investigating the events more closely. The record acquired at 100 seconds represents the reference direct transmission in the intact sample. The trace recorded at 2200 seconds seems to be very similar to the transmission in the intact sample expect for its late arrival. Particularly, the second trough of the 2200-seconds trace is larger in value than the 100-seconds trace. Looking at Figure 5-22 plots, it can be understood that this is due to the constructive interference of the transmission arrivals with the diffraction arrivals, which are close at 2200 seconds of the experiment time.

The next trace acquired at a time of 3300 seconds displays a considerable delay and an amplitude reduction in the main transmission peak. While discussing the data in Figure 5-22, this event was attributed to the effect of the dry tip area of the fracture which results in high apparent specific stiffnesses, resulting in pronounced delays and amplitude reductions.

At 5100 seconds, the fracture tip has moved forward and S1-R3 line now intersects a point on the fracture surface which is fluid-filled. This trace also shows a time delay and an amplitude reduction with respect to the intact sample transmission. These two effects are however, less pronounced than the 3300-seconds transmission. This can now be attributed to the local specific stiffness of the hydraulic fracture, at its intersection point with S1-R3 line. The ultrasonic transmission experiment on the dry and wet synthetic fractures discussed early on in this chapter demonstrated the

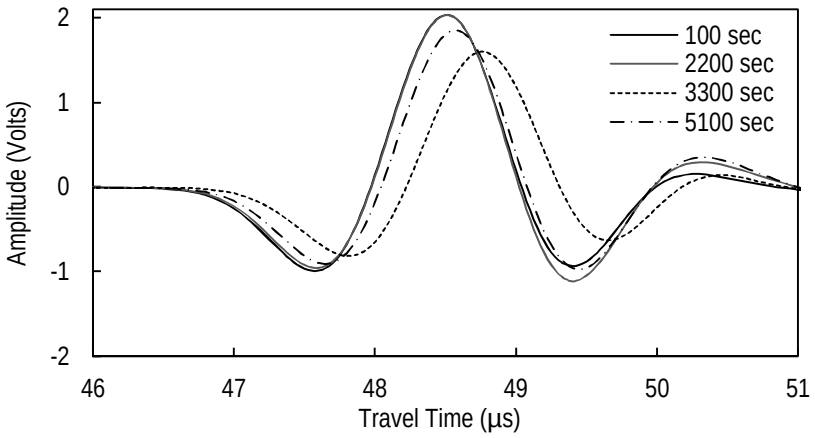

Figure 5-23 Selected transmission arrivals recorded by receiver R3 from source S1 radiations

important effect of the fracturing fluid on the transmission properties of a fracture (see Section 5.2.2). This effect was shown to be more noticeable in low normal stresses close to one megapascal. Over the experiment time, the normal stress on the hydraulic fracture was kept to a constant value of 0.69 MPa. Therefore, it is expected that the fluid inside the fracture plays a significant role in enhancing transmission of the dynamic waves. This could be the likely reason for the enhanced amplitude and shorter time delay across the fluid-filled fracture compared to its dry tip region. Note that this is in spite of the fracture's wider local width at its intersection with S1-R3 line at 5100 seconds, compared to the same value at 3300 seconds.

Transducers S3 and R7 used in these experiments are shear wave transducers. Hence, S3-R7 pair ultrasonic data could shed light on the shear wave transmission characteristics of the laboratory hydraulic fracture. As the quality of shear waves recorded over the experiment time was generally much lower than that of compressional waves, an attempt was made to increase the signal-to-noise ratio by trace stacking. The schematics shown in Figure 5-15 show that the intersection of S3-R7 line with the fracture plane coincides with the intersection point of S1-R3 line with the fracture. Thus, the transmission data from S1-R3 and S3-R7 pairs represent properties of the same physical point in the model.

Figure 5-24 shows the original data recorded by the shear transducer R7 from radiations of the shear transducer S3. The plot shows that similar to P-wave transmissions, S-wave transmissions are also affected by the tip-diffractions from

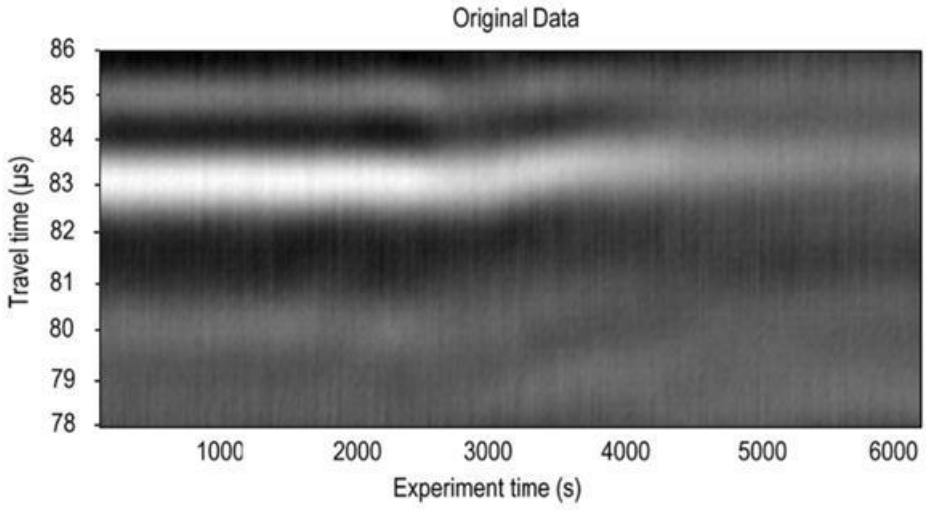

Figure 5-24 Two-dimensional surface plots of original data recorded by receiver R7 from shear wave ultrasonic emissions by source S3 over the experiment time

about 2500 seconds. S-wave transmissions are clearly delayed and their amplitude is reduced. There is, however, a major difference observed between S-wave transmission and P-wave transmission: as the fracture tip moves forward, the amplitude of S-wave transmissions is not recovered but disappears with the experiment time. Interpretation of this difference requires recalling the fact that S-wave cannot transmit through the fluid. Therefore, if the hydraulic fracture is fully open without any mechanical contacts between its surfaces, S-wave transmissions should completely disappear. However, the reduction of S-wave amplitude occurs gradually. This suggests that even after the hydraulic fracture intersects the source-receiver line, some of portion of its surfaces are in solid-solid contact which allows S-wave transmission. However, as the injection continues, the local fracture width at its intersection with S3-R7 line increases which results in a larger separation of solid-solid contacts around the area, hence disappearance of S-wave transmission. Similar shear wave shadowing events were also reported in the experimental work of Groenenboom (1998). In the case of P-wave transmissions, however, the compressional energy is still transmitted through the solid-fluid-solid media as the fracture width increases.

Figure 5-25 shows the original transmissions (top) as well as background-removed transmissions from S2-R4 pair. This transducer pair monitors the change in transmissions across the wing of the fracture which moves towards side B of the sample (see Figure 5-15). In the top plot a change in the direct transmission arrivals is observed at around 2300 seconds. Thereafter, it seems that the transmitted waves are slightly delayed and their amplitude is decreased which is possibly due to the interference of the hydraulic fracture with transmissions. This can be confirmed by looking at the background-removed data which provides more information on changes in transmissions. The bottom plot shows emergence of the diffractions from early experiment time with a continuously decreasing travel time until about 3300 seconds. Again, a sudden drift in the data is observed at around 2250 seconds which was previously noticed by S2-R6 pair as well as injection pressure data. The data suggests that in spite of a sudden propagation regime in this wing of the fracture, the fracture had intersected the S2-R4 line at around 3300 seconds, which corresponds to a radius of 4.5 cm. As S1-R5 data also indicated that the fracture reached a length of 4.5 cm at around the same time, the fracture propagation was symmetrical, at least up to 3300 seconds.

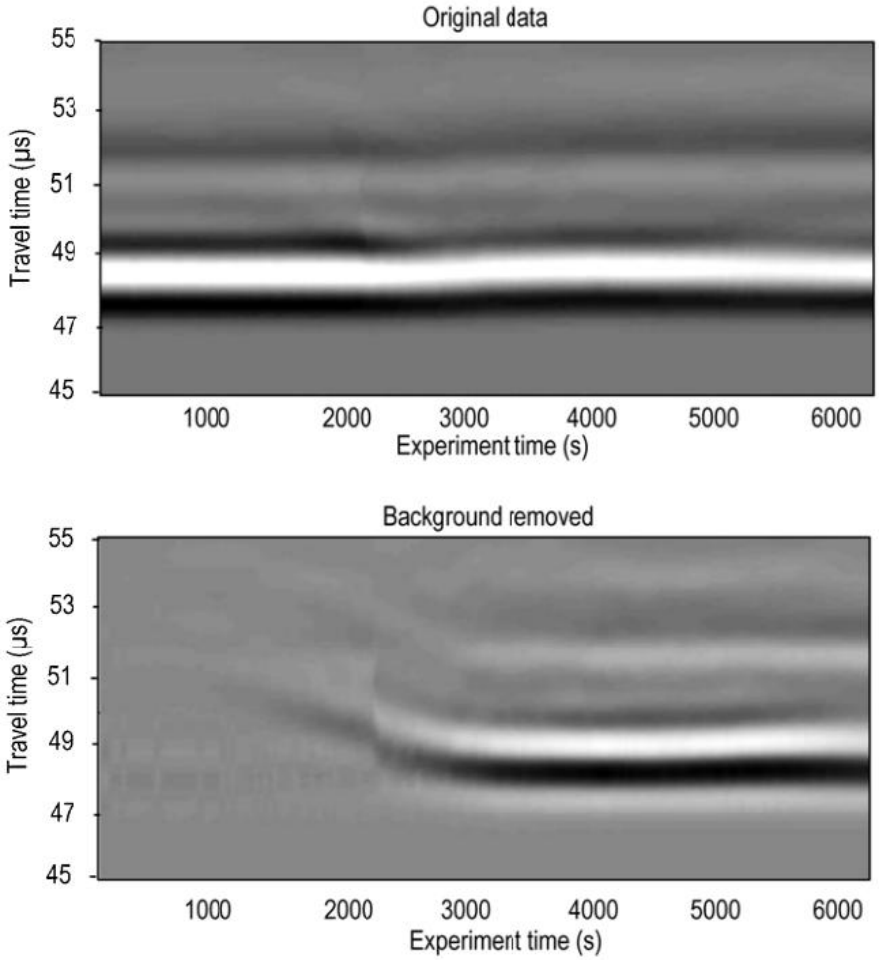

Figure 5-25 Two-dimensional surface plots of original (top) and background-removed (bottom) data recorded by receiver R4 from ultrasonic emissions by source S2 over the experiment time

From 3300 seconds onwards, no noticeable change in the amplitude or travel time of the transmissions is seen in these plots. This is different from what was shown in the background-removed plot of Figure 5-22 where separation of diffractions from transmission arrivals was recorded. The observations made on S2-R6 reflections also showed a similar response, with limited diffractions after the fracture tip passes the source-receiver line. This was revealed to be due to the asymmetrical propagation of the fracture after 3300 seconds, which stopped at a radius of 7 cm on its wing towards side B of the sample.

Figure 5-26 shows selected transmission records of S2-R4 pair. The trace recorded at 100 seconds shows the transmission in the intact sample. Similar to the event observed in Figure 5-23, the trace recorded at 2300 seconds is different from the intact sample record mainly in its late parts which is a sign of the diffraction's interference. The two other traces are recorded after the transmissions are affected by

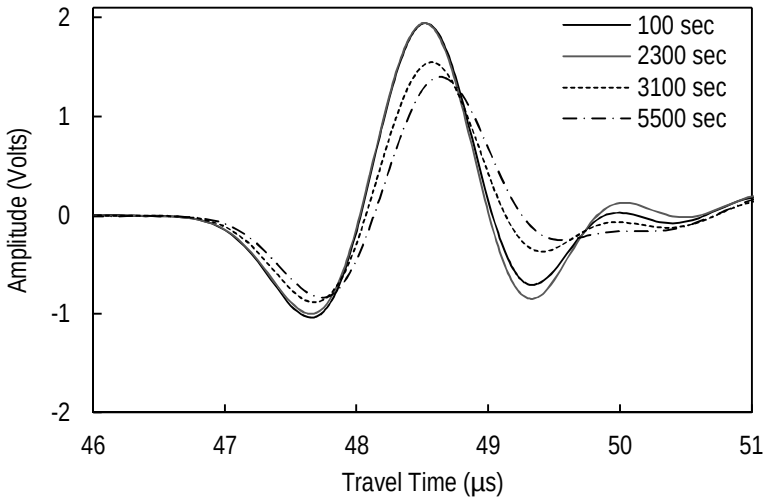

Figure 5-26 Selected transmission arrivals recorded by receiver R4 from source S2 radiations

the fracture. The trends of decreasing amplitude and increasing delay indicate a continuous decrease in the fracture specific stiffness.

These traces are further analysed by plotting their frequency spectra in Figure 5-27. The peak spectral amplitudes are shown by markers in this plot. The plot shows the peak spectral transmission amplitude in the intact sample (100-seconds trace) occurs at a frequency close to 500 KHz. As the fracture intersects the source-receiver line, the peak spectral amplitude and their corresponding frequencies are decreased to about 450 KHz. This familiar trend which was previously observed in the wet synthetic fracture transmission experiments (Figure 5-4) and the numerical transmissions across the smooth-joint fracture (Figure 3-12), indicates the decrease in the hydraulic fracture specific stiffness which in this case, is directly related to the local fracture width at its intersection with S2-R4 line.

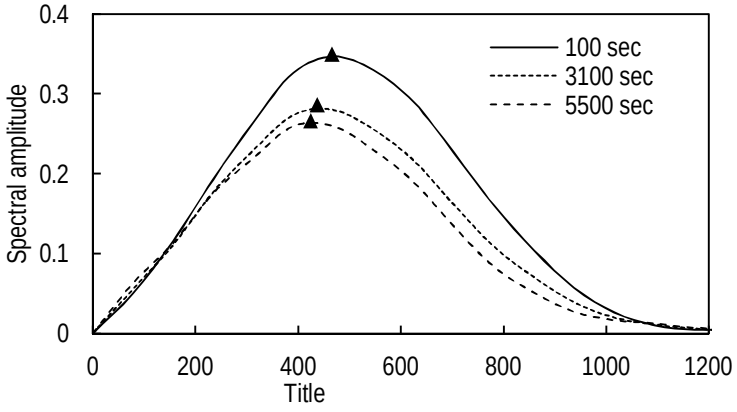

Figure 5-27 Frequency spectra of selected S2-R4 transmissions

5.3.2.3 Transmission Coefficient of Hydraulic Fracture

In order to quantify the hydraulic fracture specific stiffness, a further analysis step was taken on S2-R4 transmission data. The aim was to calculate the spectral transmission coefficients from which the local specific stiffness of the hydraulic fracture can be obtained. To do so, the spectral amplitudes of the transmission recorded across the fracture were divided by their corresponding values from the intact sample record. The process is similar to what followed in Section 3.4.2 for calculation of numerical transmission coefficients.

The top plot in Figure 5-28 shows the calculated spectral transmissions for transmission data recorded at 3100 seconds and 5500 seconds. Shown in the plot are also analytical curves of spectral transmission coefficients predicted by the displacement discontinuity theory for some known fracture specific stiffnesses. It is

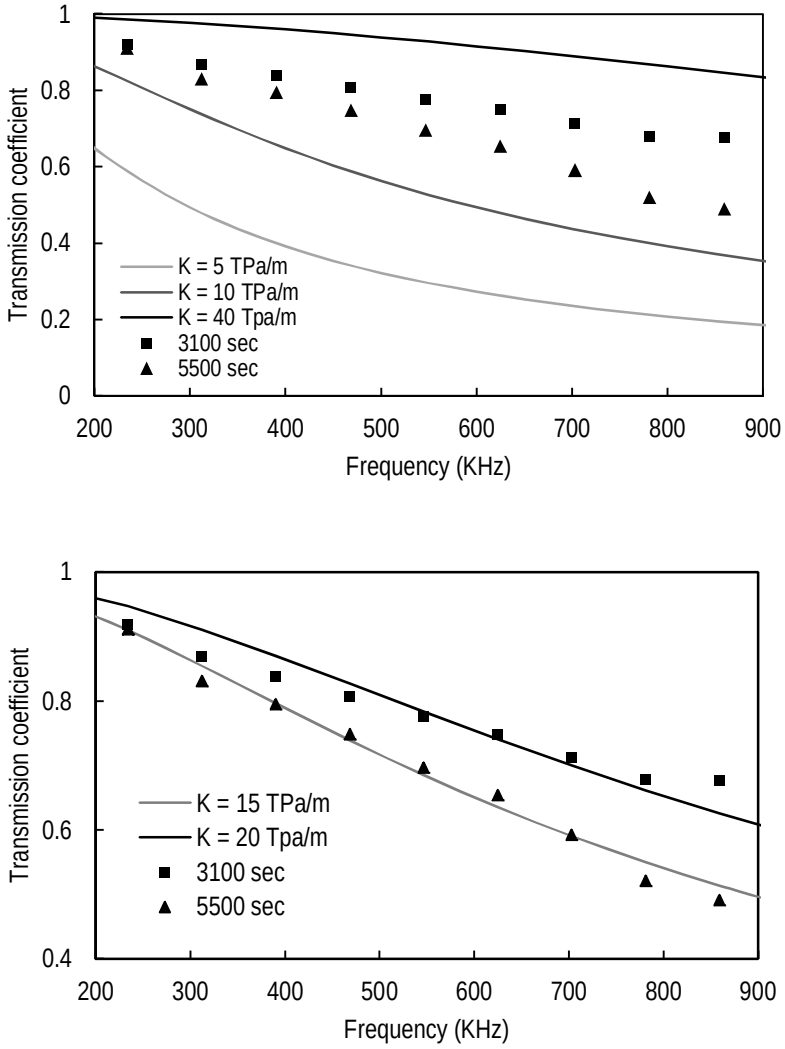

Figure 5-28 Selected experimental spectral transmissions coefficients with analytical curves for fractures with known specific stiffnesses (top) and with best-fit analytical transmission coefficient curves

apparent from the plot that the spectral transmission coefficients of the hydraulic fracture at 3100 seconds are larger than their corresponding values in 5500 seconds, indicating a higher specific stiffness of the fracture at 3100 seconds. In both sets of experimental data, the measured transmission coefficients for low frequency components are higher than those of high frequency components. This trend suggests that similar to rock natural fractures, hydraulic fractures also act as low-pass filters, transferring a higher portion of lower frequency components compared to high frequency components. This trend is also observed in the analytical plots. A comparison of the analytical plots which correspond to fractures with some known specific stiffnesses suggests that the apparent specific stiffness of the hydraulic fracture is somewhere between 10 TPa/m and 40 TPa/m. In order to find the representative specific stiffness for each set of experimental data, the best fit analytical curves were found using a least-squares method.

The best fit analytical plots together with the experimental data are plotted in the bottom graph of Figure 5-28. At 3100 and 5500 seconds the best fit curves correspond to specific stiffnesses of 20 TPa/m and approximately 15 TPa/m, respectively. This plot shows that the match between the experimental transmission coefficients and the analytical predictions is good. This match, however, is not perfect due to several reasons such as the rough surface of the hydraulic fracture, the presence of the fracturing fluid inside the fracture which adds complexity of the viscous effects into the transmission phenomena, and the inelastic behaviour of the fracture and the matrix, all of which violate the assumptions of the displacement discontinuity theory. Nevertheless, such analyses are informative in providing transmission and reflection properties of hydraulic fracture. Furthermore, magnitude and type of the deviations of experimental data from analytical predictions can be used in interpreting the causes for such deviations.

Attributing a specific stiffness to the hydraulic fracture allows a comparison to be made with the synthetic fractures discussed early in this chapter. The range of transmission coefficients for the hydraulic fracture in this experiment can be compared with those measured for the wet synthetic fracture at normal stresses more than 6.9 MPa (see Figure 5-6). As the normal stress applied to the hydraulic fracture was kept at a constant level of only 0.69 MPa, factors other than the normal stress on the fracture must have contributed to increasing the specific stiffness of the hydraulic fracture to a high level.

One of the differences between the hydraulic fracture and the wet synthetic fracture is that the fluid pressure in the hydraulic fracture, at its intersection with S2-R4 line is high, close to 6 MPa. However, in the wet synthetic fracture the fluid has ambient pressure unless it is trapped between the fracture walls under high stresses. Despite these differences, the fluid pressure is not a likely reason for increase in the hydraulic fracture transmission coefficients as the transmission experiment carried out on fracturing fluid under different pressures showed that the effect of a pressure increase up to 6.9 MPa on transmission amplitudes is not significant (see Figure 5-1).

Two other factors that are likely to contribute to enhancing the normal specific stiffness of the hydraulic fracture compared to the wet synthetic fracture are the fracture width and the fracture tensile properties. As the synthetic fracture was generated by pushing two separate cement samples together, it does not have any tensile strength and its tensile stiffness is expected to be considerably lower than the hydraulic fracture which is expected to have some degree of tensile strength at some of its points. Furthermore, it is perhaps prudent to consider the difference between fracture tensile (cohesive) and compressive stiffnesses which are shown to affect the seismic behaviour of fractures (Toomey et al., 2002). The width of the synthetic fracture was in the same order of its surface roughness when it is under high normal stresses. On the other hand, a hydraulic fracture's width is quite different along its length. In the current set-up of the experimental equipment, no independent measurement of the fracture width was possible. It would be useful to add this capability in future by placing some type of linear variable differential transformer (LVDT) in the wellbore. This would allow measurement of the fracture width at least at its opening on the wellbore wall.

The differences observed between the experimental and analytical data suggest that for proper quantification of fracture width which directly affects its transmission and reflection properties, the effect of factors such as the viscous effects of the filling fluid, the fluid pressure and fluid flow, stress concentrations around the fracture, and fracture surface roughness ought to be taken into account. Perhaps, including these factors in a combined analytical model may prove to be cumbersome. This justifies using numerical modelling approaches. The straight hydraulic fracture model presented in Chapter 3 is a good candidate for further study in this subject in that it potentially provides flexibility for including factors such as fluid properties,

fluid pressure, fluid squirt flow, inhomogeneity of the rock matrix, stress concentration around the fracture, and fracture surface asperities and roughness.

5.3.2.4 Diffraction Measurement

While diffractions from the tip of the fracture were recorded in reflection and transmission receivers, some of the transducers used in this experiment were dedicated to recording pure diffractions. For this purpose, they were located on sides of the sample towards which the fracture tip was expected to move (sides D and B in Figure 5-15).

Figure 5-29 shows two-dimensional surface plots of the ultrasonic data recorded by receiver R8 from S1 radiations (top) and recorded by receiver R9 from S2 radiations (bottom). In order to reveal the diffractions from multiple reflection

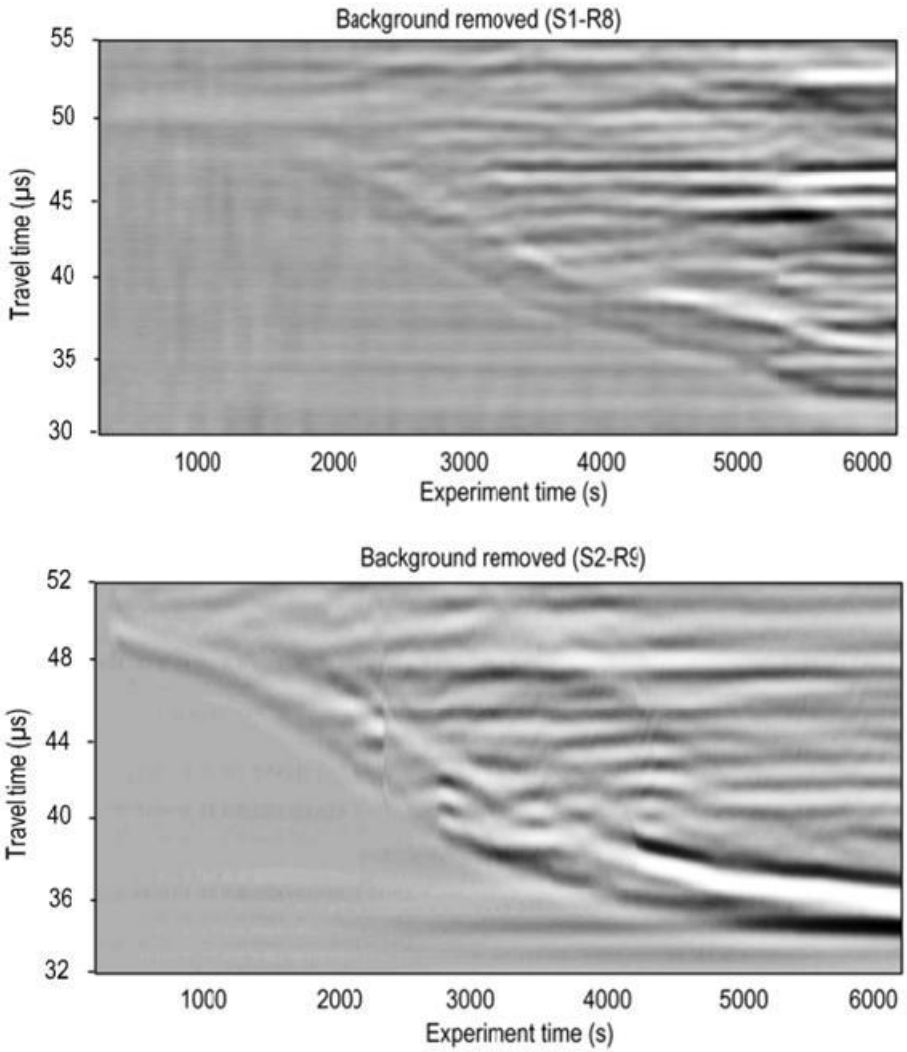

Figure 5-29 Two-dimensional surface plots of background-removed ultrasonic data from S1-R8 (top) and S2-R9 (bottom) transducer pairs

arrivals, background data was removed from the recorded data. According to the configuration shown in Figure 5-15, the top plot is affected by advancement of the hydraulic fracture tip towards side D of the sample while the bottom plot shows the profile of the other tip of the fracture which moves towards side B. The data recorded by receiver R9 seems to have higher quality (bottom plot). At around 2300 seconds of experiment time a sudden drift is observed in the diffraction data, similar to what was picked up earlier by R6 and R4 receivers.

Both plots show similar trends: diffractions from the fracture tips evolve at early moments of the experiments. This is illustrated on the data as a progressively decreasing arrival time event. Note that because of the radiation pattern of the transducers and nearly normal incidence of the diffractions on R8 and R9 transducers, the quality of the recorded diffraction events was much higher in these plots compared to the diffractions previously discussed. Furthermore, no interference occurs between the diffractions and strong reflections or transmissions. As a result, picking diffraction arrival times can be picked with higher accuracy on these plots.

It is seen in both plots that apparently two consecutive diffraction events are captured. The difference in the arrival time of these two successive diffractions varies around two microseconds. This suggests two successive diffraction sources on the fracture which should be approximately 8 mm apart. These events could be due to the fluid lag effect in the laboratory hydraulic fracture which gives rise to the dry and wet fracture tips. Hence, each tip acts as a diffractor of wave energy. Dry and wet fracture tip diffractions were also previously reported in the experimental work of Groenenboom (1998).

Not only receivers R9 and R10 can capture tip diffractions from S2 radiations, data recorded by these receivers from source S1 can also be helpful in the interpretation of possible diffractions (see Figure 5-15). As an example, the data recorded by receiver R10 from S1 radiations are plotted in Figure 5-30. Although the background events have been removed from the data set, the plot still shows a number of complicated events mostly related to boundary-reflections. There are, however, two distinct events with changing travel times observed in this data set. There is an event with a progressively reducing arrival time and another event whose travel time apparently increases with the experiment time. To distinguish these events, their approximate arrival times are marked by dashed lines in the figure. The former event is related to a moving feature of the fracture which constantly becomes

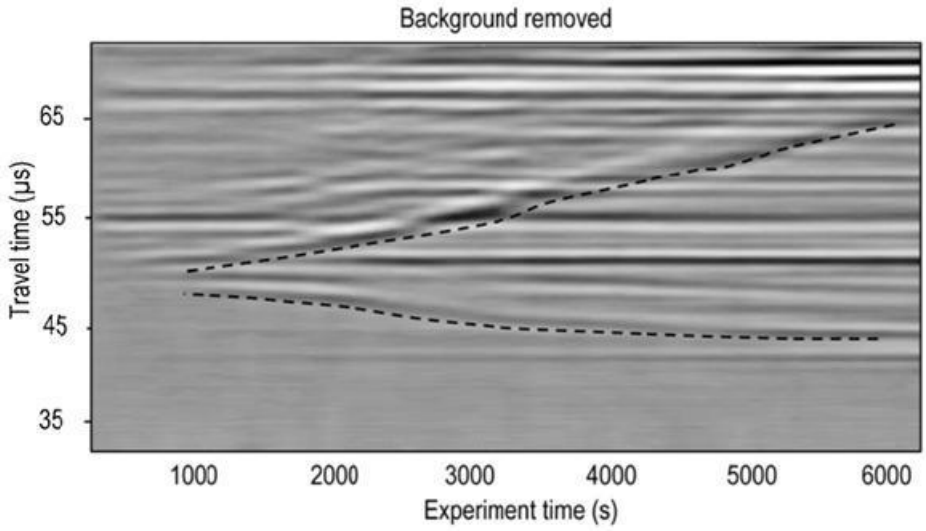

Figure 5-30 Two-dimensional surface plots of background-removed ultrasonic data from S1-R10

closer to the source S10 while the latter represents a feature getting further away from the receiver. This plot resembles the trends that were numerically observed for a propagating hydraulic fracture (e.g. Figure 3-28)

Recalling the configuration of the transducers with respect to the hydraulic fracture, it can be realised that the first event represents the diffractions from the tip of the fracture moving towards side B of the sample. Likewise, the second event represents the diffractions from the other tip of the fracture moving towards side D of the sample. At the early experiment times arrival times of the two events are very close. This is because of the small size of the fracture in the vicinity of the wellbore which results in two close tips both acting as the energy diffractors. It is also observed that the rate of increase in the arrival time of the far tip of the fracture is more than the rate of the decreases in the arrival time of the near tip. This can be explained by considering the special configuration of source, receiver, and fracture tips in this experiment in which an equal progression of the fracture tips results in a more significant change in the travel distance of the far tip diffractions compared to that of the near tip. Such diffraction data sets provide data redundancy for other available diffractions from the same fracture tip.

In an attempt to reconstruct the real-time length profile of the hydraulic fracture, the diffraction travel times where converted to the equivalent travel distances by having knowledge of the compressional wave velocity in the sample. Then, considering the fracture geometry shown in Figure 5-18, representative fracture radii (location of the fracture tip) was calculated. Figure 5-31 shows fracture

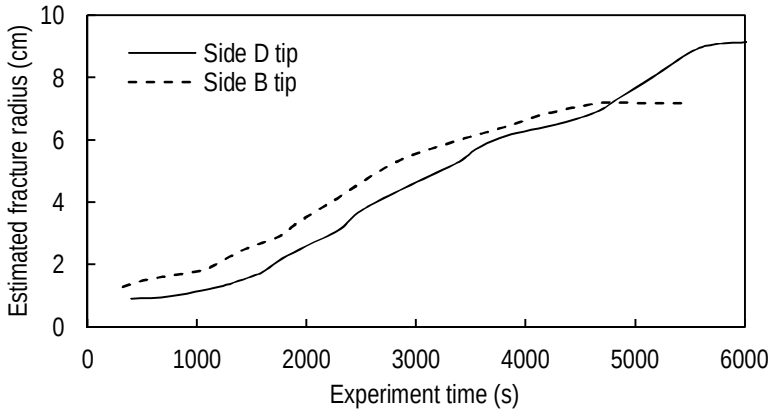

Figure 5-31 Reconstructed real-time fracture radius its wings moving towards side B and side D of the sample

radii estimated from S1-R8 and S2-R9 transducer pairs' diffraction data. The plot shows that the propagation profile of the hydraulic fracture has been almost symmetrical until after 4500 seconds. Afterwards, although the fracture continued to propagate towards side D of the sample, its propagation was stopped at a radius of about 7 cm. As discussed in a previous section, this was also confirmed after breaking the sample and investigating the fracture path (see Figure 5-14). It is worth mentioning that these calculations were carried out assuming that the wave velocity is isotropic in the sample. Measurements carried out along different axes of the sample under anisotropic stresses showed that the wave velocities did not change considerably. Therefore the isotropic wave velocity is a valid assumption in this case. However, depending on the type of the sample used and in reality, depending on the type of formation and underground stress state, velocities can be highly anisotropic which needs to be taken into account in the calculations.

The above data can now be used to quantify the propagation rate of the induced hydraulic fracture. The average propagation rates (speeds) of the fracture wings were calculated and are presented in Figure 5-32. The plot shows a maximum propagation speed of about 1.4 mm/min for the fracture wings. It is worth mentioning again that the accuracy of these calculations are dependent on how accurately the travel times are picked. Furthermore, the fracture does not follow the simplified fracture model presented in Figure 5-18. Therefore, the fracture front even on one of its wings does not necessarily have a linear shape. This adds more complexity to the matter of determining fracture real-time length profile. In the scale

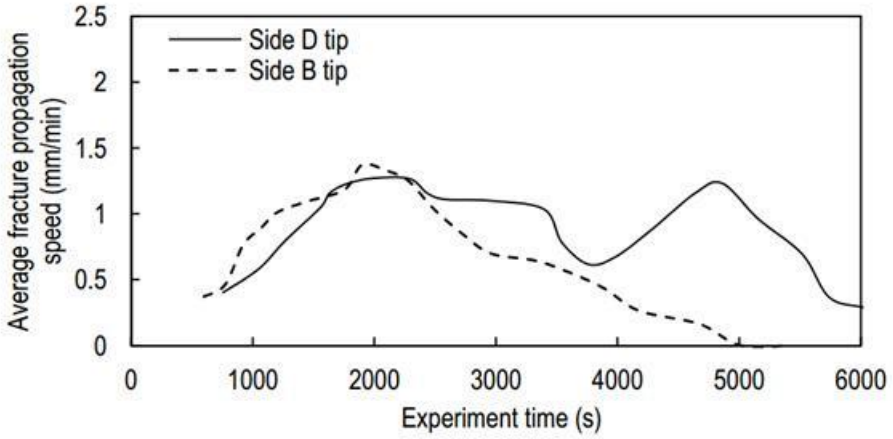

Figure 5-32 Average propagation rate of the fracture wings moving towards side B and D of the sample

of laboratory experiments, placing a number of transducers in a vertical line focusing on one wing of the fracture can help in delineating its profile. For a comprehensive local width profile of the fracture, a similar arrangement but horizontal, is desirable.

Having in-hand enough data from calculations of length and width of a fracture, it is possible to compute the real-time volume of the fracture. This in turns allows comparison of the hydraulic fracturing experimental results with those predicted by available fracture models.

The seismic events studied here have the potential to be used in field hydraulic fracturing operations as a real-time hydraulic fracture monitoring tool. Nevertheless, field conditions do not provide flexibilities available in laboratory experiments for example in terms of data acquisition configuration or injection regimes used. Possible data acquisition configurations include down-hole arrays of source and receivers that can continuously radiate and record seismic waves. Obviously, more experimental work is required in this subject before realisation of the full potential of these methods can occur.

5.4 Summary

Various experimental results obtained in this study, their interpretation, and discussion were presented in this chapter. First of all, the results were presented of ultrasonic transmissions in the fracturing fluid conducted under different pressures. These showed the sensitivity of transmissions to the pressure. In the next step, the results of ultrasonic experiments conducted on dry and wet synthetic fractures were

presented. Different normal stresses were applied to the fractures to change their specific stiffness. The experimental spectral transmission coefficients were plotted and compared with the theoretical values. Best-fit theoretical curves were obtained to determine the representative fracture specific stiffnesses. The results showed the important effect of the fracturing fluid in enhancing transmissions across the fracture particularly at low stresses. The matches between the experimental and theoretical curves were shown to be good.

Next, different sets of experimental data obtained during horizontal and vertical hydraulic fracturing experiments were presented. These included fluid pressures and flow rates for gaining general information on the fracture propagation state, as well as transmission, reflection, and diffraction data. Any change in the amplitude of transmissions and reflections were attributed to the interference of the fracture and the magnitude of these variations was attributed to the local fracture specific stiffness, and hence local fracture width. Spectral transmission coefficients of the hydraulic fracture were calculated and using the best-fit theoretical curves, its representative local specific stiffness was determined in the selected experiment recordings. Changes to the local specific stiffness of the hydraulic fracture were related to the change of its local width. Diffraction arrival times recorded at different receivers were used to estimate the location of the fracture tip. Interference of diffractions with transmissions as well as reflections was observed when the fracture tip became close to the source-receiver line. The real-time fracture length profile and fracture growth rate from both of its wings were generated. Comparison of this data with the injection pressure data indicated the high value of such ultrasonic measurements for detailed monitoring of the fracture growth which is not possible having merely pressure-rate data.

The experimental results presented in this chapter showed the high potential of active seismic monitoring techniques to be employed in field applications. This could include real-time active seismic measurements conducted in the well being fractured, or nearby wells.

6 Conclusions and Recommendations

This work investigated seismic monitoring of hydraulic fracture propagation. Real-time ultrasonic monitoring of a fracture was modelled numerically using a smooth-joint fracture model as well as a hydraulic fracture induced using the fluid-solid coupling capability of the numerical code. Considerable modifications were carried out on the TTSC equipment and a number of ultrasonic experiments were conducted on wet and dry synthetic fractures as well as horizontal and vertical hydraulic fractures. Ultrasonic data was used for monitoring geometrical properties of the hydraulic fracture in real-time. These measurements indicate the capability of active seismic methods to be used as real-time hydraulic fracturing monitoring tools in field operations. The following sections include conclusions made in this study as well as a number of recommendations for further research in this area.

6.1 Numerical Modelling

- The discrete element code, PFC2D, was used for numerical modelling in this study. The code has been rarely used for dynamic modelling of wave propagation. In this research, the wave propagation capability of the code in hexagonal assemblies was systematically verified against validated codes and available analytical solutions. The results of this research introduced the code as a competent tool for further studies on dynamic wave propagation in granular materials.
- The comparison made between the wave propagation in the square and hexagonal particle assemblies showed the dependencies of the seismic

properties of the assemblies (such as P-wave to S-wave velocity ratio) on the micro-structure of assemblies. The differences were also noticeable in the induced micro-normal and shear forces between the particles.

- For the first time, I have shown that the smooth-joint contact model of PFC2D, which conventionally has been used for modelling rock discontinuities in geomechanical applications, exhibits seismic properties in accordance with the displacement discontinuity theory. This includes variations in the amplitude and time delay of transmissions and reflections. Furthermore, numerical spectral transmission and reflection amplitudes and travel times were computed and compared with the corresponding theoretical curves and excellent matches were obtained. The flexibility of this contact model in changing other fracture parameters, such as friction angle and cohesion, makes it a potential tool for further study of discrete fractures in granular materials.
- Ultrasonic monitoring was conducted on a smooth-joint fracture with increasing length but constant specific stiffness. Recorded transmissions, reflections and diffractions were analysed and I have shown that travel times of these events could be used for measuring the length of the fracture. Interference of the fracture with the source-receiver line affects the transmission data and causes reflections from the fracture surface. The moving tip of the smooth-joint fracture acts as a diffractor of the wave energy.
- The effect of the fracture specific stiffness on the P and S diffractions was studied. I observed that the travel time and amplitude of diffractions are highly dependent on the fracture specific stiffness.
- The fluid-solid coupling capability of PFC2D was employed to model initiation and propagation of a straight hydraulic fracture in an arranged particle assembly. The study of the fluid pressure, fracture width profile and redistribution of stresses around the fracture in this arranged particle assembly revealed valuable information on the propagation process of the fracture and the fracture tip effects.
- I performed ultrasonic monitoring within the numerical hydraulic fracture and different events including diffractions, reflections, and transmissions were

recorded and analysed. I noted that the numerical modelling showed how the local fracture width affects its local specific stiffness and hence, its seismic reflection and transmission properties. Furthermore, diffractions from both fracture tips were recorded over the simulation time. These numerical data were indicative in the interpretation of experimental results of hydraulic fracture monitoring.

- The numerical modelling of hydraulic fracture propagation monitoring using the fluid-solid capability of the discrete element code is the first application of its kind. This study established the platform for further investigation of the subject using the discrete element models which allow studying the related phenomena at the micro-scale.

6.2 Experimental Studies

- The unique true triaxial stress cell (TTSC) equipment was used for the first time for hydraulic fracture monitoring experiments. Before conducting the comprehensive hydraulic fracture monitoring experiments, considerable modifications were performed by me on the equipment. I designed special transducer spacers and developed, tested and operated a multi-channel ultrasonic data acquisition system with a source multiplexing capability. As a result of this work, I built the main platform for ultrasonic monitoring of different events, such as hydraulic fracturing, in the geomechanics laboratory of the Department of Petroleum Engineering, Curtin University.
- Ultrasonic transmissions carried out on dry and wet synthetic fractures under different normal stresses showed that the increase in the normal stress enhances transmissions across the fracture, in accordance with displacement discontinuity theory. Furthermore, the filling fluid was shown to improve the transmissions particularly at low stress levels.
- Spectral transmission coefficients of the dry and wet synthetic fractures were computed and compared with the theoretical curves. I found a good match between the dry fracture experimental results and theoretical predictions while the match was not as good in the case of the wet fracture. Using the matched data, the specific stiffnesses of the fractures were computed at

different stress levels. I found that discrepancies between the experimental and theoretical results were attributed to the viscous effects which must in future be taken into account in the theory and modelling.

- Concurrent transmissions and diffractions as well as reflections and diffractions were measured in the laboratory hydraulic fracture monitoring experiments. The very low amplitude of the recorded diffractions were found to be due to geometrical spreading effects and more importantly, the radiation pattern of the transducers.
- As soon as the fracture intersected the source-receiver line, transmission data were reduced in amplitude and were delayed. Furthermore, when the fracture tip was close to the source-receiver lines, interference of the diffractions with the transmissions occurred which may result in anomalously high apparent transmission amplitudes (they were tuned-in as constructive interference).
- The travel time of reflections can be used for measuring the distance of the source-receiver mid-point from the sample boundary. Combining this with the travel time of tip-diffractions results in the construction of the real-time length profile of the fracture.
- The amplitude of reflections and transmissions are sensitive to the specific stiffness of the hydraulic fracture which in turn, is conversely related to the fracture width. Hence, the analysis of these amplitudes can be used for real-time width monitoring of the fracture.
- While pressurising the wellbore in experimental samples and before initiation of the fracture, no change in the ultrasonic data was recorded. This showed the insensitivity of ultrasonic data to the fluid pressure increase and redistribution of the stresses around the wellbore in the experimental samples used in this study.
- Diffractions from the early cracks occurred during the initiation phase of the hydraulic fracture, which can be used as the first indicators of the fracture initiation. The sensitivity of such seismic measurements was more than the fluid pressure measurements, at least under the laboratory conditions at the time.
- Shear wave transmissions across a hydraulic fracture are affected more than compressional wave transmissions due to the inability of shear waves to

transmit in fluid. The slow dimming of shear wave transmission amplitudes over the experiment time indicated the gradual opening of the fracture walls and loss of solid-solid contacts.

- Horizontal and vertical hydraulic fracture monitoring experiments were conducted using the TTSC by employing a number of source and receiver transducers. Transmissions across a fracture, reflections from the fracture surface, and diffractions from the fracture tips were analysed. Transmission and reflections travel times were used to determine the location of the source-receiver mid-point on the fracture.
- For the first time, real-time specific stiffness of the hydraulic fracture was determined by measuring the spectral transmission coefficients and comparison of the results with the theoretical curves. I observed a good match with the trend of theoretical transmission coefficients. The changes in the specific stiffness of the fracture were attributed to the variations in the local width of the fracture. However, the relatively high specific stiffness of the hydraulic fracture compared to the corresponding synthetic fracture at the same normal stress was attributed to the cohesion properties of the hydraulic fracture.
- The diffraction data from both wings of the vertical fracture was used for determination of the initiation moment and propagation profile of the hydraulic fracture, which was shown to be very difficult to determine solely based on fluid pressure data. The data showed how a hydraulic fracture can initially propagate symmetrically and at a later stage change to an asymmetric propagation regime possibly due to inhomogeneities of the sample.
- Different sets of experimental data showed the capability of active seismic measurements for real-time monitoring of hydraulic fracturing operations. Transmissions, reflections, and diffractions can be measured in field applications either in the well being fractured or nearby wells. Further study is required, however, for meaningful up-scaling of laboratory results to field conditions by considering factors such as source wavelength, fracture dimensions, and fracturing fluid properties.

6.3 Recommendations

- The smooth-joint contact model used in this study is an easy-to-use model which can be employed for modelling fractures with different geometrical and physical properties. It allows altering a number of fracture parameters such as friction angle, cohesion, dilation angle and normal and shear bond strengths. Therefore, the use of this model is recommended in future studies of numerical fracture modelling in granular materials. Furthermore, the effect of the above parameters on the seismic properties of a fracture can be investigated in future research.
- The straight hydraulic fracture model which was presented in this study is still at its early stages and there are several aspects in this model which could be further improved for the purpose of hydraulic fracture seismic monitoring. These may include, but are not limited to, the improvement of fluid-solid coupling algorithms, studying the effect of fluid pressure and fluid properties on seismic waves, including and studying different fracture roughnesses at the micro-scale, and studying fluid squirt flow inside the fracture.
- To investigate the ultrasonic events emerging due to initiation and propagation of a fracture in the medium, compressional P-waves radiated from a line source (plane wave) were used. As a further step, similar numerical experiments are recommended to be conducted focusing on source shear wave behaviour. Furthermore, in order to more closely replicate the hydraulic fracturing experiments, it would be advantageous to model wave propagation from a finite line source with a radiation pattern similar to that of the ultrasonic transducers used in the experiments.
- The number of experiments carried out in this study was limited by the allowable time frame of the study. With the unique experimental facility available, it is recommended that more hydraulic fracturing experiments be conducted. The effect of a number of factors can be investigated during hydraulic fracturing monitoring experiments with the current facility. These may include the frequency of the ultrasonic

wave, fracturing fluid properties, injection rate, elastic and strength properties of the sample, grain distribution of the sample, and new source-receiver configurations.

- The current experimental set up does not allow for an independent measurement of the hydraulic fracture width. Therefore, the experimental transmission and reflection data could not be used to directly quantify the fracture width. For this reason, in this work the focus was put on the relative changes in the data. It is recommended that the capability of measuring fracture width be added. This could be achieved by installation of a linear variable differential transformer (LVDT) in the wellbore which would provide a measurement of the fracture at least at the fracture opening in the wellbore wall. A similar configuration was presented by Groenenboom (1998).
- The current ultrasonic data acquisition system is limited to 16 channels. Due to the fact that a slight movement of a sample or transducers may deteriorate data from some of the data channels, and in order to obtain a more comprehensive three-dimensional view of the hydraulic fracture, it is recommended to increase the number of input channels (e.g. to 32 or 48). Such a comprehensive data acquisition not only will provide data redundancy, but also could be used for conducting a tomographic image of the fracture.
- In this study, the first hydraulic fracture monitoring experiments were carried out using the TTSC but only a limited set of shear-wave data was acquired. This was mainly due to the fact that handling P-wave transducers and interpreting their data is less complex than that of S-waves. Nevertheless, the limited S-wave data acquired in the current study showed the usefulness of such data in the determination of the hydraulic fracture state. Therefore, future studies in this area are recommended to be undertaken by acquiring more shear-wave data including different transmissions, reflections and diffraction events.
- Ultrasonic data can be used for measurement of fluid lag and for investigation of the effect of different experimental parameters on the lag length. Such valuable measurements could be compared to the

available fracture models for the purpose of verification or modification of these models.

- The discrepancies observed between the experimental transmission coefficients of the hydraulic fracture and those predicted by the displacement discontinuity theory indicated the requirement for inclusion of more influencing factors in the theoretical model such as the effect of fluid viscosity and cohesion of the fracture on the transmission and reflection amplitudes. More research is also required in this area.

References

Acosta-Colon, A., L. J. Pyrak-Nolte, and D. D. Nolte, 2009, Laboratory-scale study of field of view and the seismic interpretation of fracture specific stiffness: Geophysical Prospecting, v. 57, p. 209-224.

Adachi, J., 2001, Fluid-driven fracture in permeable rock: Ph.D. thesis, University of Minnesota, M.N.

Aki, K., M. Fehler, R. L. Aamodt, J. N. Albright, R. M. Potter, C. M. Pearson, and J. W. Tester, 1982, Interpretation of seismic data from hydraulic fracturing experiments at the Fenton Hill, New Mexico, Hot Dry Rock geothermal site: Journal of Geophysical Research, v. 87, p. 936-944.

Alassi, H. T., 2008, Modeling reservoir geomechanics using discrete element method: Application to reservoir monitoring: Ph.D. thesis, Norwegian University of Science and Technology (NTNU).

Anderson, J. A., C. M. Pearson, A. S. Abou-Sayed, and G. D. Meyers, 1986, Determination of fracture height by spectral gamma log analysis: 61th Annual Conference and Exhibition of the Society of Petroleum Engineers.

Arslan, A., S. M.P.J., J. J. Walsh, and C. Childs, 2010, The impact of strain, bedding plane friction and overburden pressure on joint spacing, EGU General Assembly Vienna, Austria.

Bai, Z., and S. C. Wu, 2011, Impact of joint inclination and confining pressure on strength of sandstone: Rock Mechanics: Achievements and Ambitions, p. 261-264.

Barree, R. D., M. K. Fisher, and R. A. Woodroof, 2002, A practical guide to hydraulic fracture diagnostic technologies: SPE Annual Technical Conference and Exhibition.

Bennett, L., J. Le Calvez, D. R. Sarver, K. Tanner, W. S. S. Birk, G. Waters, J. Drew, G. Michaud, P. Primiero, L. Eisner, R. Jones, D. Leslie, M. J. Williams, J. Govenlock, R. C. Klem, and K. Tezuka, 2006, The source for hydraulic fracture characterization: Oilfield Review, v. 17, p. 42-57.

Boadu, F. K., and L. T. Long, 1996, Effects of fractures on seismic-wave velocity and attenuation: Geophysical Journal International, v. 127, p. 86-110.

Board, M., T. Rorke, G. Williams, and N. Gay, 1991, Fluid injection for rockburst control in deep mining: The 33rd U.S. symposium on rock mechanics.

Bouchon, M., 1987, Diffraction of elastic waves by cracks or cavities using the discrete wavenumber method: The Journal of the Acoustical Society of America, v. 81, p. 1671-1676.

Brown, S. R., and C. H. Scholz, 1986, Closure of rock joints: Journal of Geophysical Research, v. 91, p. 4939-4948.

Burns, D. R., M. E. Willis, M. N. Toksöz, and L. Vetri, 2007, Fracture properties from seismic scattering: The Leading Edge, v. 26, p. 1186-1196.

Cai, J. G., and J. Zhao, 2000, Effects of multiple parallel fractures on apparent attenuation of stress waves in rock masses: International Journal of Rock Mechanics and Mining Sciences, v. 37, p. 661-682.

Case, S., and Y. Horie, 2007, Discrete element simulation of shock wave propagation in polycrystalline copper: Journal of the Mechanics and Physics of Solids, v. 55, p. 589-614.

Champoux, Y., M. R. Stinson, and G.A. Daigle, 1991, Air-based system for the measurement of porosity: Journal of Acoustic Society of America, v. 89(2), p. 910-916.

Chen, S. G., and J. Zhao, 1998, A study of UDEC modelling for blast wave propagation in jointed rock masses: International Journal of Rock Mechanics and Mining Sciences, v. 35, p. 93-99.

Cleary, M. P., D. E. Johnson, H. H. Kogsbøll, K. A. Owens, K. F. Perry, C. J. de Pater, A. Stachel, H. Schmidt, and M. Tambini, 1993, Field implementation of proppant slugs to avoid premature screen-out of hydraulic fractures with adequate proppant concentration: Low Permeability Reservoirs Symposium.

Coates, R. T., and M. Schoenberg, 1995, Finite-difference modelling of faults and fractures: Geophysics, v. 60, p. 1514-1526.

Cohen, C. E., W. Xu, X. Weng, and P. Tardy, 2012, Production forecast after hydraulic fracturing in naturally fractured reservoirs: coupling a complex fracturing simulator and a semi-analytical production model: SPE Hydraulic Fracturing Technology Conference.

Crampin, S., 1984, Effective anisotropic elastic constants for wave propagation through cracked solids: Geophysical Journal of the Royal Astronomical Society, v. 76, p. 135-145.

Crampin, S., 1988, Implications of temporal changes in shear-wave splitting: SEG Annual Meeting.

Cundall, P. A., 1971, A computer model for simulating progressive, large-scale movements in blocky rock systems: Symposium of International Society of Rock Mechanics.

Cundall, P. A., and O. D. L. Strack, 1979, A discrete numerical model for granualr assemblies: Géotechnique, v. 29, p. 47-65.

De La Pena, A., L. Eisner, M. P. Thornton, and S. Williams-Stroud, 2010, Detetection of mechanical failure during hyraulic fracturing through passive seismic microseismic monitoring: 72nd EAGE Conference & Exhibition incorporating SPE EUROPEC 2010.

Derov, A., G. Maximov, M. Lazarkov, B. Kashtan, and A. Bakulin, 2009, Characterizing hydraulic fractures using slow waves in the fracture and tube waves in the borehole: 2009 SEG Annual Meeting.

Desroches, J., Detournay, E., Lenoach, B., Papanastasiou, P., Pearson, J. R. A., Thiercelin M., and Cheng, A., 1994, The Crack Tip Region in Hydraulic Fracturing, Proc. R. Soc. Lond. A 8 October, vol. 447 no. 1929 39-48

Dobroskok, A. A., and A. M. Linkov, 2008, Simulation of seismicity accompanying hydraulic fracture propagation: the 42nd US Rock Mechanics Symposium and 2nd U.S.-Canada Rock Mechanics Symposium.

Fakhimi, A., F. Carvalho, T. Ishida, and J. Labuz, 2002, Simulation of failure around a circular opening in rock: International Journal of Rock Mechanics and Mining Sciences, v. 39, p. 507-515.

Falls, S. D., R. P. Young, S. R. Carlson, and T. Chow, 1992, Ultrasonic tomography and acoustic emission in hydraulically fractured Lac du Bonnet grey granite: Journal of Geophysical Research, v. 97, p. 6867-6884.

Groenenboom, J., 1998, Acoustic monitoring of hydraulic fracture growth: Ph.D. thesis, Delft University of Technology, Delft.

Groenenboom, J., and J. Falk, 2000, Scattering by hydraulic fractures: Finite difference modelling and laboratory data: Geophysics, v. 65, p. 612-622.

Groenenboom, J., and J. T. Fokkema, 1998, Monitoring the width of hydraulic fractures with acoustic waves: Geophysics, v. 63, p. 139-148.

Groenenboom, J., D. B. van Dam, and C. J. de Pater, 2001, Time-lapse ultrasonic measurements of laboratory hydraulic-fracture growth: tip behavior and width profile: SPE Journal, p. 14-24.

Gu, B., K. T. Nihei, and L. R. Myer, 1997, Numerical investigation of fracture interface waves: Journal of the Acoustical Society of America, v. 102, p. 120-127.

Gu, B., K. T. Nihei, L. R. Myer, and L. J. Pyrak-Nolte, 1996a, Fracture interface waves: Journal of Geophysical Research, v. 101, p. 827-835.

Gu, B., R. Suarez-Rivera, K. T. Nihei, and L. R. Myer, 1996b, Incidence of plane waves upon a fracture: Journal of Geophysical Research, v. 101, p. 25337-25346.

Hainey, B. W., R. G. Keck, M. B. Smith, K. W. Lynch, and J. W. Barth, 1999, On-site fracturing disposal of oilfield-waste solids in Wilmington Field, California: SPE Production & Facilities, v. 14, p. 88-93.

Hall, F., and Y. Wang, 2012, Seismic response of fractures by numerical simulation: Geophysical Journal International, v. 189, p. 591-601.

Han, Y., Damjanac, B, Nagel, N., 2012, A Microscopic Numerical System For Modeling Interaction Between Natural Fractures And Hydraulic Fracturing, 46th U.S. Rock Mechanics/Geomechanics Symposium, June 24 - 27, 2012 , Chicago, Illinois

Hazzard, J. F., S. C. Maxwell, and R. P. Young, 1998, Micromechanical modelling of acoustic emissions, Rurorock 98 Conference on Rock Mechanics, Trondheim, Norway, p. 519-525.

Hazzard, J. F., and R. P. Young, 2004, Dynamic modelling of induced seismicity: International Journal of Rock Mechanics and Mining Sciences, v. 41, p. 1365-1376.

Hazzard, J. F., R. P. Young, and S. Maxwell, 2000, Micromechanical modeling of cracking and failure in brittle rocks: Journal of Geophysical Research, v. 105, p. 16,683-16,697.

Hazzard, J. F., R. P. Young, and S. J. Oates, 2002, Numerical modeling of seismicity induced by fluid injection in a fractured reservoir: Fifth North American Rock Mechanics Symposium, p. 1023-1030.

Henry, F., 2005, Characterization of borehole fractures by the body and interface waves: Ph.D. thesis, Delft University.

Holditch, S. A., D. L. Holcomb, and Z. Rahim, 1993, Using tracers to evaluate propped fracture width: Eastern Regional Conference & EXhibition.

Hoover, W. G., W. T. Ashurst, and R. J. Olness, 1974, Two-dimensional computer studies of crystal stability and fluid viscosity: The Journal of Chemical Physics, v. 60, p. 4043-4047.

Hornby, B. E., D. L. Johnson, K. W. Winkler, and R. A. Plumb, 1989, Fracture evaluation using reflected Stoneley-wave arrivals: Geophysics, v. 54, p. 1274-1288.

House, N., and J. Shemata, 2008, Understanding hydraulic fractures in tight-gas sands through the integration of borehole microseismic data, three-dimensional surface seismic data, and three-dimensional vertical seismic

profile data: a Jonah Field case study: 2005 Vail Hedberg Conference: AAPG Hedberg Series, p. 77-86.

Hudson, J. A., 1981, Wave speed and attenuation of elastic waves in material containing cracks: Geophysical Journal of the Royal Astronomical Society, v. 64, p. 133-150.

Hunt, J. L., K. Frazier, B. P. Pendergraft, and M. Y. Soliman, 1994, Evaluation and completion procedure for produced brine and waste water disposal wells: Journal of Petroleum Science and Engineering, v. 11, p. 51-60.

Ionov, A. M., 2007, Stoneley wave generation by an incident P-wave propagating in the surrounding formation across a horizontal fluid-filled fracture: Geophysical Prospecting, v. 55, p. 71-82.

Itasca Consulting Group, I., 2008, PFC2D-Particle Flow Code in two dimensions, Minneapolis, Minnesota.

Jeffrey, R. G., 1989, The combined effect of fluid lag and fracture toughness on hydraulic fracture propagation: Low Permeability Reservoirs Symposium and Exhibition.

Johnson, R., M. Scott, R. Jeffrey, Z. Chen, L. Bennett, C. Vandenborn, and S. Tcherkashnev, 2010, Evaluating hydraulic fracture effectiveness in a coal seam gas reservoir from surface tiltmeter and microseismic monitoring: SPE Annual Technical Conference and Exhibition.

Keck, R. G., and R. J. Withers, 1994, A field demonstration of hydraulic fracturing for solids waste injection with real-time passive seismic monitoring, SPE 69th Annual Technical Conference and Exhibition, New Orleans, L.A.

King, M. S., L. R. Myer, and J. J. Rezowalli, 1986, Experimental studies of elastic-wave propagation in a columnar-jointed rock mass: Geophysical Prospecting, v. 34, p. 1185-1199.

Kleinberg, R. L., E. Y. Chow, T. J. Plona, and M. Orton, 1984, Sensitivity and reliability of two fracture detection techniques for borehole application: Journal of Petroleum Technology, v. 36, p. 657-663.

Kostek, S., D. L. Johnson, K. W. Winkler, and B. E. Hornby, 1998, The interaction of tube waves with borehole fractures; Part II, Analytical models: Geophysics, v. 63, p. 809-815.

Le Calvez, J., M. Craven, R. Klem, J. Baihly, L. Bennett, and K. Brook, 2007, Real-time microseismic monitoring of hydraulic fracture treatment: a tool to improve completion and reservoir management: SPE Hydraulic Fracturing Technology Conference.

Lecampion, B., R. Jeffrey, E. Detournay, 2005, Resolving the geometry of hydraulic fractures from tilt measurements: Pure and Applied Geophyiscs, 162(12), p.2433-2452.

Legarth, B., E. Huenges, and G. Zimmermann, 2005, Hydraulic fracturing in a sedimentary geothermal reservoir: Results and implications: International Journal of Rock Mechanics and Mining Sciences, v. 42, p. 1028-1041.

Lenoach, B., 1995, The crack tip solution for hydraulic fracturing in a permeable solid: Journal of the Mechanics and Physics of Solids, v. 43, p. 1025-1043.

Lhomme, T. P., 2005, Initiation of hydraulic fractures in natural sandstones: Ph.D. thesis, Delft Universit of Technology.

Lhomme, T. P., C. J. de Pater, and P. H. Helfferich, 2002, Experimental study of hydraulic fracture initiation in Colton sandstone: SPE/ISRM Rock Mechanics Conference.

Li, L., and E. Fjær, 2008, Investigation of the stress-dependence of static and dynamic moduli of sandstones using a discrete element method: 42th US Rock Mechanics Symposium and 2nd US-Canada Rock Mechanics Symposium.

Li, L., and R. M. Holt, 2002, Particle scale reservoir mechanics: Oil & Gas Science and Technology-Rev. IFP, v. 57, p. 525-538.

Liu, E., S. Crampin, and J. H. Queen, 1991, Fracture detection using crosshole surveys and reverse vertical seismic profiles at the Conoco Borehole Test Facility, Oklahoma: Geophysical Journal International, v. 107, p. 449-463.

Liu, O. Y., 1985, Fracture evaluation using borehole sonic velocity measurements: SPE 60th Annual Technical Conference and Exhibition.

Lubbe, R., J. Sothcott, M. H. Worthington, and C. McCann, 2008, Laboratory estimates of normal and shear fracture compliance: Geophysical Prospecting, v. 56, p. 239-247.

Lubbe, R., and M. H. Worthington, 2006, A field investigation of fracture compliance: Geophysical Prospecting, v. 54, p. 319-331.

Luthi, S. M., and P. M. Souhaite, 1990, Fracture apertures from electrical borehole scans, SEG Annual Meeting, San Francisco, California.

Majer, E. L., J. E. Peterson, T. Daley, B. Kaelin, L. Myer, J. Queen, P. D'Onfro, and W. Rizer, 1997, Fracture detection using crosswell and single well surveys: Geophysics, v. 62, p. 495-504.

Mal, A. K., 1970, Interaction of elastic waves with a penny-shaped crack: International Journal of Engineering Science, v. 8, p. 381-388.

Mas Ivars, D., M. E. Pierce, C. Darcel, J. Reyes-Montes, D. O. Potyondy, R. Paul Young, and P. A. Cundall, 2011, The synthetic rock mass approach for jointed rock mass modelling: International Journal of Rock Mechanics and Mining Sciences, v. 48, p. 219-244.

Maximov, G. A., A. Derov, D. Lesonen, B. Kashtan, and M. Lazarkov, 2010, Active monitoring of hydraulic fractures using slow waves in the fracture and tube waves in the borehole: American Geophysical Union, Fall Meeting, p. 2128.

Maxwell, S., C. Waltman, N. Warpinski, M. Mayerhofer, and N. Boroumand, 2009, Imaging seismic deformation induced by hydraulic fracture complexity: SPE Reservoir Evaluation & Engineering, v. 21, p. 48-52.

Meadows, M. A., and D. F. Winterstein, 1994, Seismic detection of a hydraulic fracture from shear-wave VSP data at Lost Hills Field, California: Geophysics, v. 59, p. 11-26.

Medlin, W. L., and L. Masse, 1984, Laboratory experiments in fracture propagation: SPE Journal, v. 24, p. 256-268.

Medlin, W. L., and D. P. Schmitt, 1994, Fracture diagnostics with tube wave reflection logs: Journal of Petroleum Technology, v. 46, p. 239-248.

Meng, C., 2010, Interaction between hydraulic fracturing process and pre-existing natural fractures: Ph.D. thesis, Delft University of Technology.

Meng, C., and C. J. de Pater, 2011, Hydraulic fracture propagation in pre-fractured natural rocks: SPE Hydraulic Fracturing Technology Conference.

Molenaar, M., D. Hill, P. Webster, E. Fidan, and B. Birch, 2011, First downhole application of distributed acoustic sensing (DAS) for hydraulic fracturing monitoring and diagnostics: SPE Hydraulic Fracturing Technology Conference and Exhibition.

Möllhoff, M., and C. Bean, 2009, Validation of elastic wave measurements of rock fracture compliance using numerical discrete particle simulations: Geophysical Prospecting, v. 57, p. 883-895.

Möllhoff, M., C. Bean, and P. Meredith, 2010, Rock fracture compliance derived from time delays of elastic waves: Geophysical Prospecting, v. 58, p. 1111-1121.

Morris, R. L., D. R. Grine, and T. E. Arkfeld, 1964, Using compressional and shear acoustic amplitude for the location of fractures: Journal of Petroleum Technology, v. 16, p. 623-632.

Mouraille, O., and S. Luding, 2008, Sound wave propagation in weakly polydisperse granular materials: Ultrasonics, v. 48, p. 498-505.

Myer, L. R., D. Hopkins, and N. G. W. Cook, 1985, Effects of contact area of an interface on acoustic wave transmission: 26th U.S. Symposium on Rock Mechanics.

Nabipour, A., B. Evans, T. Müller, and M. Sarmadivaleh, 2011, Evaluation of PFC2D for Modeling Seismic Monitoring of Hyraulic Fracture: 2nd International FLAC/DEM Symposium.

Nabipour, A., B. Evans, T. Müller, M. Sarmadivaleh, 2011a, Numerical and Experimental Study of Hydraulic Fracture Active Source Monitoring", EAGE 2011, Vienna, Austria.

Nabipour, A., B. Evans, M. Sarmadivaleh, 2011, Active Monitoring of a Hydraulic Fracture Propagation: Experimental and Numerical Study, APPEA Journal, 2011.

Nabipour, A., M. Sarmadivaleh, M. S. Asadi, J. Sabogal, and V. Rasouli, 2010, A DEM study on perforation induced damaged zones and penetration length in sandstone reservoirs: 44th U.S. Rock Mechanics Symposium and 5th U.S.-Canada Rock Mechanics Symposium.

Nakagawa, S., K. T. Nihei, and L. R. Myer, 2000, Shear-induced conversion of seismic waves across single fractures: International Journal of Rock Mechanics and Mining Sciences, v. 37, p. 203-218.

National Instruments, 2003, LabVIEW User Manual, April 2003 Edition, Austin, Texas.

Newberry, B. M., R. F. Nelson, and U. Ahmed, 1985, Prediction of vertical hydraulic fracture migration using compressional and shear wave slowness: SPE/DOE 1985 Low Permeability Gas Reservoirs.

Nikitin, A., A. Pasynkov, G. Makarychev, J. Maniere, R. S. Kalyanaraman, and S. Tcherkashnev, 2006, Differential cased hole sonic anisotropy for evaluation of propped fracture geometry in Western Siberia, Russia: SPE Russian Oil and Gas Technical Conference and Exhibition.

O'Connell, R. J., and B. Budiansky, 1974, Seismic velocities in dry and saturated cracked solids: Journal of Geophysical Research, v. 79, p. 5412-5426.

O'Brien, G. S., and C. J. Bean, 2004, A 3D discrete numerical elastic lattice method for seismic wave propagation in heterogeneous media with topography: Geophysical Research Letters, v. 31, p. L14608.

O'Brien, G. S., C. J. Bean, and H. Tapamo, 2009, Dispersion analysis and computational efficiency of elastic lattice methods for seismic wave propagation: Computers & Geosciences, v. 35, p. 1768-1775.

Orlowsky, B., E. H. Saenger, Y. Guéguen, and S. Shapiro, 2003, Effects of parallel crack distributions on effective elastic properties-A numerical study: International Journal of Fracture, v. 124, p. 171-178.

Paige, R. W., L. R. Murray, and J. D. M. Roberts, 1995, Field application of Hydraulic Impedance Testing for fracture measurement: SPE Production & Facilities, v. 10, p. 7-12.

Peterman, F., D. McCarley, K. Tanner, J. Le Calvez, W. Grant, C. F. Hals, L. Bennett, and J. C. Palacio, 2005, Hydraulic fracture monitoring as a tool to improve reservoir management: SPE Production and Operations Symposium.

Pierce, M., D. Mas Ivars, and B. Sainsbury, 2009, Use of synthetic rock masses (SRM) to investigate jointed rock mass strength and deformation behavior: International Conference on Rock Joints and Jointed Rock Masses.

Pointer, T., E. Liu, and J. A. Hudson, 1998, Numerical modelling of seismic waves scattered by hydrofractures: application of the indirect boundary element method: Geophysical Journal International, v. 135, p. 289-303.

Potyondy, D. O., and P. A. Cundall, 2004, A bonded-particle model for rock: International Journal of Rock Mechanics and Mining Sciences, v. 41, p. 1329-1364.

Potyondy, D. O., and J. F. Hazzard, 2008, Effects of stress and induced cracking on the static and dynamic moduli of rock: First International FLAC/DEM Symposium on Numerical Modeling.

Pyrak-Nolte, L. J., 1996, The seismic response of fracture and the interrelations among fracture properties: International Journal of Rock Mechanics and Mining Sciences & Geomechanics Abstracts, v. 33, p. 787-802

Pyrak-Nolte, L. J., N. G. W. Cook, and L. R. Myer, 1987a, Seismic visibility of fractures: The 28th U.S. Symposium on Rock Mechanics (USRMS).

Pyrak-Nolte, L. J., L. R. Myer, and N. G. W. Cook, 1990a, Anisotropy in seismic velocities and amplitudes from multiple parallel fractures: Journal of Geophysical Research, v. 95, p. 11345-11358.

Pyrak-Nolte, L. J., L. R. Myer, and N. G. W. Cook, 1990b, Transmission of seismic waves across single natural fractures: Journal of Geophysical Research, v. 95, p. 8617-8638.

Pyrak-Nolte, L. J., L. R. Myer, N. G. W. Cook, and P. A. Witherspoon, 1987b, Hydraulic and mechanical properties of natural fractures in low permeability rock: 6th ISRM Congress.

Pyrak-Nolte, L. J., and D. D. Nolte, 1992, Frequency dependence of fracture stiffness: Geophysical Research Letters, v. 19, p. 325-328.

Pyrak-Nolte, L. J., S. Roy, and B. L. Mullenbach, 1996a, Interface waves propagated along a fracture: Journal of Applied Geophysics, v. 35.

Pyrak-Nolte, L. J., S. J. Roy, and C. J. Neumann, 1996b, Incipient interface waves used to monitor rock failure, 2nd North American Rock Mechanics Symposium, Montreal, Quebec, Canada.

Pyrak-Nolte, L. J., F. J. Wu, and B. C. Abell, 2011, Using fracture interfaces waves to characterize fractures and fracture intersections: 45th US Rock Mechanics / Geomechanics Symposium.

Pyrak, L. J., 1988, Seismic visibility of fractures: Ph.D. thesis, University of California, Berkeley.

Raaen, A. M., E. Skomedal, H. Kjørholt, P. Markestad, and D. Økland, 2001, Stress determination from hydraulic fracturing tests: the system stiffness approach: International Journal of Rock Mechanics and Mining Sciences, v. 38, p. 529-541.

Raymond, L. J., 1996, The application of hydraulic fracturing models to characterize fracture treatments in the Brushy Canyon formation, Delaware group, Eddy County, New Mexico: Permian Basin Oil & Gas Recovery Conference.

Reis, J. C., K. Fisher, and D. Holcomb, 1996, Measuring hydraulic fracture width behind casing using a radioactive proppant: SPE Formation Damage Control Symposium

Renshaw, C. E., and D. D. Pollard, 1995, An experimentally verified criterion for propagation across unbounded frictional interfaces in brittle, linear elastic materials: International Journal of Rock Mechanics and Mining Sciences & Geomechanics Abstracts, v. 32, p. 237-249.

Resende, R., L. N. Lamas, J. V. Lemos, and R. Calçada, 2010, Micromechanical modelling of stress waves in rock and rock fractures: Rock Mechanics and Rock Engineering, v. 43, p. 741-761.

Sadd, M. H., G. Adhikari, and F. Cardoso, 2000, DEM simulation of wave propagation in granular materials: Powder technology, v. 109, p. 222-233.

Sadd, M. H., Q. Tai, and A. Shukla, 1993, Contact law effects on wave propagation in particulate materials using distinct element modeling: International journal of non-linear mechanics, v. 28, p. 251-265.

Sarmadivaleh, M., 2012, Experimental and numerical study of interaction of a pre-existing natural interface and an induced hydraulic fracture: Ph.D. thesis, Curtin University, Perth, Australia.

Sarmadivaleh, M., M. Rasouli, and N. Nabipour, 2011, A PFC2D simulation of hydraulic fracture and natural interface interaction: 2nd International FLAC/DEM Symposium.

Sasaki, S., 1998, Characteristics of microseismic events induced during hydraulic fracturing experiments at the Hijiori hot dry rock geothermal energy site, Yamagata, Japan: Tectonophysics, v. 289, p. 171-188.

Savic, M., 1995, Ultrasonic scattering from a hydraulic fracture: theory, computation and experiment: Ph.D. thesis, Delft University of Technology, Delft.

Savic, M., M. J. Cockram, and A. M. Ziolkowski, 1993, Active ultrasonic monitoring of laboratory-scale hydraulic fracturing experiments: numerical modelling vs. experiment, Offshore European Conference, Aberdeen.

Savic, M., A. M. Ziolkowski, and M. Cockram, 1991, Acoustic monitoring of laboratory scale dynamic processes under high pressure: SEG Annual Meeting.

Savic, M., A. M. Ziolkowski, and J. H. M. Hoogeveen, 1990, Hydraylic fractures - numerical and physical modelling, 52nd EAGE Meeting, Copenhagen, Denmark.

Schoenberg, M., 1980, Elastic wave behaviour across linear slip interfaces: Journal of the Acoustical Society of America v. 68, p. 1516-1521.

Schoenberg, M., and M. Sayers, 1995, Seismic anisotropy of fractured rock: Geophysics, v. 60, p. 204-211.

Scott, M., R. Johnson, A. Datey, C. Vandenborn, and R. Woodroof, 2010, Evaluating hydraulic fracture geometry from sonic anisotropy and radioactive tracer logs, SPE Asia Pacific Oil & Gas Conference and Exhibition, Brisbane, Australia.

Shukla, A., 1991, Dynamic photoelastic studies of wave propagation in granular media: Optics and Lasers in Engineering, v. 14, p. 165-184.

Sierra, J., J. Kaura, D. Gualtieri, G. Glasbergen, D. Sarker, and D. Johnson, 2008, DTS monitoring of hydraulic fracturing: experiences and lessons learned, SPE Annual Technical Conference and Exhibition, Denver, Colorado.

Swolfs, H. S., C. E. Brechtel, W. F. Brace, and H. R. Pratt, 1981, Field mechanical properties of a jointed sandstone: Geophysical Monograph Series, v. 24, p. 161-172.

Tang, X. M., and C. H. Cheng, 1989, A dynamic model for fluid flow in open borehole fractures: Journal of Geophysical Research, v. 94, p. 7567-7576.

Tang, X. M., and C. H. Cheng, 1993, Borehole Stoneley wave propagation across permeable structures: Geophysical Prospecting, v. 41, p. 165-187.

Thiercelin, M, 1993, On The Modelling Of Near Tip Processes In Hydraulic Fractures, The 34th U.S. Symposium on Rock Mechanics (USRMS), June 28 - 30, 1993 , Madison, WI

Thomas, C. N., S. Papargyri-Beskou, and G. Mylonakis, 2009, Wave dispersion in dry granular materials by the distinct element method: Soil Dynamics and Earthquake Engineering, v. 29, p. 888-897.

Toksoz, N. M., Y. Li, and J. M. Lee, 1996, Seismic imaging of fractures in geothermal reservoirs: Energy Conversion Engineering Conference, IECEC 96., Proceedings of the 31st Intersociety, p. 1647-1652 v.

Toomey, A., 2001, Particle-based numerical modelling of seismic wave propagation in fractured rock: Ph.D. thesis, University College, Belfield, Dublin, Dublin.

Toomey, A., C. Bean, and O. Scotti, 2002a, Fracture properties from seismic data- A numerical investigation: Geophysical Research Letters, v. 29.

Toomey, A., and C. J. Bean, 2000, Numerical simulation of seismic waves using a discrete particle scheme: Geophysical Journal International, v. 141, p. 595-604.

Toomey, A., C. J. Bean, and O. Scotti, 2002b, Effect of nonlinear surface interaction on seismic response of a fracture: SEG International Exhibition and 27nd Annual Meeting.

Vinegar, H. J., P. B. Wills, D. C. DeMartini, J. Shlyapobersky, W. F. J. Deeg, R. G. Adair, J. C. Woerpel, J. E. Fix, and G. G. Sorrells, 1992, Active and passive seismic imaging of a hydraulic fracture in diatomite: Journal of Petroleum Technology, v. 44, p. 28-34.

Vlastos, S., E. Liu, I. G. Main, and C. Narteau, 2007, Numerical simulation of wave propagation in 2-D fractured media: scattering attenuation at different stages of the growth of a fracture population: Geophysical Journal International, v. 171, p. 865-880.

Willis, M. E., D. R. Burns, K. M. Willis, N. J. House, and J. E. Shemeta, 2008, Hydraulic fracture quality from time lapse VSP and microseismic data: SEG Annual Meeting

Willis, M. E., K. M. Willis, D. R. Burns, J. E. Shemeta, and N. J. House, 2009, Fracture quality images from 4D VSP and microseismic data at Jonah Field, WY: SEG Annual Meeting.

Wills, P., D. DeMartini, H. Vinegar, J. Shlyapobersky, W. Deeg, J. Woerpel, G. Sorrells, and R. Adair, 1992, Active and passive imaging of hydraulic fractures: The Leading Edge, v. 11, p. 15-22.

Yoon, J., Backers, T., Dresen, G., 2012, Prototype PFC2D model for simulation of hydraulic fracturing and induced seismicity, Eurock 2012, Stokholm

Yu, T. R., and W. M. Telford, 1973, An ultrasonic system for fracture detection in rock faces: Canadian Mining and Metallurgical Bulletin v. 66, p. 96-101.

Zemanek, J., E. E. Glenn, L. J. Norton, and R. L. Caldwell, 1970, Formation evaluation by inspection with the borehole televiewer: Geophysics, v. 35, p. 254-269.

Zhao, X., and R. Young, 2009, Numerical Simulation of Seismicity Induced by Hydraulic Fracturing in Naturally Fractured Reservoirs, SPE Annual Technical Conference and Exhibition, New Orleans, Louisiana.

Zhengwen, Z., R. Jean-Claude, and G. Reid, 2003, Imaging the initiation of asymmetrical hydraulic fractures in laboratory experiments: SPE Annual Technical Conference and Exhibition.

Zhu, C. Y., A. Shukla, and M. H. Sadd, 1991, Prediction of dynamic contact loads in granular assemblies: Journal of Applied Mechanics, v. 58, p. 341-346.

Zoback, M. D., and B. C. Haimson, 1982, Status of the hydraulic fracturing method for in-situ stress measurements: The 23rd U.S Symposium on Rock Mechanics (USRMS).